Single-Voxel Proton Magnetic Resonance Spectroscopy in the Human Brain at 9.4 T: Methods and Applications

Dissertation

zur Erlangung des Grades eines
Doktors der Naturwissenschaften

der Mathematisch-Naturwissenschaftlichen Fakultät
und
der Medizinischen Fakultät
der Eberhard-Karls-Universität Tübingen

vorgelegt
von

Ioannis-Angelos I. Giapitzakis
aus Athen, Hellenische Republik

Tübingen
September – 2017

Tag der mündlichen Prüfung: 3. Mai 2018

Dekan der Math.-Nat. Fakultät:	Prof. Dr. W. Rosenstiel
Dekan der Medizinischen Fakultät:	Prof. Dr. I B. Autenrieth
1. Berichterstatter:	Prof. Dr. A. Henning
2. Berichterstatter:	Prof. Dr. U. Klose

Prüfungskommission:	Prof. Dr. A. Henning
	Prof. Dr. R. Kreis
	Prof. Dr. K. Scheffler
	Prof. Dr. U. Klose

Erklärung:

Ich erkläre, dass ich die zur Promotion eingereichte Arbeit mit dem Titel:

“Single-Voxel Proton Magnetic Resonance Spectroscopy in the Human Brain at 9.4T: Methods and Applications“

selbständig verfasst, nur die angegebenen Quellen und Hilfsmittel benutzt und wörtlich oder inhaltlich übernommene Stellen als solche gekennzeichnet habe. Ich versichere an Eides statt, dass diese Angaben wahr sind und dass ich nichts verschwiegen habe. Mir ist bekannt, dass die falsche Abgabe einer Versicherung an Eides statt mit Freiheitsstrafe bis zu drei Jahren oder mit Geldstrafe bestraft wird.

I hereby declare that I have produced the work entitled:

“Single-Voxel Proton Magnetic Resonance Spectroscopy in the Human Brain at 9.4T: Methods and Applications“

,submitted for the award of a doctorate, on my own (without external help), have used only the sources and aids indicated and have marked passages included from other works, whether verbatim or in content, as such. I swear upon oath that these statements are true and that I have not concealed anything. I am aware that making a false declaration under oath is punishable by a term of imprisonment of up to three years or by a fine.

Tübingen, den _____ _____

Datum Unterschrift

„Σα βγεις στον πηγαιμό για την Ιθάκη,
να εύχεσαι να 'ναι μακρύς ο δρόμος,
γεμάτος περιπέτειες, γεμάτος γνώσεις.
Τους Λαιστρυγόνας και τους Κύκλωπας,
τον θυμωμένο Ποσειδώνα μη φοβάσαι,
τέτοια στον δρόμο σου ποτέ σου δεν θα βρεις,
αν μέν' η σκέψις σου υψηλή, αν εκλεκτή
συγκίνησις το πνεύμα και το σώμα σου αγγίζει.
Τους Λαιστρυγόνας και τους Κύκλωπας,
τον άγριο Ποσειδώνα δεν θα συναντήσεις,
αν δεν τους κουβανείς μες στην ψυχή σου,
αν η ψυχή σου δεν τους στήνει εμπρός σου...“

Ιθάκη, Κ. Π. Καβάφης

"As you set out for Ithaka
hope your road is a long one,
full of adventure, full of discovery.
Laistrygonians, Cyclops,
angry Poseidon—don't be afraid of them:
you will never find things like that on your way
as long as you keep your thoughts raised high,
as long as a rare excitement
stirs your spirit and your body.
Laistrygonians, Cyclops,
wild Poseidon—you will not encounter them
unless you bring them along inside your soul,
unless your soul sets them up in front of you…"

Ithaka, C.P. Cavafy

CONTENTS

Abbreviations

^{1}H	Hydrogen atom
^{1}H-MRS	Proton magnetic resonance spectroscopy
AFP	Adiabatic fast passage pulse
B_0	Main static magnetic field
B_1^+	RF transmit field
BOLD	Blood oxygenation level dependent signal
CEST	Chemical exchange saturation transfer
CSD	Chemical shift displacement
CSF	Cerebrospinal fluid
fMRS	Functional magnetic resonance spectroscopy
FWHM	Full width half maximum
GM	Grey matter
MC	Metabolite cycling
MM	Macromolecules
OVS	Outer volume saturation
QA	Quality Assurance
RF	Radiofrequency
SAR	Specific absorption rate
SNR	Signal to noise ratio
SVS	Single voxel spectroscopy
T_1	Longitudinal relaxation time
T_2	Transverse relaxation time
TE	Echo time
TR	Repetition time
UHF	Ultra high field
WM	White matter tissue
WS	Water suppression
ω_o	Larmor frequency

Abstract

^{1}H magnetic resonance spectroscopy (^{1}H-MRS) is a non-invasive method allowing the detection as well as the quantification of several metabolites in the human brain. The introduction of ultra-high field (UHF) scanners (≥7 T) led to an increase of the signal-to-noise ratio and a higher frequency dispersion, hence better spectral resolution. These advantages promote the potential of MRS. Despite the significant advantages of UHF for MRS, several technical challenges (such as B_1^+efficiency and inhomogeneity, increased power deposition, chemical shift displacement etc.) must be addressed for the efficient utilization of these prospective benefits.

The methods and techniques developed during this Ph.D. demonstrated the feasibility of metabolite cycling (MC) at 9.4 T, and the advantages of non-water suppressed MRS regarding frequency and phase fluctuations. The newly developed sequences (MC-STEAM and MC-semi-LASER) enabled the acquisition of reliable spectra with enhanced frequency resolution, both upfield and downfield of water in ^{1}H spectra.

Furthermore, the designed RF coils, hardware setup (power splitters, phase cables, etc.), as well as, the gained knowledge regarding the achievement of efficient transmit fields and can be utilized in future MRS studies and applications.

As a result, the human brain macromolecular baseline was investigated revealing additional macromolecular peaks and information regarding their concentration levels.

Moreover, the chemical exchange rates of the downfield metabolites, as well as, their correlation with the upfield peaks were examined contributing further to the assignment of the downfield peaks.

Finally, the performed functional MRS studies in which the MC-semi-LASER sequences were used, demonstrated the potentials of UHF and MC regarding the simultaneous investigation of water and metabolites alterations during visual stimulation.

1. Introduction

The aim of this chapter is to provide the reader with the appropriate theoretical background for the understanding, of the potentials of UHF, of the developed methods and applications, as well as, of the technical challenges addressed during this doctoral research. A basic knowledge of quantum mechanics and nuclear magnetic resonance physics is assumed[1]. The following theoretical analysis is mainly focused on the hydrogen atom (^{1}H) since proton MRS is the topic of this thesis. However, equations for other atoms with a spin number of one-half can be derived similarly as well.

1.1 Advantages of MRS at Ultra High Fields

1.1.1 Signal to noise ratio

One of the major advantages of UHF is the increased signal to noise ratio (SNR). A short theoretical proof follows. More specifically, the magnetization at thermal equilibrium (M_0) generated by proton spins within a volume V with a proton density p in the presence of an external magnetic field (B_0) at a temperature (T) is given by the following formula [3]:

$$M_0 = (\gamma \cdot \hbar)^2 \frac{V \cdot p}{4 \cdot k \cdot T} B_0 \qquad \text{[Eq. 1.1]}$$

After the application of RF pulses and the rotation of the bulk magnetization from the longitudinal axis to the transverse plane, the magnetization will precess with an angular

[1] The reader is suggested to refer to the following references for a more detailed description: [1,2]

frequency (ω_o), the so-called Larmor frequency, around the axis of the static magnetic field. The Larmor frequency is given by the following equation:

$$\omega_o = \gamma \cdot B_0 \qquad \text{[Eq. 1.2]}$$

where γ is the gyromagnetic ratio of protons. The magnetization vector in the transverel plane (M_{xy}), assuming an application of an ideal 90 degree pulse and no off-resonance effects, will be given by the following formula:

$$M_{xy} = M_0 \cdot e^{i\omega_0 t} \qquad \text{[Eq. 1.3]}$$

This precessing transverse magnetization in combination with an RF coil will induce a detectable signal (S) in the RF coil, which according to Faraday's Law is:

$$S \propto Real\left[\frac{dM_{xy}}{dt}\right] \propto \omega_0 \cdot B_0 \propto {B_0}^2 \qquad \text{[Eq. 1.4]}$$

At the same time, the root mean square of the noise (N) produced on the RF coil, assuming thermal noise (Johnson-Nyquist noise [4]), is:

$$N = \sqrt{4 \cdot k \cdot T \cdot P_{diss} \cdot BW} \qquad \text{[Eq. 1.5]}$$

where BW is the receiver bandwidth, k the Boltzmann constant, T the absolute temperature and P_{diss} the dissipated power. In particular, P_{diss} consists of two components, the dissipated power within the sample (P_{sample}) and the losses in the coil (P_{coil}) [5].

$$P_{diss} = P_{sample} + P_{coil} \qquad \text{[Eq. 1.6]}$$

Assuming that the majority of losses are produced within the sample, Eq. 1.6 becomes:

$$P_{diss} \approx P_{sample} \propto \oint_V |E|^2 \, dV \qquad \text{[Eq. 1.7]}$$

where E is the electrical field produced by the sample with volume V. Using Maxwell's equations regarding electromagnetic waves and neglecting the displacement current term (low-frequency approximation), Eq. 1.7 becomes:

$$P_{sample} \propto \oint_V \left| {B_0}^2 \right| dV \qquad \text{[Eq. 1.8]}$$

Therefore, Eq. 1.5 becomes:

$$N = \sqrt{4 \cdot k \cdot T_{sample} \cdot P_{sample} \cdot BW} \propto \sqrt{|B_0|^2} \propto B_0 \qquad \text{[Eq. 1.9]}$$

Combining Eq. 1.4 and Eq. 1.9, the SNR per bandwidth is calculated as:

$$\frac{SNR}{\sqrt{BW}} = \frac{S}{N} \propto \frac{{B_0}^2}{B_0} \propto B_0 \qquad \text{[Eq. 1.10]}$$

Eq. 1.10 shows that the SNR increases with the static magnetic field (Figure 1-1).

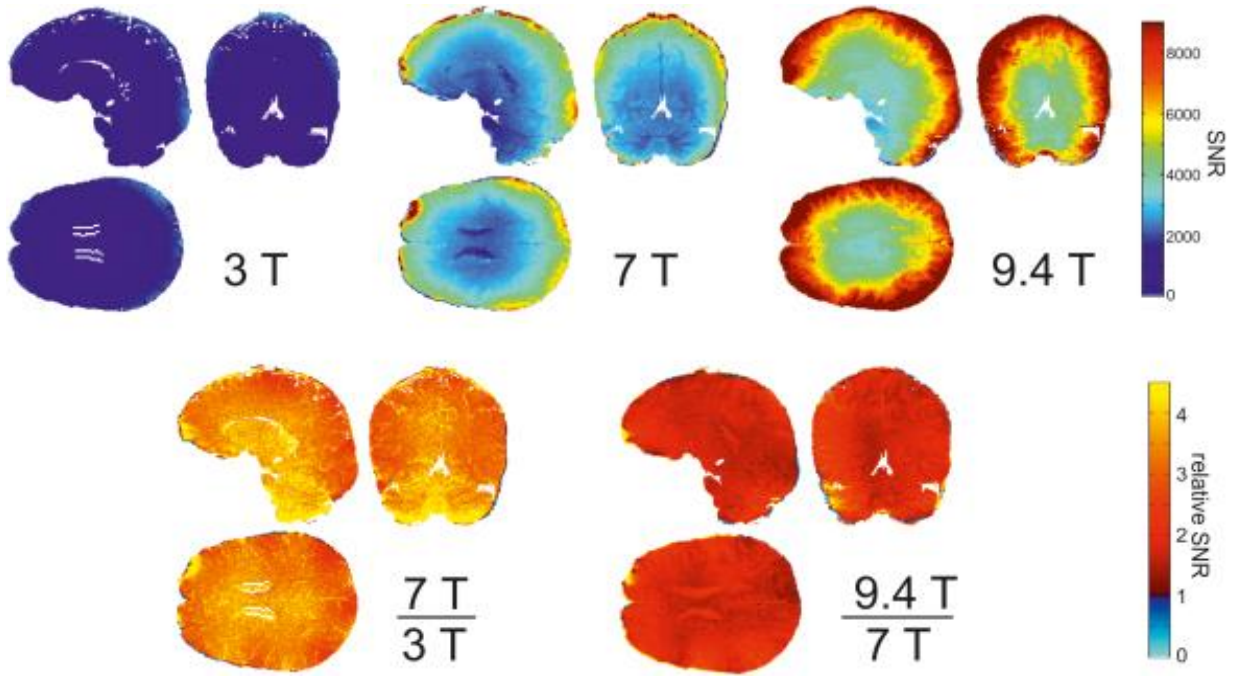

Figure 1-1: *(Top) SNR maps over three slices from the same volunteer acquired at three different static magnetic fields (3 T, 7 T and 9.4 T). (Bottom) SNR ratios between the fields. Reprinted from [6] with permission of John Wiley & Son, Inc.*

However, Eq. 1.10 involves lot of approximations and simplifications and in reality, the dependency of SNR with B_0 is super-linear. More specifically, a study [6] have shown that the SNR as a function of the external magnetic field is described by:

$$SNR = {B_0}^{\beta} \qquad \text{[Eq. 1.11]}$$

The exact value of the β parameter $(\beta >> 1)$ depends highly on the location of the acquired signal (Figure 1-2). However, a value of $\beta = 1.65$ is a good approximation for most brain compartments [6]

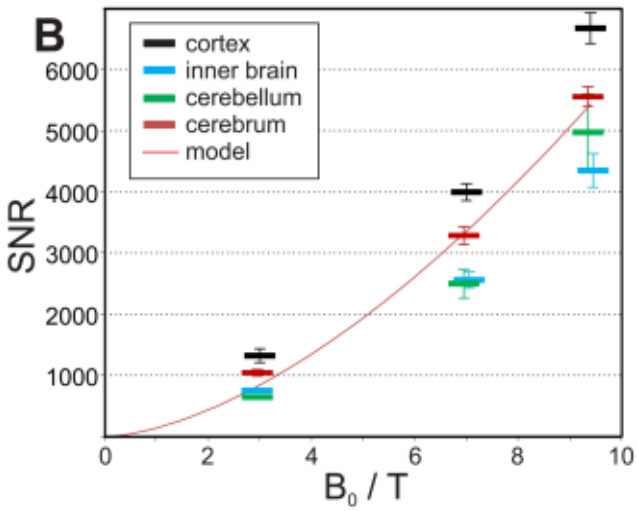

Figure 1-2: *SNR values for four different brain regions. The red line indicates fitting results on the SNR over the entire cerebrum (SNR = $B_0^{1.65}$). Adapted from [6] with permission of John Wiley & Son, Inc.*

1.1.2 Chemical shift dispersion

Proton MRS also benefits from the increased chemical shift dispersion at UHF. In particular, hydrogen spins within molecules experience different magnetic field due to the interaction of the magnetic field produced by the electrons of the molecule with the external magnetic field (B_0), the so-called chemical shift. The magnetic field (B) that is experienced by the protons' spins is

$$B = (1 - \sigma) \cdot B_0 \qquad \text{[Eq. 1.12]}$$

where σ is the chemical shift. According to Eq. 1.2 the corresponding Larmor frequency of the proton spin will be

$$\omega_0 = \gamma \cdot (1 - \sigma) \cdot B_0 \qquad \text{[Eq. 1.13]}$$

Therefore, the frequency difference ($\Delta\omega$) of two proton spins in two different chemical environments (i.e. two different metabolites) with chemical shift σ_1 and σ_2 will be:

$$\Delta\omega = \gamma \cdot (\sigma_1 - \sigma_2) \cdot B_0 \qquad \text{[Eq. 1.14]}$$

Thus, the frequency difference between these two spins increases linearly as the static magnetic field increases.

1.1.3 J-coupled spins

Another advantage of UHF regarding proton MRS is the simplification of the spectrum of strongly J-coupled spins. More specifically, the Hamiltonian ($\hat{H}_{total}$) of two strongly J-coupled hydrogen nuclei spins excluding secular dipole-dipole coupling is given by[2]:

$$\hat{H}_{total} = \omega_1 \hat{I}_{1z} + \omega_2 \hat{I}_{2z} + 2\pi \cdot J_{12} \cdot \hat{I}_1 \cdot \hat{I}_2 \qquad \text{[Eq. 1.15]}$$

where ω_1 and ω_2 are the Larmor frequencies, $\hat{I}_{1z}$ and $\hat{I}_{2z}$ the operators of the z-component of the angular momentum and $\hat{I}_1$and $\hat{I}_2$ are the operators of the angular momentum of spin 1 and spin 2 respectively and J_{12} the J-coupling constant. If matrix presentation is used for the operators, then Eq. 1.15 becomes:

$$H_{total} = \frac{1}{2}\begin{bmatrix} \omega_1+\omega_2 + \pi \cdot J_{12} & 0 & 0 & 0 \\ 0 & \omega_1-\omega_2 - \pi \cdot J_{12} & 2\pi \cdot J_{12} & 0 \\ 0 & 2\pi \cdot J_{12} & -\omega_1 + \omega_2 - \pi \cdot J_{12} & 0 \\ 0 & 0 & 0 & -\omega_1-\omega_2 + \pi \cdot J_{12} \end{bmatrix} \qquad \text{[Eq. 1.16]}$$

[2] For more details refer to chapter 14.3 in [2]

Thus, the Hamiltonian matrix ($\widehat{H}_{total}$) can be splitted in two matrices, one diagonal ($\widehat{H}_A$) and one non-diagonal ($\widehat{H}_B$):

$$\widehat{H}_{total} = \widehat{H}_A + \widehat{H}_B \qquad \text{[Eq. 1.17]}$$

where

$$H_A = \frac{1}{2}\begin{bmatrix} \omega_1+\omega_2+\pi\cdot J_{12} & 0 & 0 & 0 \\ 0 & \omega_1-\omega_2-\pi\cdot J_{12} & 0 & 0 \\ 0 & 0 & -\omega_1+\omega_2-\pi\cdot J_{12} & 0 \\ 0 & 0 & 0 & -\omega_1-\omega_2+\pi\cdot J_{12} \end{bmatrix}$$

and

$$H_B = \frac{1}{2}\begin{bmatrix} 0 & 0 & 0 & 0 \\ 0 & 0 & 2\pi\cdot J_{12} & 0 \\ 0 & 2\pi\cdot J_{12} & 0 & 0 \\ 0 & 0 & 0 & 0 \end{bmatrix} \qquad \text{[Eq. 1.18]}$$

The wavefunctions and the energy levels of the system are the eigenvectors and eigenvalues of the 4x4 Hamiltonian matrix $\widehat{H}_{total}$ respectively. Due to the presence of the off-diagonal elements, the resulting energy levels (i.e. the energy spectrum) will have more complicated form. However, if the following condition is satisfied (weak coupling condition):

$$|\pi\cdot J_{12}| \ll |\omega_1 - \omega_2| \qquad \text{[Eq. 1.19]}$$

then, the off-diagonal elements in $\widehat{H}_B$ can be ommitted since they do not contribute that much to the resulting energy levels compared to the eigenvalues of the diagonal elements in $\widehat{H}_A$. Hence, Eq. 1.17 can be approximated by (secular approximation[3]):

[3] For more details refer to Appendix A.6 in [2]

$$\widehat{H}_{total} \approx \widehat{H}_A \qquad \text{[Eq. 1.20]}$$

which is equivalent to

$$\widehat{H}_{total} = \omega_1 \hat{I}_{1z} + \omega_2 \hat{I}_{2z} + 2\pi \cdot J_{12} \cdot \hat{I}_{1z} \cdot \hat{I}_{2z} \qquad \text{[Eq. 1.21]}$$

In this case, the J-coupling interaction depends only on the z-projection of the spins, which in turn results in a simplification of the resulting spectrum of this system. Combining Eq. 1.14 and Eq.1.19 the result is the following:

$$|\pi \cdot J_{12}| \ll \gamma \cdot |\sigma_1 - \sigma_2| \cdot B_0 \qquad \text{[Eq. 1.22]}$$

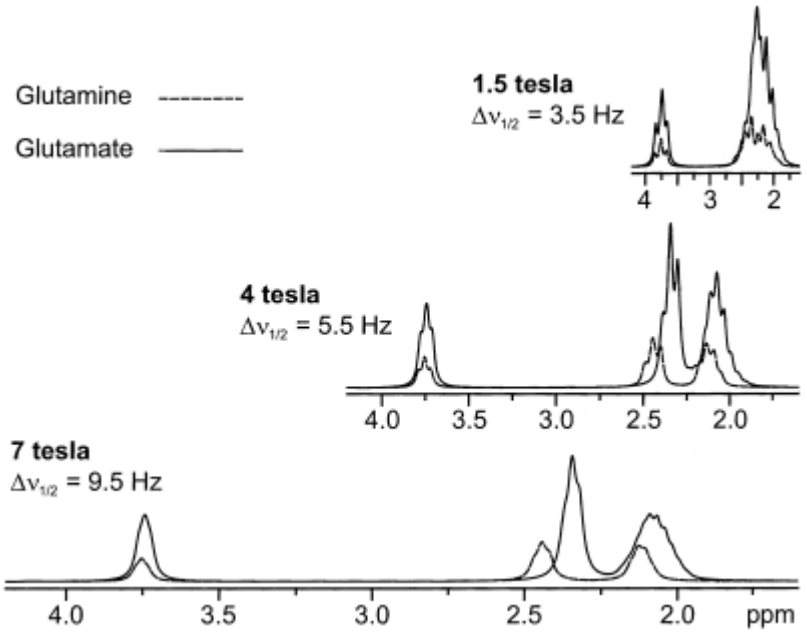

Figure 1-3: *Simulated spectra of glutamine and glutamate at different magnetic fields assuming a linear increase of linewidth ($\Delta\nu_{1/2}$) with the magnetic field. At higher fields, metabolites exhibiting strong J-coupling shift towards the weak coupling regime. As a result, strongly coupled spin systems such as glutamine and glutamate become visible at 7 T. Adapted from [7] with permission of John Wiley & Son, Inc.*

Thus, at higher magnetic fields, metabolites exhibiting strong J-coupling shift towards the weak coupling regime resulting in simplification of the energy levels and therefore of the detected spectrum (Figure 1-3).

1.1.4 Summary

To sum up, the advantages of UHF regarding MRS are:

- the higher SNR
- the increase of chemical shift dispersion
- the simplification of spectra of strongly J-coupled spins

These advantages promote and further enhance the potential of MRS [8,9] by allowing the detection and quantification of more metabolites (Figure 1-4). Noteworthy, published studies have demonstrated the detection of up to 18 metabolites both in human and rodents' brain at UHF [10-14].

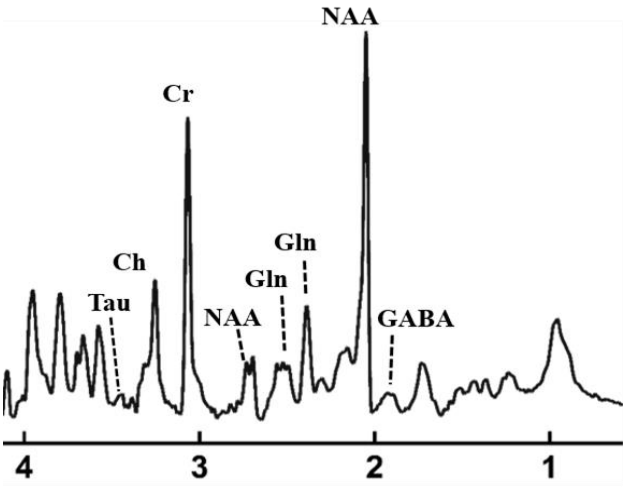

Figure 1-4: *^{1}H MR spectrum acquired at 9.4T from the occipital lobe of a healthy volunteer using metabolite cycled STEAM sequence [15]. Higher magnetic fields enable acquisition of higher spectral resolution spectra. Several metabolites can be detected at 9.4 T.*

1.2 Technical Challenges of MRS at Ultra High Fields

Despite the significant advantages of UHF for MRS, several technical challenges have to be addressed for the efficient utilization of these prospective benefits. In particular, the severe B_1^+ inhomogeneity due to destructive interference [6,16,17], the increased chemical shift displacement (CSD) of different metabolites caused by the larger frequency range induced by chemical shift and the requirement of short echo time (TE) sequences due to shorter transverse relaxation times (T_2) are critical problems.

1.2.1 Chemical shift displacement

Under the presence of a localization gradient (G_x) the Larmor frequency at position x shifts by:

$$\omega = \gamma \cdot G_x \cdot x \qquad \text{[Eq. 1.23]}$$

Thus, the total precession frequency at this point is:

$$\omega_x = \omega_0 + \omega = \omega_0 + \gamma \cdot G_x \cdot x \qquad \text{[Eq. 1.24]}$$

According to Eq. 1.24 the spatial displacement (Δ_X) between two resonances ω_1 and ω_2 ($\omega_2 = \omega_1 + \Delta\omega$) will be:

$$\Delta_X = -\frac{\omega_2 - \omega_1}{\gamma \cdot G_x} \qquad \text{[Eq. 1.25]}$$

In the case of localized spectroscopy, the dimension of the excited voxel along axis x (V_x) is given by:

$$V_x = \frac{BW_{RF}}{\gamma \cdot G_x} \qquad \text{[Eq. 1.26]}$$

where BW_{RF} is the bandwidth of the excitation pulse. Thus, the chemical shift displacement (CSD_x) in direction x between two resonances with frequency difference $\Delta\omega$ produced by an excitation pulse with a bandwidth BW is described by the following expression (combining Eq. 1.25 and 1.26):

$$CSD_x = -\frac{\omega_2 - \omega_1}{BW_{RF}} V_x \qquad \text{[Eq. 1.27]}$$

The negative sign indicates the direction of the displacement. In particular, when $\omega_2 > \omega_1$ then $CSD_x < 0$, which means that the voxel of resonance ω_2 will shift to more negative x

values (x-) compare to ω_1 (Figure 1-5). In the opposite scenario, $\omega_2 < \omega_1$, CSD_x will be positive which means that the voxel of resonance ω_2 will shift to more positive x values (x+) compare to ω_1. Eq. 1.27 in combination with Eq 1.14 becomes:

$$CSD_x = -\frac{\gamma \cdot (\sigma_1 - \sigma_2) \cdot B_0}{BW_{RF}} V_x \qquad \text{[Eq. 1.28]}$$

Thus for a given BW_{RF}, CSD increases as the magnetic field increases. Consequently, due to the CSD, acquired signals are generated from different voxels, which in turn results in degradation of spatial accuracy and artifacts such as lipid contamination.

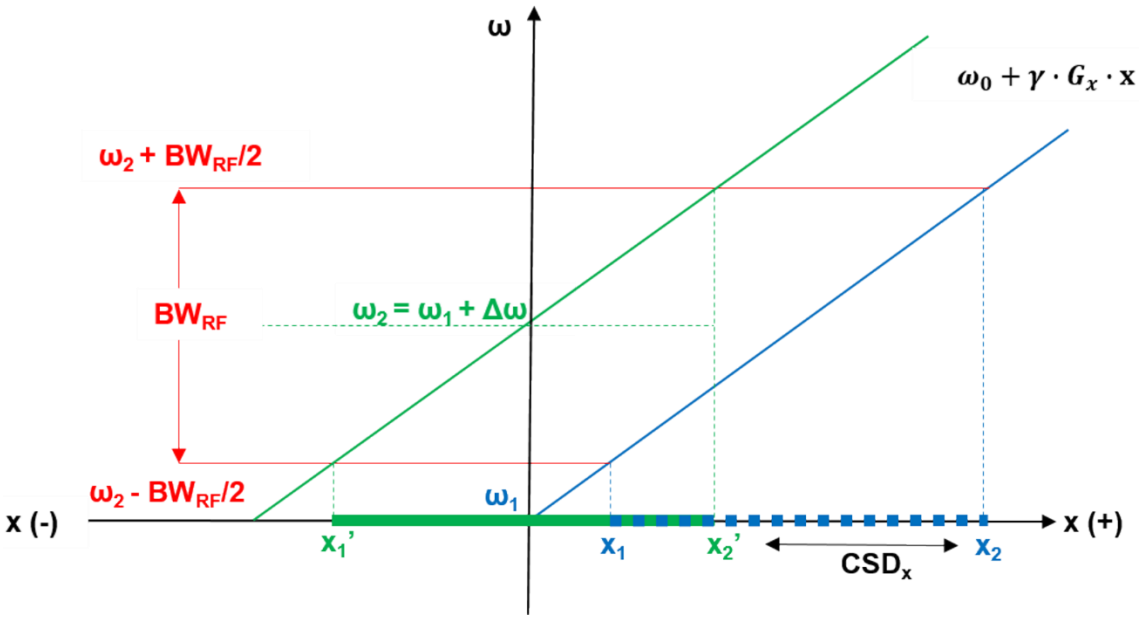

Figure 1-5: *Schematic diagram indicating chemical shift effect. Metabolites with different Larmor frequency are excited in different locations under the presence of a localization gradient. As a result, signals from the several metabolites are generated from different voxels. The chemical shift displacement between two metabolites depends on the frequency difference, the bandwidth of the excitation pulse and the voxel size.*

1.2.2 B_1^+ inhomogeneity

The increase of B_1^+ inhomogeneity at UHF can be explained using electromagnetic wave theory. In particular, the wavenumber (k) of a plane wave in a general lossy medium is given by the following equation[4] [18]:

$$k = \omega \sqrt{\mu_r \cdot \mu_0 \cdot \varepsilon_r \cdot \varepsilon_0 (1 - j \frac{\sigma}{\omega \cdot \varepsilon_r \cdot \varepsilon_0})} \qquad \text{[Eq. 1.29]}$$

where ω is the frequency, ε_0 and μ_0 the permittivity and permeability in vacuum respectively, ε_r and $\mu_r$the relative permittivity and permeability of the medium respectively, and σ the conductivity. Both ε_r and σ are frequency-dependent [19] (Figure 1-6). As Figure 1-6 illustrates, k increases as the frequency increase for a brain region with a composition of 50% white matter and 50% gray matter.

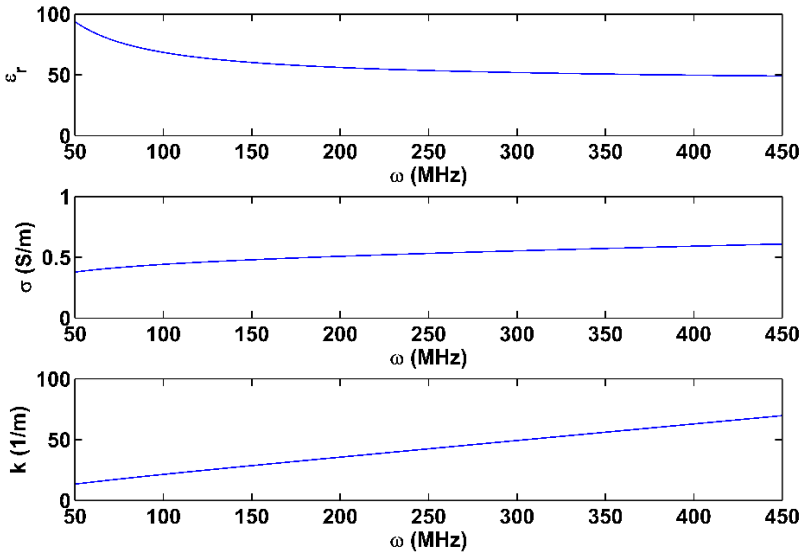

***Figure 1-6**: (Top) Relative permittivity (ε_r); (Middle) Conductivity (σ) and (Bottom) Wavenumber (k) as a function of frequency (i.e. External magnetic field). The graphs were derived using published values in [19] assuming a brain region consisting of 50% gray and 50% white matter. Wavenumber (1/m) increases as the frequency increases.*

[4] For more details please refer to Eq. 1.51 (Chapter 1.4) in the following book: [18]

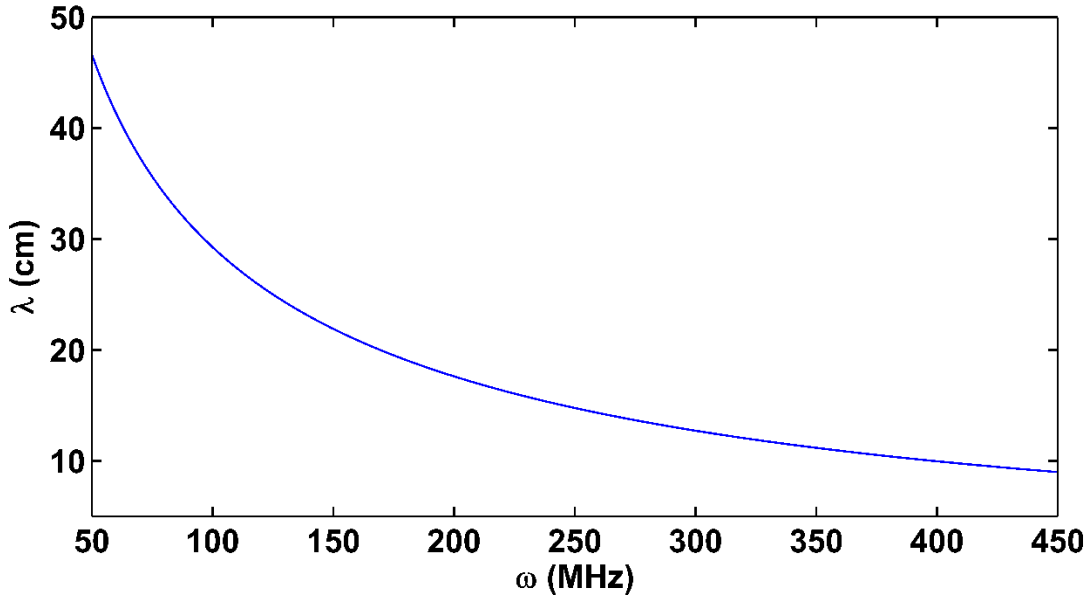

Figure 1-7: *Magnitude of wavelength (λ) as a function of frequency (MHz) calculated based on Eq. 1.30 and 1.29 using published values in [19]. As the magnetic field increases (i.e., the frequency) the wavelength becomes smaller and comparable to human brain size. Consequently, standing wave effects occur in the B_1^+ excitation profile (see also* Figure 1-8*).*

However, the wavelength (λ) of an electromagnetic wave is inversional proportional of the wavenumber k (Eq. 1.30).

$$\lambda = \frac{2\pi}{k} \qquad \text{[Eq. 1.30]}$$

Figure 1-7 demonstrates the wavelength of electromagnetic waves as a function of frequency. In particular, at 300 MHz (7 T) the wavelength is about 12cm while at 400 MHz is about 10cm in the human brain, which is comparable to the size of the human head, as well as, of other parts of the human body. As a result, standing wave effects occur in the B_1^+ excitation profile leading to an increase of the B_1^+ inhomogeneity (Figure 1-8).

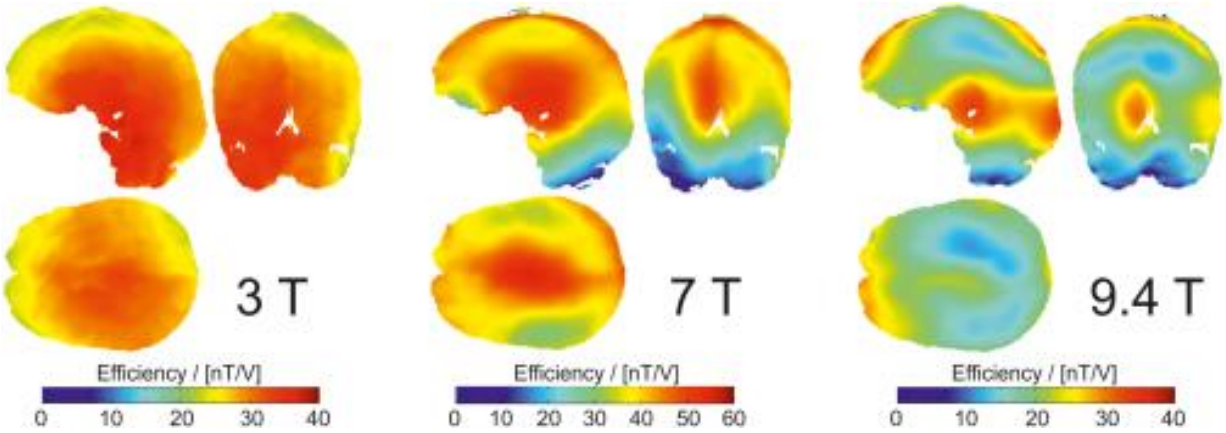

Figure 1-8: *B_1^+ maps (nT/V) of three similar coils used in different external magnetic fields strength (3 T, 7 T and 9.4 T). Reprinted from [6] with permission of John Wiley & Son, Inc.*

1.2.3 B_1^+ efficiency and SAR

The deposited power in the sample per kilogram (kg), the so-called specific absorption rate (SAR), at location $\vec{r}$ is given by:

$$SAR(\vec{r}) = \frac{\sigma(\vec{r}) \cdot \left|\vec{E}(\vec{r})\right|^2}{2 \cdot \rho(\vec{r})} \qquad \text{[Eq. 1.31]}$$

where $\vec{E}(\vec{r})$ is the local electric field, $\sigma(\vec{r})$ is the local conductivity and $\rho(\vec{r})$ is the density. Both $\vec{E}(\vec{r})$[5] and, $\sigma(\vec{r})$ increases as the static magnetic field increases (see Figure 1-6 C). Consequently, at higher magnetic fields, the energy absorbed by the subject elevates and the required power for the achievement of a given B_1^+ increases (since greater part of the energy converts to thermal energy[6]). Hence, the B_1^+ efficiency (μT/W) decreases (Figure 1-8) and SAR increases at UHF.

[5] According to Maxwell-Faraday Equation: $\vec{\nabla} \times \vec{E} = -i\omega_0 \overrightarrow{B_1}$, where ω_0 the Larmor frequency (see Eq. 1.2).

[6] The main mechanism for the heating is the induction of eddy currents due to the nonzero conductivity of the tissue (induction heating) [20].

1.2.4 B_0 inhomogeneity

According to electromagnetic theory, an external magnetic field H will produce a magnetic induction B within a material. In the case of a linear, isotropic, nondispersive medium, the relationship between the external magnetic field and the magnetic induction is given by the following relationship:

$$B = \mu \cdot H \overset{H=B_0}{\Longrightarrow} B = \mu \cdot B_0 \qquad \text{[Eq. 1.32]}$$

where μ is the magnetic permeability of the medium, and B_0 is the external static magnetic field. Different tissues have different magnetic permeabilities ($\Delta\mu$), resulting in different magnetic inductions between the tissues, the so-called B_0 inhomogeneity (ΔB_0; Eq. 1.33 and Figure 1-9).

$$\Delta B_0 = \Delta\mu \cdot B_0 \qquad \text{[Eq. 1.33]}$$

Eq. 1.33 indicates that the B_0 inhomogeneity scales up with increasing B_0. Additionally, B_0 inhomogeneity results in a faster relaxation of the transverse magnetization, the so-called T_2^* which is given by the following formula:

$$\frac{1}{T_2^*} = \frac{1}{T_2^+} + \gamma \cdot \Delta B_0 \qquad \text{[Eq. 1.34]}$$

where T_2^+ is the apparent relaxation time of the transverse magnetization (see chapter 1.2.5) and γ is the gyromagnetic ratio. At the same time, the linewidth of the Lorentzian peak of a metabolite in the frequency domain, expressed as the full width half maximum ($FWHM$), is given by the following equation:

$$FWHM = \frac{1}{\pi T_2^*} \overset{Eq.1.34}{\Longleftrightarrow} FWHM = \frac{1}{T_2^+} + \gamma \cdot \Delta B_0 \qquad \text{[Eq. 1.35]}$$

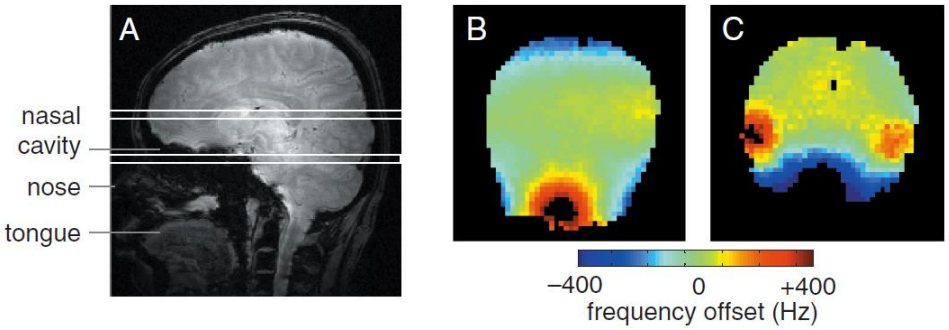

Figure 1-9: *A) Anatomical image of a human head, sagittal plane. B & C) Axial B_0 maps acquired at 4T from different locations shown in (A) after the performance of second-order shimming. Regions with different tissues and properties such as the sinus cavity (air) and the auditory tracts exhibit high B_0 inhomogeneity. The figure was adapted from [3] with permission of John Wiley & Son, Inc.*

According to Eq. 1.35, increased static magnetic field inhomogeneity results in broadening of metabolites peaks. Thus, reduction of frequency resolution (Figure 1-10).

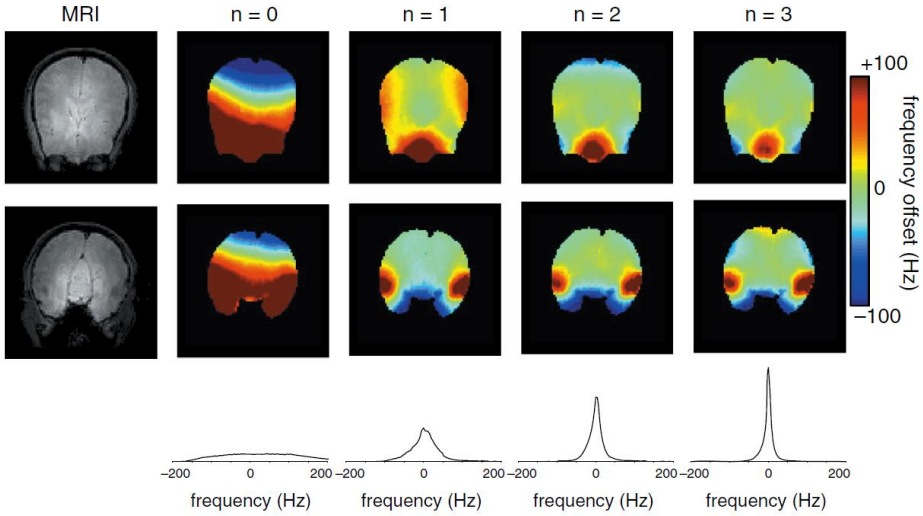

Figure 1-10**:** *The effect of B_0 inhomogeneity on water linewidth of the entire human head at 4T. As the shimming order increases (n) the inhomogeneity of the external magnetic field decreases. As a result, the linewidth of water decreases and the water peak is better observable. Adapted from [3] with permission of John Wiley & Son, Inc.*

1.2.5 T_1 and T_2 relaxation time

The first complete theory describing the origins of the relaxation of the longitudinal (T_1) and transverse (T_2) magnetization was proposed by Bloembergen, Purcell, and Pound in 1948, the so-called BPP theory [21]. In this theory, the main cause of the relaxation is the dipole-dipole interaction between the different molecules. The dependency of the relaxation times T_1 and T_2 as a function of the frequency (i.e. the external static magnetic field) is given by the following equations[7]:

$$\frac{1}{T_1} = \frac{3}{10}\frac{\gamma^4 h^2}{4\pi^2 r^6}\left(\frac{\tau_c}{1+\omega^2\tau_c^2} + \frac{4\tau_c}{1+4\omega^2\tau_c^2}\right) \qquad \text{[Eq. 1.36]}$$

$$\frac{1}{T_2} = \frac{3}{20}\frac{\gamma^4 h^2}{4\pi^2 r^6}\left(3\tau_c + \frac{5\tau_c}{1+\omega^2\tau_c^2} + \frac{2\tau_c}{1+4\omega^2\tau_c^2}\right) \qquad \text{[Eq. 1.37]}$$

The τ_c number is the so-called rotation correlation time and characterizes the frequency of the rotational processes. In general, molecules with slow rotational frequencies exhibit smaller T_2 and T_1 relaxation times. Eq. 1.36 and 1.37, as well as, Figure 1-11 indicate that T_1 increases with higher magnetic fields, while T_2 appears virtually independent from the external magnetic field. However, in vivo T_2 relaxation time demonstrate a decrease with increasing magnetic field. The reason for this disagreement, between in-vivo measured T_2 relaxation times [22-25] and BPP theory has to do with the fact that in BPP theory mainly the dipole-dipole interaction is taken into consideration. In reality, diffusion and other processes contribute to the total T_2. More specifically, the apparent transverse relaxation time (T_2^+) is given by the following equation [22]:

$$\frac{1}{T_2^+} = \frac{1}{T_2} + \frac{1}{T_{2,Diffusion}} + \frac{1}{T_{2,Exchange}} \qquad \text{[Eq. 1.38]}$$

[7] For the derivation of the equations and the rotation correlation time t_c, please refer to chapter 3.2.1 in [3]

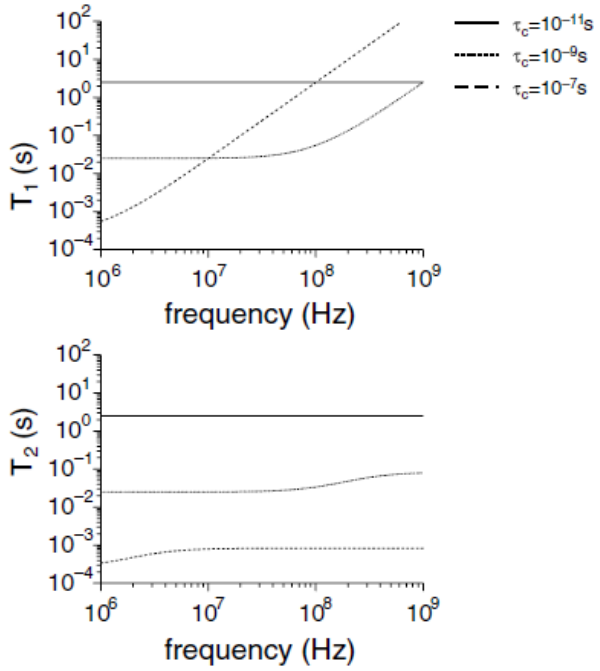

Figure 1-11: *T_1 and T_2 relaxation time as a function of the magnetic field for three different correlation times t_c. For chemical compounds with slow rotation, the T_1 demonstrates a high increase with increasing magnetic field. However, T_2, based on BPP theory seems to be independent of the external magnetic field assuming only dipole-dipole interaction. Adapted from [3] with permission of John Wiley & Son, Inc.*

where T_2 is the intrinsic relaxation time mainly due to the dipole-dipole interaction and $T_{2,Diffusion}$ and $T_{2,Exchange}$ the relaxation times due to the diffusion of the molecules and exchange of spins between locations with different magnetic fields (i.e. bound to distinct molecules) respectively. Neglecting the relaxation time due to the exchange and utilizing the study of Carr and Purcell [26] in which they investigate the diffusion of water with the application of refocusing pulses with interpulse interval τ_{cp}, Eq. 1.38 simplifies to:

$$\frac{1}{T_2^+} = \frac{1}{T_2} + \frac{D}{12}(G \cdot \gamma \cdot \tau_{cp})^2 \qquad \text{[Eq. 1.39]}$$

where D is the apparent diffusion and G is the magnetic field gradient which is created either by the externally applied gradient pulses or the microscopic susceptibility gradient induced by the heterogeneous tissues. However, as it was described in chapter 1.2.4, both the macroscopic and microscopic susceptibility variations scale linearly with the magnetic field (see Eq. 1.33). Thus, at higher magnetic fields the T_2^+ is smaller (Figure 1-12). Additionally, in MR sequences, the SNR of the signal acquired at a given TE is inversely proportional to T_2^+[8].

$$SNR \propto e^{-\frac{TE}{T_2^+}} \qquad \text{[Eq. 1.40]}$$

Hence, at higher magnetic fields, the SNR of the signal decreases quicker for a given TE. For this purpose, sequences with short TE are required at UHF to maintain the full SNR gain.

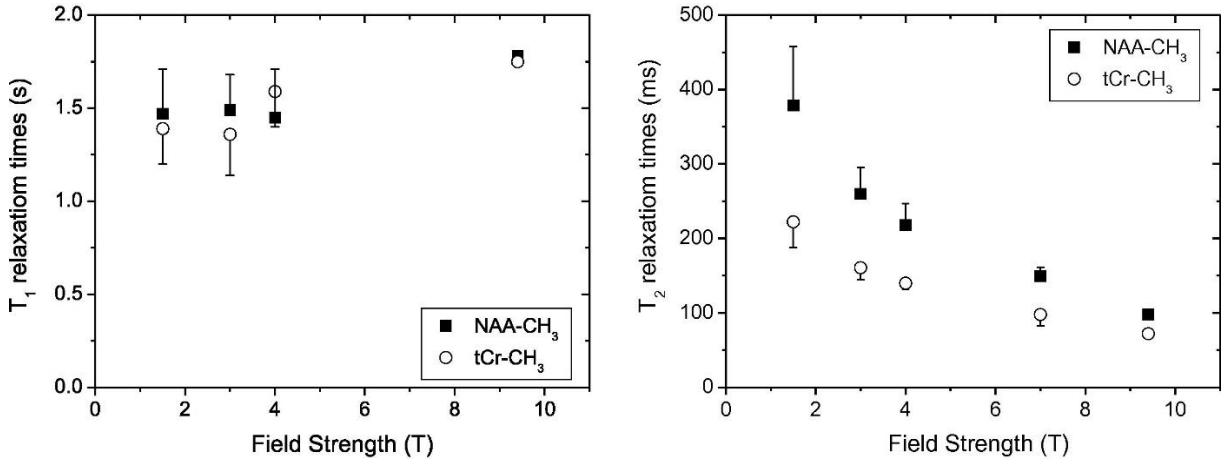

***Figure 1-12**: T_1 and T_2^+ (indicated as T_2) relaxation times of in vivo measured NAA (acetyl moiety) and total creatine (tCr) in the human head at 9.4T as a function of the magnetic field. T_2^+ decreases as the magnetic field increases. The figure was copied from [23] with permission of Elsevier, Inc.*

[8] For the rest of this document, the apparent transverse relaxation time (T_2^+) will be indicated as T_2

2. Thesis Synopsis

2.1 Scientific Goals

The purposes of this doctoral study were the utilization of the advantages of ultra-high fields (UHF) and the development of new methods for the performance of single-voxel proton magnetic resonance spectroscopy (^{1}H-MRS) in the human brain at 9.4 T. The developed methods were implemented in applications such as the characterization of human brain macromolecules, the investigation of the downfield spectrum and the changes of the human brain metabolites and water signal under visual stimulation (f-MRS).

During this Ph.D. research, several methods and techniques regarding MRS localization, post-processing, radiofrequency (RF) coils were developed and optimized. The projects conducted during this Ph.D. are presented and discussed in chronological order to highlight the steps and the way that each technical challenge was addressed.

Note: The purposes of this section is to provide to the reader a synopsis for each manuscript avoiding a detailed description. For more details please refer to the corresponding publication/manuscript (chapter 7).

2.2 Safety evaluation of self-developed RF coils

Summary of the published journal paper entitled “Safety testing and operational procedures for self-developed radiofrequency coils” (NMR Biomed 2016;29:1131-44). Please refer to the List of Publications and Statement of Contibutions sections for more details.

2.2.1 Introduction

One of the first steps for the acquisition of reliable MRS spectra was the use of RF coils that could provide efficient B_1^+ fields and good reception as well. As it mentioned in the

introduction section (paragraphs 1.2.2 and 1.2.3), at UHF B_1^+ efficiency and inhomogeneity is a critical technical challenge.

For this purpose, the development and the design of self-developed RF coils were essential. This necessity also arose from the fact that no commercial coils were available for 9.4 T since no company produced RF coils for human applications at 9.4 T, mainly due to the small market interest (at the time of this Ph.D. only four sites worldwide were equipped with 9.4 T scanner systems for humans).

Therefore, our department had to develop its own RF coils. However, any RF coil must meet the strict requirements for safe application on humans [27-31] with respect to mechanical and electrical safety. Also, RF transmission during the MR examination must comply with specific SAR limits and must not raise the tissue temperature above certain levels. Although limits for local energy deposition and temperature increase are defined, e.g. by International Electrotechnical Commission (IEC) norms [27], a standardized method to test UHF RF coils for safe operation in compliance with these limits was lacking.

Thus, safety evaluation of our coils was an essential step before any in vivo measurement, and it was demanded by the local ethics committee. However, an assessment of our developed coil by third parties would request a significant amount of money per coil evaluation (> 40,000 euros). Also, the evaluation procedure would include mainly safety tests regarding the electrical and electronic components of the coil and no

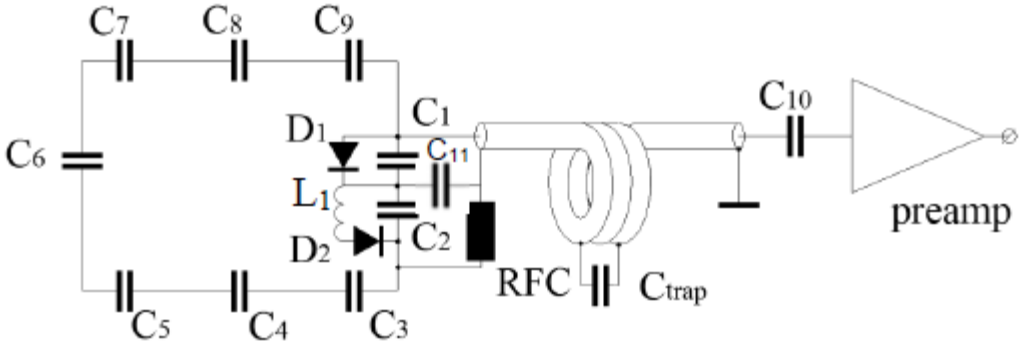

***Figure 2-1**: An example of a schematic of a vertical receive-only loop used in an 8Tx16Rx coil [32].*

other crucial issues at UHF such as SAR distribution. Moreover, potential evaluation of our coils by externals would restrict our research due to the high cost demanded for the evaluation of the different coils, as well as, the necessity of external re-evaluation of our coil in case of modifications (such as the introduction of additional receivers, different phase arrangements or power distributions).

For this purpose, in April of 2013, the department of High-Field Magnetic Resonance at the Max Planck Institute for Biological Cybernetics initiated an effort to develop a protocol consisting of a series of operational procedures for the development, testing, and application of self-developed MR Coils [28]. The procedures comprise i) coil and system type specification; (ii) electrical and mechanical safety and performance tests; (iii) numerical SAR analysis; (iv) electrical failure mode and risk analysis; and (v) documentation, user training and quality assurance (QA) (Figure 2-1).

2.2.2 Electrical and Mechanical Safety and Performance Tests

The tests are conducted on phantoms with similar dielectric properties and loading conditions of the human body. Performance evaluation of the coil ensures optimal image quality and signal to noise ratio. Safety tests are obligatory for the safe function of the coil (Figure 2-2).

2.2.3 Numerical SAR Analysis

Except the safety and performance tests ensuring good image quality and safe operation of the coil, the SAR distribution within the human body has to be determined (Figure 2-3). Temperature and SAR limits set by the IEC [27] have to be complied by the coil. Finally, validation of the SAR prediction method by comparison with experimentally accessible data is performed in accordance with IEC guidelines (Figure 2-4).

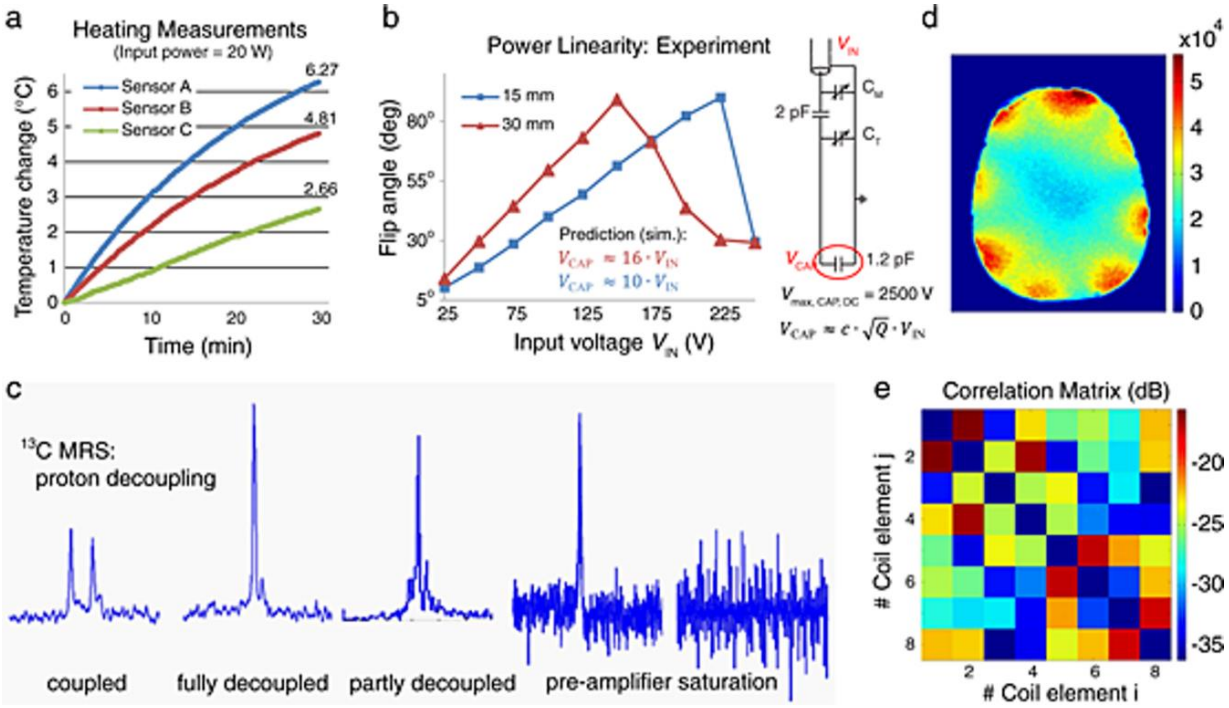

Figure 2-2: *Examples of performance and safety tests. (a) Temperature increase during the radiofrequency (RF) heating test measured on the housing of a four-channel surface coil . (b) Measurement of the linear relationship between flip angle and input voltage for a microstrip element at two distances to a phantom. As predicted by simulations, the voltage at the terminating capacitor (red circle) exceeds its maximum working voltage and starts to fail (sparking). (c) Proton decoupling test in the case of a nested ^{1}H and ^{13}C dual-tuned birdcage coil arrangement. The desired decoupling behavior is illustrated by the two figures on the left. The characteristic spectral pattern in the case of insufficient proton power, resulting in incomplete decoupling (middle right), and noise enhancement and spikes caused by pre-amplifier saturation (right) resulting from insufficient isolation of the ^{1}H and ^{13}C coils. (d) Signal-to-noise ratio (SNR) map in a phantom. (e) Noise correlation matrix (dB) for an eight-channel transmit/receive (Tx/Rx) array. Figure replicated from [28] with permission of John Wiley and Sons, Inc.*

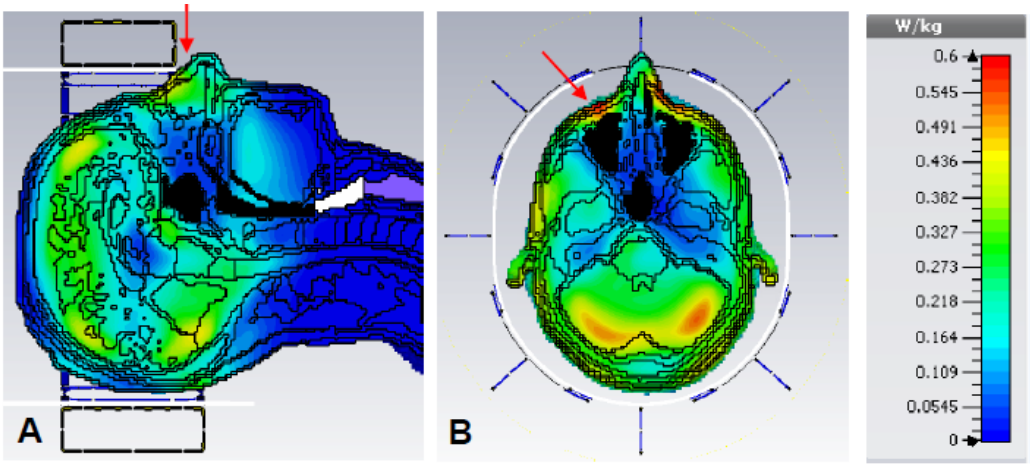

***Figure 2-3**: A) Sagittal and B) transverse SAR maps calculated for the circular polarized (CP) excitation mode of an 8Tx16Rx array [33]. Arrows show the position of the transverse slice (A) and the maximal local SAR (B). Figure adapted from the coil file of the 8Tx16Rx array.*

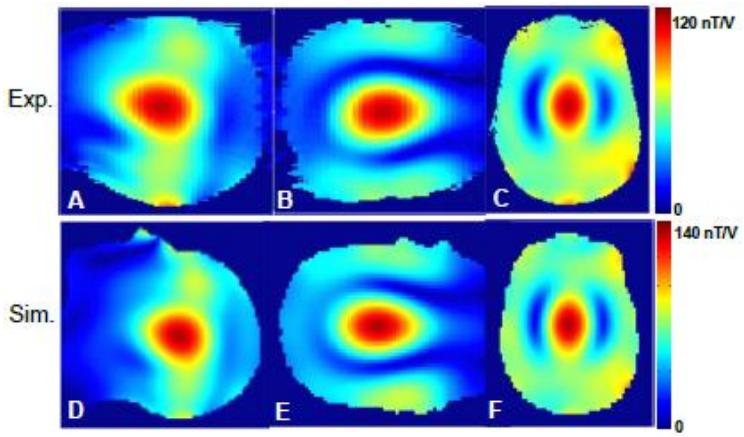

***Figure 2-4:** Experimental (A,B,C) AFI and simulated (D,E,F) B1+ maps of the CP mode obtained for sagittal (A,D), coronal (B,E), and transverse (C,F) projections through the center of a head/shoulder phantom produced by an 16Tx30Rx array [34], which approximately corresponds to the maximal value of the B1+ field. The maximum scale for all maps is calculated using the average B1+ over corresponding transverse slice multiplied by a factor of 1.5. Figure copied from the coil file of the 16Tx30Rx array.*

2.2.4 Electrical Failure Mode and Risk Analysis

The rationale of this step is to investigate the potential failure modes of the electrical components in the coil during function and the potential threat for the subject (Table 2-1). Each risk is characterized by two values: (i) the severity (S) of the possible adverse consequence; and (ii) the likelihood (L) of occurrence of each consequence. The rating (R) of each risk factor is estimated using the product of the severity multiplied by the likelihood (R = L × S). Finally, each potential danger is placed in a risk profile matrix in which the columns and rows show the severity and likelihood, respectively. Serious injuries during the operation of RF coils, such as an electrical shock or skin burn, can be practically eliminated by the coil design, the safety test procedures and the regular QA.

2.2.5 Documentation, User Training and Quality Assurance (QA)

Documentation, extensive user training, and regular tests are essential for the optimal and correct operation of the coil. A detailed documentation of each coil is provided to the user. The documentation provides a description of the electrical components and characteristics of the coils, instructions for the installation and correct usage of the coil, as well as, records describing the history of the coil.

2.2.6 Conclusion

After the establishment of the procedures for the evaluation of self-developed coils several RF coils and new designs were developed enabling the acquisition of MR data at 9.4 T, as well as, the increase of B_1^+ efficiency, which is essential for single voxel spectroscopy (SVS) at 9.4 T. The reader can find more information regarding some of the new coils produced in our institute in the following references: [32,34-37], as well as, in the next chapters.

#	Item	Potential Failure Mode	Potential Effect of Failure	Potential Cause of Failure	Risk Control by Design	Risk Control by Action
1	Distributed Capacitors (C_{4-13}) TX mode	Component failure Open/Short	Coil element detunes causing change of the E-field and B-field pattern and thus change with regard to SAR.	Improper component selection; aging of components	Use capacitors with appropriate power rating (see 5.1, 6.6); regular QA to recognize aging early on	scanner implemented power monitoring system stops the scan in case of high power reflection
2	Decoupling RID Circuits (C_{14} and corresponding Inductors) TX mode	Component failure Open/Short	RID failure produces coupling b/w elements causing change of the E-field and B-field pattern and thus change with regard to SAR.	Improper component selection; aging of components	Use capacitors with appropriate power rating (see 5.1, 6.6)	Perform periodic image quality check
3	Matching Circuit (C_{1-3}) TX mode	Component failure Open/Short	RF power reflection causing change of the E-field and B-field pattern and thus change with regard to SAR.	Improper component selection; aging of components	Use capacitors with appropriate power rating (see 5.1, 6.6)	Perform periodic image quality check
4	Pre-amplifier RX mode	Component failure Open/Short	Degradation in SNR	Improper component selection; aging of components	Protection diodes are installed on each preamplifier. Preamplifier reliability was verified via test.	Perform periodic image quality check
5	Cable traps (C_{15})	Component failure Open/Short	High shield current	Improper component selection;	The traps on the single channel have capacitors	Cable traps are installed in such a way that they

Table 2-1: *Example of some of the potential hazards with a 8Tx16Rx array [32]. Table reproduced from the coil file of the 8Tx16Rx array.*

2.3 Metabolite-cycled STEAM and semi-LASER at 9.4 T

Summary of the published journal paper entitled “Metabolite-cycled STEAM and semi-LASER localization for MR spectroscopy of the human brain at 9.4T” (*Magnetic Resonance in Medicine*, DOI: 10.1002/mrm.26873). Please refer to the List of Publications and Statement of Contibutions sections for more details.

2.3.1 Introduction

After the development of coils for the acquisition of MRS data at 9.4 T (see the previous paragraph), the design and the optimization of new spectroscopic sequences at 9.4 T were essential. For this purpose, two new sequences for UHF MRS in the human brain at 9.4T utilizing the so-called metabolite cycling (MC) technique were developed. In particular, an asymmetric adiabatic fast passage pulse (AFP) optimized for MC at 9.4 T was incorporated with STEAM and semi-LASER optimized to account for inhomogeneous transmit fields and minimizing CSD.

In particular, a previous study at 9.4 T has shown the potentials of MRS at 9.4 T for the quantification of metabolites in the occipital lobe of the human brain [23]. Due to the increased B_1^+ inhomogeneity at UHF, most studies at UHF utilize localization schemes based on adiabatic refocusing [11,38]. The advantage of adiabatic pulses is their insensitivity against B_1^+ inhomogeneity. However, AFP requires normally high B_1^+ peak power. As a consequence, their implementation can introduce high SAR. A suitable compromise between TE and power deposition with adiabatic refocusing is the semi-LASER sequence [11,39,40]. In semi-LASER, localization is performed by a conventional slice-selective excitation pulse followed by two pairs of refocusing AFP. In this way, a full intensity signal is acquired at reasonably short TEs (e.g. 25 ms [11]). Moreover, the high bandwidth of the refocusing AFP leads to lower CSD. In addition, refocusing AFP pulses typically have good slice profiles with little refocusing outside of their bandwidth leading to improved excitation profiles largely devoid of lipid contaminations and significantly reduces the need for outer volume suppression (OVS) (Figure 2-5).

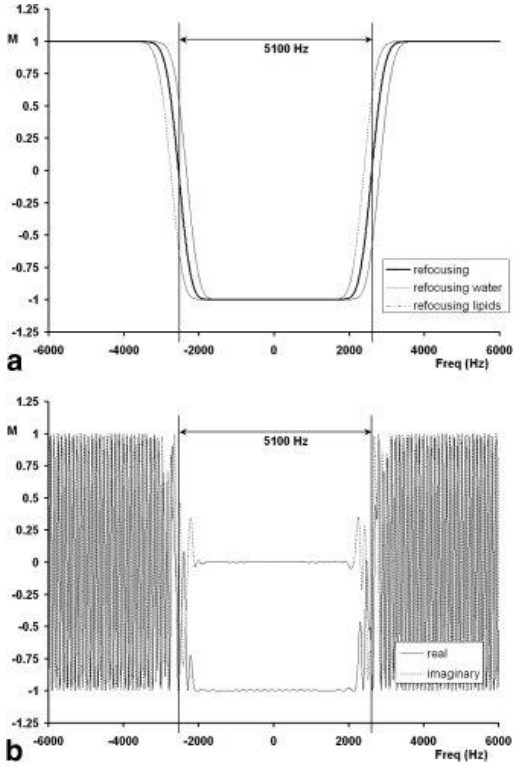

***Figure 2-5**: Magnetization profile of one adiabatic full passage 180° refocusing pulse. Magnetization inversion over the slice profile (**a**) is done with a spectral bandwidth of 5100 Hz. Due to the high bandwidth the CSD of different compounds at 3T is relatively small. The phase of the magnetization is refocused by the second AFP pulse (**b**): outside the slice profile the spins are not refocused. Figure was replicated from [39] with permission of John Wiley and Sons, Inc.*

2.3.2 Asymmetric Adiabatic Pulse for Metabolite Cycling at 9.4 T

Water suppression is an essential part of MRS [41,42] for the prevention of gradient modulation sidebands and baseline distortions, which become more crucial at UHF since stronger gradient amplitudes are required.

However, studies implementing non-water-suppressed MRS techniques, such as MC [43], have shown their potential in addressing these challenges. MC allows the simultaneous acquisition of water and metabolite spectra without scan time prolongation or the requirement for a water reference scan.

The principle of MC is the adiabatic inversion of the upfield and downfield part of the spectrum in an alternative manner without affecting the water signal. Consequently, subtraction of two successive acquisitions leads to a “pure” metabolite spectrum while a summation to a water reference signal (Figure 2-6).

MC has been implemented in PRESS, LASER sequences[9] [45-47] where the non-water-suppressed signal was used for frequency, and phase alignment before averaging as well as eddy current correction [48-50]. MC technique has also been utilized for chemical exchange saturation transfer experiments of the downfield resonances in the human brain and muscle [47,51,52]. In this study, for the inversion of upfield and downfield metabolite signals at 9.4 T, an asymmetric adiabatic pulse (InvP) was designed.

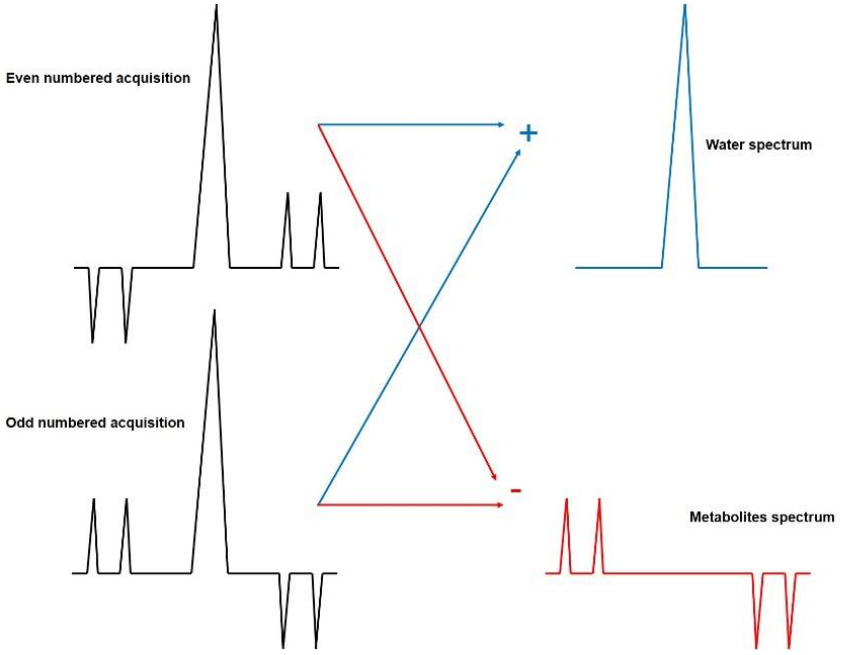

***Figure 2-6**: Schematic representation of metabolite cycling technique. Adiabatic inversion pulses are used to invert the metabolite signals on alternating scans (either the resonances upfield or downfield from water), so that subtraction of even from odd scans results in ‘water suppressed’ spectra*

[9] MC was also combined with a STEAM sequence in a pilot study at 7T. However, the resulting spectra exhibited some artifacts due to hardware issues [44].

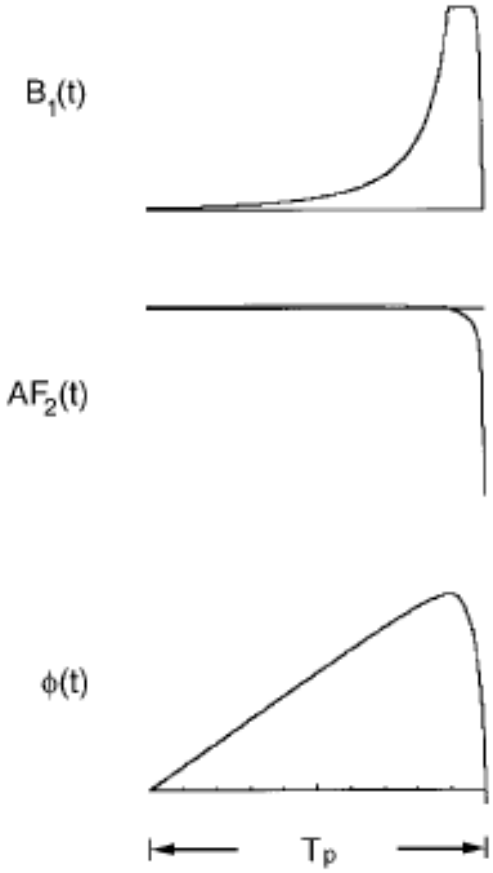

Figure 2-7: *Modulations functions of InvP for MC. The InvP of duration T_p is constructed of the first half of a sech pulse ($HS_{1/2}$, R = 31.415) for 0.9 T_p and the second half of a tanh/tan pulse (R=100) for 0.1 T_p. (Top) Amplitude modulation function. (Middle) Frequecy modulation. (Bottom) Phase modulation. Figure replicated from [53] with permission of Elsevier, Inc.*

The InvP of duration T_p was composed of the first half of a sech pulse ($HS_{1/2}$, R = 31.415) for 0.9 T_p and the second half of a tanh/tan pulse (R=100) for 0.1 T_p (Figure 2-7). The detailed shape and characteristics of the pulse are given in the paper of Hwang et al. [53]. The InvP as an asymmetric AFP pulse features a narrow transition bandwidth (BW_{trans}, frequency range in which longitudinal magnetization M_z: $-0.95 \leq M_z/M_o \leq 0.95$) on the

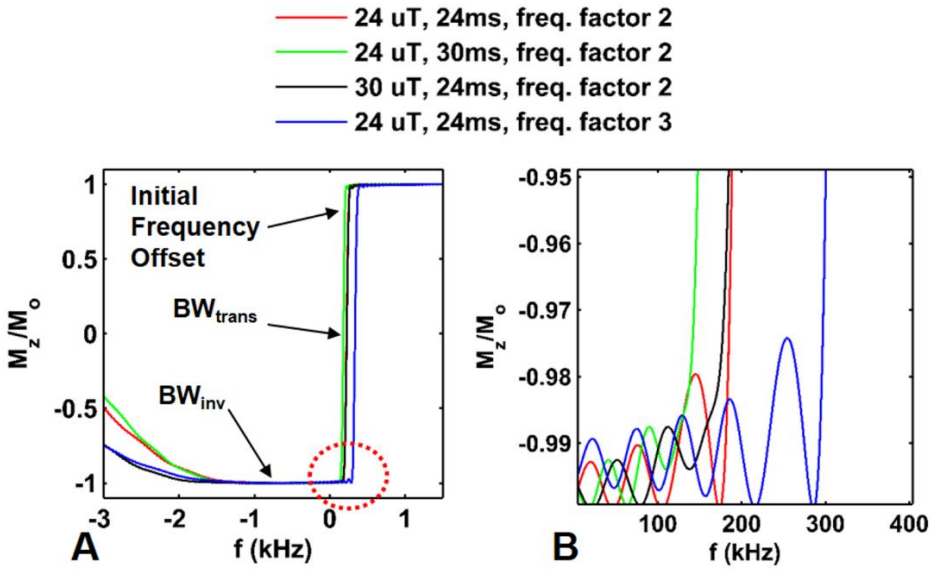

Figure 2-8: *Simulations and experimental results of the asymmetric adiabatic pulse for inversion of the upfield part of the spectrum. A) Longitudinal magnetization profile of the inversion pulse simulated for different B_1^+ values, pulse durations and frequency factors. B) Zoomed region of panel A illustrates detailed behavior at the transition from full inversion to the transition band. The initial frequency offset is also demonstrated. Figure adapted from [46] with permission of John Wiley and Sons, Inc.*

water side and a broad inversion bandwidth (BW_{inv}, $M_z/M_o \leq -0.95$; Figure 2-8). For applications in the human brain at 9.4 T the desired frequency range is about 1400 kHz. BW_{inv} and BW_{trans} were investigated for the following parameter ranges: pulse duration from 20 to 30 ms, frequency factor from 1 to 4 (see below), and B_1^+ values from 15 µT to 30 µT (Figure 2-9). The frequency factor is simply a number that is multiplied with the frequency sweep range of the FM and defines the resulting BW_{inv}. Additionally, the frequency profile of the InvP exhibits an initial frequency offset ($M_z/M_o = 0.95$) due to the asymmetry of the pulse, which was also studied for different B_1^+ values, pulse durations and frequency factors (Figure 2-8, B).

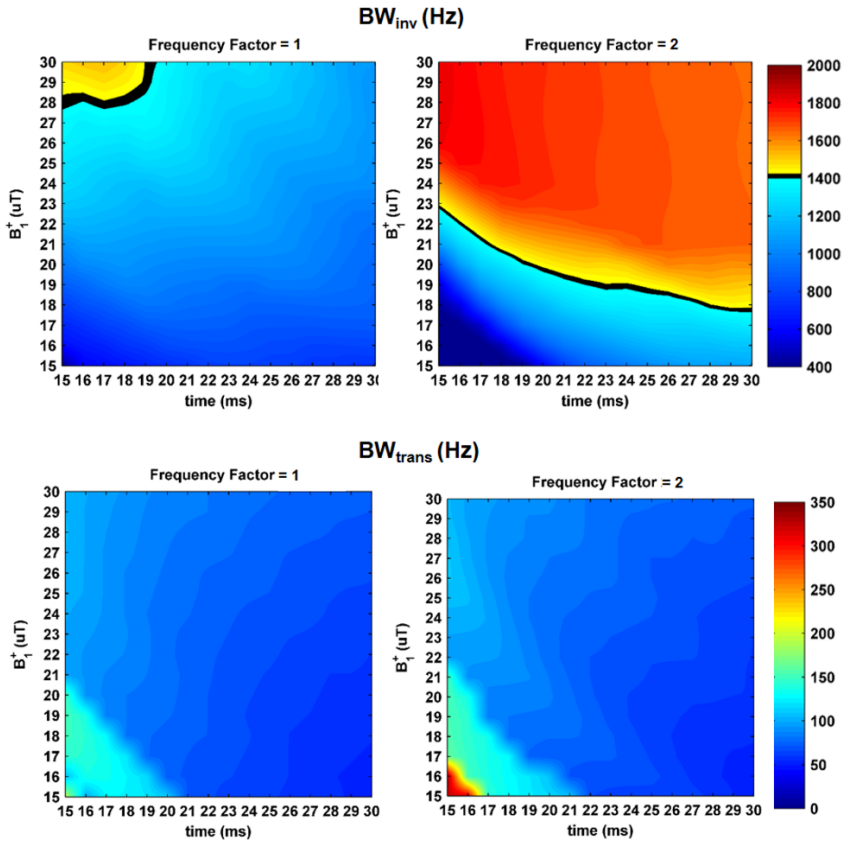

Figure 2-9: *Simulation results for BW_{inv} and BW_{trans} as a function of B_1^+ amplitude, pulse duration, and frequency factor (left frequency factor = 1.0, right = 2.0). (Upper panel). BW_{inv} results in Hz. The black contour line indicates 1400Hz which is the required frequency range for spectroscopic applications at 9.4 T. (Lower panel) BW_{trans} results in Hz. For both simulated frequency factors, for durations larger than 22 ms the BW_{trans} ranges from 60 to 80Hz which corresponds to 0.15 to 0.2 ppm at 9.4 T. Figure replicated from [46] with permission of John Wiley and Sons, Inc.*

2.3.3 Development of MC-STEAM and MC-semi-LASER

MC-STEAM and MC-semi-LASER were designed based on the MC principle in combination with conventional spectroscopy sequences. The first scheme consisted of a conventional STEAM sequence in which an InvP for MC was incorporated during the mixing time (Figure 2-10, A). The second localization strategy involved a semi-LASER

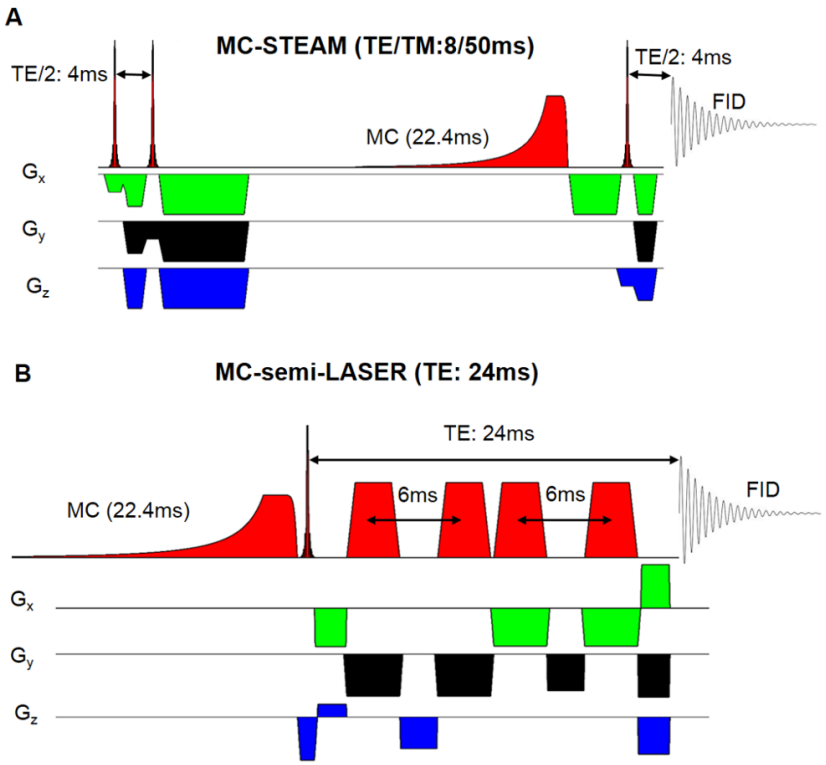

Figure 2-10: *Sequence diagrams. A) MC-STEAM sequence with a TE of 8 ms and a TM of 50 ms. MC was incorporated during the mixing period without an extension of TE, therefore without any loss of signal due to T_2 relaxation. B) MC-semi-LASER sequence with TE of 24 ms. A metabolite cycling pulse is introduced directly before the localization. Figure replicated from [46] with permission of John Wiley and Sons, Inc .*

sequence [11] that was preceded by a MC pulse (Figure 2-10, B). For the semi-LASER sequence, both sagittal and coronal slices were selected using a pair of refocusing offset independent trapezoidal adiabatic pulses [11] optimized for 9.4 T.

2.3.4 In vivo spectra from occipital lobe

A voxel (2x2x2 cm^2) was placed in a mixed gray (GM) and white matter area (WM) in the occipital lobe. Placement of the voxel was facilitated using high-resolution images from 2D FLASH scans acquired in three orientations (axial, sagittal and coronal). First and second order B_0 shimming was performed using FASTE(ST)MAP [54] and voxel-based

power calibration was executed [55]. MR spectra using the MC-STEAM and MC-semi-LASER were acquired from 8 healthy volunteers (6 male and 2 female, age: 29 ± 4 years). The repetition time was 6000 ms, ensuring an acceptable SAR level. Totally, 96 averages were acquired with 4096 time-points and an 8 kHz receive-bandwidth (Figure 2-11).

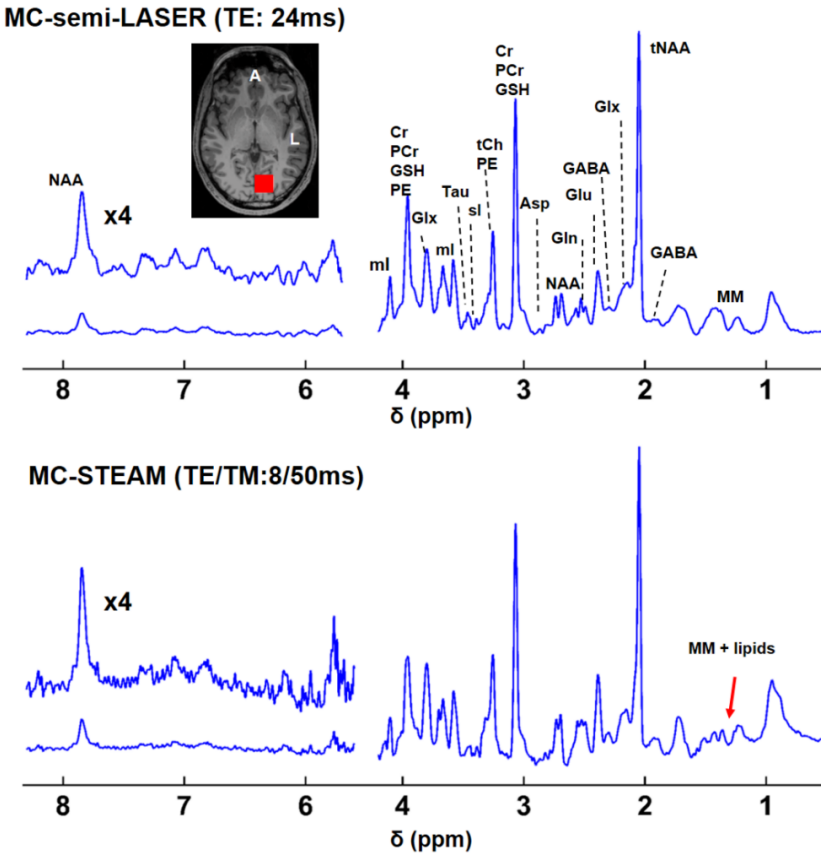

Figure 2-11: *Sample spectra acquired from the same volunteer using MC-semi-LASER and MC-STEAM from a voxel in the occipital lobe (red square). Both, the upfield and downfield parts of the spectrum are detected with good quality with both sequences. Red arrow indicates some contributions in the MC-STEAM spectrum that are likely to arise from outer volume lipid signals. Spectra have been filtered for illustration purposes using a Voigt filter (Gaussian part: 50ms, Lorentzian part: 7.8Hz). Figure reproduced from [46] with permission of John Wiley and Sons, Inc.*

2.3.5 Conclusions

To conclude, this was the first study, where semi-LASER is applied at 9.4 T and the MC technique is implemented on a whole body 9.4T UHF system. The outcomes of this work highlight the advantages of semi-LASER compared to STEAM in terms of excitation profile and lipid contamination, and indicate the importance of frequency and phase alignment for MRS at 9.4T in the human brain. MC-semi-LASER is an attractive choice for measurements at UHF since it enables the constructive summation of the different FIDs without the need for additional water reference scans for frequency alignment and eddy current correction, optimized OVS, or lengthy water suppression schemes. Additionally, MC-semi-LASER results in the doubling of the SNR_{NAA} compared to MC-STEAM. This SNR benefit is inherent in the spin echo based LASER techniques in comparison to STEAM and was not substantially compromised by the somewhat longer but still short TE in semi-LASER.

2.4 Characterization of macromolecular baseline at 9.4 T

Summary of the submitted manuscript entitled “Characterization of macromolecular baseline at 9.4 T” (*Magnetic Resonance in Medicine* DOI: 10.1002/mrm.27070). Please refer to the List of Publications and Statement of Contibutions sections for more details.

2.4.1 Introduction

Macromolecular resonances (MM) arise mainly from cytosolic proteins and overlap with resonance lines of metabolites in ^{1}H-MRS [56-60]. Consequently, MM can influence the precision and the accuracy of metabolite quantification due to baseline distortion. This effect becomes even more severe in the case of short TE due to their fast transverse relaxation time (T_2) [59,61]. Because of their short T_2, MM appear in ^{1}H-MRS spectra as an underlying baseline consisting of several broad peaks.

In addition to their significance regarding the quantification of metabolite levels, macromolecules can potentially be valuable biomarkers for several diseases and

pathologies [62-68]. Moreover, several studies have investigated potential differences in MM between different age groups and brain regions. However, many of the reported results are contradictory to each other. Particularly, early studies at 3 T demonstrated differences between various areas of the brain indicating that a regional specific MM baseline was required for quantification [69,70].

The increased spectral resolution at UHF comes at the cost of more elaborate handling of the MM baseline for adequate quantification. More specifically, at low static magnetic fields, MM in ^{1}H-MRS spectra can be sufficiently handled by different fitting software (e.g. LCModel [71]) using polynomial functions (e.g. splines) or simulated macromolecule resonances [38,72]. However, at higher fields, it has been shown that a measured MM baseline is required to be included in the fitting model due to the higher frequency resolution [60].

Hence, the objective of this study was the quantitative characterization of the human brain macromolecular baseline for the first time at 9.4 T in occipital lobe (OccL) and left parietal lobe (lPL) exploiting the advantages of UHF. In this work, a double IR scheme was combined for the first time with MC semi-LASER [46,73] (see also chapter 1.3) for metabolite nulling at 9.4 T. For this purpose, an AFP pulse for inversion was optimized. In addition, a multi-channel array circumscribing the entire head [74-77] utilizing appropriate phase arrangement and power distribution was used, enabling the production of high and efficient B_1^+ fields in both OccL and lPL. MM spectra were acquired from 7 volunteers from these two brain regions and volunteer's MM baselines were averaged and then smoothed utilizing cubic splines creating a MM template, which was parametrized using 15 simulated Lorentzian lines within LCModel. Quantification, corrected for different tissue composition and T_1 relaxation, was performed for each MM peak.

2.4.2 Double Inversion Recovery for Metabolite Nulling at 9.4 T

For the suppression of metabolites' signals, a double IR technique was implemented and optimized since it is less susceptible to T_1 variations of the metabolites [78]. It was implemented in combination with a previously developed MC semi-LASER sequence [46]

(see also chapter 1.3). For the inversion of the metabolites, a 3T AFP pulse was adapted and optimised to address the increased B_1^+ inhomogeneity at 9.4 T (the minimum B_1^+ for adiabatic condition was 15μT). Specifically, the amplitude modulation (AM) of the pulse was constructed using a hyperbolic secant pulse (HS1; [79]) and the frequency modulation (FM) using a hyperbolic tangent function (Figure 2-12, A and B).

For the calculation of a set of IR times (TI_1 and TI_2) suitable for metabolite nulling, Bloch equation simulations were performed assuming different T_1 for metabolites (1000 ms to 2000 ms) and MM (400 ms) using reported values from studies at 7 T [80]. Afterward, the developed InvP was incorporated into a double IR scheme preceding the localization scheme, in this case, MC semi-LASER. The final selected inversion times were 2360 ms and 625 ms respectively.

2.4.3 Macromolecular Baseline Templates

The double IR in combination with the MC semi-LASER enables the reliable acquisition of MM spectra with the absence of lipid contamination (Figure 2-13). The pattern of MM baselines for the same brain region among different volunteers is consistent. However, potential differences in peak amplitudes between the various volunteers can be observed in the spectral area from 1 ppm to 2 ppm (M2 to M5) by visual inspection. The deviations in these MM, which can be seen in another study [61], probably indicate physiological variations (e.g. motion of free proteins).

Moreover, the average-smoothed (using cubic splines within MATLAB, smoothing parameter p = 0.001) MM baselines acquired from seven healthy volunteers from a voxel within the OccL and the lPL do not show notable differences. Nevertheless, minor variations in peaks amplitudes can be noticed in the frequency area from 3.8 ppm to 4 ppm (M12 to M15; Figure 2-13). The average SNR of M1 peak (peak at 0.9 ppm; Figure 2-13) between the occipital lobe and the left parietal lobe exhibits a statistical difference ($P < 0.05$). Particularly, the SNR values are 54 and 24 for the occipital lobe and the left parietal lobe respectively. The FWHM of the M1 peak is 45 Hz and 41 Hz in both regions accordingly. Smoothing procedure using cubic splines do not affect the linewidth of MM peaks, while improving the SNR of the MM baseline template.

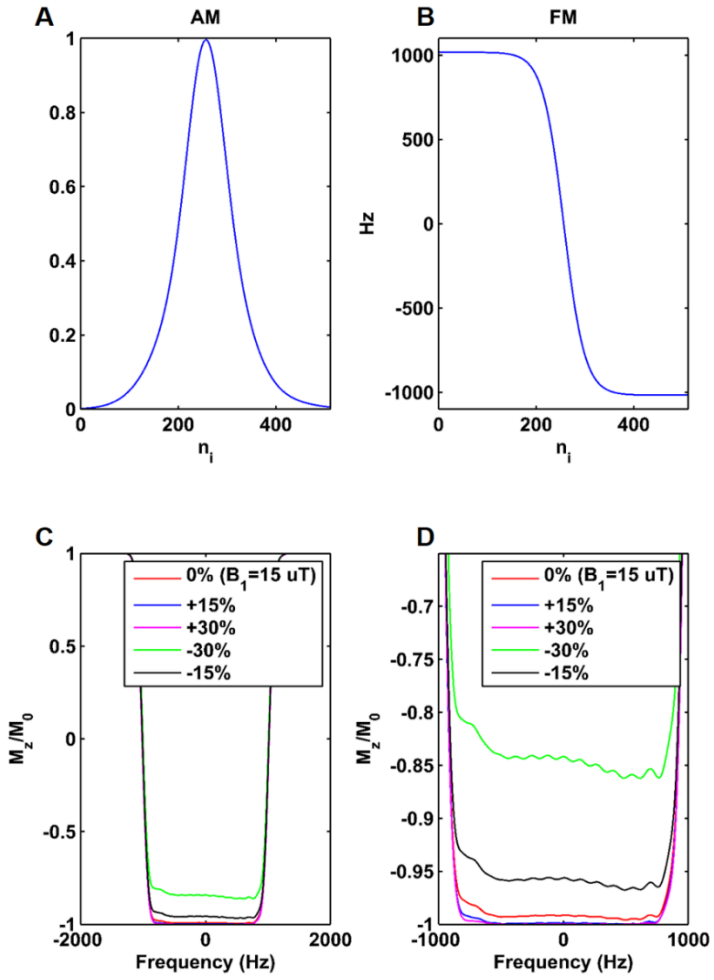

Figure 2-12: *Design of the adiabatic inversion pulse (InvP) for metabolite nulling at 9.4 T (A) Amplitude modulation (AM) (normalized) of InvP as a function of time (B) Frequency modulation (FM) function of InvP in Hz as a function of time C) Inversion profile of InvP simulated using Bloch equation simulations for different B_1^+ levels assuming a pulse duration of 15ms. The minimum B_1^+ for adiabatic condition was 15μT (red line). The resulting inversion bandwidth is about 1650 Hz and the transition bandwidth roughly 500 Hz. D) Same as subplot C using a smaller frequency range for the illustration of inversion profile details.*

.

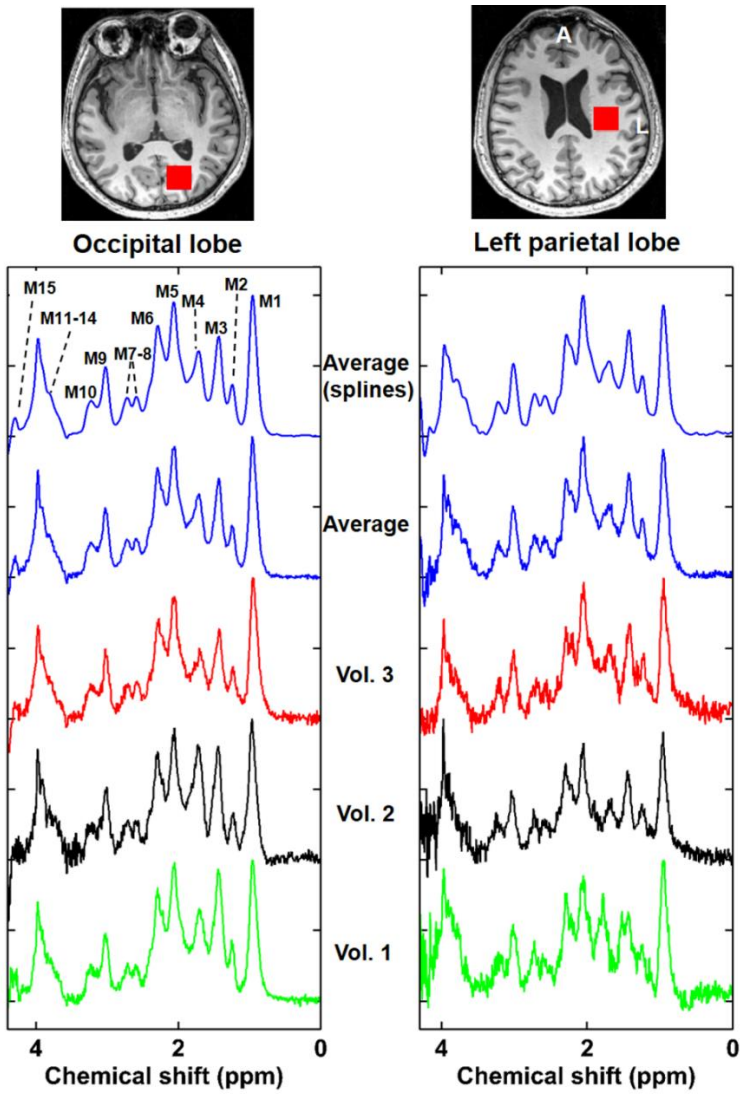

***Figure 2-13**: Macromolecular spectra acquired from 3 different volunteers (Vol.1, Vol.2 and Vol.3) from a voxel of 2x2x2 cm^3 (red square in anatomical images) placed in a mixed area of GM, WM and CSF in the occipital lobe (left) and in the left parietal lobe (right), respectively. The averaged MM spectra (n=7) and the smoothed averaged MM spectra using cubic splines are illustrated in addition (top). 15 MM peaks are observed by a visual inspection (M1-15). White letters L and A stand for left and anterior coordinates respectively.*

Noteworthy, two new MM peaks at 2.57 ppm (M7) and 2.74 ppm (M8) are easily observable. These peaks appear in MM spectra of other studies in which more advanced MRS techniques were used (e.g. 2D COSY) [56,59,61], however, they have not been reported.

2.4.4 Conclusions

In this study, we obtained macromolecular spectra acquired for first time from two different regions of the human brain at 9.4 T, occipital lobe and left parietal lobe, using a double inversion recovery technique in combination with MC semi-LASER. We demonstrated a coil setup enabling the achievement of efficient B_1^+ fields in different brain locations without the need of different coils. In addition, we demonstrate an AFP appropriate for inversion of MM and metabolites at 9.4 T. Double inversion which was combined for first time with MC semi-LASER enabled the acquisition of high spectral resolution MM spectra where 15 MM peaks were detected for both brain regions at 9.4 T. MM baseline models for both locations were established, and mean concentration levels for each of the 15 MM components were calculated utilizing water referecne scans. In addition, in this study, two new MM peaks (M7 and M8) were reported for first time and potentially assigned to β-methylene protons of aspartyl-groups.

2.5 Characterization of the downfield ^{1}H MR spectra of human brain at 9.4 T

Summary of the published journal paper entitled “In vivo characterization of the downfield part of 1H MR spectra of human brain at 9.4T: Magnetization exchange with water and relation to conventionally determined metabolite content” (*Magnetic Resonance in Medicine,* DOI: 10.1002/mrm.26968). Please refer to the List of Publications and Statement of Contibutions sections for more details.

2.5.1 Introduction

The use of water suppression also results in suppression of peaks from exchanging protons. Using a non-water suppressed sequence, such as the developed MC-STEAM (see chapter 2.3) allows for exchange rate measurements using methods such as inversion transfer. In particular, several peaks on the downfield side of water (typically between 5.0 – 10.0 ppm) have protons, which exchange with water. In contrast to upfield metabolites, most of the downfield peaks remain unlabeled [47,81-83].

Knowledge of exchange rates allows the optimization of spectroscopy experiments and sequence parameters, as well as, the investigation of pathologies where concentrations may vary with the degree of disease severity or metabolic activity, or where exchange rates may vary with changes in pH. Chemical Exchange Saturation Transfer (CEST) experiments utilize chemical exchange for the measurement of the enhanced signal from exchanging species [84], as well as, for the study of tumor severity and treatment [47,81-83]. CEST can measure exchange from a range of species with varying exchange rates, and mostly investigates species downfield of water. Therefore, study of the downfield resonances is of high importance for the CEST community for a better understanding of CEST effect.

Although suggestions of labels for several downfield resonances have been made [85,86], most remain unlabeled. Hence, characterization of downfield peaks and comparison to upfield concentrations in grey and white matter may contribute to determine peak labels. For this purpose, UHF can play an important role due to higher spectral resolution (see chapter 1.1.4). However, as field strength is increased, the shorter T_2 values of the downfield peaks requires sequences with short TE in order to minimize signal loss (see chapter 1.2.5). In this study, exchange rate and T_1 measurements were performed utilizing, MC STEAM in combination with inversion transfer to investigate in vivo brain metabolites downfield of water.

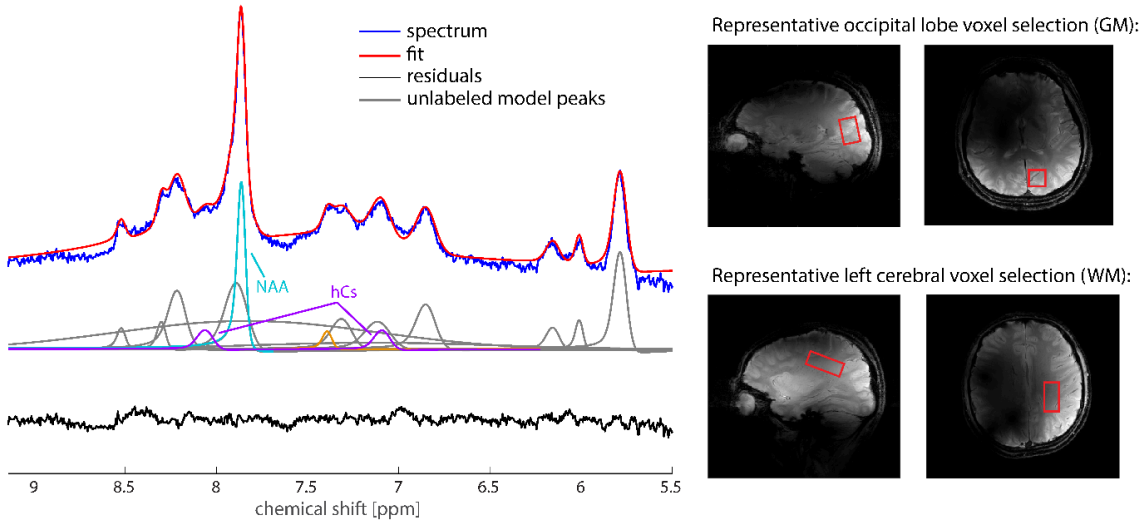

***Figure 2-14**: Average downfield spectrum with no water pre-inversion for the GM ROI series, overlaid with the fitted spectrum, the model peaks (grey for unlabeled, colour for NAA and homocarnosine (hCs) with their respective labels), and with residuals shown below. Residuals indicate a decent fit for most peaks. No filtering was used. The WM ROI model is the same except for one removed peak, at 7.4 ppm, highlighted in orange. Also shown are representative locations of the voxels in the occipital lobe (above) and in the white matter region on the left cerebral side above the ventricles (below).*

2.5.2 In vivo downfield spectra from human brain at 9.4 T

In this study, the acquired data demonstrated higher spectral resolution and exchanging peak intensity compared to lower field strength [47] or water-suppressed experiments [85]. Consequently, further separable peaks in the 8.2-8.5 ppm region and additional exchanging peaks closer to water could be observed (Figure 2-14)Totally, thirteen and fourteen peaks for WM and GM were evaluated respectively, utilizing the inversion transfer experiment (inversion delay times: 41, 96, 171, 321, 671, 1321, 3021 ms). This study also included upfield data in both WM and GM for additional peak concentration comparisons in order to determine any correlations between known upfield metabolite concentrations and the unknown downfield resonances.

2.5.3 Chemical exchanges rates and T_1 of human brain downfield metabolites at 9.4 T

Exchange measurements at 9.4 T enabled the investigation of additional peaks (peaks at 5.8 ppm and the peaks of the amide region from 8.2-8.5 ppm), which could not be studied in a previous study at 3 T [47] (Figure 2-15). The 5.8 ppm peak, which was previously suggested to be urea [85], has a mean exchange rate of 7.4 Hz from the combined GM and WM experiments. The amide region has a range of exchange rates, from a mean of 3.7 Hz for the 8.5 ppm peak, which is significantly slower than the 8.9 Hz found at 3 T, to 9.9 and 13.6 Hz, for the 8.2 and 8.3 ppm peaks, respectively, which are

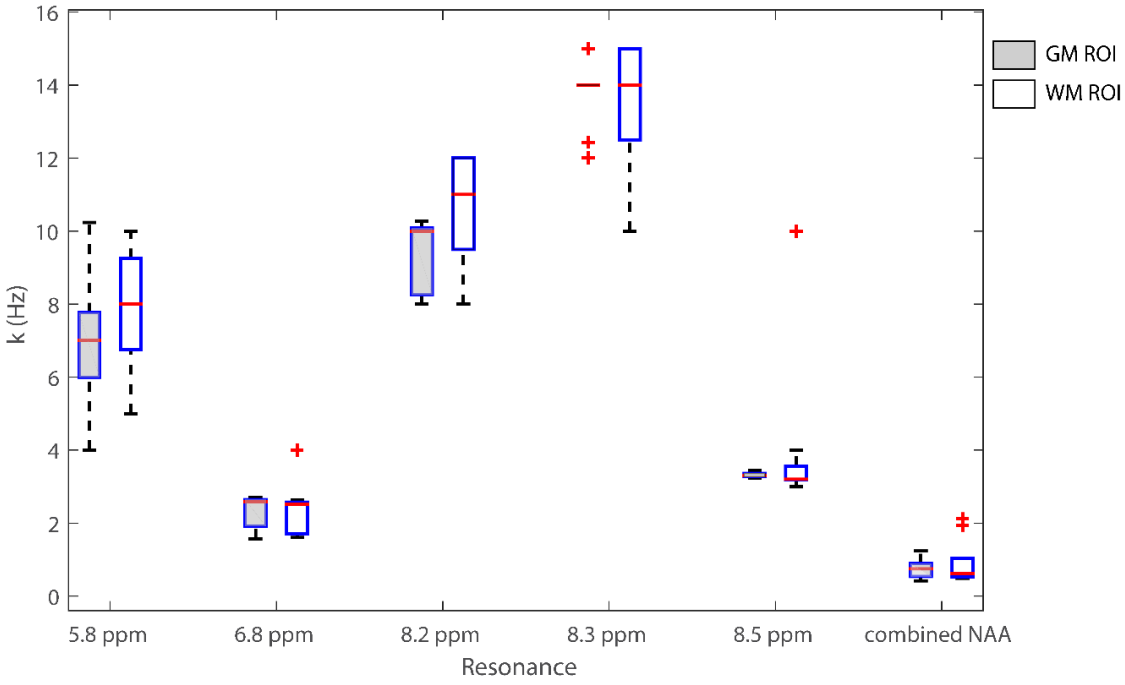

***Figure 2-15**: Boxplots indicating the range of exchange rates (k) for the different resonances fitted with the Bloch-McConnell model [87]. The edges of the box plots are at the 25th and 75th percentiles, while the red line in between indicates the median. Whiskers extend to the extremes of the data within 1.5 times the interquartile range (if no data lies within that range, they extend to the minimum or maximum). Outliers beyond the interquartile range are denoted by a cross. No significant differences were found between white and gray matter exchange rates.*

higher rates than the 7.5 Hz found for the broader 8.2 ppm peak fitted at 3 T [47]. However, the exchange rates found in the the 7.5 Hz found for the broader 8.2 ppm peak fitted at 3 T [47]. However, the exchange rates found in the current study are in agreement with what has been reported previously for the amide region using water exchange-filtered experiments [88]. Downfield T_1 relaxation values, varying from 0.22 s to 0.77 s, are shorter than previously published upfield values at 7 and 9.4 T [23,80], and are on the order of macromolecular T_1 values, which suggests that macromolecular components are contributing to the peaks (Figure 2-16). The downfield T_1 values are also higher than those found downfield at 3 T for similar experiments, a finding that is expected, since T_1 relaxation times increase with field strength [25]. The combined NAA peak here has a much lower T_1 than that found for NAA at 7 T; however, in this case the combined NAA peak cannot give us a meaningful estimate of T_1, and was of more interest for its exchange rate. At 3 T, this peak was modeled as one peak only, due to the broader peaks at lower field strengths.

Correlations between downfield peaks and upfield representations of metabolites were of particular interest for these experiments, in order to investigate potential labels for peaks as previously indicated in the literature [86,89]. Downfield NAA positively correlates with upfield NAA concentrations, with a Spearman correlation coefficient of $r = 0.63$ ($p < 0.01$). However, none of the other downfield peaks significantly correlates with upfield metabolite concentrations. Thus, while these and other upfield metabolites may certainly still be present as small components of the different downfield peaks, they do not appear to represent large proportions of these peaks.

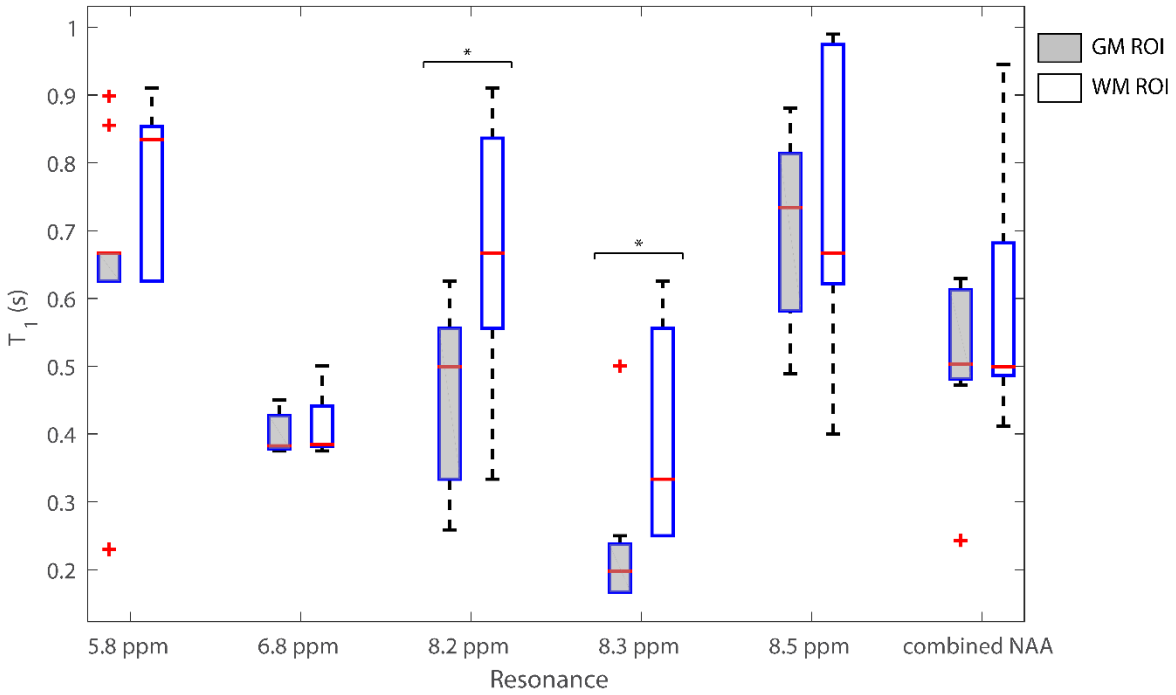

***Figure 2-16**: Boxplots are indicating the range of T_1 values for the different resonances fitted with the Bloch-McConnell model [87]. The edges of the box plots are at the 25th and 75th percentiles, while the red line in between indicates the median. Whiskers extend to the extremes of the data within 1.5 times the interquartile range (if no data lies within that range, they extend to the minimum or maximum). Outliers beyond the interquartile range are denoted by a cross. Significant differences ($p < 0.05$) between WM and GM ROIs are denoted with asterisks.*

2.5.4 Conclusions

This is the first study in which downfield metabolites were investigated at 9.4 T, as well as, first comparisons of downfield and upfield peak concentrations were performed. Furthermore, exchange rates and T_1 values for at least six of the twelve measured resonances downfield were calculated. Increased peak separation of the 8.2-8.5 ppm region allowed for improved characterization of the amide region and corresponding exchange rates. Moreover, for the first time it was possible to quantify the exchange rate

of the 5.8 ppm peak, tentatively assigned to urea [85,90], in vivo in human brain. Correlations between downfield peaks and known upfield metabolite concentrations were insignificant, except for NAA. This suggests that, while the compared metabolites might form components of these peaks, they do not make up a significant portion of them.

2.6 Functional Magnetic Resonance Spectroscopy (fMRS) at 9.4 T

2.6.1 Introduction

The introduction of UHF in spectroscopy applications enables the investigation of dynamic changes of metabolites under different types of functional stimulation, the so-called functional MR spectroscopy (fMRS).
In particular, several studies utilize the advantages of 7 T to investigate the dynamic changes of brain metabolites under different types of functional stimulation [91-95]. However, along with lactate (Lac) and glutamate (Glu) increases that were reported by all previous studies additional metabolite changes (glucose [93,94], aspartate [92,93], glutamine and glycine decrease and GSH increase [92]) have been reported inconsistently. Thus, the purposes of this pilot study[10] were:

- Evaluate the capabilities of the MC semi-LASER sequence (see chapter 2.3) applied at 9.4T for fMRS under visual stimulation.

- The synchronous investigation of dynamic alternation of the BOLD effect (water) and metabolite levels based on the MC technique (simultaneous acquisition of water and metabolites).

- The investigation of potential changes in the downfield spectrum (including water exchanging peaks) based on the MC technique in (see chapter 2.5).

[10] This study was submitted and presented in ISMRM 2017 conference [96]

2.6.2 Study design

All measurements were performed using a home-built proton 4Tx8Rx half-volume coil [32,36] with an appropriate power distribution and phase increment for the achievement of efficient an B_1^+ field in the area of the occipital lobe (Figure 2-17). Eleven healthy volunteers participated in this study. Two paradigms were applied (Figure 2-18). The first was a visual stimulus (STIM) and consisted of a radial red-black checkerboard that flickered with 10 Hz (ON), alternating with a black screen (OFF). The second paradigm was exactly like the first. However, only a black screen was projected with the absence of any stimulus (no-STIM). During the paradigms, fMRS data were acquired from a voxel (2x2x2 cm^3) in the visual cortex (V1) using the MC-semi-LASER sequence (TE/TR: 24/6000 ms). 244 averages were acquired for each subject during a stimulation period of 22'24''. Neither WS nor OVS was implemented.

The fMRS data were corrected for eddy currents, frequency and phase fluctuations based on the MC water peak [46,97]. Afterwards, the data from all the volunteers were averaged and smoothed using a moving average over 16 acquisitions. As a result, the final data set conisted of 97 time-point where each time-points was the average of 352 (2x11x16) excitations (Figure 2-19).

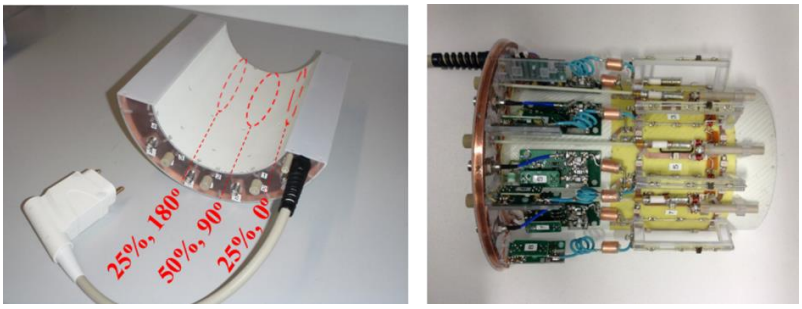

Figure 2-17*: (Left) The half-volume array coil (4Tx8Rx) used for the fMRS experiments. For the increase of the B_1^+ efficiency only three transceiver elements were utilized (red circles). The percentage numbers (%) indicate the power delivered to each Tx element. A phase step of 90° was implemented. (Right) Internal view of the coil. For the reception, four vertical loops were used along with four transceiver elements [32].*

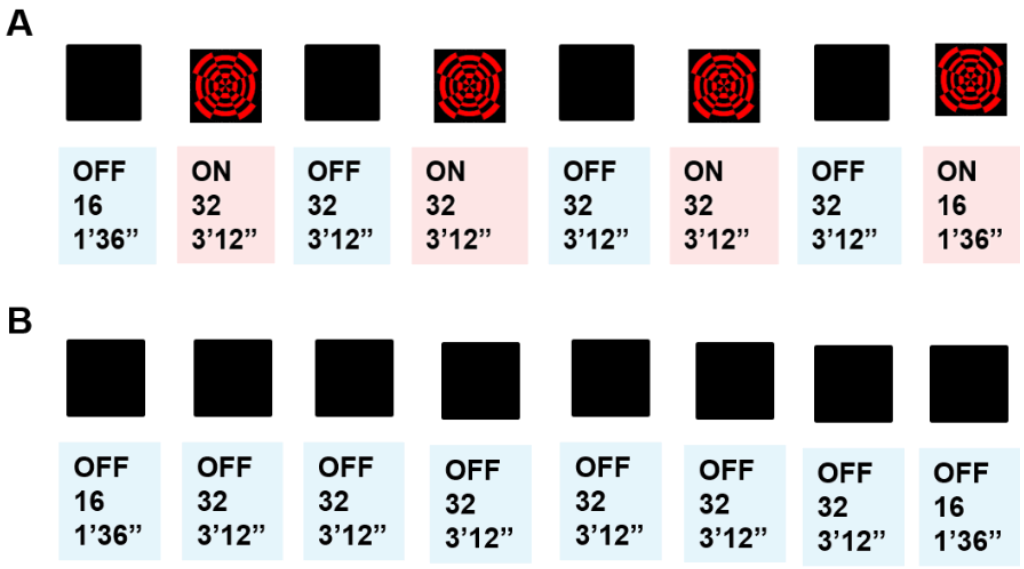

Figure 2-18*: The two paradigms used for the fMRS experiments. A) The STIM paradigm in which* a visual stimulus consisted of a radial red-black checkerboard that flickered with 10 Hz (ON), alternating with a black screen (OFF). *B) The no-STIM pattern in which no stimulus was used.*

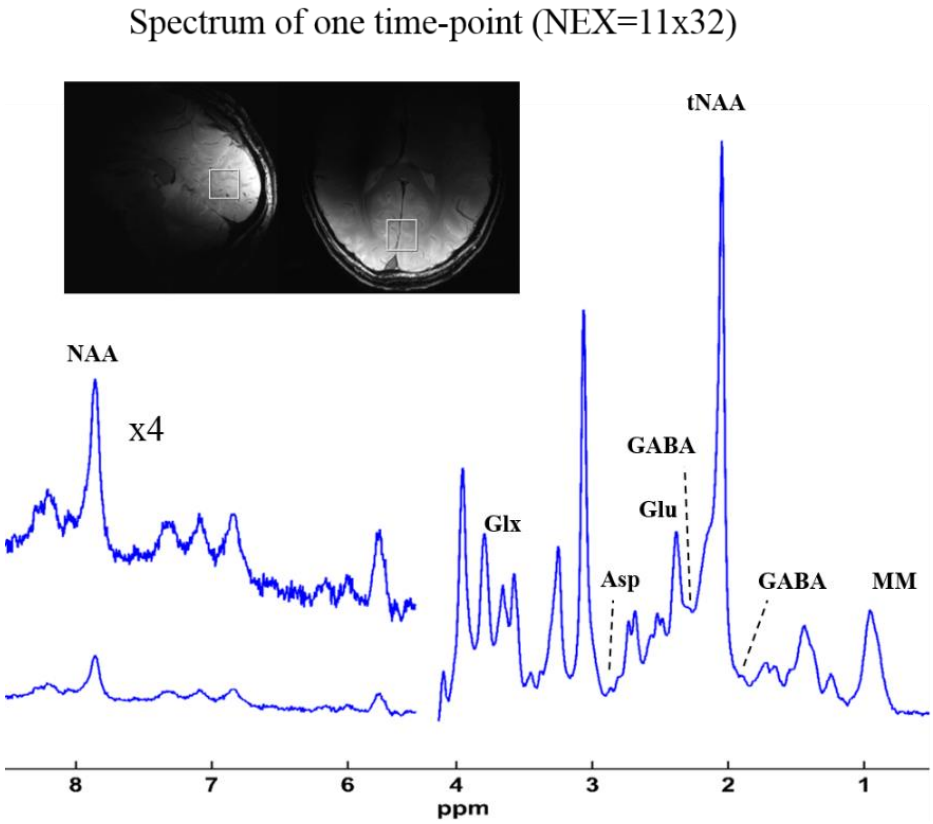

***Figure 2-19**: A spectrum of one time-point. Each time-point spectrum is the average of 352 NEX. The fMRS spectra demonstrated high spectral resolution and decent quality for the downfield part of the spectrum (>4 ppm). The data were acquired from a voxel placed in V1 (white square).*

2.6.3 Water and metabolic dynamic changes during visual stimulus

The resulting spectra demonstrate a high reliability and reproducibility of the spectral acquisitions in both the upfield and downfield frequency range (Figure 2-19). The SNR of the water peak (SNR_{H20}) of the STIM data followed the stimulus paradigm pattern (Figure 2-18). In addition, the changes of SNR_{H20} were highly correlated with the linewidth changes of the water peak ($FWHM_{H20}$) during the stimulus period (*R= -0.99, P<0.001*), proving that SNR_{H20} variations of the STIM water data were mainly due to the BOLD effect [98]. Contrariwise, the changes of SNR_{H20} of the REST data did not exhibit any correlation (Figure 2-20).

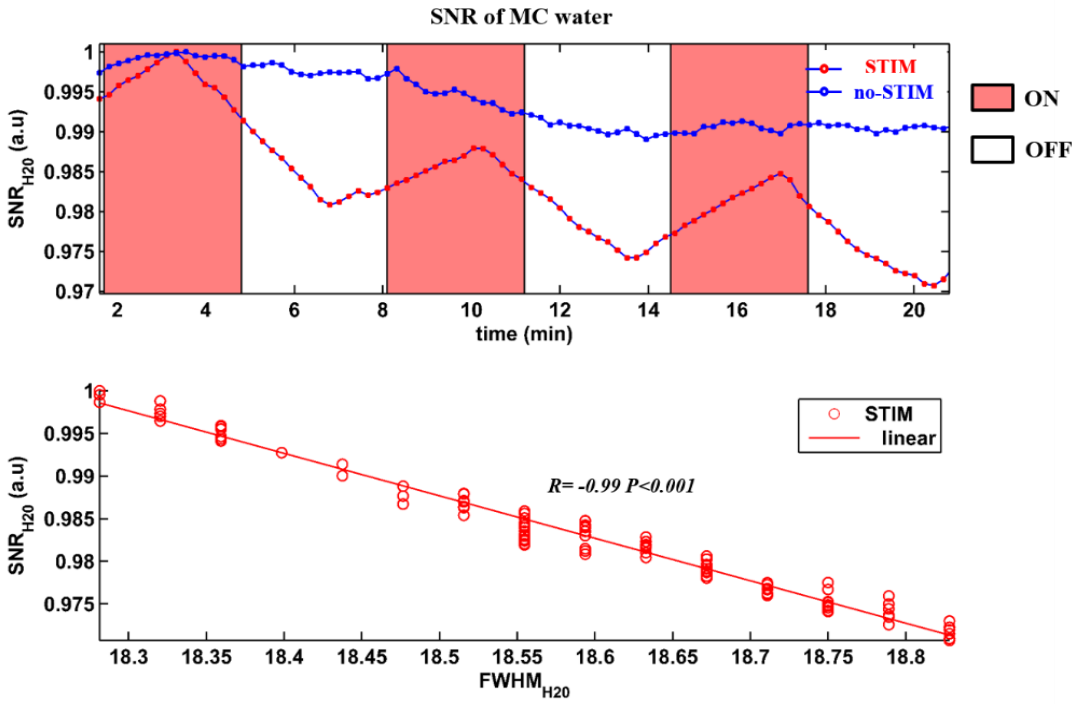

Figure 2-20: *(Top) SNR of the water signal (SNR_{H20}) over the fMRS study for both STIM and no-STIM experiments. (Bottom) SNR_{H20} variations were highly correlated with $FHWM_{H20}$ changes for the STIM experiment.*

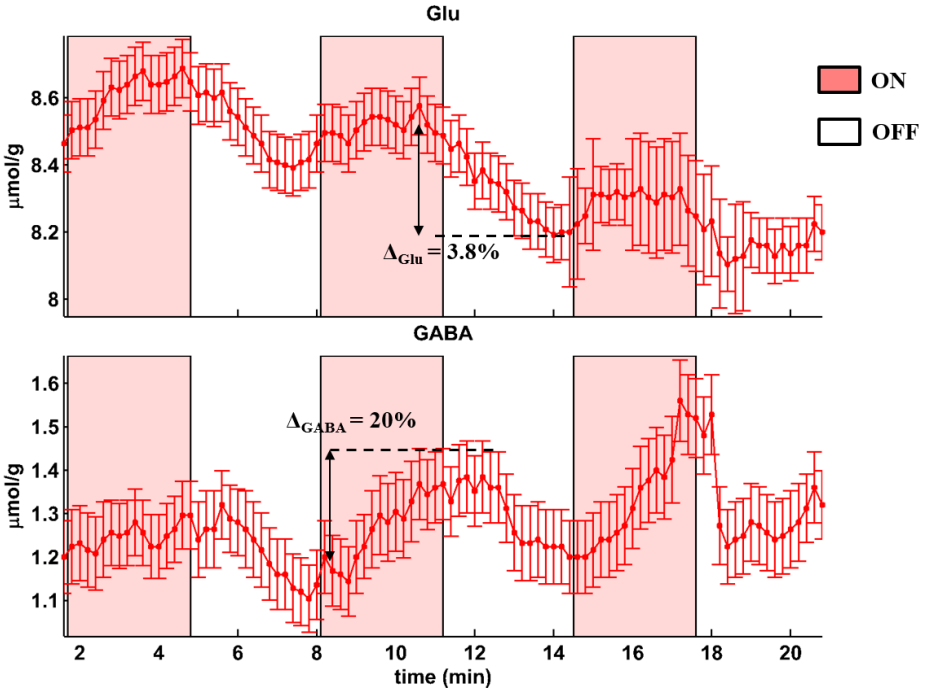

Figure 2-21: *Time-course of Glu and GABA metabolites during the visual stimulus*

Except the alterations of $FWHM_{H20}$ and SNR_{H20}, the MC technique enabled the simultaneous investigation of the dynamic changes of the metabolites. In particular, variations of about 3.8% and 20% were observed in Glu and GABA respectively during the visual stimulus (Figure 2-21). These findings are in agreement with older fMRS studies [91-95], as well as, with recently published studies [99,100].

Moreover, the influence of the inclusion of an experimentally measured MM baseline in the resulting quantification was investigated. More specifically, the quantification of the concentration levels was performed utilizing the LCModel [71], which is considered the „gold“ standard in MRS for metabolite quantification. As explained in chapter 2.4, it is quite crucial at UHF to include the MM baseline in the basis set model due to the high spectral resolution of the MM at UHF. However, the LCModel (V6.3-1L) does not provide any options for fixing the concentration levels of MM. As a result, the fitted MM concentration varies during the different timepoints which in turn may lead to potential alterations of metabolite levels. The results demonstrated an alteration of the MM

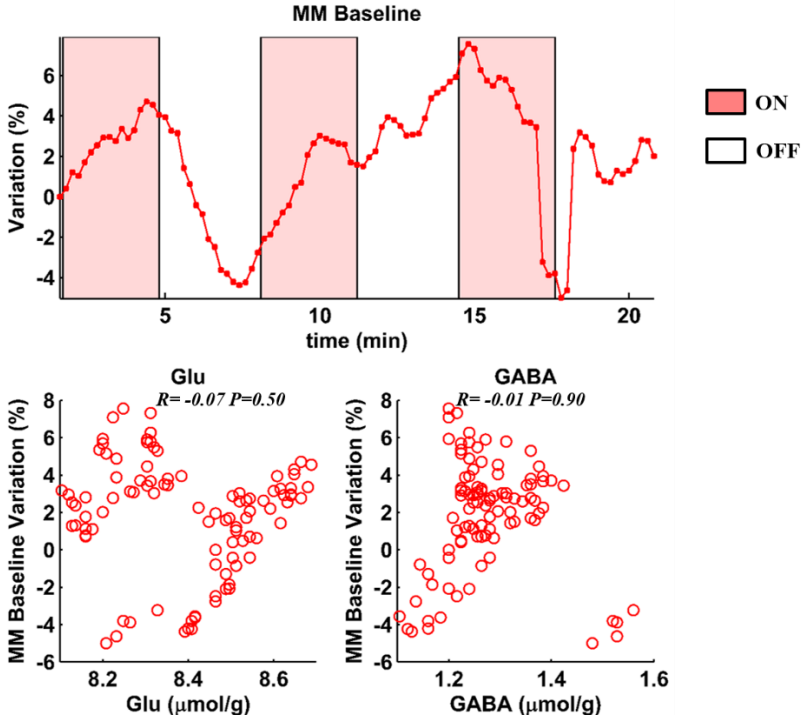

Figure 2-22: *(Top) MM variation introduced by LCModel quantification. These variations indicate a quantification variation related to the LCModel estimation model rather than a real alteration of the MM during the visual stimulus. (Bottom) Correlation graphs of Glu and GABA with MM variation. Glu alterations seem to be uncorrelated with the MM estimation variations.*

baseline during the different timepoints (Figure 2-22). However, these alterations did not correlate with the Glu level variations indicating that Glu changes were a result of physiological changes due to the visual stimulus rather than the influence of the MM baseline fit. In contrast, a correlation between the changes of the MM and GABA levels demonstrated a potential influence of the MM baseline fit in GABA timecourses.

Furthermore, the linewidth of total creatine (tCr) and total NAA (tNAA) varied during the STIM experiment. These variations were highly correlated (>0.85) with the MC water signal changes with a statistical significance ($P<0.001$; Figure 2-23) indicating that these alterations were due to BOLD effect. Moreover, the use of the MC technique instead of a WS enabled the investigation of potential variations of the downfield part of the spectrum

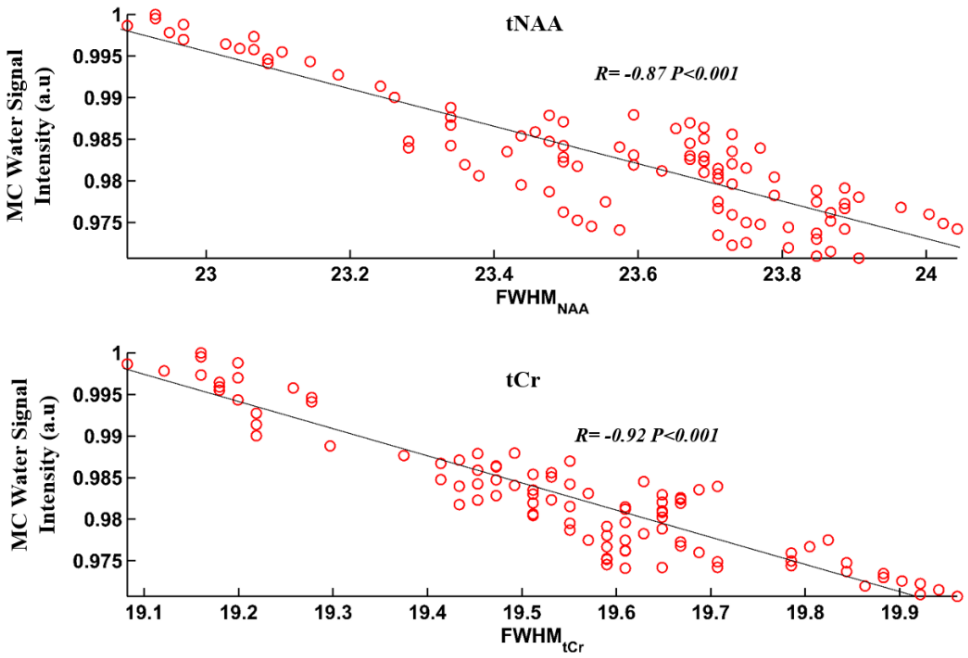

***Figure 2-23**: tNAA and tCr linewidths were highly correlated with the MC water signal intensity (a.u.) indicating that linewidth changes were introduced mainly from the BOLD effect*

due to the absence of a WS (see chapter 2.5). More specifically, for both experiments (STIM and no-STIM), the acquisitions acquired during the ON period were summed in one block and likewise the acquisitions during the OFF period in another. Then the OFF block data were subtracted from the ON block data using the appropriate linewidth (δ_{FWHM}= -0.2 Hz) and frequency correction (δ_{f0}= 0.1Hz) for the BOLD effect. The difference spectrum demonstrated potential changes (Figure 2-24).

However, since some of these peaks also appear in the no-STIM difference spectrum, it is not clear if these changes were due to physiological changes or because of some system instability (e.g. gradient modulations). Hence, further investigation is required to draw reliable conclusions.

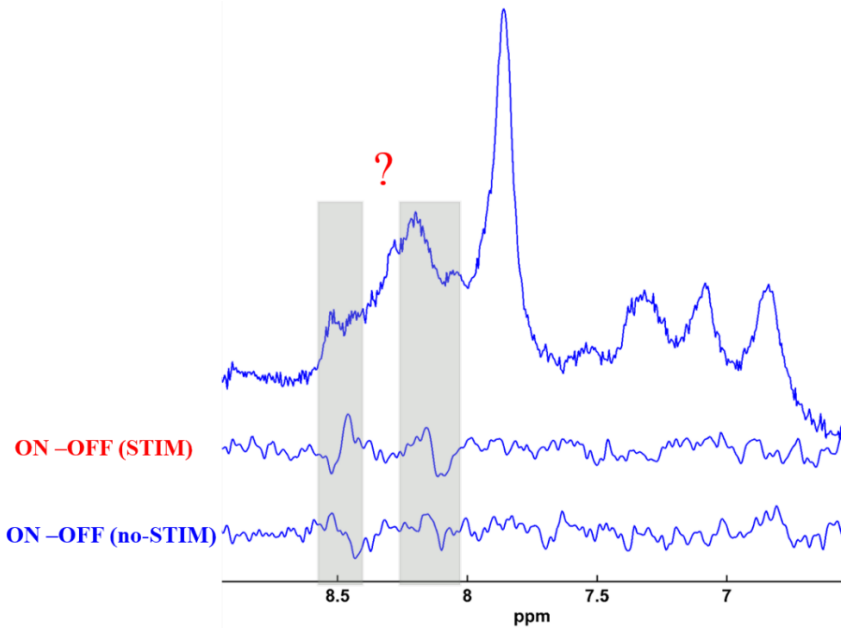

Figure 2-24*: Difference spectrum of the downfield part of the spectrum. The difference spectrum demonstrates potential changes. However, since some of these peaks also appear in the no-STIM difference spectrum, it is not clear if these changes were due to physiological changes or because of some system instability (e.g. gradient modulations).*

2.6.4 Conclusions

This study is the first trial of ^{1}H fMRS at 9.4 T in the human brain. Hence, preliminary data are reported. This is also the first study where water and metabolic alterations are detected simultaneously based on the MC technique, highlighting the potential of MC for fMRS experiments. In particular, MC seems an attractive method for fMRS due to its advantages such as frequency and phase fluctuations correction, simultaneous acquisition of water and metabolite signals, as well as, the detection of downfield metabolites. Moreover, high correlation of the MC water signal intensity with the linewidth of tNAA and tCr variations was reported indicating that the linewidth alterations of these metabolites are mainly due to the BOLD effect. Furthermore, the time-courses of Glu and GABA during visual stimulation are presented and variations of about 4% and 20% are reported respectively. In this study, the influence of the MM baseline in the metabolite's time-courses is investigated. Finally potential changes of the downfield metabolites during visual stimulation are reported. However, further investigation and measurements are required.

3. Bibliography

[1] Keeler J. Understanding NMR Spectroscopy. 2nd ed. doi: John Wiley & Sons, Ltd; 2010.

[2] Levitt MH. Spin Dynamics: Basics of Nuclear Magnetic Resonance. 2nd ed. doi: John Wiley & Sons, Ltd; 2008.

[3] de Graaf RA. In Vivo NMR Spectroscopy. 2nd ed. doi: 10.1002/9780470512968: John Wiley & Sons, Ltd; 2007.

[4] Johnson JB. Thermal agitation of electricity in conductors. Physical review 1928;32:97.

[5] Collins CM, Wang Z. Calculation of radiofrequency electromagnetic fields and their effects in MRI of human subjects. Magnetic Resonance in Medicine 2011;65:1470-1482.

[6] Pohmann R, Speck O, Scheffler K. Signal-to-noise ratio and MR tissue parameters in human brain imaging at 3, 7, and 9.4 tesla using current receive coil arrays. Magnetic Resonance in Medicine 2016;75:801-809.

[7] Tkac I, Oz G, Adriany G, Ugurbil K, Gruetter R. In vivo 1H NMR spectroscopy of the human brain at high magnetic fields: metabolite quantification at 4T vs. 7T. Magn Reson Med 2009;62:868-879.

[8] Bandettini PA, Bowtell R, Jezzard P, Turner R. Ultrahigh field systems and applications at 7 T and beyond: progress, pitfalls, and potential. Magn Reson Med 2012;67:317-321.

[9] Ugurbil K, Adriany G, Andersen P, Chen W, Garwood M, Gruetter R, Henry PG, Kim SG, Lieu H, Tkac I and others. Ultrahigh field magnetic resonance imaging and spectroscopy. Magn Reson Imaging 2003;21:1263-1281.

[10] Hong ST, Balla DZ, Shajan G, Choi C, Ugurbil K, Pohmann R. Enhanced neurochemical profile of the rat brain using in vivo (1)H NMR spectroscopy at 16.4 T. Magn Reson Med 2011;65:28-34.

[11] Boer VO, van Lier AL, Hoogduin JM, Wijnen JP, Luijten PR, Klomp DW. 7-T (1) H MRS with adiabatic refocusing at short TE using radiofrequency focusing with a dual-channel volume transmit coil. NMR Biomed 2011;24:1038-1046.

[12] Mekle R, Mlynarik V, Gambarota G, Hergt M, Krueger G, Gruetter R. MR spectroscopy of the human brain with enhanced signal intensity at ultrashort echo times on a clinical platform at 3T and 7T. Magn Reson Med 2009;61:1279-1285.

[13] Pfeuffer J, Tkac I, Provencher SW, Gruetter R. Toward an in vivo neurochemical profile: quantification of 18 metabolites in short-echo-time (1)H NMR spectra of the rat brain. J Magn Reson 1999;141:104-120.

[14] Tkac I, Andersen P, Adriany G, Merkle H, Ugurbil K, Gruetter R. In vivo 1H NMR spectroscopy of the human brain at 7 T. Magn Reson Med 2001;46:451-456.

[15] Giapitzakis IA, T. S, Avdievich N, Kreis R, Henning A. Optimisation of Asymmetric Adiabatic Pulses for Single Voxel Metabolite Cycled 1H-MRS in the Human Brain at 9.4 Tesla. Joint Annual Meeting ISMRM-ESMRMB. In: Proceedings of the Joint Annual Meeting ISMRM-ESMRMB, Milano, Italy, 2014. p 2895.

[16] Vaughan T, DelaBarre L, Snyder C, Tian J, Akgun C, Shrivastava D, Liu W, Olson C, Adriany G, Strupp J and others. 9.4T human MRI: preliminary results. Magn Reson Med 2006;56:1274-1282.

[17] Vaughan JT, Garwood M, Collins CM, Liu W, DelaBarre L, Adriany G, Andersen P, Merkle H, Goebel R, Smith MB and others. 7T vs. 4T: RF power, homogeneity, and signal-to-noise comparison in head images. Magnetic Resonance in Medicine 2001;46:24-30.

[18] Pozar DM. Microwave Engineering. 3rd ed. doi: John Wiley & Sons, Ltd; 2005.

[19] Gabriel S, Lau R, Gabriel C. The dielectric properties of biological tissues: III. Parametric models for the dielectric spectrum of tissues. Physics in medicine and biology 1996;41:2271.

[20] Bottomley PA. Turning Up the Heat on MRI. Journal of the American College of Radiology 2008;5:853-855.

[21] Bloembergen N, Purcell EM, Pound RV. Relaxation Effects in Nuclear Magnetic Resonance Absorption. Physical Review 1948;73:679-712.

[22] Michaeli S, Garwood M, Zhu XH, DelaBarre L, Andersen P, Adriany G, Merkle H, Ugurbil K, Chen W. Proton T2 relaxation study of water, N-acetylaspartate, and creatine in human brain using Hahn and Carr-Purcell spin echoes at 4T and 7T. Magn Reson Med 2002;47:629-633.

[23] Deelchand DK, Van de Moortele PF, Adriany G, Iltis I, Andersen P, Strupp JP, Vaughan JT, Ugurbil K, Henry PG. In vivo 1H NMR spectroscopy of the human brain at 9.4 T: initial results. J Magn Reson 2010;206:74-80.

[24] Bartha R, Michaeli S, Merkle H, Adriany G, Andersen P, Chen W, Ugurbil K, Garwood M. In vivo 1H2O T2+ measurement in the human occipital lobe at 4T and 7T by Carr-Purcell MRI: detection of microscopic susceptibility contrast. Magn Reson Med 2002;47:742-750.

[25] de Graaf RA, Brown PB, McIntyre S, Nixon TW, Behar KL, Rothman DL. High magnetic field water and metabolite proton T1 and T2 relaxation in rat brain in vivo. Magn Reson Med 2006;56:386-394.

[26] Carr HY, Purcell EM. Effects of Diffusion on Free Precession in Nuclear Magnetic Resonance Experiments. Physical Review 1954;94:630-638.

[27] Commission IE. Medical electrical equipment.-Part 2-33: particular requirements for the basic safety and essential performance of magnetic resonance equipment for medical diagnosis. IEC; 2010.

[28] Hoffmann J, Henning A, Giapitzakis IA, Scheffler K, Shajan G, Pohmann R, Avdievich NI. Safety testing and operational procedures for self-developed radiofrequency coils. NMR Biomed 2016;29:1131-1144.

[29] Mark T. Medical electrical equipment Part 1: General requirements for basic safety and essential performance. 2005. doi.

[30] STANDARD B, ISO B. Medical devices—Application of risk management to medical devices. 2007. doi.

[31] Zaremba LA. Guidance for industry and FDA staff: Criteria for significant risk investigations of magnetic resonance diagnostic devices. US Department of Health and Human Services, Food and Drug Administration 2003;14.

[32] Avdievich NI, Giapitzakis IA, Henning A. Optimization of the Receive Performance of a Tight-Fit Transceiver Phased Array for Human Brain Imaging at 9.4T. In:

Proceedings of the 25th Annual Meeting of International Society of Magnetic Resonace in Medicine, Honolulu, HI, USA, 2017. p 4309.

[33] Avdievich N, Giapitzakis IA, Henning A. Optimization of the receive performance of a tight-fit reansceiver phased array for human brain imaging at 9.4T. In: Proceedings of the 25th Annual Meeting of the International Society of Magnetic Resonance in Medicine, Honolulu, USA, 2017. p 2575.

[34] Avdievich NI, Giapitzakis IA, Henning A. Double-Row 16-element Tight-Fit Transceiver Phased Array with High Transmit Performance for Whole Human Brain Imaging at 9.4T. In: Proceedings of the 25th Annual Meeting of International Society of Magnetic Resonace in Medicine, Honolulu, HI, USA, 2017. p

[35] Avdievich NI, Giapitzakis IA, Henning A. Novel splittable N-Tx/2N-Rx transceiver phased array to optimize both signal-to-noise ratio and transmit efficiency at 9.4T. Magn Reson Med 2016;76:1621-1628.

[36] Pfrommer A, Avdievich NI, Henning A. Four Channel Transceiver Array for Functional Magnetic Resonance Spectroscopy in the Human Visual Cortex at 9.4 T. In: Proceedings of the 22nd Annual Meeting of ISMRM, Milan, Italy, 2014. p 1305.

[37] Shajan G, Kozlov M, Hoffmann J, Turner R, Scheffler K, Pohmann R. A 16-channel dual-row transmit array in combination with a 31-element receive array for human brain imaging at 9.4 T. Magn Reson Med 2014;71:870-879.

[38] Fuchs A, Luttje M, Boesiger P, Henning A. SPECIAL semi-LASER with lipid artifact compensation for 1H MRS at 7 T. Magn Reson Med 2013;69:603-612.

[39] Scheenen TW, Klomp DW, Wijnen JP, Heerschap A. Short echo time 1H-MRSI of the human brain at 3T with minimal chemical shift displacement errors using adiabatic refocusing pulses. Magn Reson Med 2008;59:1-6.

[40] van de Bank BL, Emir UE, Boer VO, van Asten JJ, Maas MC, Wijnen JP, Kan HE, Oz G, Klomp DW, Scheenen TW. Multi-center reproducibility of neurochemical profiles in the human brain at 7 T. NMR Biomed 2015;28:306-316.

[41] Tkáč I, Starčuk Z, Choi IY, Gruetter R. In vivo 1H NMR spectroscopy of rat brain at 1 ms echo time. Magnetic Resonance in Medicine 1999;41:649-656.

[42] Haase A, Frahm J, Hanicke W, Matthaei D. 1H NMR chemical shift selective (CHESS) imaging. Phys Med Biol 1985;30:341-344.

[43] Dreher W, Leibfritz D. New method for the simultaneous detection of metabolites and water in localized in vivo 1H nuclear magnetic resonance spectroscopy. Magn Reson Med 2005;54:190-195.

[44] MacMillan EL, Kreis R, Fuchs A, Versluis MJ, Boesch C, Boesiger P, Henning A. New technique for metabolite cycled non-water-suppressed proton spectroscopy in the human brain at 7T In: Proceedings of the 19th Scientific Meeting of the International Society for Magnetic Resonance in Medicine, Montreal, Canada, 2011. p 666.

[45] de Graaf RA, Sacolick LO, Rothman DL. Water and Metabolite-Modulated MR Spectroscopy and Spectroscopic Imaging. In: Proceedings of the 14th Scientific Meeting of the International Society of Magnetic Resonance in Medicine, Seattle, Washington, USA, 2006. p 3063.

[46] Giapitzakis I-A, Shao T, Avdievich N, Mekle R, Kreis R, Henning A. Metabolite-cycled STEAM and semi-LASER localization for MR spectroscopy of the human brain at 9.4T. Magnetic Resonance in Medicine 2017. doi: 10.1002/mrm.26873.

[47] MacMillan EL, Chong DG, Dreher W, Henning A, Boesch C, Kreis R. Magnetization exchange with water and T1 relaxation of the downfield resonances in human brain spectra at 3.0 T. Magn Reson Med 2011;65:1239-1246.

[48] Hock A, Henning A, Boesiger P, Kollias SS. (1)H-MR spectroscopy in the human spinal cord. AJNR Am J Neuroradiol 2013;34:1682-1689.

[49] Hock A, MacMillan EL, Fuchs A, Kreis R, Boesiger P, Kollias SS, Henning A. Non-water-suppressed proton MR spectroscopy improves spectral quality in the human spinal cord. Magn Reson Med 2013;69:1253-1260.

[50] Kreis R, Bolliger CS, MacMillan EL, Boettcher U, Boesch C. GABA editing without water suppression. In: Proceedings of the 20th Annual Meeting of the International Society for Magnetic Resonance in Medicine, Melbourne, Australia, 2012. p 1745.

[51] MacMillan EL, Bolliger CS, Boesch C, Kreis R. Influence of muscle fiber orientation on water and metabolite relaxation times, magnetization transfer, and visibility in human skeletal muscle. Magn Reson Med 2016;75:1764-1770.

[52] MacMillan EL, Boesch C, Kreis R. Magnetization exchange observed in human skeletal muscle by non-water-suppressed proton magnetic resonance spectroscopy. Magn Reson Med 2013;70:916-924.

[53] Hwang TL, van Zijl PC, Garwood M. Asymmetric adiabatic pulses for NH selection. J Magn Reson 1999;138:173-177.

[54] Gruetter R, Tkac I. Field mapping without reference scan using asymmetric echo-planar techniques. Magn Reson Med 2000;43:319-323.

[55] Versluis MJ, Kan HE, van Buchem MA, Webb AG. Improved signal to noise in proton spectroscopy of the human calf muscle at 7 T using localized B1 calibration. Magnetic Resonance in Medicine 2010;63:207-211.

[56] Behar KL, Ogino T. Characterization of macromolecule resonances in the 1H NMR spectrum of rat brain. Magn Reson Med 1993;30:38-44.

[57] Kauppinen RA, Niskanen T, Hakumäki J, Williams SR. Quantitative analysis of 1H NMR detected proteins in the rat cerebral cortex in vivo and in vitro. NMR in Biomedicine 1993;6:242-247.

[58] Kauppinen RA, Kokko H, Williams SR. Detection of Mobile Proteins by Proton Nuclear Magnetic Resonance Spectroscopy in the Guinea Pig Brain Ex Vivo and Their Partial Purification. Journal of Neurochemistry 1992;58:967-974.

[59] Behar KL, Rothman DL, Spencer DD, Petroff OA. Analysis of macromolecule resonances in 1H NMR spectra of human brain. Magn Reson Med 1994;32:294-302.

[60] Cudalbu C, Mlynarik V, Gruetter R. Handling macromolecule signals in the quantification of the neurochemical profile. J Alzheimers Dis 2012;31 Suppl 3:S101-115.

[61] Schaller B, Xin L, Gruetter R. Is the macromolecule signal tissue-specific in healthy human brain? A 1H MRS study at 7 tesla in the occipital lobe. Magnetic Resonance in Medicine 2014;72:934-940.

[62] Davie CA, Hawkins CP, Barker GJ, Brennan A, Tofts PS, Miller DH, McDonald WI. Detection of myelin breakdown products by proton magnetic resonance spectroscopy. Lancet 1993;341:630-631.

[63] Opstad KS, Bell BA, Griffiths JR, Howe FA. Toward accurate quantification of metabolites, lipids, and macromolecules in HRMAS spectra of human brain tumor biopsies using LCModel. Magn Reson Med 2008;60:1237-1242.

[64] Hwang JH, Graham GD, Behar KL, Alger JR, Prichard JW, Rothman DL. Short echo time proton magnetic resonance spectroscopic imaging of macromolecule and metabolite signal intensities in the human brain. Magn Reson Med 1996;35:633-639.

[65] Graham GD, Hwang JH, Rothman DL, Prichard JW. Spectroscopic assessment of alterations in macromolecule and small-molecule metabolites in human brain after stroke. Stroke 2001;32:2797-2802.

[66] Mader I, Seeger U, Karitzky J, Erb M, Schick F, Klose U. Proton magnetic resonance spectroscopy with metabolite nulling reveals regional differences of macromolecules in normal human brain. J Magn Reson Imaging 2002;16:538-546.

[67] Saunders DE, Howe FA, van den Boogaart A, Griffiths JR, Brown MM. Discrimination of metabolite from lipid and macromolecule resonances in cerebral infarction in humans using short echo proton spectroscopy. J Magn Reson Imaging 1997;7:1116-1121.

[68] Seeger U, Klose U, Mader I, Grodd W, Nagele T. Parameterized evaluation of macromolecules and lipids in proton MR spectroscopy of brain diseases. Magn Reson Med 2003;49:19-28.

[69] Chong DG, Kreis R, Bolliger CS, Boesch C, Slotboom J. Two-dimensional linear-combination model fitting of magnetic resonance spectra to define the macromolecule baseline using FiTAID, a Fitting Tool for Arrays of Interrelated Datasets. MAGMA 2011;24:147-164.

[70] Hofmann L, Slotboom J, Boesch C, Kreis R. Characterization of the macromolecule baseline in localized (1)H-MR spectra of human brain. Magn Reson Med 2001;46:855-863.

[71] Provencher SW. Automatic quantitation of localized in vivo 1H spectra with LCModel. NMR Biomed 2001;14:260-264.

[72] Schaller B, Xin L, Cudalbu C, Gruetter R. Quantification of the neurochemical profile using simulated macromolecule resonances at 3 T. NMR Biomed 2013;26:593-599.

[73] Giapitzakis IA, Kreis R, Henning A. Characterization of the macromolecular baseline with a metabolite-cycled double-inversion recovery sequence in the human brain at 9.4T. In: Proceedings of the 24th Annual Meeting of the International Society for Magnetic Resonance in Medicine, Singapore, 2016. p 0016.

[74] Avdievich NI. Transceiver-Phased Arrays for Human Brain Studies at 7 T. Appl Magn Reson 2011;41:483-506.

[75] Adriany G, Van de Moortele PF, Ritter J, Moeller S, Auerbach EJ, Akgun C, Snyder CJ, Vaughan T, Ugurbil K. A geometrically adjustable 16-channel transmit/receive transmission line array for improved RF efficiency and parallel imaging performance at 7 Tesla. Magn Reson Med 2008;59:590-597.

[76] Gilbert KM, Belliveau JG, Curtis AT, Gati JS, Klassen LM, Menon RS. A conformal transceive array for 7 T neuroimaging. Magn Reson Med 2012;67:1487-1496.

[77] Avdievich NI, Hoffmann J, Shajan G, Pfrommer A, Giapitzakis IA, Scheffler K, Henning A. Evaluation of transmit efficiency and SAR for a tight fit transceiver human head phased array at 9.4 T. NMR Biomed 2017;30.

[78] Dixon WT, Sardashti M, Castillo M, Stomp GP. Multiple inversion recovery reduces static tissue signal in angiograms. Magn Reson Med 1991;18:257-268.

[79] Tannús A, Garwood M. Improved Performance of Frequency-Swept Pulses Using Offset-Independent Adiabaticity. Journal of Magnetic Resonance, Series A 1996;120:133-137.

[80] Xin L, Schaller B, Mlynarik V, Lu H, Gruetter R. Proton T1 relaxation times of metabolites in human occipital white and gray matter at 7 T. Magn Reson Med 2013;69:931-936.

[81] Xu X, Yadav NN, Knutsson L, Hua J, Kalyani R, Hall E, Laterra J, Blakeley J, Strowd R, Pomper M and others. Dynamic Glucose-Enhanced (DGE) MRI: Translation to Human Scanning and First Results in Glioma Patients. Tomography 2015;1:105-114.

[82] Jones CK, Schlosser MJ, van Zijl PC, Pomper MG, Golay X, Zhou J. Amide proton transfer imaging of human brain tumors at 3T. Magn Reson Med 2006;56:585-592.

[83] McLean MA, Barker GJ. Concentrations and magnetization transfer ratios of metabolites in gray and white matter. Magn Reson Med 2006;56:1365-1370.

[84] Ward KM, Aletras AH, Balaban RS. A new class of contrast agents for MRI based on proton chemical exchange dependent saturation transfer (CEST). J Magn Reson 2000;143:79-87.

[85] Fichtner ND, Henning A, Zoelch N, Boesch C, Kreis R. Elucidation of the downfield spectrum of human brain at 7 T using multiple inversion recovery delays and echo times. Magn Reson Med 2017;78:11-19.

[86] Henning A, Fuchs A, Boesch C, Boesiger P, Kreis R. Downfield spectra at ultrahigh field. In: Proceedings of the 16th Annual Meeting of International Society of Magnetic Resonace in Medicine, Toronto,Canada, 2008. p 777.

[87] McConnell HM. Reaction Rates by Nuclear Magnetic Resonance. The Journal of Chemical Physics 1958;28:430-431.

[88] van Zijl PC, Zhou J, Mori N, Payen JF, Wilson D, Mori S. Mechanism of magnetization transfer during on-resonance water saturation. A new approach to detect mobile proteins, peptides, and lipids. Magn Reson Med 2003;49:440-449.

[89] Fichtner ND, Henning A, Zoelch N, Boesch C, Kreis R. Elucidation of the downfield spectrum of human brain at 7 T using multiple inversion recovery delays and echo times. Magnetic Resonance in Medicine 2017;78:11-19.

[90] Watanabe T, Frahm J, Michaelis T. Amide proton signals as pH indicator for in vivo MRS and MRI of the brain-Responses to hypercapnia and hypothermia. Neuroimage 2016;133:390-398.

[91] Bednarik P, Tkac I, Giove F, DiNuzzo M, Deelchand DK, Emir UE, Eberly LE, Mangia S. Neurochemical and BOLD responses during neuronal activation measured in the human visual cortex at 7 Tesla. J Cereb Blood Flow Metab 2015;35:601-610.

[92] Lin Y, Stephenson MC, Xin L, Napolitano A, Morris PG. Investigating the metabolic changes due to visual stimulation using functional proton magnetic resonance spectroscopy at 7 T. J Cereb Blood Flow Metab 2012;32:1484-1495.

[93] Mangia S, Tkac I, Gruetter R, Van de Moortele PF, Maraviglia B, Ugurbil K. Sustained neuronal activation raises oxidative metabolism to a new steady-state level: evidence from 1H NMR spectroscopy in the human visual cortex. J Cereb Blood Flow Metab 2007;27:1055-1063.

[94] Schaller B, Mekle R, Xin L, Kunz N, Gruetter R. Net increase of lactate and glutamate concentration in activated human visual cortex detected with magnetic resonance spectroscopy at 7 tesla. J Neurosci Res 2013;91:1076-1083.

[95] Schaller B, Xin L, O'Brien K, Magill AW, Gruetter R. Are glutamate and lactate increases ubiquitous to physiological activation? A (1)H functional MR spectroscopy study during motor activation in human brain at 7Tesla. Neuroimage 2014;93 Pt 1:138-145.

[96] Giapitzakis IA, Avdievich N, S.M M, Fichtner N, Kreis R, Henning A. Functional Magnetic Resonance Spectroscopy (fMRS) using metabolite cycled semi-LASER at 9.4T: a pilot study. In: Proceedings of the 25th Annual Meeting and Exhibition of the International Society for Magnetic Resonance in Medicine, Honolulu, HI, USA, 2017. p 277.

[97] Klose U. In vivo proton spectroscopy in presence of eddy currents. Magn Reson Med 1990;14:26-30.

[98] Zhu XH, Chen W. Observed BOLD effects on cerebral metabolite resonances in human visual cortex during visual stimulation: a functional (1)H MRS study at 4 T. Magn Reson Med 2001;46:841-847.

[99] Betina Ip I, Berrington A, Hess AT, Parker AJ, Emir UE, Bridge H. Combined fMRI-MRS acquires simultaneous glutamate and BOLD-fMRI signals in the human brain. Neuroimage 2017;155:113-119.

[100] Chen C, Sigurdsson HP, Pepes SE, Auer DP, Morris PG, Morgan PS, Gowland PA, Jackson SR. Activation induced changes in GABA: Functional MRS at 7T with MEGA-sLASER. Neuroimage 2017;156:207-213.

4. List of Publications & Statement of Contributions

Articles included in this doctoral thesis*

1. Hoffmann J, Henning A, **Giapitzakis IA**, Scheffler K, Shajan G, Pohmann R, Avdievich NI. *Safety testing and operational procedures for self-developed radiofrequency coils*. NMR Biomed 2016;29:1131-44.

   Hoffman J. wrote the major part of this paper, performed the majority of the experiments, set some of the safety tests and developed most of the post-processing routines for the analysis of the data. *Henning A*. Coordinated safety operational procedures and paper, defined some of the tests and wrote parts of the paper. *Giapitzakis IA* wrote about the QA part of the paper and developed post-processing routines regarding the QA. *Scheffler K* wrote parts of the paper and contributed to the structure of the paper. *Shajan G* wrote parts of the paper and provided technical information regarding RF coils, *Pohmann R* wrote parts of the papers, provided technical details regarding the safety operations of the scanner and contributed to the structure of the paper. *Avdievich NI* wrote parts of the paper and provided technical information regarding RF coils.

2. **Giapitzakis I.A**, Shao S, Avdievich NI, Mekle R, Kreis R and Henning A. *Metabolite-cycled STEAM and semi-LASER localization for MR spectroscopy of the human brain at 9.4T.* Magn Reson Med 2018;79:1841-1850 DOI: 10.1002/mrm.26873

   Giapitzakis I.A. developed the sequences, the post-processing techniques, installed the B_0 shimming technique to the scanner (FASTE(ST)MAP), recruited

* For the full list of publications during the PhD please refer to the Academic CV chapter

the volunteers, performed the experiments, analyzed the data and wrote this paper. *Shao T.*, performed the 2D simulations for the excitation profile of the MC-semi-LASER sequence, as well as, developed the matlab code for the Bloch equation simulations*. Avdievich N.I.* designed the coil. *Mekle R.* provided the code for the voxel-based power optimization. *Kreis R.* and *Henning A.* supervised the project and proofread the text.

3. **Giapitzakis I.A**, Avdievich NI, Henning A. *Characterization of macromolecular baseline at 9.4 T*. Magn Reson Med . DOI: 10.1002/mrm.27070 (Epub ahead)

Giapitzakis I.A. developed the sequences, the post-processing techniques, recruited the volunteers, performed the experiments, analyzed the data and wrote the major part of this this paper*. Avdievich N.I.* designed the coil, the 3-way splitter, performed the SAR simulations and wrote part of this paper. *Henning A.* supervised the project and proofread the text.

4. Fichtner N*, **Giapitzakis I.A***, Avdievich NI, Mekle R, Zaldivar D, Henning A and Kreis R*. In vivo characterization of the downfield part of 1H MR spectra of human brain at 9.4T: Magnetization exchange with water and relation to conventionally determined metabolite content*. Magn Med Reson 2018;79:2863-2873 DOI: 10.1002/mrm.26968, (***equal contribution**)

Fichtner N. developed the model for the chemical exchange of the downfield metabolites, performed the experiments, analysed the data and wrote the major part of this paper. *Giapitzakis I.A* develoepd the sequences, the post-processing techniques, provided the settings for the LCModel analysis, recruited the volunteers, performed the experiments and wrote some parts of this paper.

Avdievich N.I. designed the coil. *Mekle R.* provided the code for the voxel-based power optimization. *Zaldivar D.* was the physician in charge for the performance of the in vivo experiments. *Kreis R.* and *Henning A.* supervised the project and proofread the text.

5. Acknowledgements

Every achievement and any project in life is not possible without the support of other people, regarding either financial support or moral support. Thus, in the following sentences, I would like to thank all of those individuals who motivated me, inspired me and made the years of my Ph.D. a joyful and a constructive experience.

Firstly, I would like to thank my family, my grandmothers, my sister Eleni and especially my parents Iosif and Anna Maria, who gave me the opportunity to pursue my goals and develop my skills. Without their encouragement from the beginning of my life, every feather that was added to my cap so far would not be feasible.

My heartfelt thanks to my supervisor Prof. Dr. Anke Henning and my co-supervisor Prof. Dr. Roland Kreis who assigned me this project and believed in my skills and abilities. Their suggestions, constructive comments, and fruitful discussions were essential for the completion of my Ph.D. projects and helped me to become (hopefully) a better scientist with a more critical way of thinking regarding science. Except the purely scientific aspect of our collaboration, our daily interaction and conversations were beneficial and gave me many insights regarding life and research as well. Moreover, I would like to thank my third co-supervisor, Prof. Dr. Klaus Scheffler who was always willing to discuss issues with me regarding my projects and to assist me when required.

The truth is that a Ph.D. can be a quite stressful procedure (especially in cases of deadlines ☺), however, in my case, the joyful interaction with my colleagues and friends was crucial to have all these nice moments which I shared with them. For this purpose, I would like to thank all of my colleagues one by one starting from the former members of the group: Dr. Erin McMilan, Dr. Andreas Hock and Dr. Alex Fuchs, for our productive discussions regarding MRS postprocessing and metabolite cycling technique. Dr Niklaus Zoelch for our informative conversations concerning MRS absolute quantification. Dr. Ariane Filmer, for her invaluable insights into B_0 shimming and our collaboration about

the incorporation of the MC technique with the SPECIAL sequence at 7 T. Dr. Thomas Kirchner for our talks relating to MRSI techniques and challenges at ultra-high fields. Dr. Milan Scheidegger, for our conversations about neurosciences and human brain physiology.

Dr. Nicolai Avdievich, without his technical contribution regarding the design of new coils the achievement of my Ph.D. would be impossible. Moreover, our technical dialogues regarding RF coils enhanced my knowledge with respect to the hardware components of an MR scanner. Tingting Shao who was not only for being a nice colleague and flatmate, but was a really good friend. Andreas Pfrommer, my officemate, with whom I had the chance to have a lot of interesting discussions during the “boring” time of writing papers. Dr. Nicole Fichtner with whom I had the opportunity to perform several experiments and discuss several issues during long experiments it the scanner room. Sahar Nassirpour and Paul Chang with whom I had the chance to collaborate on several projects with, enlightening my knowledge of MRSI and B0 Shimming in the process. Tamas Borbath and Saipavitra Murali Manohar with whom I had an excellent collaboration across several projects. I would also like to mention the newbies of our group: Johanna Dorst, Ole Geldschlager and Theresia Ziegs.

In addition, I express my gratitude to Liam Connah, Saipavitra Murali Manohar, Dr. Vinod Kumar and Andrew Wright for proof-reading parts of this thesis, as well as, for their constructive comments.

Not to forget, I would like to acknowledge many previous and current colleagues of the MPI campus and UHF department who I have had the chance to collaborate and interact with: Dr. Philipp Ehses, Bause Jonas, Pais Patricia, Dr. Pohmann Rolf, Dr. David Balla, Dr. Nevenka Cakic, Dr. Chadzynski Grzegorz, Dr. Hoffmann Jens, Dr. Mirkes Christian, Dr. Zivkovic Irena, Rosa Pujales-Paradela, Adrianni Rina, Symeonidou Eva, Despoina Paschalidou, Dr. Dimitrios Tzionas, Fatemeh Molaei.

Furthermore, my special thanks to Severine Boissard. Her support was vital for the completion of my Ph.D. and her encouragement gave me the motivation and yearning for new ideas.

Finally yet importantly, I am grateful to the citizens of the Hellenic Republic, as well as, the Greek State Scholarships Foundation (IKY) who have supported me financially all through years since parts of this thesis were co-sponsored by the European Social Fund and national funds (NSRF 2007-2013) through the IKY. I hope that with the knowledge I have gained and the important skills I have developed, will be able to one day contribute to the development and the improvement of the Hellenic Republic.

6. Academic CV

PERSONAL INFORMATION

Full name	Ioannis-Angelos Giapitzakis
✉ :	ioannis.giapitzakis@gmail.com
☎ mobile:	+ 49 177 86 35 679
Birthday/ Birthplace:	28th September 1988/ Athens, Hellenic Republic
Nationality	Hellenic/ Italian

EDUCATION

2012 Nov.- 2017 Dec.	**Ph.D. candidate** in Neurosciences Max Planck Institute for Biological Cybernetics & University of Tübingen, Tübingen, Germany
2011- 2012	**M.Sc., DIC** in Biomedical Engineering with Medical Physics, Imperial College London, London, U.K. **(Grade: 75.9%**)
2006-2011	**Dip.** in Applied Mathematical and Physical Sciences (5-years degree), National Technical Uni. of Athens, Greece (**Grade: 8.25/10; Top 5%)** Majors: Nuclear Physics and Optoelectronics

RESEARCH EXPERIENCE

2017 Oct- 2018 Jan	**Research Scientist** Max Planck Institute for Biological Cybernetics, Tübingen, Germany

2012 Nov.-2017 Oct	**Ph.D. student** Max Planck Institute for Biological Cybernetics, Tübingen, Germany **Project title***: Magnetic Resonance Spectroscopy in the human brain at Ultra High Field Strength): Methods and Applications.*
2012 April –Sep.	**Postgraduate research scientist** Radiological Sciences Unit, Charing Cross Hospital, Imperial College Healthcare, London and C3NL, Hammersmith Hospital, London, UK **Project title**: *Co-analysis of resting state functional magnetic resonance imaging and diffusion tensor imaging for correlation of default mode network and ultra-structural deficit in posterior cortical atrophy*
2011 April –Sep.	**Undergraduate research scientist** Diagnostic Centre Euromedica “Encephalos”, Athens, Greece **Project Title**: *The magnetic Tractography in the investigation of myelination in the human brain*

SCHOLARSHIPS/GRANTS/AWARDS

2017	**Summa Cum Laude** (Top 5%) & **Magna Cum Laude** (Top 10%) awards from the International Society for Magnetic Resonance in Medicine (ISMRM)
2016	**Magna Cum Laude** award (Top 10%) from ISMRM
2012-2016	**Grant** from Max Planck Institute Society for Doctoral studies
2012-2015 .	**Scholarship** from State Scholarships Foundation (Greece) and European Social Fund for Doctoral studies
2012-2013	Institute of Engineering and Physics in Medicine (IPEM) award for the **best M.Sc. project in Medical Physics**

2011-2012	M.Sc. from Imperial College London with honors (**Merit**)
2011-2012	**Scholarship** from State Scholarships Foundation (Greece) and European Social Fund for Postgraduate studies

RESEARCH INTERESTS

Neurosciences, Medical Physics, Medical Imaging, Biomedical Engineering. Medical Technology, ^{1}H-MRS, Development of MRS Sequences,, f-MRS, Macromolecules, MR Safety, MR Coils Quality Control, Brain Metabolism

PUBLICATIONS

- Articles: 12 (accepted, submitted and under preparation)
- Book chapters: 1
- Talks in international conferences: 15
- Conference Proceedings (Peer-Reviewed): 21

Articles (12)

1. **Giapitzakis I.A**, Borbath T., Manohar M.S, Avdievich NI and Henning A (December-2017) Influence of tissue specific macromolecular baseline in human brain metabolites quantification at 9.4T. (submitted)

2. Avdievich NI, **Giapitzakis I.A**, Pfrommer A and Henning A (June-2017) Decoupling of a Double-Row 16-element Tight-Fit Transceiver Phased Array for Human Whole Brain Imaging at 9.4T. *NMR in Biomedicine* (under review)

3. **Giapitzakis I.A**, Avdievich NI, Henning A (December -2017) Characterization of macromolecular baseline at 9.4 T. *Magnetic Resonance in Medicine.* DOI: 10.1002/mrm.27070

4. Wyss P, Bianchini C, Scheidegger M, **Giapitzakis I-A**, Hock A, Fuchs A and Henning A (December-2017) In vivo estimation of transverse relaxation time constant (T_2) of 17 human brain metabolites at 3T *Magnetic Resonance in Medicine*. DOI: 10.1002/mrm.27067

5. Avdievich NI, **Giapitzakis IA** and Henning A (November-2017) Combined Surface Loop/ 'Vertical' Loop Element Improve Receive Performance of a Human Head Transceiver Array at 9.4T: an Alternative to Surface Loop/ Dipole Antenna Combination *NMR in Biomedicine.* DOI: 10.1002/nmb.3878

6. Avdievich NI, Pfrommer A, **Giapitzakis IA** and Henning A (Octoober-2017) Analytical Modeling Provides New Insight into Complex Mutual Coupling between Surface Loops at Ultra High Fields *NMR in Biomedicine* 30(10) 1-13.

7. Fichtner N***,Giapitzakis I.A***, Avdievich NI, Mekle R, Zaldivar D, Henning A and Kreis R (October-2017) In vivo characterization of the downfield part of 1H MR spectra of human brain at 9.4T: Magnetization exchange with water and relation to conventionally determined metabolite content *Magnetic Resonance in Medicine***. *equal contribution** DOI: 10.1002/mrm.26968

8. **Giapitzakis I.A**, Tingting S, Avdievich NI, Mekle R, Kreis R and Henning A (August-2017) Metabolite-cycled STEAM and semi-LASER localization for MR spectroscopy of the human brain at 9.4T *Magnetic Resonance in Medicine*. DOI: 10.1002/mrm.26873

9. Avdievich NI, **Giapitzakis I.A**, Pfrommer A and Henning A (June-2017) Decoupling of a Tight-Fit Transceiver Phased Array for Human Brain Imaging at 9.4T: Loop Overlapping Rediscovered *Magnetic Resonance in Medicine*. DOI: 10.1002/mrm.26754

10. Avdievich NI, Hoffmann J, Shajan G, Pfrommer A, **Giapitzakis IA**, Scheffler K and Henning A (February-2017) Evaluation of transmit efficiency and SAR for a tight fit transceiver human head phased array at 9.4 T *NMR in Biomedicine* 30(2) 1-12.

11. Avdievich NI, **Giapitzakis IA** and Henning A (November-2016) Novel splittable N-Tx/2N-Rx transceiver phased array to optimize both signal-to-noise ratio and transmit efficiency at 9.4T *Magnetic Resonance in Medicine* 76(5) 1621-1628.

12. Hoffmann J, Henning A, **Giapitzakis IA**, Scheffler K, Shajan G, Pohmann R and Avdievich NI (September-2016) Safety testing and operational procedures for self-developed radiofrequency coils *NMR in Biomedicine* 29(9) 1131–1144

Book Chapters (1)

1. **Giapitzakis IA** and Henning A: MRS Sequences and Protocols, -. In: *Clinical MR Spectroscopy*, (Ed) J. McNulty, Springer International Publishing, Cham, Switzerland, (February-2018). in press

Talks (15)

1. Avdievich N, **Giapitzakis I** and Henning A (October-20-2017) Abstract Talk: Combined Surface Loop/"Vertical" Loop Elements Improve Receive Performance of a Human Head Transceiver Phased Array at 9.4T: an Alternative to Surface Loop/Dipole Antenna Combination, 34th Annual Scientific Meeting of the European Society for Magnetic Resonance in Medicine and Biology (ESMRMB 2017), Barcelona, Spain, Magnetic Resonance Materials in Physics, Biology and Medicine, 30(Supplement 1) S297-S298.

2. **Giapitzakis I-A**, Fichtner N, Zaldivar D, Avdievich N, Manohar S, Kreis R and Henning A (October-20-2017) Abstract Talk: Simultaneous detection of water and metabolites alternations under visual stimulation in human visual cortex utilizing metabolite cycled semi-LASER at 9.4T: preliminary results, 34th Annual Scientific Meeting of the European Society for Magnetic Resonance in Medicine and Biology (ESMRMB 2017), Barcelona, Spain, Magnetic Resonance Materials in Physics, Biology and Medicine, 30(Supplement 1) S246-S247.

3. Borbáth T, **Giapitzakis I**, Murali Manohar SV and Henning A (October-19-2017) Abstract Talk: Do macromolecular and spline baselines affect the metabolite quantification at 9.4T?, 34th Annual Scientific Meeting of the European Society for Magnetic Resonance in Medicine and Biology (ESMRMB 2017), Barcelona, Spain, Magnetic Resonance Materials in Physics, Biology and Medicine, 30(Supplement 1) S115-S116.

4. **Giapitzakis I-A**, Shao T, Avdievitsch N, Fichtner N, Merkle R, Kreis R and Henning A (April-27-2017) Abstract Talk: Metabolite cycled semi-LASER and STEAM at 9.4T: Comparison and in vivo results, 25th Annual Meeting and Exhibition of the International Society for Magnetic Resonance in Medicine (ISMRM 2017), Honolulu, HI, USA(1061).

5. Martínez-Maestro M, Labadie C, **Giapitzakis I** and Möller H (April-25-2017) Abstract Talk: Dynamic changes of glutamate detected by functional MR spectroscopy in human visual cortex in regions with positive and negative BOLD

response, 25th Annual Meeting and Exhibition of the International Society for Magnetic Resonance in Medicine (ISMRM 2017), Honolulu, HI, USA(0404).

6. **Giapitzakis IA**, Avdievitch N, Manohar SM, Fichtner N, Kreis R and Henning A (April-25-2017) Abstract Talk: Functional Magnetic Resonance Spectroscopy (fMRS) using metabolite cycled semi-LASER at 9.4T: a pilot study, 25th Annual Meeting and Exhibition of the International Society for Magnetic Resonance in Medicine (ISMRM 2017), Honolulu, HI, USA(0402).

7. Fichtner ND, **Giapitzakis I-A**, Avdievich N, Merkle R, Zaldivar D, Henning A and Kreis R (February-2-2017) Abstract Talk: Measuring Exchange Between Brain Metabolites and Water Using Ultra-High Field Magnetic Resonance Spectroscopy, GCB Symposium 2017: Graduate School for Cellular and Biomedical Sciences, Bern, Switzerland.

8. **Giapitzakis I-A** (August-16-2016) Abstract Talk: Metabolite Cycled Semi-LASER in Human Brain at 9.4T: In-Vivo Results, ISMRM Workshop on MR Spectroscopy: From Current Best Practice to Latest Frontiers, Allensbach-Hegne, Germany.

9. **Giapitzakis IA**, Kreis R and Henning A (May-9-2016) Abstract Talk: Characterization of the macromolecular baseline with a metabolite-cycled double-inversion recovery sequence in the human brain at 9.4T, 24th Annual Meeting and Exhibition of the International Society for Magnetic Resonance in Medicine (ISMRM 2016), Singapore(0016)

10. Avdievich NI, **Giapitzakis IA**, Pfrommer A and Henning A (May-9-2016) Abstract Talk: Optimization of the Transceiver Phased Array for Human Brain Imaging at 9.4T: Loop Overlapping Rediscovered, 24th Annual Meeting and Exhibition of the International Society for Magnetic Resonance in Medicine (ISMRM 2016), Singapore (0169).

11. **Giapitzakis IA**, Nassirpour S, Avdievich NI, Kreis R and Henning A (October-2015) Abstract Talk: 1H single voxel spectroscopy at occipital lobe of human brain at 9.4 T, 32nd Annual Scientific Meeting ESMRMB 2015, Edinburgh, UK, Magnetic Resonance Materials in Physics, Biology and Medicine, 28(1 Supplement) S208-S209.

12. Avdievich NI, **Giapitzakis IA** and Henning A (October-2015) Abstract Talk: Novel Splittable N-Tx/2N-Rx Transceiver Phased Array to Optimize both SNR

and Transmit Efficiency at 9.4T, 32nd Annual Scientific Meeting ESMRMB 2015, Edinburgh, UK, Magnetic Resonance Materials in Physics, Biology and Medicine, 28(1 Supplement) S57.

13. **Giapitzakis IA**, Nassirpour S and Henning A (October-2015) Abstract Talk: Short duration water suppresion using optimised flip angles (SODA) at ultra high fields, 32nd Annual Scientific Meeting ESMRMB 2015, Edinburgh, UK, Magnetic Resonance Materials in Physics, Biology and Medicine, 28(1 Supplement) S401-S402.

14. Scheidegger M, Fuchs A, Ametamey S, Kuhn F, **Giapitzakis IA**, Johayem A, Buck A, Seifritz E and Henning A (March-20-2015) Abstract Talk: Observation of synaptic plasticity in the healthy human brain upon Ketamine infusion by 11C-ABP688-PET and 2D J-resolved 1H MRS, 10th Annual Meeting of the European Society for Molecular Imaging (EMIM 2015), Tübingen, Germany(300).

15. **Giapitzakis I** (September-13-2013) Invited Lecture: Functional magnetic resonance spectroscopy at ultra-high field strength, Networks! 2013: 4th German Neurophysiology PhD Meeting, Tübingen, Germany.

Conference Proceedings (21)

1. **Giapitzakis I-A**, Avdievich N and Henning A (October-21-2017): Characterization of macromolecular baseline of human brain using metabolite cycled semi-LASER at 9.4 T, 34th Annual Scientific Meeting of the European Society for Magnetic Resonance in Medicine and Biology (ESMRMB 2017), Barcelona, Spain, Magnetic Resonance Materials in Physics, Biology and Medicine, 30(Supplement 1) S475-S476.

2. Avdievich N, **Giapitzakis I** and Henning A (October-20-2017): Double-Row 16-element Tight-Fit Transceiver Phased Array with High Transmit Performance for Whole Human Brain Imaging at 9.4T, 34th Annual Scientific Meeting of the European Society for Magnetic Resonance in Medicine and Biology (ESMRMB 2017), Barcelona, Spain, Magnetic Resonance Materials in Physics, Biology and Medicine, 30(Supplement 1) S25

3. **Giapitzakis I-A** and Henning A (April-27-2017): Basis set optimization for quantification of semi-LASER at 9.4T under consideration of CP effect and

relaxation, 25th Annual Meeting and Exhibition of the International Society for Magnetic Resonance in Medicine (ISMRM 2017), Honolulu, HI, USA.

4. Borbáth T, **Giapitzakis IA**, Murali Manohar SV and Henning A (April-27-2017): Fitting comparison for 9.4T 1D semi-LASER and 2D-J-resolved semi-LASER data, 25th Annual Meeting and Exhibition of the International Society for Magnetic Resonance in Medicine (ISMRM 2017), Honolulu, HI, USA.

5. Fichtner N, **Giapitzakis I-A**, Avdievich N, Mekle R, Zaldivar D, Henning A and Kreis R (April-27-2017): Magnetization exchange between water and downfield metabolites in human brain at 9.4T, 25th Annual Meeting and Exhibition of the International Society for Magnetic Resonance in Medicine (ISMRM 2017), Honolulu, HI, USA.

6. Murali Manohar SV, **Giapitzakis IA**, Borbáth T, Gaertner M and Henning A (April-27-2017): Qualitative Comparison between In Vivo J-Resolved Semi-LASER at 3 T and 9.4 T, 25th Annual Meeting and Exhibition of the International Society for Magnetic Resonance in Medicine (ISMRM 2017), Honolulu, HI, USA.

7. Fillmer A, **Giapitzakis I**, Mekle R, Aydin S, Henning A, Ittermann B and Schubert R (April-27-2017): Very Short Echo Time MRS for Single Voxel Spectroscopy in Small Voxels, 25th Annual Meeting and Exhibition of the International Society for Magnetic Resonance in Medicine (ISMRM 2017), Honolulu, HI, USA.

8. Avdievich N, **Giapitzakis I** and Henning A (April-26-2017): Double-Row 16-element Tight-Fit Transceiver Phased Array with High Transmit Performance for Whole Human Brain Imaging at 9.4T, 25th Annual Meeting and Exhibition of the International Society for Magnetic Resonance in Medicine (ISMRM 2017), Honolulu, HI, USA.

9. Avdievich N, **Giapitzakis I** and Henning A (April-25-2017): Effect of Mismatching on the Transmit and Receive Performance of a Human Head 9.4T Tight-Fit Transceiver Phased Array, 25th Annual Meeting and Exhibition of the International Society for Magnetic Resonance in Medicine (ISMRM 2017), Honolulu, HI, USA.

10. Avdievich N, **Giapitzakis I** and Henning A (April-25-2017): Optimization of the Receive Performance of a Tight-Fit Transceiver Phased Array for Human Brain Imaging at 9.4T, 25th Annual Meeting and Exhibition of the International Society for Magnetic Resonance in Medicine (ISMRM 2017), Honolulu, HI, USA.

11. Fichtner ND, **Giapitzakis IA**, Avdievich N, Henning A and Kreis R (May-11-2016): Downfield spectra of human brain obtained with and without water suppression at 9.4T, 24th Annual Meeting and Exhibition of the International Society for Magnetic Resonance in Medicine (ISMRM 2016), Singapore.

12. Avdievich NI, Pfrommer A, **Giapitzakis IA** and Henning A (May-10-2016): Analytical Modeling of the Coupling within a Human Head Surface Loop Transmit Phased Array at Ultra-High Fields, 24th Annual Meeting and Exhibition of the International Society for Magnetic Resonance in Medicine (ISMRM 2016), Singapore.

13. Fichtner N, Henning A**, Giapitzakis I**, Zoelch N, Avdievich N, Boesch C and Kreis R (March-31-2016): Downfield MR Spectroscopy at Ultrahigh Magnetic Fields, 11th Annual Meeting Brain Connectivity, Bern, Switzerland.

14. Nassirpour S, Kirchner T, **Giapitzakis IA** and Henning A (June-4-2015): Accelerated Multi-slice 1H FID-MRSI in the human brain at 9.4 T, 23rd Annual Meeting and Exhibition of the International Society for Magnetic Resonance in Medicine (ISMRM 2015), Toronto, Canada.

15. **Giapitzakis IA**, Nassirpour S, Avdievich N, Kreis R and Henning A (June-4-2015): Metabolite cycled single voxel 1H spectroscopy at 9.4T, 23rd Annual Meeting and Exhibition of the International Society for Magnetic Resonance in Medicine (ISMRM 2015), Toronto, Canada.

16. **Giapitzakis IA** and Henning A (June-3-2015): Comparison of different methods for combination of multichannel spectroscopy data, 23rd Annual Meeting and Exhibition of the International Society for Magnetic Resonance in Medicine (ISMRM 2015), Toronto, Canada.

17. Avdievich NI, **Giapitzakis IA** and Henning A (June-2-2015): Novel Splittable N-Tx/2N-Rx Transceiver Phased Array to Optimize both SNR and Transmit Efficiency at 9.4 T, 23rd Annual Meeting and Exhibition of the International Society for Magnetic Resonance in Medicine (ISMRM 2015), Toronto, Canada.

18. Avdievich NI, **Giapitzakis IA** and Henning A (June-1-2015): Asymmetric Transceiver Phased Array for Functional Imaging and Spectroscopy of the Visual Cortex at 9.4 T, 23rd Annual Meeting and Exhibition of the International Society for Magnetic Resonance in Medicine (ISMRM 2015), Toronto, Canada.

19. **Giapitzakis IA**, Nassirpour S, Kreis R, Avdievich NI and Henning A (March-19-2015): Metabolite cycled proton magnetic resonance spectroscopy at 9.4T, 10th Annual Meeting of the European Society for Molecular Imaging (EMIM 2015), Tübingen, Germany.

20. **Giapitzakis IA**, Shao T, Avdievich N, Kreis R and Henning A (May-15-2014): Optimisation of Asymmetric Adiabatic Pulses for Single Voxel Metabolite Cycled 1H-MRS in the Human Brain at 9.4 Tesla, Joint Annual Meeting ISMRM-ESMRMB 2014, Milano, Italy.

21. **Giapitzakis I**, Quest RA and Waldman AD (October-3-2013): Co-analysis of resting state functional magnetic resonance imaging and diffusion tensor imaging for correlation of default mode network and ultra-structural deficit in posterior cortical atrophy, 30th Annual Scientific Meeting ESMRMB 2013, Toulouse, France, Magnetic Resonance Materials in Physics, Biology and Medicine, 19(Supplement 1) 84-85.

7. Appended publications

© The reprints of the publications are made with permission of John Wiley & Sons, Inc.

Special issue research article

NMR IN BIOMEDICINE

Received: 30 September 2014, Revised: 25 February 2015, Accepted: 25 February 2015, Published online in Wiley Online Library: 6 April 2015

(wileyonlinelibrary.com) DOI: 10.1002/nbm.3290

Safety testing and operational procedures for self-developed radiofrequency coils

Jens Hoffmann[a]*†, Anke Henning[a,b†], Ioannis A. Giapitzakis[a], Klaus Scheffler[a,c], G. Shajan[a], Rolf Pohmann[a†] and Nikolai I. Avdievich[a†]

The development of novel radiofrequency (RF) coils for human ultrahigh-field (≥7 T), non-proton and body applications is an active field of research in many MR groups. Any RF coil must meet the strict requirements for safe application on humans with respect to mechanical and electrical safety, as well as the specific absorption rate (SAR) limits. For this purpose, regulations such as the International Electrotechnical Commission (IEC) standard for medical electrical equipment, vendor-suggested test specifications for third party coils and custom-developed test procedures exist. However, for higher frequencies and shorter wavelengths in ultrahigh-field MR, the RF fields may become extremely inhomogeneous in biological tissue and the risk of localized areas with elevated power deposition increases, which is usually not considered by existing safety testing and operational procedures. In addition, important aspects, such as risk analysis and comprehensive electrical performance and safety tests, are often neglected. In this article, we describe the guidelines used in our institution for electrical and mechanical safety tests, SAR simulation and verification, risk analysis and operational procedures, including coil documentation, user training and regular quality assurance testing, which help to recognize and eliminate safety issues during coil design and operation. Although the procedure is generally applicable to all field strengths, specific requirements with regard to SAR-related safety and electrical performance at ultrahigh-field are considered. The protocol describes an internal procedure and does not reflect consensus among a large number of research groups, but rather aims to stimulate further discussion related to minimum coil safety standards. Furthermore, it may help other research groups to establish their own procedures.
Copyright © 2015 John Wiley & Sons, Ltd.
Additional supporting information may be found in the online version of this article at the publisher's web site.

Keywords: Ultrahigh-field; RF Safety; SAR; Numerical Simulations; RF transmit coils; RF receive coils

MOTIVATION

The development of novel radiofrequency (RF) coils for human ultrahigh-field (UHF) (≥7 T), non-proton and body applications is an active field of research in many MR groups, as suitable coils are often not commercially available. Any RF coil must meet the strict requirements for safe application on humans (1–5) with respect to mechanical and electrical safety. In addition, RF transmission during the MR examination must comply with specific absorption rate (SAR) limits and must not raise the tissue temperature above critical levels. The latter is challenging at high RF frequencies because of the reduced wavelength and increased local power deposition, especially in the case of multichannel parallel transmission (pTx). Although limits for local energy deposition and temperature increase are clearly defined, e.g. by International Electrotechnical Commission (IEC) norms (3), a standardized method to test UHF RF coils for safe operation in compliance with these limits is lacking.

In this article, we present testing and operational procedures that must be conducted for any self-built RF coil at the Max Planck Institute for Biological Cybernetics before clearance for *in vivo* use is granted. These procedures were assembled to ensure the safety of human subjects against potential coil-related risks during MR examinations, to train the concerned staff regarding the appropriate use of the coils and to ensure their good condition and long-term functionality. Although the proposed procedures are not part of a document issued by a

* *Correspondence to: J. Hoffmann, High-Field Magnetic Resonance Center, Max Planck Institute for Biological Cybernetics, Spemannstr. 41, 72076 Tübingen, Germany.*
E-mail: jens.hoffmann@tuebingen.mpg.de

a *J. Hoffmann, A. Henning, I. A. Giapitzakis, K. Scheffler, G. Shajan, R. Pohmann, N. I. Avdievich*
High-Field Magnetic Resonance Center, Max Planck Institute for Biological Cybernetics, Tübingen, Germany

b *A. Henning*
Institute for Biomedical Engineering, University and ETH Zurich, Zurich, Switzerland

c *K. Scheffler*
Department for Biomedical Magnetic Resonance, University of Tübingen, Tübingen, Germany

† *These authors contributed equally to this work.*

Abbreviations used: *B_0, static magnetic field; B_1^+, clockwise circularly polarized component of the RF magnetic field; EM, electromagnetic; FDTD, Finite Difference Time Domain; FEM, Finite Element; FIT, Finite Integration Technique; IEC, International Electrotechnical Commission; IEEE, Institute of Electrical and Electronics Engineers; LNA, low-noise preamplifier; NEMA, National Electrical Manufacturers' Association; PRF, proton resonance frequency; pTx, parallel transmission; QA, quality assurance; RF, radiofrequency; RFPA, radiofrequency power amplifier; Rx, receive; S_{11}, power reflection coefficient; S_{12}, power transmission coefficient; SAR, specific absorption rate; SNR, signal-to-noise ratio; Tx, transmit; UHF, ultrahigh field; VOP, virtual observation point.*

Copyright © 2015 John Wiley & Sons, Ltd.

regulatory body, they follow the IEC standard for medical electrical equipment, European Union (EU) regulations (2–5), and Siemens and Philips test specifications for third party coils. However, they go beyond these documents to consider specific requirements for RF coils in general and for simulation and verification of SAR at UHF.

Our procedures comprise: (i) coil and system type specification; (ii) electrical and mechanical safety and performance tests; (iii) numerical SAR analysis; (iv) electrical failure mode and risk analysis; and (v) documentation, user training and quality assurance (QA). These procedures may serve as a template for other MR groups (a complete set of test sheets with more detailed descriptions is available on request). However, they do not reflect a consensus among a larger research community, nor do they represent a technical specification discussed by a regulatory body, and we raise no claim that these procedures are mandatory or complete, but rather wish to stimulate discussion related to minimum standards.

COIL AND SYSTEM TYPE SPECIFICATIONS

The number and type of required safety and performance tests depend on the coil design (see Tables S1 and S2). Therefore, any test protocol includes coil specifications that define the coil's name, the code with which it is recognized by the scanner, the operating frequency, the number of transmit (Tx) and receive (Rx) elements, its interface to the scanner and the coil type. The most commonly used coil types are transceiver (Tx/Rx) coils (which are used for transmission and reception), Tx-only and Rx-only coils, and combinations of Tx-only and Rx-only coils. Each of the four types can be further separated into single-tuned and dual-tuned coils, the latter of which are tuned to two resonance frequencies. For an array coil with independent Tx elements, it must be specified whether it is used together with a pTx system.

The coil specification also includes schematics and a description of all parts comprising the coil. Figure 1 shows an equivalent circuit of a single coil (array element) for illustration with all the typical components, including an RF power amplifier (RFPA), a low-noise preamplifier (LNA), a cable trap, a matching circuit, a detuning element and a decoupling element. The specific RF coil element can differ from the most common loop shape, i.e. stripline (6), dipole antenna (7) or travelling wave transmission (8) set-ups.

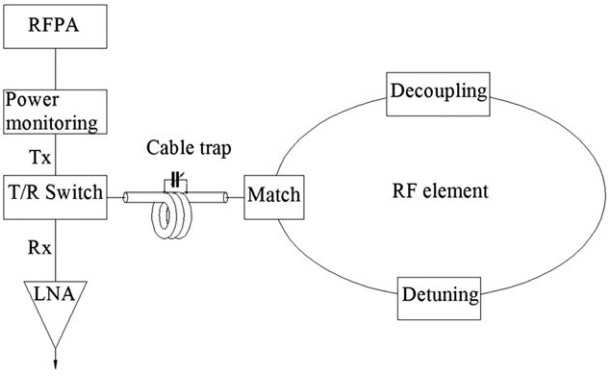

Figure 1. Schematic diagram showing the typical components of a radiofrequency (RF) transmit (Tx) and receive (Rx) chain together with the equivalent circuit of an RF coil (array element). LNA, low-noise preamplifier; RFPA, radiofrequency power amplifier.

ELECTRICAL AND MECHANICAL SAFETY AND PERFORMANCE TESTS

The tests are separated into two categories: safety and performance. Tests in the performance section are highly recommended for QA and are a prerequisite for optimal image quality and signal-to-noise ratio (SNR). Tests in the safety section are mandatory for safe operation of the coil.

All test measurements described below are performed using phantoms that load the coil in a comparable manner to the human body. Parameters of the phantoms are documented as a base for reproducible QA tests and electromagnetic (EM) modelling. In the case of unshielded coils, all measurements should be performed in the scanner bore or in an RF shield of identical dimensions. For comparison with standard or reference coils, we refer to suitable commercial coils or coils that have already passed the test procedure. Every specific test is documented in respective data sheets and the results are controlled by RF experts.

Safety tests

Prevention of superficial burns, electrical shock and injury

Potential hazards of RF coils during transmission include skin burn caused by heating of coil components or cables and electrical shock caused by poor electrical isolation. In addition, mechanical and material properties can be a source of potential injury.

Electrical and thermal isolation of the coil housing. All materials used for the housing must provide sufficient electrical and thermal isolation for protection against electrical shock and sparks [Sections 6.2 and 8.8.3 of ref. (2)]. The required electrical isolation of plastic materials is estimated on the basis of an analysis of the highest possible voltage generated across components such as capacitors (see section: Evaluation of maximum power/voltage across components). The dielectric strength (V/mm) of the corresponding material can be found in ref. (9). In line with industry standards on flammability rating, the deflection temperature should be at least 80 °C and the ignition temperature at least 350 °C (4) to prevent injury by melting plastic in the case of electrical sparks. If material properties are unknown, a high-voltage test and a flammability test of the material are performed.

Heating of the coil housing. To verify the absence of significant heating of the coil housing by component warming during normal operation [Section 11.1 of ref. (2)], continuous RF power that corresponds to the 6-min average SAR limit for Tx volume coils in the respective body part in normal mode operation (see Table 1) is delivered for 30 min. Temperature hotspots can be identified by an infrared camera. For quantitative assessment of the temperature rise, measurements with temperature probes placed in predetermined temperature hotspots are conducted (Fig. 2a). This test is meant to detect and prevent significant heating along the inner surface of the coil housing that might cause discomfort to the subject or deflection of the housing material.

Shield current trap (cable traps). During transmission, high currents can be induced in the shields of cables. The resulting

Copyright © 2015 John Wiley & Sons, Ltd.

Table 1. Specific absorption rate (SAR) limits according to International Electrotechnical Commission (IEC) standard 60601-2-33, 201.12.4.103. SAR averaged over any 10-s period may exceed the 6-min limits by a factor of two

Averaging time	6 min					
Transmit (Tx) coil type	Volume Tx coils (global SAR)			Local Tx coils (local SAR)		
SAR type	Whole body SAR (W/kg)	Head SAR (W/kg)	Partial body SAR (W/kg)	Local head SAR (W/kg)	Local trunk SAR (W/kg)	Local extremity SAR (W/kg)
Normal mode	2	3.2	2–10	10	10	20
First controlled mode	4	3.2	4–10	20	20	40

Global SAR, absorbed radiofrequency (RF) power in a specific body part divided by the mass of the respective body part. Local SAR, SAR averaged over 10 g of tissue.

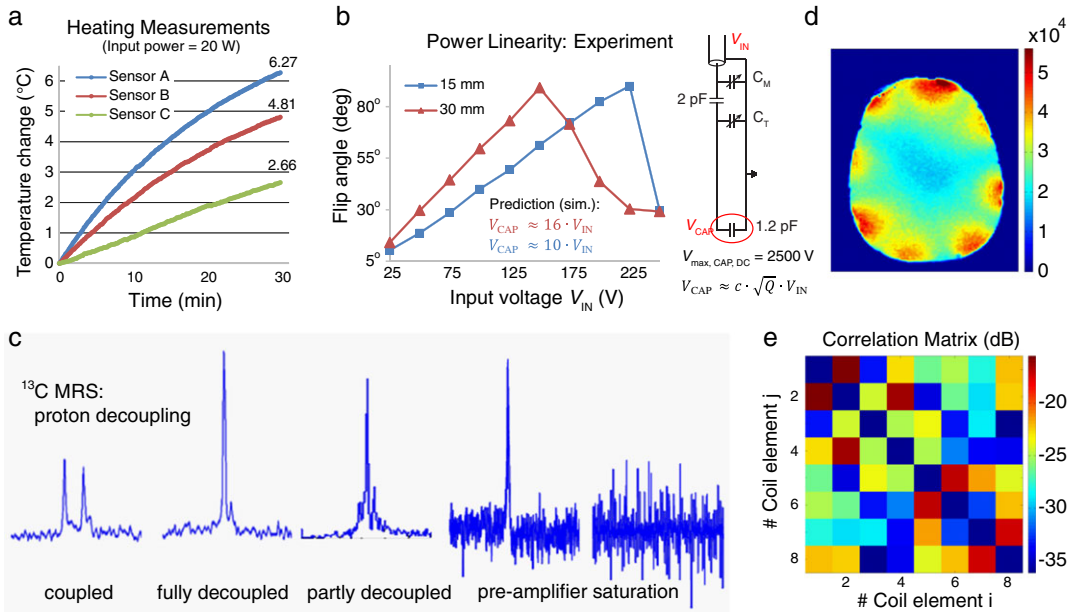

Figure 2. Examples of performance and safety tests. (a) Temperature increase during the radiofrequency (RF) heating test as measured by three fiber-optic temperature sensors on the housing of a four-channel surface coil (10). (b) Measurement of the linear relationship between flip angle and input voltage for a microstrip element at two distances to a phantom. As predicted by simulations, the voltage at the terminating capacitor (red circle, ATC 100C) exceeds its maximum working voltage and starts to fail (sparking). The allowed V_{IN} depends on the *Q*-factor and coil design (factor C). (c) Proton decoupling test in the case of a nested ^{1}H and ^{13}C dual-tuned birdcage coil arrangement. The desired decoupling behavior is illustrated by the two figures on the left. Characteristic spectral pattern in the case of insufficient proton power, resulting in incomplete decoupling (middle right), and noise enhancement and spikes caused by pre-amplifier saturation (right) caused by insufficient isolation of the ^{1}H and ^{13}C coils. (d) Signal-to-noise ratio (SNR) map in a phantom. (e) Noise correlation matrix (dB) for an eight-channel transmit/receive (Tx/Rx) array.

heat can cause skin burns if cables are placed too close to a patient's skin. Cable traps reduce these currents (11,12) and thus represent a safety measure [Section 4.6 of ref. (2)]. In addition, cable traps can substantially reduce parasitic coupling between array elements and improve Scattering Parameter (*S*-parameter) stability, and thus ensure consistency with regard to *S*-parameter measurements and simulations. Placement of the cable traps in both Tx and Rx coils is documented, including a short description of trap designs, total number of traps and their locations. Changes in *S*-parameters during tuning/matching and decoupling on touching the coil cables or moving their relative positions should be minimized.

Coil cables. The coil cables must provide sufficient electrical and thermal isolation and need to be positioned with sufficient distance to the patient's skin to prevent skin burn in the case of the malfunction of shield traps [Section 4.6 of ref. (2)]. This might require additional padding, especially in the case of coil cables running across the patient's body.

Biocompatibility, toxicity and allergic potential. Coil housing and cable insulation materials must be non-toxic and must not cause potential allergic reactions if in contact with the skin (i.e. latex) [Section 11.7 of ref. (2)].

Mechanical properties and stability of the coil housing and mounting. To prevent injury as a result of the mechanical properties or instable positioning of the coil, to ensure the integrity of the RF coil during continued usage and to prevent a number of electrical failure modes, the mechanical stability and quality of

Copyright © 2015 John Wiley & Sons, Ltd.

the housing and mounting must be in accordance with Sections 8.10, 9.3, 9.4, 11.6 and 15.3 of ref. (2). More specifically, the coil housing should not contain sharp edges or a rough housing surface that can cause skin injury [Section 9.3 of ref. (2)], nor should it easily tip over in operation or in its storage position [Section 9.4 of ref. (2)]. In addition, the coil should be mechanically stable [Sections 8.10 and 15.3 of ref. (2)] to ensure its integrity during continued usage and to prevent failure modes, such as poor electrical isolation caused by broken housing or failure of electrical components as a result of mechanical shock. Finally, the coil housing should be ideally splash proof to prevent water damage of electrical circuits during cleaning of the coil or in the case of spillage of body fluids [Section 11.6 of ref. (2)].

Electrical properties related to SAR safety, Tx efficiency and avoidance of component failure

Changes in the electrical properties of Tx coils as a result of aging or malfunction of coil components can alter the RF current distribution and thus the resulting RF field, Tx performance and local SAR distribution.

Tuning and matching of Tx coils. This is verified by measuring the power reflection coefficient (S_{11}) using a network analyzer and a tissue-mimicking phantom. The measured S_{11} values are documented for the QA test and for comparison with the EM model. The loading characteristics of single-input RF coils or individual array elements, determined as the linewidth of the *S*-parameter frequency dependence (i.e. relative *Q* factors), are measured (13) to ensure compliance with numerical models and as an input for regular QA tests. For arrays, the relative phase shift between the RF signal at the coil plug [which is often the reference plane for the MR system's RF phase measurements (14)] and the phase of the current in the coil element is measured [e.g. using a pickup probe (15)], so that the identical phase shift can be applied in SAR simulations.

Decoupling of Tx arrays and dual-tuned coils. Decoupling of all elements within a Tx array is verified by measuring the power transmission coefficient (S_{12}) using a network analyzer. Acceptable decoupling values depend on the specific coil design and application requirements. For example, for eight-channel Tx head arrays for pTx, we aim for decoupling values better than at least −15 dB (16). For dual-tuned coils and arrays, we aim for decoupling values better than −25 dB for ^{1}H and X-nuclei elements, which is usually sufficient not to compromise the Tx performance (16). The *S*-parameter matrix must be investigated for a realistic load range to ensure compliance with SAR models and as input for regular QA tests.

T/R switch performance. The T/R switch connects each element of the transceiver array either to an RFPA during transmission or to an LNA during reception (Fig. 1). Failure of the T/R switch may cause SNR degradation during reception and SAR increase during transmission. The T/R switch performance is checked by measuring S_{12} between all three ports for both the Tx and Rx state (T/R switch is ON or OFF). The necessary protection for the LNA is derived by its power handling capacity and the maximum Tx power. The switching speed is also documented.

Rx coil detuning during transmission (protective circuitry). Detuning minimizes the interaction between combined Rx and Tx coils (17,18). Safe operation of any Tx-only/Rx-only coil combination requires at least two levels of protection to ensure safety in the case of malfunction. Commonly, an active, i.e. electronically controlled, detuning circuit provides a primary level, whereas the secondary level is provided, for example, by using fuses or passive detuning circuits (cross-diodes, etc.). Alternatively, the secondary level can also be provided by an active electronic circuitry, which verifies the correct functionality of PIN diodes in the detuning.

Primary protection level (active detuning). Commonly, the test is performed using a decoupled double pickup probe (18). Acceptable decoupling, measured as a difference in S_{12} when detune circuits are ON (activated) and OFF (not active), depends on the specific coil and interface design; however, from our experience, −25 dB is usually sufficient not to spoil Tx coil performance. The test should be performed for the entire Tx/Rx coil combination for both Tx and Rx modes. The switching speed of the circuits should also be documented.

Secondary protection level (fuses, passive detuning, etc.). It is difficult to experimentally evaluate the functionality of passive protective circuitry, such as fuses or cross-diodes. However, related component specifications, such as speed and current ratings, are evaluated and the number of incorporated fuses and current ratings are reported.

Tx performance in the presence of an Rx coil. The goal of this test is to verify that the presence of an Rx-only coil does not strongly alter the Tx performance and B_1^+ field distribution of a Tx coil. This is tested by RF field probes on the bench or by the acquisition of B_1^+ maps in the presence and absence of the Rx coil. This test is necessary as simulation models for SAR evaluation often do not include Rx coils.

Evaluation of maximum power/voltage across components. The purpose of this procedure is to ensure that all elements of Tx coils are capable of withholding high power (voltage) generated during the Tx phase [Section 4.8 of ref. (2)]. The evaluation of the voltage values across components as a function of power or voltage applied to the coil can be performed by analytical calculations or numerical simulations (see Fig. 2b for an example). From these data, a maximum allowed power delivered to the coil at the level of the coil plug is defined.

Power linearity of the Tx coil. The power linearity test verifies that all non-linear devices (e.g. PIN diodes in the detune circuits) do not compromise the linearity (linear relationship between Tx voltage and B_1^+ field) of the Tx coils. In addition, it ensures that all components operate correctly at high Tx voltages. The test is performed at the scanner by increasing the RF input power up to the highest allowed power with simultaneous measurements of B_1^+ generated in a phantom (Fig. 2b).

Installation of the coil at the scanner

Safe operation builds up on correct installation of the coil, including the recognition of the specific coil by the scanner and correct specifications within the related coil file, such as switching logic, RF power limits and SAR limits.

Copyright © 2015 John Wiley & Sons, Ltd.

System plug connection test (bench and scanner). All vendors take measures to identify the connected RF coil and to link it to coil-specific settings in the scanner software (coil file), e.g. to define control voltage and current settings. The coil recognition is usually performed by implementing resistors into the coil plug that define a coil-specific code. Related bench tests include: (i) coil code ground isolation (>2 MΩ); (ii) coil code resistance verification; (iii) preamplifier current consumption and bias voltage verification; and (iv) PIN diode current source verification and voltage drop measurements [Sections 8.5 and 13 of ref. (2)]. Scanner tests include: (i) coil plug layout test, i.e. compatibility of the plugs and the pin layouts on the coil and the system connectors; (ii) coil plug exclusion test, i.e. compatibility of mechanical codes to exclude connection of coils not suited for the system; and (iii) coil code verification, i.e. the coil is properly recognized by the system [Sections 8.5 and 13 of ref. (2)].

Correctness of the coil file and coil functionality verification. The coil file, among other things, comprises safety limits and the control logic, and must be verified to ensure correct implementation of SAR and power limits, as well as Tx/Rx switching and active detuning [Sections 12.4, 13 and 14 of ref (2)]. In addition, poor contacts at the coil plug must be excluded. The functionality of all Tx and Rx channels of the coil is verified by the acquisition of channel-wise and combined-mode B_1^+ maps and gradient echo images.

Performance tests

SNR and parallel imaging performance

Important performance parameters of an RF coil include Tx and Rx efficiency, as well as the *g*-factor of Tx and Rx coils, which depend on the degree of coupling between coil elements. As related parameters for Tx coils have been discussed in the 'Safety tests' section above, the focus here is on Rx coils and specific requirements for dual-tuned coils.

Tuning and matching (Rx-only coils). Tuning and matching of individual coils is checked by measuring S_{11} using a network analyzer. We usually consider S_{11} values of better than –10 dB as acceptable, which corresponds to an SNR drop of 5% for an individual Rx coil.

Decoupling of Rx-only arrays. In most cases, passive decoupling of Rx-only arrays is limited to the decoupling of adjacent elements (18,19), which is checked by measuring S_{12} using a network analyzer and a decoupled double pickup probe (18). Decoupling values of –10 dB or better are usually acceptable. In general, the effects of coupling on Rx coil performance (i.e. SNR, parallel imaging, etc.) (20–22) may differ for specific coil geometries. Preamplifier decoupling of array elements further improves this by an additional –15 to –20 dB (18,19). Measurements are carried out for every element of the array. Specifications of the preamplifier should also be attached.

Tx coil detuning during reception. A single detuning level is sufficient for Tx coils, as their malfunction during the Rx phase can only cause SNR degradation. Decoupling is measured as the difference in S_{12} when detuning circuits are ON and OFF. Based on our experience, a value of –25 dB is usually sufficient not to compromise Rx coil performance.

Rx SNR and noise covariance. As a base for regular QA testing, Rx SNR maps and a noise covariance matrix using a standard phantom are calculated (Fig. 2d, e). In the case of the Rx array being compatible with different Tx coils, a change in the SNR map and noise covariance between a standard Tx coil and a local Tx coil should not occur, which is tested by comparative measurements (20,23).

Proton decoupling performance of ^{1}H/X-nuclei coils. This test is to verify that decoupling of proton and X-nucleus spins is possible with dual-tuned and, more specifically, ^{1}H/^{31}P and ^{1}H/^{13}C coils. Decoupling requires high power transmission on the proton channel during reception with the X-nucleus channel. The proton power level must be sufficient to ensure complete reunification of split lines in X-nuclei spectra without side bands or major line broadening. In addition, the proton and X-nucleus coils must be sufficiently decoupled to avoid preamplifier-saturation indicated by additional spikes or noise enhancement (Fig. 2c).

Image quality and artefacts

Another important performance aspect is the lack of artifacts induced by the RF coil.

Eddy currents. Eddy currents produced on the RF coil or on its shield can lead to artifacts in imaging and spectroscopy (24). Single-voxel water spectra are acquired at different positions in a water-rich phantom that is easy to B_0 shim. Line shape distortions are compared with results obtained with a reference coil.

B_0 field distortions. Materials used in RF coils can cause significant inhomogeneity of the static magnetic field (B_0) with potential negative impact on image quality. B_0 maps of a phantom are acquired with the new coil set-up *versus* a standard set-up, and the absence of local B_0 artifacts is verified.

Parasitic coupling and RF noise. To exclude parasitic coupling to other RF sources inside and outside the scanner room, which leads to image artifacts and quantification errors not present in the presence of standard coils, gradient echo images are acquired to verify the lack of additional image artifacts.

MR signal from housing. Material used for housing of the coil (e.g. glue or cables) can produce an MR signal. Therefore, a gradient echo image at short TE (<1 ms) is acquired from a large field of view, encompassing all coil housing and cables, to verify that the signal level and location do not potentially impair *in vivo* imaging.

NUMERICAL SAR ANALYSIS

Purpose

This section guides the implementation and verification of numerical simulations for the assessment of the SAR generated by the RF coil in the subject's body. The SAR at location r is determined by the local electric field $\vec{E}\left(\vec{r}\right)$ as well as the local conductivity $\sigma\left(\vec{r}\right)$ and mass density $\rho\left(\vec{r}\right)$ of tissue:

$$\mathrm{SAR}\left(\vec{r}\right) = \frac{\sigma\left(\vec{r}\right)\cdot\left|\vec{E}\left(\vec{r}\right)\right|^2}{2\rho\left(\vec{r}\right)}$$

Copyright © 2015 John Wiley & Sons, Ltd.

This describes the absorbed RF power per tissue mass and can be directly related to tissue heating. As defined in ref. (3), SAR is averaged across entire body parts (whole body, partial body and head SAR), which we herein summarize as global SAR, or over volumes containing 10 g of tissue (local SAR). Currently, a new standard [Institute of Electrical and Electronics Engineers (IEEE)/IEC 62704-1] is in preparation which defines procedures to determine the peak spatial average SAR in the range of 30 MHz to 6 GHz (25).

The relationship between the applied RF power and expected energy deposition can be easily calculated and measured for low RF frequencies, assuming a homogeneous RF field distribution across the sample. For higher frequencies and shorter wavelengths, the RF fields may become extremely inhomogeneous in biological tissue, and the risk of localized areas with elevated power deposition increases. In addition, the RF field distribution at high fields becomes more susceptible to variations in load, coil geometry, tuning conditions and scanner environment. For arrays, SAR depends on the coupling characteristics and is a function of the excitation mode, i.e. the relationship between the complex voltages at the single array elements. Therefore, a realistic numerical SAR assessment must take these issues into account and simulated results must be carefully verified.

Once a reliable simulation set-up is established, its task is to relate the RF power sent towards the coil to the SAR produced in the subject. This information is passed to the MR system and is used to restrict the RF power so that the MR scan complies with SAR and temperature limits defined by corresponding regulations (1,3,26).

SAR and temperature limits

We comply with limits recommended by the IEC (3) to protect the subject from excessive heating and local tissue damage. Temperature is the primary safety criterion: the body core temperature may not be raised by more than 0.5 °C and not above 39 °C in 'normal mode', and not by more than 1 °C and not above 40 °C in 'first controlled mode'. The latter operating condition poses more physiological stress to the subject, but is still considered as safe. To comply with temperature limits, the IEC specifies limits on whole body, partial body and head SAR (herein referred to as global SAR limits), as well as on local SAR for different body parts, all averaged over time intervals of 6 min and 10 s (3). Table 1 provides a summary of these limits.

High-field RF coils, especially arrays, often display features of volume coils and local coils at the same time; therefore, they must satisfy all local and global SAR limits. For many coils, however, the most critical body part can be defined as the part of the body in which SAR limits are exceeded first, independent of the excitation mode.

EM modelling

A realistic numerical model of the RF coil within the scanner environment must be constructed. To this end, simulation packages are available that solve the full Maxwell equations in a three-dimensional numerical domain. Examples of commonly used software include Finite Difference Time Domain (FDTD), Finite Integration Technique (FIT) or Finite Element (FEM) solvers, such as CST Studio Suite (CST, Darmstadt, Germany), XFDTD (Remcom, State College, PA, USA), SEMCAD (SPEAG, Zurich, Switzerland) and HFSS (ANSYS, Canonsburg, PA, USA).

The model should comprise all details relevant for the strength and distribution of the EM field (27,28). This includes an exact replication of the coil geometry, its material properties, relevant capacitors and inductors, input and decoupling circuits, as well as interaction with the load and all parts of the scanner environment that have a significant influence on the RF field propagation, e.g. the gradient's RF screen (Fig. 3). Sources of power and efficiency loss, such as cable attenuation or resistive loss in capacitors, should be incorporated into the simulations. Numerical accuracy is ensured by an appropriate choice of simulation parameters, including mesh density, convergence criteria and boundary conditions. The power budget, i.e. the sum of the dissipated and radiated power, is compared with the total power entering the computational domain (28).

For experimental verification and safety assessment, simulations should be able to predict the following: (i) the component values (e.g. capacitances) necessary to adjust the loaded coil to the frequency of operation; (ii) the *S*-parameter response; (iii) the EM field distribution and strength for any relevant excitation mode; (iv) the expected voltages across the coil components; and (v) the local and global SAR per input power for any relevant excitation mode.

Validation of the numerical EM model

Validation of the SAR prediction method by comparison with experimentally accessible data is required according to IEC guidelines [Section 201.12.4.105.3 of ref. (3)]. However, recommended procedures, such as the National Electrical Manufacturers' Association (NEMA) MS 8 Standard (29), are only valid for homogeneous volume coils at low field strength and are not applicable for high RF frequencies.

Instead, we compare performance measures in a well-defined experimental set-up with results obtained from a numerical representation of precisely the same set-up. As the primary test set-up, the RF coil is positioned inside the MR scanner and is adjusted to a phantom that is similar in size and dielectric properties to the concerned body part. The numerical coil model is loaded with a precise replication of this phantom at exactly the same position (Fig. 3) and is adjusted to the Larmor frequency using the same procedure as for the actual coil.

The first two comparisons are consistency checks to rule out fundamental errors in the simulations and to ensure similar loading and tuning conditions compared with experiment, as different tuning conditions can considerably affect SAR (30). These checks are independent of the excitation mode.

(1) A comparison between simulated and measured coil components is performed. Simulated capacitances and inductances should not deviate considerably from the components actually used as this may indicate a different current distribution on the real and simulated coil. An agreement on the order of 15% has been reported previously for a 400-MHz Tx array (27), but the achievable precision depends on the coil's complexity and the level of detail used in the simulations. From our experience with EM modeling of UHF RF coils, in the case of large systematic deviations, e.g. more than 50% in capacitances, the simulation model should be checked in order to detect the causes of the divergence.
(2) Simulated and measured *S*-parameters are compared (Fig. 4a). For a realistic description of loading characteristics, the relative *Q* factors, determined as the linewidth of the

Copyright © 2015 John Wiley & Sons, Ltd.

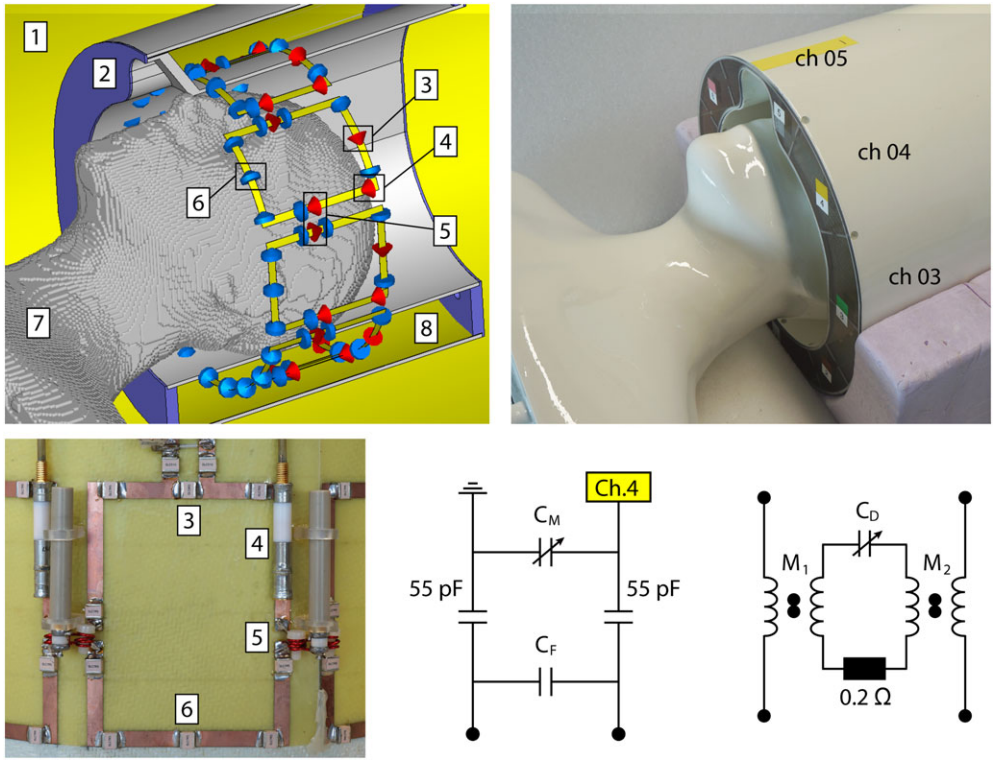

Figure 3. Specific absorption rate (SAR) simulation set-up of a 400-MHz eight-channel array. Screenshot of the simulation set-up constructed in CST Studio Suite (top left) including the gradient's radiofrequency (RF) screen (1), coil housing (2), input network (3), tuning capacitor (4), decoupling network (5), fixed capacitors (6), a tissue-equivalent phantom (7) and the coil's local RF shield (8). Photographs of the experimental set-up (top right) and a single coil element (bottom left) are shown for comparison. Input and decoupling networks as realized in circuit co-simulation are shown at the bottom center and bottom right, respectively.

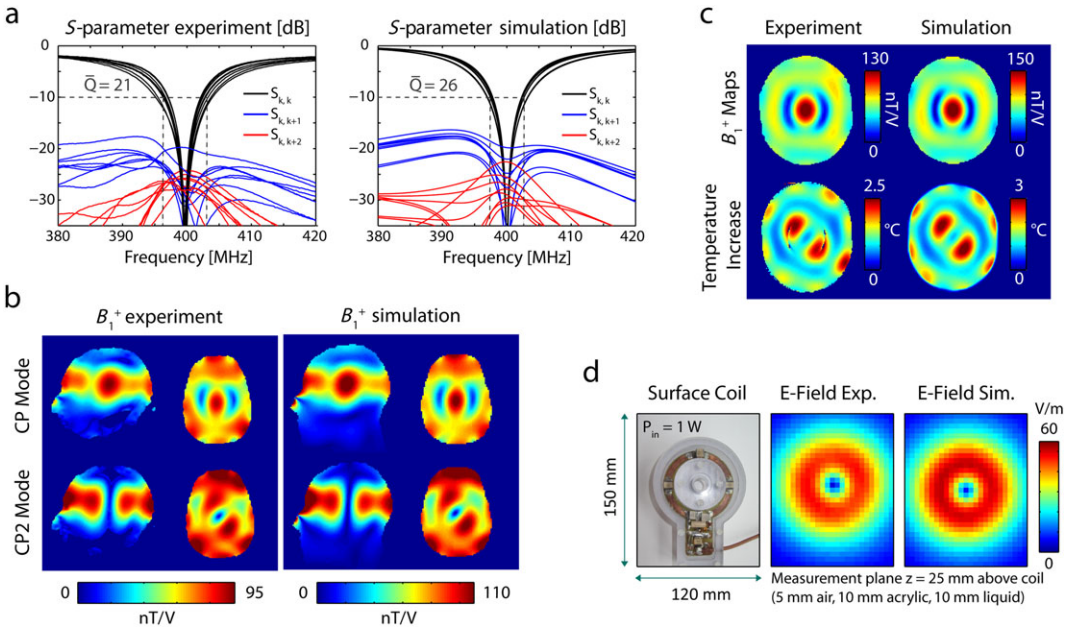

Figure 4. Validation of the simulations. A comparison of the measured and simulated *S*-parameters (a) and B_1^+ fields in two excitation modes (b) in a head phantom using the 400-MHz eight-channel array (set-up according to Fig. 3) shows reasonable agreement in B_1^+ distribution and strength, decoupling levels and *Q*-factors. (c) RF heating experiment using the eight-channel array in CP mode and an elliptical gel phantom [ε_r = 78; σ = 0.59 S/m; proton resonance frequency (PRF) coefficient, 0.01 ppm/°C; C_ρ = 3994 J/(K kg)]. Transverse B_1^+ maps (top) are shown together with the temperature increase (bottom) after 138 s of RF transmission with an average power of 162 W using the sequence described in ref. (33). (d) Electric field probe measurement (EASY4MRI, Speag, Zurich, Switzerland) and simulation inside a rectangular phantom 25 mm above a 400-MHz loop surface coil.

Copyright © 2015 John Wiley & Sons, Ltd.

resonance curve in simulations, should be consistent with experiment. For example, deviations of less than 30% could be achieved for the eight-channel array shown in Fig. 4a. The decoupling between a pair of array channels (in dB) is converted to a power crosstalk in per cent. The requirements on an acceptable deviation between simulated and measured crosstalk depend on the coil design. For example, at a given average level of decoupling, the total percentage of input power that couples to other elements increases with the channel count. Based on our practical experience, for eight-channel arrays for pTx operation, we consider a difference in crosstalk below 4% as acceptable to realistically capture the effects of coupling on reflected power and on the RF field distribution in different excitation modes. For other designs or arrays with fewer channels, the requirements may be relaxed.

The following tests confirm the RF field distribution and depend on the excitation mode. For pTx operation, we recommend that the tests are performed for at least two different modes to ensure a robust validation.

(3) For each excitation mode, simulated B_1^+ distributions and measured B_1^+ maps, normalized (e.g. $B_1^+/\sqrt{power}$) and referring to the same position in the RF Tx chain, are compared (Fig. 4b). There must be qualitative agreement of the $|B_1^+|$ distributions, which is confirmed by at least two RF experts. The quantitative agreement is checked by comparing the average B_1^+ strength. For the array shown in Fig. 4b, for example, the simulated B_1^+ efficiency exceeds the experimental efficiency by about 15%, which suggests a SAR overestimation by about 30%. Large quantitative and qualitative deviations imply that simulations cannot predict the actual RF field and SAR with sufficient accuracy.

(4) Similarity of the simulated and measured B_1^+ fields does not necessarily imply a similar agreement of the electric fields in any location; therefore, a calorimetric method is performed to assess SAR. The RF-induced temperature increase in a suitable temperature phantom is measured using the proton resonance frequency (PRF) shift method (31–33). Desired phantom characteristics include: MR visibility, dielectric properties similar to human tissue, known thermal properties, low heat conductivity and diffusivity (e.g. gel-based phantoms), reasonable T_1 and T_2* decay times and a linear relationship between the signal phase and temperature change (34). The temperature sensitivity of the chemical shift can be increased, e.g. by adding paramagnetic lanthanide complexes (35). Following a short excessive RF heating period τ, the temperature increase ΔT is virtually linear and can be converted to SAR (36), and vice versa, via the specific heat C_ρ:

$$\Delta T \approx \tau \cdot \frac{\mathrm{SAR}}{C_\rho}$$

The temperature maps are compared with corresponding simulated data in equal measure as performed for the B_1^+ fields. Figure 4c demonstrates the results of a thermometry experiment. According to $\mathrm{SAR} \propto |E|^2$, deviations in efficiency between simulated and measured RF fields must consistently manifest in the RF heating experiment.

(5) As an alternative to tests (3) and (4), the EM field, SAR and temperature distributions can be obtained by field probe measurements in a phantom during continuous-wave RF exposure (37) (Fig. 4d). This method is suited to the accurate validation of numerical simulations in well-defined test scenarios (37), as it includes direct access to the electric field, in contrast with MR-based validation techniques. However, it requires a special test arrangement that precisely moves the probes through the phantom liquid, a task that is difficult to perform with realistically shaped phantoms and with the RF coil positioned inside the scanner. Therefore, this method is not a regular part of our current procedure.

Only if phantom tests (1)–(4) have been successfully performed can the actual coil be used for volunteer scanning after SAR analysis, as described in the next section. In the case of large deviations, especially if the experimental RF field is stronger than the simulated field, the EM model or the actual coil needs to be adapted to improve agreement, or safety margins (see below) must be increased considerably.

Calculation of SAR and power limits for *in vivo* application

After validation, the simulation set-up is used to predict SAR in the human body. In our present procedure, we use a time-domain solver (CST Studio Suite) and two human voxel models with 2-mm^3 resolution (Duke and Ella from the virtual family) with dielectric tissue properties valid at the Larmor frequency (38,39). Alternatively, frequency domain solvers and surface-based models can be used (30). If possible, the performance of SAR calculations with additional models or even patient-specific models is preferable, whereas the models may be truncated to reduce the computational cost as long as it does not compromise the RF field in the body part under evaluation. The distribution of SAR across the models is calculated as a function of input power and excitation mode (Fig. 5). Local SAR averaging is performed using standard IEEE/IEC 62704-1. If several positions of the body relative to the coil are possible, multiple simulations are performed to obtain SAR data as a function of position.

The conversion from input power to SAR must be transferred to the scanner, which supervises and restricts the RF power in order to comply with IEC limits (14). In the following, we distinguish between single-channel operation, i.e. transmission with a fixed excitation mode, and pTx operation. The supervision concept refers to Siemens Magnetom scanners and a Tx Array Step 2 pTx system, respectively.

Single-channel operation

For a fixed excitation mode and subject position, SAR is proportional to the total power accepted by the coil (forward minus reflected power). Therefore, two factors are calculated that relate the accepted power at the coil plug to the maximum local SAR and to the global SAR in the most critical body part, respectively. The more conservative of the two factors is loaded to the scanner to restrict RF power for compliance with 6-min and 10-s SAR limits. If a single factor is used to cover different subjects and positions, the most conservative factor across all corresponding simulations is used.

Copyright © 2015 John Wiley & Sons, Ltd.

NMR IN BIOMEDICINE

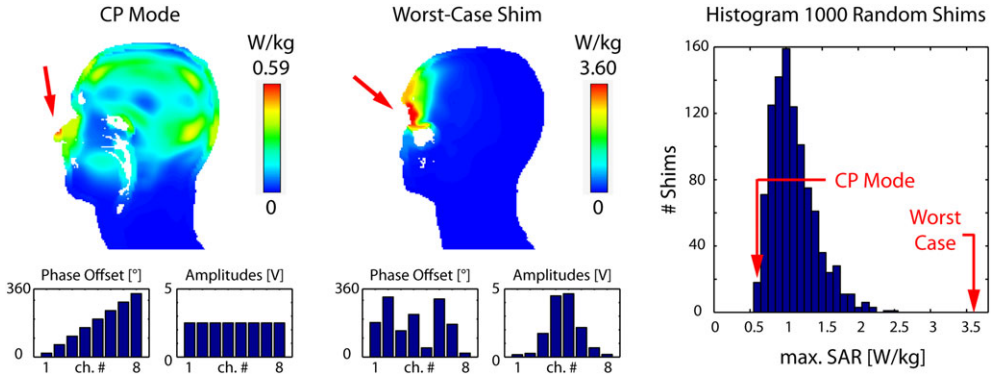

Figure 5. Specific absorption rate (SAR) caused by an eight-channel array (cf. Fig. 3) in the Duke model for an input power of 1 W. In CP mode (left), maximum local SAR appears in the nose because of its proximity to the coil conductors. The worst-case shim (center) focuses the *E*-field on the left eye, causing a sixfold increase in the maximum SAR compared with the CP mode. A histogram of maximum local SAR for 1000 random radiofrequency (RF) shims is displayed on the right.

pTx operation

For pTx, SAR is a function of the complex RF voltages (amplitude and phase) applied to individual array channels. For each voxel model and position, the electric fields resulting from separate transmission through the single coil elements (considering coil coupling) are determined and normalized to a predefined input power level at the coil plug. Together with local tissue properties, a 10-g averaged *Q*-matrix (40,41) is calculated for every voxel in the human model. This approach separates spatial and temporal dependences, and local SAR in every voxel in the model can be derived for an arbitrary excitation mode by multiplication of the *Q*-matrix with the vector of complex voltages.

For online local SAR supervision, the number of *Q*-matrices is compressed to a few hundred 'virtual observation points' (VOPs) (41) and the results are loaded to the scanner software. During scanning, the amplitudes and phases of the RF signal at the Tx channels are monitored and used to perform a real-time local SAR calculation. Correct calculation and implementation of local SAR data is confirmed by comparison between SAR displayed at the scanner and SAR calculated by *Q*-matrices, VOPs and the EM simulation software.

Alternatively, a conservative worst-case power limit that complies with the local SAR limit, independent of the current excitation mode, can be derived by calculating the maximum eigenvalue across all *Q*-matrices. This number gives the highest possible local SAR if the RF power can be freely distributed among the coil channels (Fig. 5); the corresponding eigenvector describes the worst-case excitation mode (40).

For additional global SAR supervision, simulations provide the limit on the accepted power that complies with the global SAR limits of the most critical body part. These numbers are derived to be valid for any excitation mode.

Safety margins

Uncertainties (42–45) in the conversion from the measured RF signal in the Tx chain to the real SAR in the subject are estimated and converted into a safety margin for the allowed Tx RF power.

Assuming the correct implementation of the EM simulation code, we consider several uncertainties (42–45). First, inaccuracies in RF power and voltage measurement are derived from the vendor's specifications for the respective hardware (14). Second, numerical inaccuracies (e.g. arising from meshing, boundary conditions, power budget, SAR averaging method, etc.) and uncertainties in the numerical representation of the coil are assessed via multiple simulations with varying parameters and with the verification procedure as described above. Third, the difference between voxel or surface models and the actual human subject (e.g. in shape, position, dielectric properties) can be estimated by simulating multiple different models (46) at slightly varying positions.

The final safety margin reflects the combined uncertainty in SAR, considering that many errors may be treated as

Table 2. Risk values: for each probability and each severity of occurrence a value has been assigned.

Value	Likelihood	Severity	Description of severity
1	Very low	Negligible	No effect
2	Low	Minor	Degradation in image quality or SNR Cessation of scanning procedure Potential sensations experienced by subject
3	Medium	Moderate	Potential minor injury of the subject (local skin burn)
4	High	Critical	Potential severe injury of the subject (extended skin burn, electrical shock, burns in tissue other than skin)
5	Very high	Catastrophic	Disability or death of the subject

SNR, signal-to-noise ratio.

 Copyright © 2015 John Wiley & Sons, Ltd.

normally distributed and statistically independent. A more precise discussion of SAR simulation procedures is the subject of upcoming IEEE/IEC standards, in particular IEEE/IEC 62704-1 (25).

Future developments may include more efficient simulations (47), patient-specific voxel or surface models (48), an improved understanding of SAR variations caused by subject position and shape (46), tuning and loading conditions (30) or uncertainties in dielectric properties (49), as well as improved pTx hardware that is able to monitor changes in B_1^+ levels, loading and coupling (e.g. using pickup probes) in order to instantaneously detect malfunctions or patient movement (50,51). Future RF supervision concepts may strive towards temperature rather than SAR monitoring.

Table 3. Risk profile matrix: incidents corresponding to the risk situations indicated in white are considered to be acceptable, whereas those indicated in black are not acceptable and will be avoided by the risk management measures taken during the design and operation of the radiofrequency (RF) coils

Likelihood					
Very high	5	10	15	20	25
High	4	8	12	16	20
Moderate	3	6	9	12	15
Low	2	4	6	8	10
Very low	1	2	3	4	5
Severity	Negligible	Minor	Moderate	Critical	Catastrophic

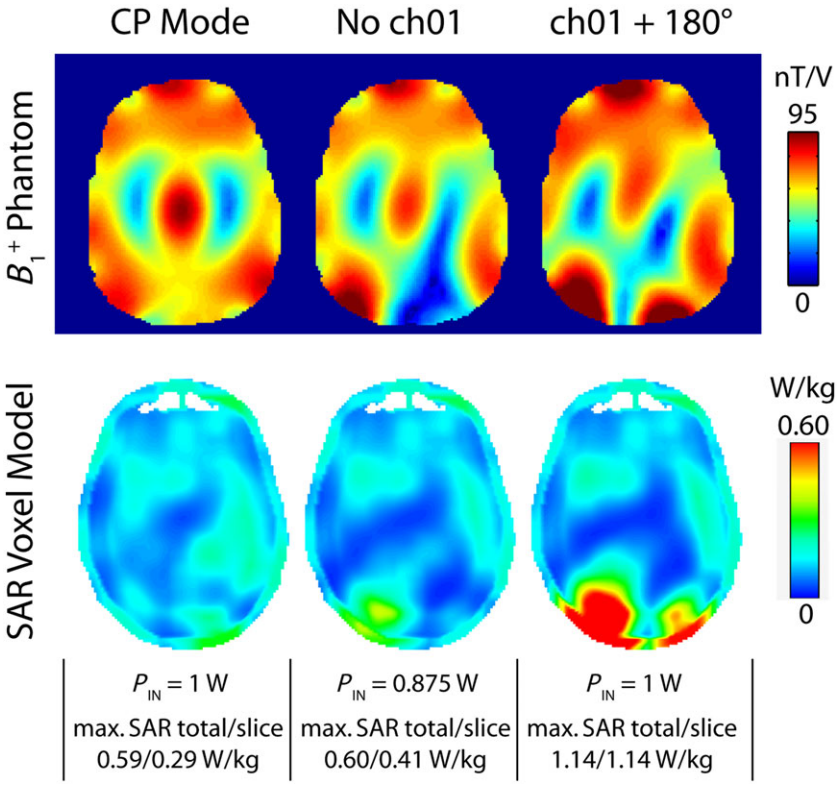

Figure 6. Impact of element failure in an eight-channel array (cf. Fig. 3) on B_1^+ in a phantom (top row) and specific absorption rate (SAR) in the Duke model (bottom row). As *E*-fields in the CP mode (left column) tend to interfere destructively between neighboring elements, the absence of the posterior transmit (Tx) element locally increases SAR (middle column). A phase shift of 180° causes twice the maximum local SAR across the model (right column). In the absence of hardware supervision, such malfunctions can be detected via rapid B_1^+ mapping prior to *in vivo* scanning (top row).

Copyright © 2015 John Wiley & Sons, Ltd.

ELECTRICAL FAILURE MODE AND RISK ANALYSIS

Purpose

The purpose of this procedure is to analyze the possible failure modes of the electrical components in the coil during operation and the potential hazard for the subject. This represents the basis for a succeeding risk analysis [Sections 4.2 and 12.4 of ref. (2), and Section 201.13 of ref. (3)].

Risk analysis

Each hazard risk is characterized by two quantities: (i) the severity (S) of the possible adverse consequence; and (ii) the likelihood (L) of occurrence of each consequence (Table 2). The rating (R) of each risk factor is calculated using the product of the severity multiplied by the likelihood ($R = L \times S$).

Finally, each hazard risk is placed in a risk profile matrix in which the columns and rows indicate the severity and likelihood, respectively (Table 3). For our RF coils, we defined acceptable risks to be those up to a risk value of '8' for negligible to moderate severity and up to a risk value of '4' for critical and catastrophic severity (Table 3), in order to rule out incidents with severe negative impact on the volunteers.

Electrical failure mode analysis with risk assessment

Severe injuries during the operation of RF coils, such as an electrical shock or skin burn, can be practically excluded by the safety test procedures and the regular QA.

Therefore, the major potential risk is an unexpected increase in SAR as a result of failure of one or multiple RF coil components during transmission. These failures can, in principle, be identified by the quality control of previously acquired images or the result of pre-scan adjustments performed before each scan (Fig. 6). Substantial heating is only expected if elevated power absorption occurs over a prolonged time, whereas most scan protocols take only a few minutes. However, SAR-enhancing failures occurring during a prolonged single scan protocol or multiple scan protocols performed without QA are still problematic and must be prevented by additional safety measures during coil design (Table 4) and, in the best case, by monitoring system parameters, such as the forward and reflected power, Tx phase

Table 4. A radiofrequency (RF) coil-specific detailed failure mode analysis is provided with entries similar to the examples provided herein. The resulting risk number $R = L \times S$ is given, considering risk control by design and action, and must correspond to the white fields in Table 3. The examples given here do not represent a complete analysis of a specific RF coil, but only illustrate the principle of electrical failure mode and risk analysis based on typical cases

Item	Potential failure mode	Potential effect of failure	Potential cause of failure	Risk control by design	Risk control by action	$R = L \times S$
Distributed capacitors in Tx array coil element	Component failure, open/ short circuit	Coil element detunes causing change in the RF field pattern and thus change with regard to SAR	Improper component selection; aging of components	Appropriate capacitor power rating; regular QA	Scanner implemented power monitoring system should stop the scan in the case of high-power reflection	1×2
Cable traps	Component failure, open/ short circuit	High shield current on the cables	Improper component selection; poor manufacturing	Appropriate capacitor power rating; cable traps tuned to the Larmor frequency and appropriately isolated	Cable traps are not accessible to the subject; extra thermal insulation of cables near human body	1×2
Detuning circuit in Rx-only coils	Component failure	Rx coil stays tuned during transmission; alteration of RF field and SAR	Improper component selection; aging of components; wire that provides current for active detuning ripped off	Fuses must be added to the Rx coil loops	Scanner control stops the scan if resistance of detune circuit is outside the specifications	1×2
Housing	Mechanical damage	Contact of the subject with high-voltage components	Improper material; improper handling of the RF coil, i.e. dropping	Use of robust material for housing	Check for mechanical integrity before scanning; handle RF coils with care	1×1

QA, quality assurance; Rx, receive; SAR, specific absorption rate; Tx, transmit.

Copyright © 2015 John Wiley & Sons, Ltd.

or integrity of detune circuits during operation, and automatic cessation of the scan if safety-related thresholds are violated (51).

The related electrical failure mode analysis is performed based on the coil-specific schematics and specification on the design (Fig. 1). Potential failure modes, the cause and effect of these failures, and the available risk controls by design and action during operation are tabulated for each component (see example in Table 4). A risk analysis after consideration of the risk control by design and action must result in the cases indicated in white in Table 3, otherwise coil design and operational procedures will need to be adapted further.

DOCUMENTATION, USER TRAINING AND QA

Even after successful completion of all safety and performance tests, safe operation of the RF coil can only be ensured if the integrity of the coil and its correct installation and usage are guaranteed. Thus, a comprehensive documentation, rigorous user training and regular tests of the appropriate functioning of the coil are required. A responsible person, usually the main user, is identified for each coil to perform these tasks in cooperation with the coil designer.

Coil documentation

The documentation serves as a reference for the routine user. First, it contains a technical description of the coil to provide elaborate insight into its design and function. This includes electrical circuit layouts, coil file specifications and details on SAR simulations. Second, the documentation contains brief and comprehensible instructions for installation and correct usage of the coil, also in combination with other equipment. Third, it gives detailed instructions, together with typical results, for coil function tests that are performed before each human measurement and for tests performed at regular intervals. Finally, the documentation records the history of the coil, containing information on the tests performed, repairs, modifications and user training.

Quality and safety assurance

Before each *in vivo* scan, the Tx and Rx functionality of the coil is quickly verified using predefined tests performed on a standardized phantom with the parameter settings given in the documentation. As malfunction in a Tx element will probably change the RF field (Fig. 6), scout images or rapid B_1^+ maps are acquired and compared with reference images or maps. If obvious deviations are detected, SAR predictions are considered as invalid and experiments on humans are not allowed. The Rx functionality is tested by comparing the free induction decay signal after a single, non-selective excitation pulse on the single Rx channels with reference data. For the pTx system, in addition, a coupling matrix is acquired and the functioning of the SAR supervision unit is verified according to the procedure described by the vendor (14).

More thorough quantitative tests are performed by the person responsible for the coil at regular intervals of not more than half a year. The tests include a check of the *S*-parameters, the power linearity of the coil, the acquisition of B_1^+ maps and images acquired with each Rx channel separately. The results are compared with the reference values. These regular tests serve as further QA and are used for the early detection of coil degeneration or failure.

User training

Before *in vivo* application, the user is instructed on the safe usage by the person responsible for the coil. The training includes the coil's correct installation with regard to the connection to the scanner, and ensures that the positioning of the coil and subject complies with SAR simulations. Further, the user must be familiarized with the test scan procedure that is performed before every human experiment and informed how to properly remove and store the coil after usage. Apart from the coil-specific training, every user undergoes general site-specific MRI safety instructions.

CONCLUSION

The above-described guidelines on safety tests, SAR simulation, risk analysis and operational procedures, including coil documentation, user training and regular QA testing, help to recognize and eliminate safety issues during coil design and operation. However, they represent current knowledge, and open questions, for instance on the validity of human models for SAR evaluation, the impact of the variety of body sizes and shapes, the relationship between SAR and temperature *in vivo*, the best possible approach for the online observation of safety-related system parameters and universally applicable specifications or limits for a number of safety and performance tests, remain to be answered. Hence, it is recommended to always operate with sufficiently large safety margins. The research community is invited to actively participate in extending the knowledge on which the safety procedures are based in an open discourse about best possible practice.

Acknowledgement

The authors thank Drs Cornelis A. T. van den Berg, Mark Ladd, Andreas Bitz and Christopher Wiggins for proofreading the internal safety procedure and for valuable comments and contributions. Further, we acknowledge Yacine Noureddine and Jonas Bause for their contributions to the *E*-field measurements.

REFERENCES

1. US Food and Drug Administration. *Guidance for Industry and FDA Staff: Criteria for Significant Risk Investigations of Magnetic Resonance Diagnostic Devices*. US Food and Drug Administration: Silver Spring, MD; 2003.
2. IEC 60601-1. *Medical Electrical Equipment – Part 1: General Requirements for Basic Safety and Essential Performance Amendment 1*. International Electrotechnical Commission: Geneva; 2012.
3. IEC 60601-2-33. *Medical Electrical Equipment – Part 2-33: Particular Requirements for the Basic Safety and Essential Performance of Magnetic Resonance Equipment for Medical Diagnosis*, Edition 3.1. International Electrotechnical Commission: Geneva; 2013.
4. IEC/DIN EN 60695-11-10. *Flammability Rating of Plastic Materials for Parts in Devices and Applications*. International Electrotechnical Commission: Geneva; 2010.
5. I.S. EN ISO 14971. Medical Devices – Application of Risk Management to Medical Devices [Authority: The European Union Per Directive 90/385/EEC]; 2012.
6. Zhang X, Ugurbil K, Chen W. Microstrip RF surface coil design for extremely high-field MRI and spectroscopy. Magn. Reson. Med. 2001; 46: 443–450.

Copyright © 2015 John Wiley & Sons, Ltd.

7. Raaijmakers AJ, Ipek O, Klomp DW, Possanzini C, Harvey RP, Lagendijk JJ, van den Berg CA. Design of a radiative surface coil array element at 7T: the single-side adaptive dipole antenna. Magn. Reson. Med. 2011; 66(5): 1488–1497.
8. Brunner DO, De Zanche N, Fröhlich J, Paska J, Pruessmann KP. Travelling-wave nuclear magnetic resonance. Nature 2009; 457: 994–998.
9. *Reference Data for Radio Engineers*, 6th edn. Howard W. Sams/ITT: New York; 1982, pp. 4–29.
10. Pfrommer A, Avdievich NI, Henning A. Four channel transceiver array for functional magnetic resonance spectroscopy in the human visual cortex at 9.4 T. *Proceedings of the 22nd Annual Meeting ISMRM*, Milan, Italy, 2014; 1305.
11. Peterson DM, Beck BL, Duensing GR, Fitzsimmons JR. Common mode signal rejection methods for MRI: reduction of cable shield currents for high static magnetic field systems. Conc. Magn. Reson. B: Magn. Reson. Eng. 2003; 19B(1): 1–8.
12. Seeber DA, Jevtic I, Menon A. Floating shield current suppression trap. Concepts Magn. Reson. 2004; 21B(1): 26–31.
13. Ginzton EL. *Microwave Measurements*. McGraw-Hill: New York; 1957.
14. *MAGNETOM 7T Operator Manual - Tx Array System syngo MR B17*. Siemens Healthcare: Erlangen, Germany; 2012.
15. Roleson S. Evaluate EMI reduction schemes with shielded-loop antennas. EDN 1984; 29(10): 203–207.
16. Avdievich NI. Transceiver phased arrays for human brain studies at 7 T. Appl. Magn. Res. 2011; 41(2): 483–506.
17. Edelstein WA, Hardy CJ, Mueller OM. Electronic decoupling of surface-coil receivers for NMR imaging and spectroscopy. J. Magn. Reson. 1986; 67: 156–161.
18. Fujita H, Zheng T, Yang X, Finnerty MJ, Handa S. RF surface receive array coils: the art of an LC circuit. J. Magn. Reson. Imaging 2013; 38(1): 12–25.
19. Roemer PB, Edelstein WA, Hayes CE, Souza SP, Mueller OM. The NMR phased array. Magn. Reson. Med. 1990; 16: 192–225.
20. Shajan G, Kozlov M, Hoffmann J, Turner R, Scheffler K, Pohmann R. A 16-channel dual-row transmit array in combination with a 31-element receive array for human brain imaging at 9.4 T. Magn. Reson. Med. 2014; 71: 870–879.
21. Ohliger MA, Ledden L, McKenzie CA, Sodickson DK. Effects of inductive coupling on parallel MR image reconstructions. Magn. Reson. Med. 2004; 52: 628–639.
22. Tropp J, Derby K. The loss of signal to noise due to imperfect isolation between the channels of a quadrature nuclear magnetic resonance probe. Rev. Sci. Instrum. 1991; 62(11): 2646–2653.
23. Robson PM, Grant AK, Madhuranthakam AJ, Lattanzi R, Sodickson DK, McKenzie CA. Comprehensive quantification of signal-to-noise ratio and g-factor for image-based and k-space-based parallel imaging reconstructions. Magn. Reson. Med. 2008; 60(4): 895–907.
24. Klose U. In vivo proton spectroscopy in presence of eddy currents. Magn. Reson. Med. 1990; 14: 26–30.
25. IEC/IEEE P62704-1. *Draft Standard for Determining the Peak Spatial Average Specific Absorption Rate (SAR) in the Human Body from Wireless Communications Devices, 30 MHz–6 GHz. Part 1: General Requirements for Using the Finite Difference Time Domain (FDTD) Method for SAR Calculations*. International Electrotechnical Commission/ Institute of Electrical and Electronics Engineers: Geneva/New York; in preparation.
26. Criteria for Significant Risk Investigations of Magnetic Resonance Diagnostic Devices. Guidance for Industry and Food and Drug Administration Staff. U.S. Department of Health and Human Services, Food and Drug Administration (FDA), 2014.
27. Hoffmann J, Shajan G, Scheffler K, Pohmann R. Numerical and experimental evaluation of RF shimming in the human brain at 9.4 T using a dual-row transmit array. Magn. Reson. Mater. Phys. 2014; 27(5): 373–386.
28. Kozlov M, Turner R. Effects of simplifying RF coil 3-D EM simulation models on power balance and SAR. *Proceedings of the 18th Annual Meeting ISMRM*, Stockholm, Sweden, 2010; 1445.
29. NEMA Standards Publication MS 8-2008. Characterization of the Specific Absorption Rate (SAR) for Magnetic Resonance Imaging Systems. National Electrical Manufacturer's Association, Rosslyn, VA, 2008.
30. Kozlov M, Turner R. Effects of tuning condition, head size and position on the SAR of MRI dual-row transmit arrays. *Proceedings of the 43rd European Microwave Conference*, 2013; 708–711.
31. De Poorter J, De Wagter C, De Deene Y, Thomsen C, Stahlberg F, Achten E. Noninvasive MRI thermometry with the proton resonance frequency (PRF) method: in vivo results in human muscle. Magn. Reson. Med. 1995; 33(1): 74–81.
32. Van den Bergen B, Klomp DW, Raaijmakers AJ, de Castro CA, Boer VO, Kroeze H, Luijten PR, Lagendijk JJ, van den Berg CA. Uniform prostate imaging and spectroscopy at 7 T: comparison between a microstrip array and an endorectal coil. NMR Biomed. 2011; 24(4): 358–365.
33. Ehses P, Fidler, F, Nordbeck P, Pracht ED, Warmuth M, Jakob PM, Bauer WR. MRI thermometry: fast mapping of RF-induced heating along conductive wires. Magn. Reson. Med. 2008; 60: 457–461.
34. Duan Q, Duyn JH, Gudino N, de Zwart JA, van Gelderen P, Sodickson DK, Brown R. Characterization of a dielectric phantom for high-field magnetic resonance imaging applications. Med. Phys. 2014; 41: 102303 http://dx.doi.org/10.1118/1.4895823
35. Hekmatyar SK, Hopewell P, Pakin SK, Babsky A, Bansal N. Noninvasive MR thermometry using paramagnetic lanthanide complexes of 1,4,7,10-tetraazacyclododecane-α,α′,α″,α‴-tetramethyl-1,4,7,10-tetraacetic acid ($DOTMA^{4-}$). Magn. Reson. Med. 2005; 53(2): 294–303.
36. Cloos MA, Alon L, Chen G, Wiggins GC, Sodickson D. Rapid RF safety evaluation for transmit-array coils. *Proceedings of the 21st Annual Meeting ISMRM*, Salt Lake City, UT, USA, 2013; 286.
37. Bitz AK, Kraff O, Orzada S, Maderwald S, Brote I, Johst S, Ladd ME. Assessment of RF safety of Tx coils at 7 Tesla by experimental and numerical procedures. *Proceedings of the 19th Annual Meeting ISMRM*, Montreal, QC, Canada, 2011; 490.
38. Christ A, Kainz W, Hahn EG, Honegger K, Zefferer M, Neufeld E, Rascher W, Janka R, Bautz W, Chen J, Kiefer B, Schmitt P, Hollenbach H-P, Shen J, Oberle M, Szczerba D, Kam A, Guag JW, Kuster N. The virtual family–development of surface based anatomical models of two adults and two children for dosimetric simulations. Phys. Med. Biol. 2010; 55(2): N23–N38.
39. Hasgal PA, Di Gennaro F, Baumgartner C, Neufeld E, Gosselin MC, Payne D, Klingenböck A, Kuster N. IT'IS Database for thermal and electromagnetic parameters of biological tissues, Version 2.5, August 1st, 2014. www.itis.ethz.ch/database
40. Homann H, Graesslin I, Nehrke K, Vernickel P, Katscher U, Dössel O, Börnert P. Local SAR management by RF shimming: a simulation study with multiple human body models. Magn. Reson. Mater. Phys. 2012; 25(3): 193–204.
41. Eichfelder G, Gebhardt M. Local specific absorption rate control for parallel transmission by virtual observation points. Magn. Reson. Med. 2011; 66(5): 1468–1476.
42. *Guide to the Expression of Uncertainty in Measurement*, 1st corrected edn. International Organization for Standardization (ISO): Geneva; 1995.
43. ISO/TS 21748. *Guide to the Use of Repeatability, Reproducibility and Trueness Estimates in Measurement Uncertainty Estimation*. International Organization for Standardization (ISO): Geneva; 2002.
44. ISO 13485:2003. *Medical Devices — Quality Management Systems — Requirements for Regulatory Purposes*. International Organization for Standardization (ISO): Geneva; 2003.
45. SO/IEC Guide 51:1999. *Safety Aspects — Guidelines for their Inclusion in Standards*; 1999.
46. De Greef M, Ipek O, Raaijmakers AJ, Crezee J, van den Berg CA. Specific absorption rate intersubject variability in 7T parallel transmit MRI of the head. Magn. Reson. Med. 2013; 69(5): 1476–1485.
47. Villena JF, Polimeridis AG, Guerin B, Eryaman Y, Wald LL, Adalsteinsson E, White JK, Daniel L. Fast electromagnetic analysis of transmit RF coils based on accelerated integral equation methods. *Proceedings of the 22nd Annual Meeting ISMRM*, Milan, Italy, 2014; 623.
48. Homann H, Boernert P, Eggers H, Nehrke K, Doessel O, Graesslin I. Toward individualized SAR models and in vivo validation. Magn. Reson. Med. 2011; 66(6): 1767–1776.
49. Chishti MH, Wang Z, Yeo D. Local SAR prediction errors with variation of electrical properties in the head at 7T. *Proceedings of the 21st Annual Meeting ISMRM*, Salt Lake City, UT, USA, 2013; 2835.
50. Graesslin I, Homann H, Biederer S, Börnert P, Nehrke K, Vernickel P, Mens G, Harvey P, Katscher U. A specific absorption rate prediction concept for parallel transmission MR. Magn. Reson. Med. 2012; 68(5): 1664–1674.

Copyright © 2015 John Wiley & Sons, Ltd.

51. Graesslin I, Vernickel P, Börnert P, Nehrke K, Mens G, Harvey P, Katscher U. Comprehensive RF safety concept for parallel transmission MR. Magn. Reson. Med. 10.1002/mrm.25425 [Epub ahead of print], 2014.

SUPPORTING INFORMATION

Additional supporting information may be found in the online version of this article at the publisher's web site.

Copyright © 2015 John Wiley & Sons, Ltd.

SPECTROSCOPIC METHODOLOGY – Full Papers

Magnetic Resonance in Medicine 79:1841–1850 (2018)

Metabolite-Cycled STEAM and Semi-LASER Localization for MR Spectroscopy of the Human Brain at 9.4T

Ioannis-Angelos Giapitzakis,[1,2]* Tingting Shao,[1] Nikolai Avdievich,[1] Ralf Mekle,[3] Roland Kreis,[4] and Anke Henning[1,5]

Purpose: Metabolite cycling (MC) is an MRS technique for the simultaneous acquisition of water and metabolite spectra that avoids chemical exchange saturation transfer effects and for which water may serve as a reference signal or contain additional information in functional or diffusion studies. Here, MC was developed for human investigations at ultrahigh field.

Methods: MC-STEAM and MC-semi-LASER are introduced at 9.4T with an optimized inversion pulse and elaborate coil setup. Experimental and simulation results are given for the implementation of adiabatic inversion pulses for MC. The two techniques are compared, and the effect of frequency and phase correction based on the MC water spectra is evaluated. Finally, absolute quantification of metabolites is performed.

Results: The proposed coil configuration results in a maximum B_1^+ of 48 μT in a voxel within the occipital lobe. Frequency and phase correction of single acquisitions improve signal-to-noise ratio (SNR) and linewidth, leading to high-resolution spectra. The improvement of SNR of N-acetylaspartate (SNR_{NAA}) for frequency aligned data, acquired with MC-STEAM and MC-semi-LASER, are 37% and 30%, respectively ($P < 0.05$). Moreover, a doubling of the SNR_{NAA} for MC-semi-LASER in comparison with MC-STEAM is observed ($P < 0.05$). Concentration levels for 18 metabolites from the human occipital lobe are reported, as acquired with both MC-STEAM and MC-semi-LASER.

Conclusion: This work introduces a novel methodology for single-voxel MRS on a 9.4T whole-body scanner and highlights the advantages of semi-LASER compared to STEAM in terms of excitation profile. In comparison with MC-STEAM, MC-semi-LASER yields spectra with higher SNR. **Magn Reson Med 79:1841–1850, 2018. © 2017 International Society for Magnetic Resonance in Medicine.**

Key words: Metabolite cycling; MR spectroscopy; non-water suppression; STEAM; semi-LASER

INTRODUCTION

^{1}H MRS is a noninvasive method allowing the detection as well as the quantification of several metabolites in the human brain. The introduction of ultrahigh field (UHF) scanners ($\geq$7T) lead to an increase of the signal-to-noise ratio (SNR) and a higher frequency dispersion, hence better spectral resolution. These advantages promote the potential of MRS (1,2). Noteworthy, multiple studies have demonstrated the detection of up to 18 metabolites both in human and rodent brains at UHF (3–7).

Despite the significant advantages of UHF for MRS, several technical challenges have to be addressed for efficient utilization of these prospective benefits. In particular, the severe B_1^+ inhomogeneity due to destructive interference (8), the increased chemical shift displacement (CSD) between different metabolites, and the requirement of short echo time (TE) sequences due to shorter T_2 relaxation times are critical problems for MRS at UHF. Previous work has demonstrated the feasibility and prospects of the stimulated echo acquisition mode (STEAM) sequence and localization by adiabatic selective refocusing (LASER) sequence, along with optimized outer-volume saturation (OVS) and water-suppression (WS) schemes for the quantification of metabolites in the occipital lobe of the human brain at 9.4T (9). Furthermore, studies have demonstrated the advantages of localization schemes using adiabatic refocusing at 7T (4,10). Adiabatic pulses provide localization profiles that are robust against B_1^+ inhomogeneity. However, their implementation can introduce high specific absorption rates (SAR) due to high B_1^+ peak power requirements and longer TEs compared to nonadiabatic sequences such as STEAM (11). On the other hand, in STEAM only half of the available signal is detected. A suitable compromise between TE and power deposition with adiabatic refocusing is the semi-LASER sequence (4,12,13). In this technique, localization is performed by a conventional slice-selective excitation pulse followed by two pairs of refocusing adiabatic fast passage pulses (AFP). In this way, a full-intensity free induction decay (FID) is acquired at reasonably short TEs (e.g., 25 ms (4)). Moreover, the high bandwidth of the refocusing AFP leads to lower CSD. The fact that refocusing AFP pulses typically have good slice profiles with little refocusing outside of their bandwidth and that in semi-LASER the pair of refocusing AFP is repeated twice leads to improved excitation profiles largely devoid of lipid contaminations and greatly reduces the need for OVS. In addition, J evolution is reduced for J-coupled metabolites due to the Carr-Purcell train behavior of semi-LASER (14,15).

[1]High-Field Magnetic Resonance, Max Planck Institute for Biological Cybernetics, Tübingen, Germany.

[2]IMPRS for Cognitive & Systems Neuroscience, Tübingen, Germany.

[3]Center for Stroke Research Berlin (CSB), Charité Universitätsmedizin Berlin, Berlin, Germany.

[4]Departments of Radiology and Clinical Research, University Bern, Bern, Switzerland.

[5]Institute of Physics, University of Greifswald, Greifswald, Germany.

Grant sponsor: Supported by the European Social Fund and national funds (NSRF 2007-2013, I.A. Giapitzakis) through the Greek State Scholarships Foundation (IKY). Part of the project also was cosponsored by the Swiss National Science Foundation (SNSF #320030-156952; R. Kreis) and by the Horizon 2020/ ERC Starting Grant (SYNAPLAST MR; A. Henning).

*Correspondence to: Ioannis-Angelos Giapitzakis M.Sc., High-Field Magnetic Resonance, Max Planck Institute for Biological Cybernetics, Tübingen, Germany. E-mail: ioannis.giapitzakis@tuebingen.mpg.de.

Received 3 February 2017; revised 25 July 2017; accepted 25 July 2017
DOI 10.1002/mrm.26873
Published online 15 August 2017 in Wiley Online Library (wileyonlinelibrary.com).

© 2017 International Society for Magnetic Resonance in Medicine

The need for higher B_1^+ fields with the use of adiabatic pulses requires the implementation of more efficient coil setups at UHF. For this purpose, transceiver channel coils are placed adjacent to the area of interest, combined with optimal B_1^+ phase shimming (9,16,17).

Another technical challenge at UHF is the increased and variable inhomogeneity of the static magnetic field (B_0) due to susceptibility effects as well as physiological and involuntary gross head motion. Minor bulk motion or breathing-related field variation can shift the frequency and phase of the acquired FID signals, increasing the linewidth of the summed spectra and decreasing the SNR because of the nonconstructive summation of acquisitions.

Water suppression is an essential part of MRS for the prevention of gradient modulation sidebands and baseline distortions. This complication becomes more critical at UHF because stronger gradient amplitudes are used to realize short TE sequences and minimal CSD.

Nevertheless, several studies implementing non-water–suppressed MRS techniques such as metabolite cycling (MC) (18) have shown their potential in addressing these challenges. MC allows the simultaneous acquisition of water and metabolite spectra without scan time prolongation or the need for a water reference scan. MC, which involves alternating the adiabatic inversion of the upfield and downfield part of the spectrum without alteration of the water signal, has been incorporated in point-resolved spectroscopy (PRESS), LASER, and STEAM sequences (19–22).

Studies utilizing MC-PRESS have demonstrated the advantages of this technique compared to water-suppression techniques. In particular, the non-water–suppressed signal can be used for frequency, and phase alignment prior to averaging as well as eddy current correction, which is of particular value in very small voxels of interest for applications in the spinal cord and the myocardium as well as for GABA editing at 3T (23–25). MC-PRESS also has been utilized for the measurement of magnetization exchange of the downfield resonances in the human brain and muscle (20,26,27). At 3T, diffusion-weighted MC-STEAM has been shown to offer ways to prevent motion-induced overestimation of diffusion coefficients (28). Furthermore, MC MRS holds potential for the simultaneous detection of blood-oxygen-level–dependent changes in water and metabolite alterations under functional stimulation (29). However, PRESS uses non-adiabatic refocusing and suffers from a large CSD due to limited radiofrequency (RF) bandwidths, especially in human applications.

Thus, the purpose of this study was the development of two new sequences for UHF MRS in the human brain at 9.4T utilizing the MC technique and thus preparing the ground for follow-up investigations with regard to exchange spectroscopy, functional spectroscopy, and diffusion-weighted spectroscopy at 9.4T. In particular, an asymmetric adiabatic inversion pulse (InvP) optimized for MC at 9.4T was incorporated with STEAM and semi-LASER optimized to account for inhomogeneous transmit fields and minimizing CSD. These two new sequences, along with the appropriate hardware setup, were then used for the acquisition of in vivo data from the occipital lobe of the human brain and their performance was compared. In particular, frequency fluctuations at 9.4T were quantitatively investigated, and the related effect of frequency and phase correction from the MC water spectra on the overall spectral quality was studied. Finally, absolute metabolite quantification was carried out deploying LCModel (30).

METHODS

Technical Description and Subjects

All measurements were performed on a Siemens 9.4T whole-body MRI scanner (Erlangen, Germany) equipped with a SC72 gradient system having a maximal nominal amplitude of 40 mT/m and a maximal slew rate of 200T/m/s. All measurements were performed using a home-built proton coil with eight transmit and 16 receive channels (31,32). Available peak power from the amplifiers was 8 kW, with 50% line loss. To obtain high B_1^+ values for the excitation of a voxel within the occipital lobe, the entire power was applied only to the three bottom coil elements using a three-way power splitter (Supporting Fig. S1). As a result, on average a maximum B_1^+ of 48 μT (ranging from 44 μT to 56 μT) could be achieved in a voxel within the occipital lobe (more detail provided in the Supporting Information and Supporting Fig. S1). The coil was tuned and matched for each volunteer individually before the beginning of the experiment using a homebuilt tuning and matching box (33) and a portable probe tuning device (Morris Instruments Inc., Ottawa, Canada), ensuring minimal reflected power. Eight healthy volunteers (six male and two female, age: 29 ± 4 years) participated in this study. Written informed consent was given by all subjects prior to the examination, and the study had been approved by the local ethics board.

Optimization of Asymmetric Adiabatic Pulse for Metabolite Cycling at 9.4T

For the inversion of upfield and downfield metabolite signals without affecting the water peak, an InvP was applied. In this study, the InvP with pulse length, T_{pulse}, is constructed of the first half of a sech pulse ($HS_{1/2}$, $R = 31.415$) for $0.9\,T_{pulse}$, and the second half of a tanh/tan pulse ($R = 100$) for $0.1\,T_{pulse}$. The detailed nomenclature and the pulse parameters are described in the study of Hwang et al. (34). The InvP as an asymmetric AFP pulse features a steep transition bandwidth (BW_{trans}, frequency range in which longitudinal magnetization M_z: $-0.95 \leq M_z/M_o \leq 0.95$; M_o: magnetization at thermal equilibrium) on the water side and a broad inversion bandwidth (BW_{inv}, $M_z/M_o \leq -0.95$) (Fig. 1a). However, adaptation and optimization of the InvP for applications in the human brain at 9.4T were necessary for efficient inversion of the desired frequency range. On the upfield part of the spectrum (< 4.7 ppm), the main metabolites extend from 1.3 ppm (lactate) to 4.1 ppm (myo-inositol). Similarly, in the down-field region (> 4.7 ppm), the hydrogen compounds of interest lie within a range of about 3 ppm as well (5.2–8.2 ppm). Thus, the required

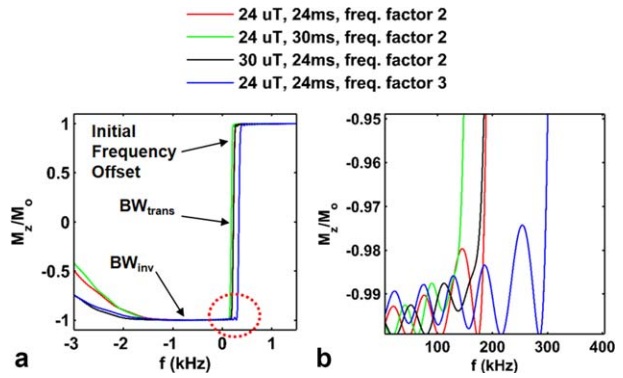

FIG. 1. Simulations and experimental results of the asymmetric adiabatic pulse for inversion of the upfield part of the spectrum. **a**) Longitudinal magnetization profile of the inversion pulse simulated for different B_1^+ values, pulse durations, and frequency factors. The numbers in the annotation correspond to the B_1^+ value, pulse duration, and frequency factor, respectively. The arrows point at the inversion bandwidth BW_{inv} (frequency range in which $M_z/M_o \leq -0.95$), the transition bandwidth BW_{trans} (frequency range in which $-0.95 \leq M_z/M_o \leq 0.95$), and the initial frequency offset ($M_z/M_o = 0.95$). The red dotted circle indicates the zoomed region illustrated in panel B. **b**) Zoomed region of panel A illustrates detailed behavior at the transition from full inversion to the transition band. The initial frequency offset also is demonstrated.

frequency range for inversion is 3.5 ppm, which is equivalent to 1,400 Hz at 9.4T.

BW_{inv} and BW_{trans} depend on three parameters: 1) the duration of the InvP, T_{pulse}, 2) the frequency sweep range of the frequency modulation function (FM), and 3) the B_1^+ amplitude. The acceptable combination of these three factors is restricted by the fulfillment of the adiabatic condition (35).

Bloch equation simulations were performed using in-house scripts in MatLab 2012b (MathWorks, Natick, Massachusetts, USA) to find optimal parameter sets. BW_{inv} and BW_{trans} were studied as a function of the three influencing factors for the following parameter ranges: pulse duration from 20 to 30 ms, frequency factor from 1 to 4 (see below), and B_1^+ values from 15 μT to 30 μT (Fig. 2). The frequency factor is simply a number that is multiplied with the frequency sweep range of the FM. The original sweep range of the FM extended from −11.36 kHz to 0.12 kHz (18,34). Therefore, the frequency factor modifies the FM function of the adiabatic pulse and defines the resulting BW_{inv}.

Aside from that, the frequency profile of the InvP exhibits an initial frequency offset ($M_z/M_o = 0.95$) due to the asymmetry of the pulse, which also was investigated for different B_1^+ values, pulse durations, and frequency factors (Fig. 1b). After simulations and the selection of appropriate parameters for the InvP, validation experiments were performed using a spectroscopic phantom containing lactate and acetate (Supporting Information and Supporting Fig. S2).

Development of Metabolite Cycled Localization Schemes

Two localization schemes were developed exploiting MC advantages based on conventional spectroscopy sequences. The first scheme consisted of a conventional STEAM sequence in which an InvP for MC was incorporated during the mixing time (Fig. 3a). The second localization strategy involved a semi-LASER sequence (4) that was preceded by a MC pulse (Fig. 3b). For both sequences, a hamming-filtered 90-degree sinc pulse with a bandwidth of ∼8 kHz was used. The characteristics of InvP for MC were: minimum $B_1^+ = 22$ μT, pulse duration = 22.4 ms, frequency factor = 2, and $Freq_{invP} = \pm 350$ Hz.

For the semi-LASER sequence, both sagittal and coronal slices were selected using a pair of refocusing offset independent trapezoidal adiabatic pulses (4) optimized for 9.4T. The pulse duration was 3.5 ms, with a bandwidth of 8 kHz and a minimum required B_1^+ of 24 μT. The moment for all the spoiler gradients was set to 53 mT/m*ms.

MRS Data Acquisition

Placement of the spectroscopy voxel was facilitated using high-resolution images from 2D FLASH scans (in-plane resolution: $0.7 \times 0.7\ mm^2$, slice thickness = 3.5 mm, 25 slices) acquired in three orientations (axial, sagittal, and coronal) and a 3D MPRAGE scan (36). Afterward, a voxel ($2 \times 2 \times 2\ cm^2$) was chosen in a mixed gray (GM) and white matter area (WM) within the occipital lobe. First- and second-order Bo shimming was performed using FASTESTMAP (37) and voxel-based power calibration was executed (38). Next, localized MR spectra using the two described MC localization schemes were acquired from each volunteer (MC-semi-LASER with TE = 24 ms, MC-STEAM with TE = 8 ms, and mixture time (TM) = 50 ms). For both cases, the repetition time was 6,000 ms, ensuring an acceptable SAR level (average SAR as a percentage of the maximum allowed value was 30% for MC-STEAM and 90% for MC-semi-LASER) and almost complete T_1 recovery; 96 averages were acquired with 4,096 time points and an 8 kHz receive-bandwidth. $|Freq_{invP}|$ was set to 350 Hz. A phase-cycling scheme of 16 steps (4) was applied. The transmit reference frequency was set at 2.3 ppm for the reduction of CSD and minimization of lipid excitation. Neither water presaturation nor OVS was applied. The slice-selection gradients' polarity was selected such that the CSD-shifted ROI of upfield fat peaks would be moved away from the skull (toward the anterior–right direction). Furthermore, macromolecular spectra were acquired for each volunteer (number of excitations (NEX): 64), with both sequences using a double inversion recovery technique ($T_{inv1} = 2{,}360$ ms and $T_{inv2} = 625$ ms) with a repetition time (TR) of 10 s (39,40). Finally, to avoid any influence of MC pulses on absolute quantification, water reference signals (NEX: 16) were measured with both sequences without MC and WS. The total exam time for each subject was about 50 min.

MRS Data Analysis

Raw data were analyzed in MatLab (MathWorks) with in-house processing routines. Data processing involved the following steps: Step 1 was zero filling with a factor of two. Step 2 was frequency and phase alignment (MC Corr) in the time domain (utilizing the fminsearch

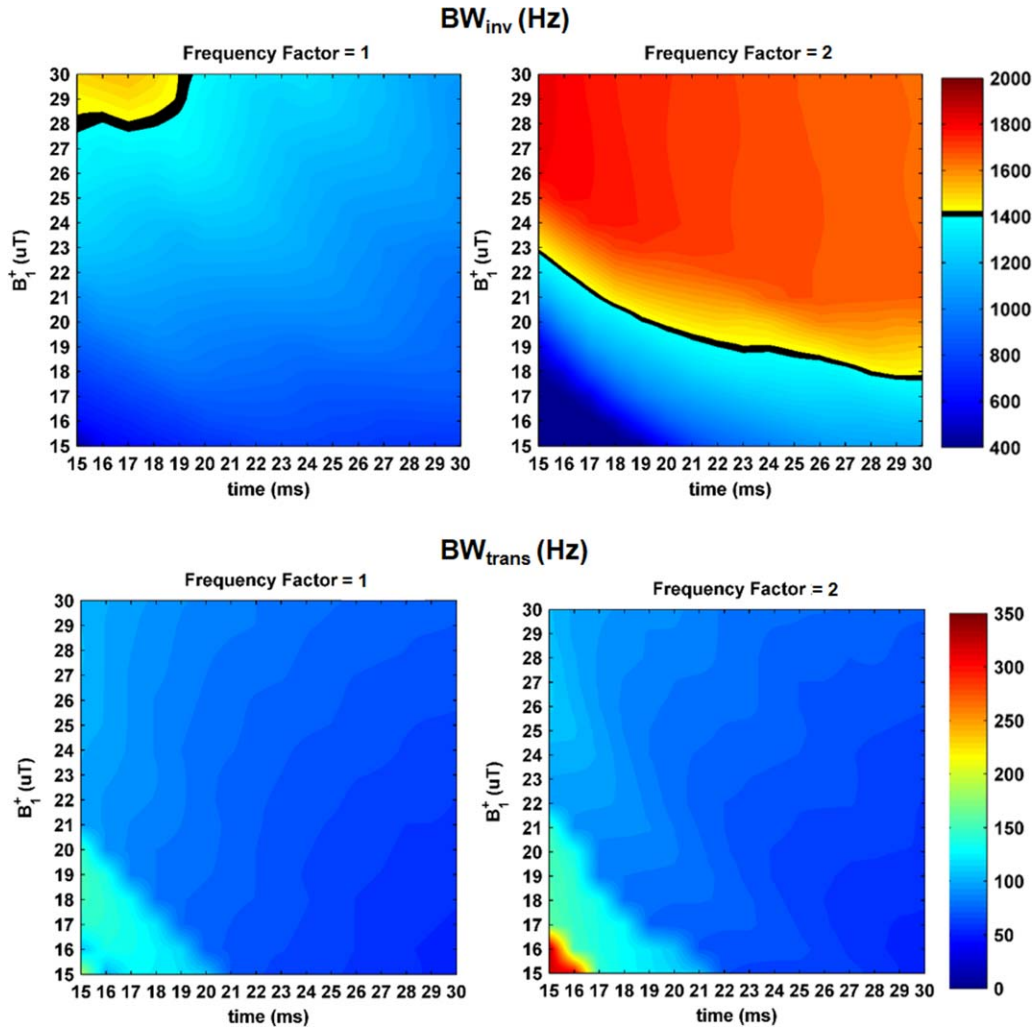

FIG. 2. Simulation results for BW_{inv} and BW_{trans} as a function of B_1^+ amplitude, pulse duration T_{pulse}, and frequency factor (left frequency factor = 1.0, right = 2.0). (Upper panel) BW_{inv} results in Hz. The black contour line indicates 1,400 Hz, which is the required frequency range for spectroscopic applications at 9.4T. (Lower panel) BW_{trans} results in Hz. For both simulated frequency factors, for durations longer than 22 ms, the BW_{trans} ranges from 60 to 80 Hz, which corresponds to 0.15 to 0.2 ppm at 9.4T. BW_{inv}, inversion bandwidth; BW_{trans}, transition bandwidth.

function within MatLab (MathWorks)) by minimizing the difference between individual FIDs. For comparison purposes, the data also were analyzed without frequency correction (MC Uncorr). Step 3 was minimization of the residual water signal in the MC metabolite spectrum: Even-numbered MC spectra were multiplied by a scaling factor (F_s) between 0.90 to 0.97 before signal, as described in (18). The F_s was calculated ensuring minimal residual water in the metabolite spectra. In step 4, water spectra were created by averaging odd and even numbered acquisitions. Metabolite data were calculated by subtracting even numbered averages from odd numbered FIDs. Step 5 was truncation of FIDs at 250 ms. Step 6 was zero-order phase and eddy current correction using the phase information of the water signal (41). In step 7, signals from all 16 receive channels were combined using a singular value decomposition method (42) based on MC water data. Step 8 was manual first-order phase correction for each dataset (0.015 ± 0.011 degrees/Hz). Step 9 was the removal of water residuals using Hankel Singular Value Decomposition (HSVD (43), only performed on MC Uncorr.)

Finally, full-width half maximum (FWHM) of the water and creatine (Cr) peaks, as well as the SNR of N-acetylaspartate (NAA) (SNR_{NAA}) and glutamate (Glu) (SNR_{Glu}) peaks were calculated. SNR_{NAA} and SNR_{Glu} were measured as NAA and Glu amplitude (frequency domain) at 2.01 ppm and 2.35 ppm, respectively, divided by the standard deviation of 1,000 points from 14.7 ppm to 12.3 ppm. For the creation of macromolecular template signals (39), all the subjects' macromolecular signals were summed, and the averaged macromolecular spectrum was smoothed using cubic splines within MatLab (MathWorks) (smoothing parameter $P = 0.001$) for noise reduction.

Statistical hypothesis testing for differences between STEAM and semi-LASER regarding FWHM, SNR, and F_s was performed within MatLab (MathWorks) using one-tailed nonparametric rank test (Wilcoxon signed rank test for equal and matched sample size) and the Holm-Bonferroni method for multiple comparisons correction.

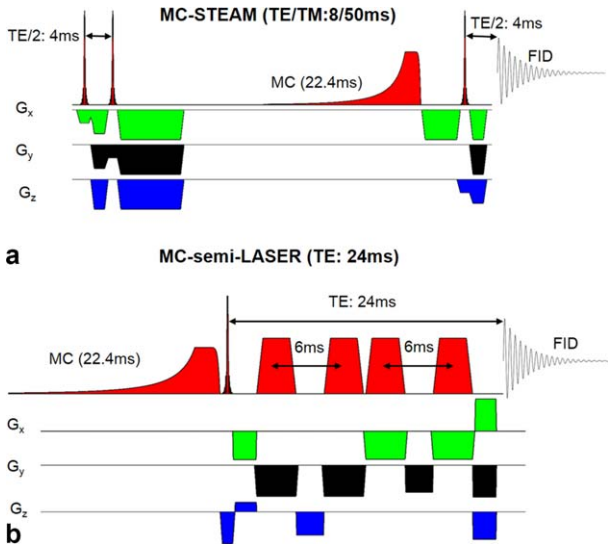

FIG. 3. Sequence diagrams. **a**) MC-STEAM sequence with a TE of 8 ms and a TM of 50 ms. MC was incorporated during the mixing period without an extension of TE, therefore without any loss of signal due to T_2 relaxation. **b**) MC-semi-LASER sequence with TE of 24 ms. A metabolite cycling pulse is introduced directly before localization.

MRS Data Quantification

For calculation of the metabolites' concentrations, the spectra were analyzed using LCModel V6.3-1L (30). A basis set consisting of 19 metabolites was simulated using PyGAMMA (44) based on experimentally measured chemical shifts and J-coupling values (45–47). The MC-STEAM basis set was simulated using a STEAM sequence (TE/TM: 8/50 ms) with ideal pulses, whereas the MC-semi-LASER was simulated using a spin echo sequence with ideal pulses and a TE of 6.5 ms corresponding to the apparent TE of the real sequence (4,15). The apparent TE was defined after comparing in vivo spectra, in particular, the NAA aspartate moiety, with simulated spectra (48). Measured macromolecular templates were included in the models for both localization strategies. More details regarding quantification are provided in the text in the Supporting Information. Absolute metabolite concentrations in mM ($[\mathrm{Met}]_{\mathrm{mM}}$) without correction for relaxation were calculated using LCModel water normalized concentrations ($[\mathrm{Met}]_{\mathrm{Nwater}}$) through the following equation (49):

$$[\mathrm{Met}]_{\mathrm{mM}} = [\mathrm{Met}]_{\mathrm{Nwater}} \cdot 55126\ \mathrm{mM} \cdot \frac{(\mathrm{f_{GM}} \cdot a_{GM} + \mathrm{f_{WM}} \cdot a_{WM} + \mathrm{f_{CSF}} \cdot a_{CSF})}{1 - \mathrm{f_{CSF}}} \cdot \frac{2}{1 + F_s}$$

where 55,126 mM is the concentration of pure water at body temperature. $\mathrm{f_{GM}}$, $\mathrm{f_{WM}}$, and $\mathrm{f_{CSF}}$ correspond to the GM, WM, and cerebrospinal fluid (CSF) percentages, respectively, and the relative densities of NMR-visible water ($a_{GM} = 0.78, a_{WM} = 0.65,\ a_{CSF} = 0.97$) were found in (50). The denominator $1 - f_{CSF}$ was implemented for partial-volume correction (30,50). The factor $\frac{2}{1+F_s}$) was introduced to correct for the multiplication of even numbered acquisitions with the Fs (18). No exclusion criteria were used for the calculation of cohort average metabolites levels for the avoidance of biased estimated mean concentrations (51).

RESULTS

Coil Setup Performance

Phantom measurements demonstrate that the coil setup along with the appropriate phase increment and power distribution results in a maximum B_1^+ efficiency of 0.16 μT/V and an average value of 0.13 μT/V (Supporting Fig. S1C). These findings are in agreement with in vivo results in which an average B_1^+ of 0.106 μT/V was achieved in the occipital lobe. Thus, a B_1^+ of 48 μT could be achieved with the maximum allowed voltage of 450 V. In addition, coupling values of different coil loops were small (< 18 dB); therefore, prior whitening of the data was not required (52).

Figure 1 illustrates the simulated profile of the longitudinal magnetization for different B_1^+ levels, pulse durations, and frequency factors. The results demonstrate that the initial frequency offset of the inversion pulse remains practically unchanged with variations of B_1^+. However, it increases for larger frequency factors and pulse durations (Fig. 1b). Additionally, $\mathrm{BW_{inv}}$ increases significantly for higher frequency factors and

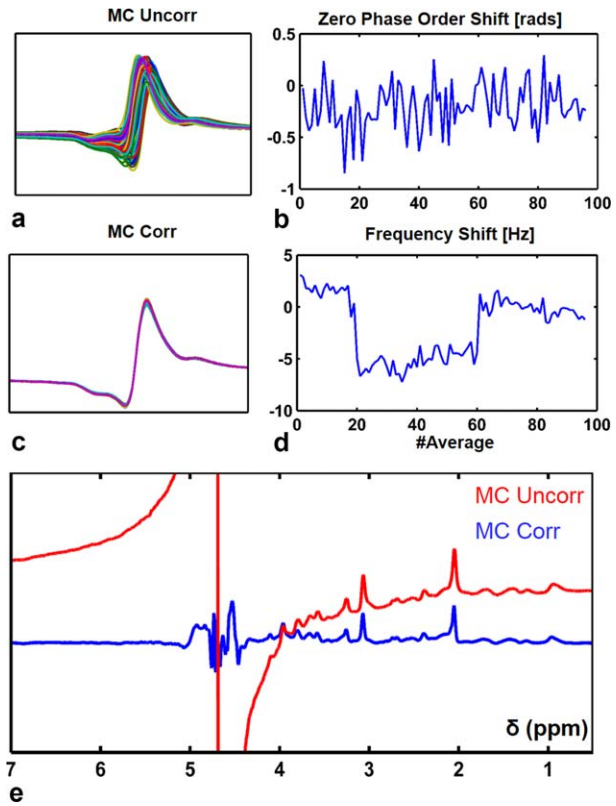

FIG. 4. The effect of frequency and phase alignment of acquisitions. **a–b**) Individual water signals before and after frequency alignment. **c–d**) Zero-order phase and frequency shift for each acquisition. **e**) MC Corr and MC Uncorr metabolite data. Spectra acquired from a volunteer using MC-semi-LASER (TE/TR: 24/6,000 ms, NEX: 96) from a voxel in the occipital lobe ($2 \times 2 \times 2\ \mathrm{cm}^3$).

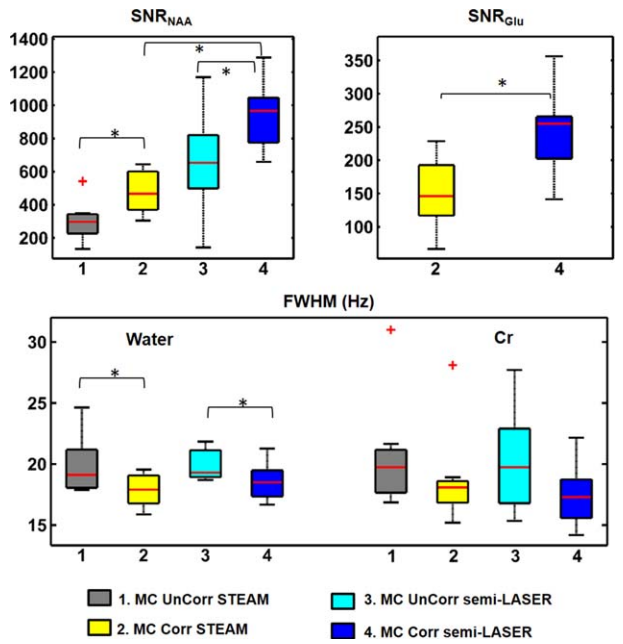

FIG. 5. Cohort comparison of SNR for NAA (SNR_{NAA}) and FWHM of water and creatine before and after the described reference correction scheme for both MC-STEAM and MC-semi-LASER. In addition, SNR_{Glu} is illustrated after the described reference correction scheme for both MC-STEAM and MC-semi-LASER. Red horizontal lines indicate median values; error bars illustrate the range of values; and red crosses show outliers. Statistically significant differences corrected for multiple comparisons are displayed with asterisks (*$P < 0.05$).

for higher B_1^+ amplitudes (Fig. 2). Simulations showed that lower B_1^+ fields are required for longer pulse durations to achieve a given BW_{inv}. For a frequency factor equal to 1 (left part of Fig. 2), which corresponds to the pulse settings used in (18), a notably high B_1^+ is demanded to obtain a BW_{inv} sufficiently large for spectroscopic applications at 9.4T. BW_{trans} ranges from 60 to 80 Hz (0.15 to 0.2 ppm at 9.4T) for durations longer than 22 ms and varies slightly with alterations of B_1^+. Finally, the experimental results from a spectroscopic phantom using a parameter set suitable for the chosen experimental setup ($B_{1(min)} =$ 22 μT, pulse duration = 23 ms, freq. factor = 2, $|Freq_{invP}| = 325$ Hz) verified the simulations and resulted in high-quality phantom spectra (Supporting Fig. S2).

Sequence Testing

Due to high coil efficiency and strong gradient system performance, a short TE of 8 ms for MC-STEAM and 24 ms for MC-semi-LASER, respectively, could be achieved (Fig. 3). In particular, the duration of the Hamming-filtered sinc pulses used for slice selection in both localization techniques ranged from 1 to 1.2 ms, which in turn resulted in an excitation bandwidth of about 8 kHz. As a result, CSD was 5% per ppm for each voxel dimension. As a consequence, because the reference frequency was set at 2.3 ppm, CSD for the myo-Inositol peak at 4.05 ppm was 9% (1.8 mm), for the lactate peak at 1.31 was 5% (1 mm), and for the NAA downfield peak at 7.82 ppm was 28% (5.6 mm).

In Vivo Data: Effect of Reference Correction

Physiological motion during the scan led to frequency and phase fluctuations of the acquired signal (Fig. 4). If uncorrected (MC Uncorr), spectra exhibit significant water residuals and baseline distortion. However, appropriate previous alignment of different MC metabolite signals gives rise to spectra with a flat baseline and water peak residual in the order of the NAA amplitude (Fig. 4, bottom panel).

MC-semi-LASER results show that average SNR_{NAA} for MC Corr and MC Uncorr are 940 and 657, respectively, with a statistically significant improvement ($P < 0.05$) of 30% (Fig. 5). For MC-STEAM data, the mean SNR_{NAA} is 477 for MC Corr and 301 for MC Uncorr, with a similar improvement of 37% ($P < 0.05$) for MC Corr. In addition, a doubling of the SNR_{NAA} for MC-semi-LASER in comparison with the MC-STEAM sequence is observed ($P < 0.05$). Moreover, SNR_{Glu} of MC Corr data for MC-semi-LASER and MC STEAM are 243 and 151, respectively, resulting in statistically significant increase ($P < 0.05$) of 60%. In the case of MC-semi-LASER,

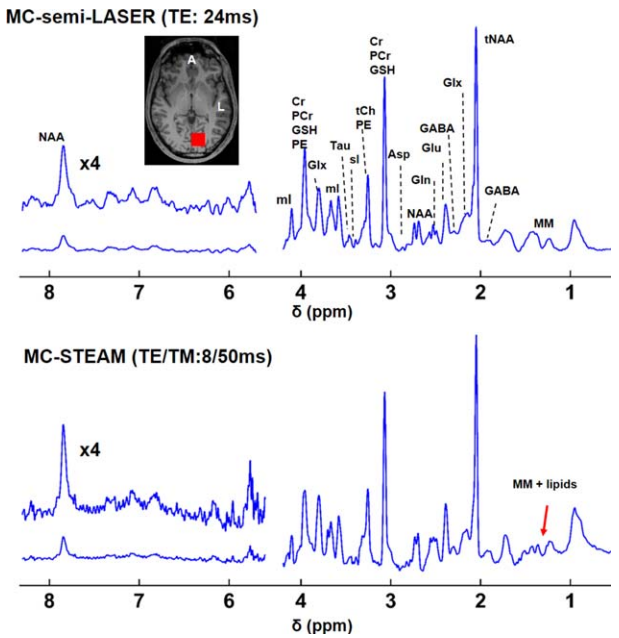

FIG. 6. Sample spectra acquired from the same volunteer using MC-semi-LASER and MC-STEAM from a voxel in the occipital lobe (red square; 96 averages, $2 \times 2 \times 2$ cm^3). Both the upfield and downfield parts of the spectrum are detected with good quality using both sequences. The red arrow indicates some contributions in the MC-STEAM spectrum likely to arise from outer-volume lipid signals. Spectra have been filtered for illustration purposes using a Voigt filter (Gaussian part: 50 ms, Lorentzian part: 7.8 Hz). Asp, aspartate; Cr, creatine; GABA, γ-aminobutyric acid; Gln, glutamine; Glu, glutamate; Glx, Glu + Gln; GPC, glycerophosphocholine; GSH, glutathione; Lac, lactate; ml, myo-Inositol; MM, macromolecules; NAA, N-acetylaspartate; NAAG, N-acetylaspartylglutamate; PCh, phophsocholine; PCr, phoshocreatine; PE, phosphorylethanolamine and ethanolamine; sI, scyllo-inositol; Tau, taurine; tCh, PCh + GPC; tNAA, NAA + NAAG.

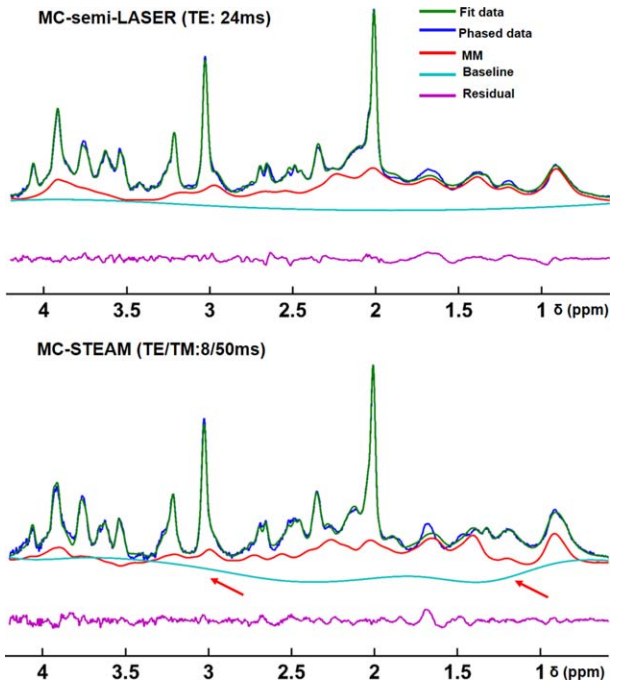

FIG. 7. LCModel fitting results of the same MC-semi-LASER (TE: 24 ms) and MC-STEAM (TE/TM: 8/50 ms) spectra displayed in Figure 8. The red arrows indicate baseline distortion in the MC-STEAM spectrum due to some lipid contamination. For both cases, the voxel size was $2 \times 2 \times 2\,cm^3$ and 96 averages were acquired. The basis set included the following 18 metabolites: N-acetylaspartate, N-acetylaspartylglutamate, glutamine, glutamate, aspartate, γ-aminobutyric acid, glycine, glucose, phosphorylethanolamine, glycerophosphocholine, glutathione, phoshocreatine, creatine, choline, phophsocholine, myo-inositol, scyllo-inositol, lactate, and a measured macromolecular (MM) baseline.

frequency alignment reduces the FWHM of the water and Cr peaks by 1.5 Hz ($P < 0.05$) and 3.5 Hz ($P < 0.05$), respectively, whereas for MC-STEAM the improvements are 2.0 Hz and 1.8 Hz, although no statistically significant difference was observed due to multiple comparisons correction.

MRS Data Quantification

MRS spectra from the GM voxel of a volunteer, as acquired with MC-semi-LASER and MC-STEAM, are illustrated in Figure 6. Results demonstrate the higher SNR of MC-semi-LASER data, despite the longer TE. The MC-STEAM spectrum also features some slight contributions that are likely to arise from outer-volume lipid signals (highlighted by arrow in the Fig. 6). The LCModel fit shows an almost flat spline baseline and a well-fitted macromolecular template for MC-semi-LASER, whereas the MC-STEAM fit features a more varying spline baseline (Fig. 7).

Frequency resolution in both localization schemes enables the quantification of 18 metabolite peaks (Fig. 8), with Cramer-Rao lower bounds (CRLBs) lower than or equal to 100%, in both the upfield and downfield parts of the spectrum (Supporting Fig. S3). In addition, clear differences between the two sequences are observed regarding the shape of the aspartate moiety peaks of NAA at 2.67 ppm and 2.48 ppm due to J-evolution.

Absolute concentrations (not corrected for T_2 relaxation) for 18 metabolites, illustrated in Figure 8, do not demonstrate any statistically significant difference after multiple comparisons correction.

CRLB values are systematically smaller for MC-semi-LASER than for MC-STEAM, however, without any statistically significant difference after multiple comparisons correction (Supporting Fig. S3) (Supporting Table S1). The average percentages of GM, WM, and CSF within the voxel were 39.5%, 57%, and 3.5%, respectively, which corresponds to a water content of 73.6% using the assumptions mentioned in Methods. Absolute concentrations values illustrated in Figure 8 also are reported in the Supporting Table S2.

DISCUSSION

In this study, two new sequences utilizing the MC technique, MC-STEAM, and MC-semi-LASER are introduced, implemented with the setup of optimized RF coils, and used to measure metabolite content from human brain

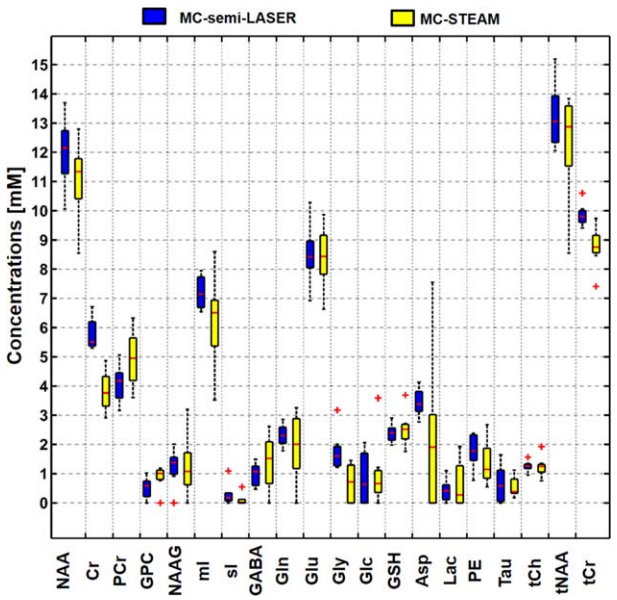

FIG. 8. Absolute concentration (not corrected for relaxation) values for 18 metabolites from spectra acquired from eight volunteers (n = 8) with MC-semi-LASER and MC-STEAM. Red lines indicate median values (50% quartile), whereas the bottom and top box boundaries demonstrate 25% (Q1) and 75% (Q3) quartile, respectively. Small red (+) indicate data points beyond the whiskers (outliers). A statistical comparison was performed using a two-tailed Wilcoxon signed rank test for equal and matched sample size. No statistically significant difference was observed after applying the Holm-Bonferroni method for multiple comparisons correction. Median, Q1, and Q3 values for metabolite levels are reported in Supporting Table S2. Asp, aspartate; Cr, creatine; GABA, γ-aminobutyric acid; Glc, glucose; Gly, glycine; Gln, glutamine; Glu, glutamate; GPC, glycerophosphocholine; GSH, glutathione; Lac, lactate; NAA, N-acetylaspartate; NAAG, N-acetylaspartylglutamate; mI, myo-Inositol; PCr, phoshocreatine; PE, phosphorylethanolamine and ethanolamine; sI, scyllo-inositol; Tau, taurine; tCh, PCh + GPC; tCr, Cr+ PCr; tNAA, NAA + NAAG.

gray matter at 9.4T. Moreover, a detailed description including experimental and simulation results is given for optimization of the InvP for MC at very high field.

Results demonstrate that utilization of three coil elements with appropriate phase and power distribution at the location of the examined voxel (see anatomical image in Fig. 6) yield high and fairly homogeneous B_1^+ fields (48 μT). Efficient B_1^+ is necessary at UHF for the implementation of adiabatic MC pulses, for reduced CSD, and for short TE. The same coil along with different phase increments and power distribution can be utilized for the acquisition of spectra from other locations, such as parietal white matter (39,53).

Simulations highlight the demand for higher B_1^+ fields and longer pulse durations to achieve a large-enough inversion bandwidth. This outcome is in agreement with the adiabatic principle (35) and previous study results (34). The simulations also show that, for the achievement of an efficient inversion bandwidth with pulse durations of 20 to 25 ms, strong B_1^+ fields ($> 20\,\mu T$) and large frequency sweep ranges are required at UHF.

Frequency and phase alignment of acquisitions strongly affects the resulting linewidths and SNR of the final spectrum. MC-corrected data for both sequences exhibits an increase of SNR for NAA by 45% and a decrease of the water FWHM of about 2 Hz. This finding confirms the outcomes of a previous MC study in the human spinal cord at 3T (24). For WS single-scan data, frequency and phase correction routinely are performed using the NAA peak (9,54–56); however, this method could not be investigated in this study because a fair comparison would necessitate water-suppressed data using WS scheme optimized for B1 + inhomogeneity. Using MC-semi-LASER results in the doubling of the SNRNAA compared to MC-STEAM. This SNR benefit is inherent in the spin echo-based LASER techniques in comparison to STEAM and was not substantially compromised by the somewhat longer but still short TE in semi-LASER. The gain of SNR between semi-LASER and STEAM also has been reported in studies at 4T and 7T (4,15). Moreover, SNRGlu increases by 60% in the case of MC-semi-LASER (TE = 24 ms) in comparison to MC-STEAM (TE = 8 ms), despite the longer TE. This gain is the result of the full signal acquisition within semi-LASER and of the similar J-evolution of Glu in both methods because semi-LASER behaves as a Carr-Purcell sequence (14) and J-coupled metabolites were found to effectively evolve with a free evolution time of about 6.5 ms. Of note, the accuracy of the estimated metabolite SNR values is limited by spectral overlap with the underlying macromolecule signals.

Both MC-semi-LASER and MC-STEAM acquisitions provide well-resolved spectra in which 18 metabolites are detected. The quality of the MC-STEAM spectra is equivalent to published data using STEAM along with OVS at 9.4T (9). In addition, the average FWHM of the water peak for MC-semi-LASER and MC-STEAM in this study are 18.6 ± 0.5 Hz (n = 8) and 17.9 ± 0.5 Hz (n = 8), respectively, whereas in (9) a mean water linewidth of 15.7 ± 1.3 (n = 6) was reported. This variation of both mean values and standard deviations can be assigned to the different B_0 shimming system (maximum amplitude for each shimming term), the different voxel location within the occipital lobe, and to the different calculation of FWHM. In this study, the FWHM of water was measured after averaging of the 96 acquisitions for each volunteer.

Although in this study shim variations between acquisitions were found to be minor, larger frequency and shim fluctuations related to significant displacement of the voxel severely could affect the resulting spectra because MC is a subtraction-based scheme (57). In particular, large voxel shifts would result in water signals with different shape and size acquired from different locations. As a consequence, significant water residuals might be unavoidable in the metabolite spectra after signal subtraction. However, such degraded subtraction also could be largely prevented by elimination of outliers that can easily be detected based on the large water signal (28).

Direct comparison of quantification results for the reported 18 metabolites (Fig. 8) with other published studies at 7T and 9.4T (4,5,58–60) is not trivial due to three reasons: Firstly, many of the previously reported absolute concentration levels either do not include correction for tissue composition, or a water content of 80% is assumed. In this work, the mean percentages of the different tissue types correspond to a water content of 73.6%. As a result, the currently reported values are expected to be about 7% lower compared to the case in which one assumes 80% water content. Secondly, in this study concentration levels are reported in mM (moles per tissue volume) and not in moles per tissue weight (μmol/g), which introduces another systematic difference of about 5%. Finally, relaxation correction is usually avoided in cases of long TR (> 4,000 ms) and short TE (< 30 ms). However, at UHF this assumption may introduce quantification errors due to a shorter T_2 and longer T_1 of the metabolites. Moreover, different T_2 values of metabolites are expected between the STEAM and semi-LASER techniques because the latter behaves like a Carr-Purcell spin-echo sequence and longer T_2 values have been reported (14,58,59,61). Thus, interpretation of the current concentrations must be performed with care. However, a comparison with a semi-LASER study at 7T (62) shows good agreement in most of the metabolites' concentrations except myo-inositol, total creatine (tCr), and glycine. This difference can be assigned to the shorter T_2 relaxation times at 9.4T, as well as to potential lipid contamination due to the absence of OVS in this study.

CRLBs of MC-semi-LASER data are systematically lower than those for MC-STEAM (Supporting Fig. S3). This improvement of quantification is achieved due to the increased SNR in MC-semi-LASER in comparison with MC-STEAM. Moreover, the dissimilarity in CRLBs also arises because of LCModel noise-level estimation using the residuals and not true noise outside the spectrum. Lower lipid contamination in MC-semi-LASER also is highlighted from the fitting outcomes in which a basis set in combination with a measured macromolecular baseline results in a flat spline fit. Concentration levels for all the metabolites measured with both sequences do not demonstrate any statistically significant difference

after multiple comparisons correction. However, Figure 8 indicates a difference in the concentrations of Cr and tCr between the two methods. This variation can be assigned to the small lipid contamination in MC-STEAM, which in turn results in a non-flat spline fit under the Cr peak at 3 ppm, as illustrated in Figure 7.

To conclude, this is the first study in which semi-LASER is applied at 9.4T and the MC technique is implemented on a whole body 9.4T UHF system. The outcomes of this work highlight the advantages of semi-LASER compared to STEAM in terms of excitation profile, and indicate the importance of frequency and phase alignment for MRS at 9.4T in the human brain. MC-semi-LASER is an attractive choice for measurements at UHF because it enables the constructive summation of the different FIDs without the need for additional water reference scans for frequency alignment and eddy current correction, optimized OVS, or lengthy water suppression schemes. However, despite several disadvantages of MC-STEAM, it remains useful for measurements in which a short TE or TR is required due to the small number of pulses. In fact, MC-STEAM already has been used in a preliminary study for the measurement of the magnetization exchange between water and downfield metabolites in the human brain at 9.4T (53). Furthermore, MC-semi-LASER was utilized in pilot studies for the characterization of the macromolecular baseline at 9.4T (39) and for functional MRS during visual stimulation at 9.4T, enabling the synchronous detection of functional changes of water and metabolites signals (29).

ACKNOWLEDGMENT

The authors of this study would like to thank Nicole Fichtner and Liam Connah for proofreading this paper, as well as Dr. Erin McMillan and Dr. Andreas Hock for their helpful discussions and suggestions.

REFERENCES

1. Bandettini PA, Bowtell R, Jezzard P, Turner R. Ultrahigh field systems and applications at 7 T and beyond: progress, pitfalls, and potential. Magn Reson Med 2012;67:317–321.
2. Ugurbil K, Adriany G, Andersen P, et al. Ultrahigh field magnetic resonance imaging and spectroscopy. Magn Reson Imaging 2003;21:1263–1281.
3. Hong ST, Balla DZ, Shajan G, Choi C, Ugurbil K, Pohmann R. Enhanced neurochemical profile of the rat brain using in vivo (1)H NMR spectroscopy at 16.4 T. Magn Reson Med 2011;65:28–34.
4. Boer VO, van Lier AL, Hoogduin JM, Wijnen JP, Luijten PR, Klomp DW. 7-T (1) H MRS with adiabatic refocusing at short TE using radiofrequency focusing with a dual-channel volume transmit coil. NMR Biomed 2011;24:1038–1046.
5. Mekle R, Mlynarik V, Gambarota G, Hergt M, Krueger G, Gruetter R. MR spectroscopy of the human brain with enhanced signal intensity at ultrashort echo times on a clinical platform at 3T and 7T. Magn Reson Med 2009;61:1279–1285.
6. Pfeuffer J, Tkac I, Provencher SW, Gruetter R. Toward an in vivo neurochemical profile: quantification of 18 metabolites in short-echo-time (1)H NMR spectra of the rat brain. J Magn Reson 1999;141:104–120.
7. Tkac I, Andersen P, Adriany G, Merkle H, Ugurbil K, Gruetter R. In vivo 1H NMR spectroscopy of the human brain at 7 T. Magn Reson Med 2001;46:451–456.
8. Vaughan T, DelaBarre L, Snyder C, et al. 9.4T human MRI: preliminary results. Magn Reson Med 2006;56:1274–1282.
9. Deelchand DK, Van de Moortele PF, Adriany G, Iltis I, Andersen P, Strupp JP, Vaughan JT, Ugurbil K, Henry PG. In vivo 1H NMR spectroscopy of the human brain at 9.4 T: initial results. J Magn Reson 2010;206:74–80.
10. Fuchs A, Luttje M, Boesiger P, Henning A. SPECIAL semi-LASER with lipid artifact compensation for 1H MRS at 7 T. Magn Reson Med 2013;69:603–612.
11. Frahm J, Bruhn H, Gyngell ML, Merboldt KD, Hanicke W, Sauter R. Localized high-resolution proton NMR spectroscopy using stimulated echoes: initial applications to human brain in vivo. Magn Reson Med 1989;9:79–93.
12. Scheenen TW, Klomp DW, Wijnen JP, Heerschap A. Short echo time 1H-MRSI of the human brain at 3T with minimal chemical shift displacement errors using adiabatic refocusing pulses. Magn Reson Med 2008;59:1–6.
13. van de Bank BL, Emir UE, Boer VO, van Asten JJ, Maas MC, Wijnen JP, Kan HE, Oz G, Klomp DW, Scheenen TW. Multi-center reproducibility of neurochemical profiles in the human brain at 7 T. NMR Biomed 2015;28:306–316.
14. Allerhand A, Thiele E. Analysis of Carr-Purcell spin-echo NMR experiments on multiple-spin systems. II. The effect of chemical exchange. J Cheml Phys 1966;45:902–916.
15. Oz G, Tkac I. Short-echo, single-shot, full-intensity proton magnetic resonance spectroscopy for neurochemical profiling at 4 T: validation in the cerebellum and brainstem. Magn Reson Med 2011;65:901–910.
16. Boer VO, Klomp DW, Juchem C, Luijten PR, de Graaf RA. Multislice (1)H MRSI of the human brain at 7 T using dynamic B(0) and B(1) shimming. Magn Reson Med 2012;68:662–670.
17. Emir UE, Auerbach EJ, Van De Moortele PF, Marjanska M, Ugurbil K, Terpstra M, Tkac I, Oz G. Regional neurochemical profiles in the human brain measured by (1)H MRS at 7 T using local B(1) shimming. NMR Biomed 2012;25:152–160.
18. Dreher W, Leibfritz D. New method for the simultaneous detection of metabolites and water in localized in vivo 1H nuclear magnetic resonance spectroscopy. Magn Reson Med 2005;54:190–195.
19. de Graaf RA, Sacolick LO, Rothman DL. Water and metabolite-modulated MR spectroscopy and spectroscopic imaging. In Proceedings of the 14th Annual Meeting of ISMRM, Seattle, Washington, USA, 2006. p. 3063.
20. MacMillan EL, Chong DG, Dreher W, Henning A, Boesch C, Kreis R. Magnetization exchange with water and T_1 relaxation of the downfield resonances in human brain spectra at 3.0 T. Magn Reson Med 2011;65:1239–1246.
21. Giapitzakis IA, Shao T, Avdievich N, Kreis R, Henning A. Optimisation of asymmetric adiabatic pulses for single voxel metabolite cycled 1H-MRS in the human brain at 9.4 Tesla. In Proceedings of the 22nd Annual Meeting of ISMRM, Milan, Italy, 2014. p. 2895.
22. MacMillan EL, Kreis R, Fuchs A, Versluis MJ, Boesch C, Boesiger P, Henning A. New technique for metabolite cycled non-water-suppressed proton spectroscopy in the human brain at 7T In Proceedings of the 19th Annual Meeting of ISMRM, Montréal, Canada, 2011. p. 666.
23. Hock A, Henning A, Boesiger P, Kollias SS. (1)H-MR spectroscopy in the human spinal cord. AJNR Am J Neuroradiol 2013;34:1682–1689.
24. Hock A, MacMillan EL, Fuchs A, Kreis R, Boesiger P, Kollias SS, Henning A. Non-water-suppressed proton MR spectroscopy improves spectral quality in the human spinal cord. Magn Reson Med 2013;69:1253–1260.
25. Kreis R, Bolliger CS, MacMillan EL, Boettcher U, Boesch C. GABA editing without water suppression. In Proceedings of the 20th Annual Meeting of ISMRM, Melbourne, Australia, 2012. p. 1745.
26. MacMillan EL, Bolliger CS, Boesch C, Kreis R. Influence of muscle fiber orientation on water and metabolite relaxation times, #magnetization |transfer, and visibility in human skeletal muscle. Magn Reson Med 2016;75:1764–1770.
27. MacMillan EL, Boesch C, Kreis R. Magnetization exchange observed in human skeletal muscle by non-water-suppressed proton magnetic resonance spectroscopy. Magn Reson Med 2013;70:916–924.
28. Döring A, Brandejsky V, Boesch C, Kreis R. Diffusion weighted MR spectroscopy without water suppression allows to use water as inherent reference signal to correct for motion-related signal drop. In Proceedings of the 24th Annual Meeting of ISMRM, Singapore, 2016. p. 2395.
29. Giapitzakis IA, Avdievich N, Manohar SM, Fichtner N, Kreis R, Henning A. Functional Magnetic Resonance Spectroscopy (fMRS)

using metabolite cycled semi-LASER at 9.4T: a pilot study. In Proceedings of the 25th Annual Meeting of ISMRM, Honolulu, Hawaii, USA, 2017. p. 277.
30. Provencher SW. Automatic quantitation of localized in vivo 1H spectra with LCModel. NMR Biomed 2001;14:260–264.
31. Avdievich N, Giapitzakis IA, Henning A. Optimization of the receive performance of a tight-fit reansceiver phased array for human brain imaging at 9.4T. In Proceedings of the 25th Annual Meeting of ISMRM, Honolulu, Hawaii, USA, 2017. p. 2575.
32. Hoffmann J, Henning A, Giapitzakis IA, Scheffler K, Shajan G, Pohmann R, Avdievich NI. Safety testing and operational procedures for self-developed radiofrequency coils. NMR Biomed 2016;29:1131–1144.
33. Avdievich N, Walzog J, Steffen T, Henning A. Development of a low cost multi-channel tune and match device for transceiver arrays at high magnetic fields. In Proceedings of the 32nd Annual Scientific Meeting of the European Society of Magnetic Reconance in Medicine and Biology, Edinburgh, UK, 2015. p. S445.
34. Hwang TL, van Zijl PC, Garwood M. Asymmetric adiabatic pulses for NH selection. J Magn Reson 1999;138:173–177.
35. Garwood M, DelaBarre L. The return of the frequency sweep: designing adiabatic pulses for contemporary NMR. J Magn Reson 2001;153:155–177.
36. Mugler JP 3rd, Brookeman JR. Three-dimensional magnetization-prepared rapid gradient-echo imaging (3D MP RAGE). Magn Reson Med 1990;15:152–157.
37. Gruetter R, Tkac I. Field mapping without reference scan using asymmetric echo-planar techniques. Magn Reson Med 2000;43:319–323.
38. Versluis MJ, Kan HE, van Buchem MA, Webb AG. Improved signal to noise in proton spectroscopy of the human calf muscle at 7 T using localized B1 calibration. Magn Reson Med 2010;63:207–211.
39. Giapitzakis IA, Kreis R, Henning A. Characterization of the macromolecular baseline with a metabolite-cycled double-inversion recovery sequence in the human brain at 9.4T. In Proceedings of the 24th Annual Meeting of ISMRM, Singapore, 2016. p. 0016.
40. Cudalbu C, Mlynarik V, Gruetter R. Handling macromolecule signals in the quantification of the neurochemical profile. J Alzheimers Dis 2012;31(suppl 3):S101–S115.
41. Klose U. In vivo proton spectroscopy in presence of eddy currents. Magn Reson Med 1990;14:26–30.
42. Bydder M, Hamilton G, Yokoo T, Sirlin CB. Optimal phased-array combination for spectroscopy. Magn Reson Imaging 2008;26:847–850.
43. Vanhamme L, Sundin T, Hecke PV, Huffel SV. MR spectroscopy quantitation: a review of time-domain methods. NMR Biomed 2001;14:233–246.
44. Smith SA, Levante TO, Meier BH, Ernst RR. Computer simulations in magnetic resonance. An object-oriented programming approach. J Magn Reson Ser A 1994;106:75–105.
45. Govind V, Young K, Maudsley AA. Corrigendum: proton NMR chemical shifts and coupling constants for brain metabolites. Govindaraju V, Young K, Maudsley AA, NMR Biomed. 2000; 13: 129–153. NMR Biomed 2015;28:923–924.
46. Govindaraju V, Young K, Maudsley AA. Proton NMR chemical shifts and coupling constants for brain metabolites. NMR Biomed 2000;13:129–153.
47. Kreis R, Bolliger CS. The need for updates of spin system parameters, illustrated for the case of gamma-aminobutyric acid. NMR Biomed 2012;25:1401–1403.
48. Giapitzakis IA, Henning A. Basis set optimization for quantification of semi-LASER at 9.4T under consideration of CP effect, relaxation and J-coupling strength In Proceedings of the 25th Annual Meeting of ISMRM, Honolulu, Hawaii, USA, 2017. p. 453.
49. Gasparovic C, Song T, Devier D, Bockholt HJ, Caprihan A, Mullins PG, Posse S, Jung RE, Morrison LA. Use of tissue water as a concentration reference for proton spectroscopic imaging. Magn Reson Med 2006;55:1219–1226.
50. Ernst T, Kreis R, Ross BD. Absolute quantitation of water and metabolites in the human brain. I. Compartments and Water. J Magn Reson Ser B 1993;102:1–8.
51. Kreis R. The trouble with quality filtering based on relative Cramér-Rao lower bounds. Magn Reson Med 2016;75:15–18.
52. Rodgers CT, Robson MD. Receive array magnetic resonance spectroscopy: whitened singular value decomposition (WSVD) gives optimal Bayesian solution. Magn Reson Med 2010;63:881–891.
53. Fichtner N, Giapitzakis IA, Avdievich N, Mekle R, Zaldivar D, Henning A, Kreis R. Magnetization exchange between water and downfield metabolites in human brain at 9.4T. In Proceedings of the 25th Annual Meeting of ISMRM, Honolulu, Hawaii, USA, 2017. p. 5466.
54. Oz G, Tkac I, Charnas LR, Choi IY, Bjoraker KJ, Shapiro EG, Gruetter R. Assessment of adrenoleukodystrophy lesions by high field MRS in non-sedated pediatric patients. Neurology 2005;64:434–441.
55. Mangia S, Tkac I, Gruetter R, Van de Moortele PF, Maraviglia B, Ugurbil K. Sustained neuronal activation raises oxidative metabolism to a new steady-state level: evidence from 1H NMR spectroscopy in the human visual cortex. J Cereb Blood Flow Metab 2007;27:1055–1063.
56. Lin Y, Stephenson MC, Xin L, Napolitano A, Morris PG. Investigating the metabolic changes due to visual stimulation using functional proton magnetic resonance spectroscopy at 7 T. J Cereb Blood Flow Metab 2012;32:1484–1495.
57. Wilm BJ, Duerst Y, Dietrich BE, Wyss M, Vannesjo SJ, Schmid T, Brunner DO, Barmet C, Pruessmann KP. Feedback field control improves linewidths in in vivo magnetic resonance spectroscopy. Magn Reson Med 2014;71:1657–1662.
58. Bartha R, Michaeli S, Merkle H, Adriany G, Andersen P, Chen W, Ugurbil K, Garwood M. In vivo 1H2O T2 + measurement in the human occipital lobe at 4T and 7T by Carr-Purcell MRI: detection of microscopic susceptibility contrast. Magn Reson Med 2002;47:742–750.
59. Deelchand DK, Henry PG, Marjanska M. Effect of Carr-Purcell refocusing pulse trains on transverse relaxation times of metabolites in rat brain at 9.4 Tesla. Magn Reson Med 2015;73:13–20.
60. Marjanska M, Auerbach EJ, Valabregue R, Van de Moortele PF, Adriany G, Garwood M. Localized 1H NMR spectroscopy in different regions of human brain in vivo at 7 T: T2 relaxation times and concentrations of cerebral metabolites. NMR Biomed 2012;25:332–339.
61. Michaeli S, Garwood M, Zhu XH, DelaBarre L, Andersen P, Adriany G, Merkle H, Ugurbil K, Chen W. Proton T2 relaxation study of water, N-acetylaspartate, and creatine in human brain using Hahn and Carr-Purcell spin echoes at 4T and 7T. Magn Reson Med 2002;47:629–633.
62. Penner J, Bartha R. Semi-LASER 1 H MR spectroscopy at 7 Tesla in human brain: metabolite quantification incorporating subject-specific macromolecule removal. Magn Reson Med 2014;74:4–12.

SUPPORTING INFORMATION

Additional supporting information may be found in the online version of this article.

Fig. S1. RF coil setup and resulting B_1^+ profile. A) Coil and 3-way power splitter. B) A phantom is placed in the coil, representing subject position. Red dotted circles illustrate coil loops used for transmission. Only the 3 bottom coil elements are connected with the power splitter. C) B_1^+ profile (in μT/V) produced by the three coil elements (phantom measurement). The gray ellipses mark the coil loops. The numbers next to each loop indicate the phase and the delivered power respectively used for each individual coil element. Maximum value of B_1^+ was 0.16 μT/V. Given that the maximum voltage allowed by our RF system amplifiers are 450 V, a maximum B_1^+ value of 48 uT can be achieved.

Fig. S2. Phantom spectroscopy measurements where the inversion pulse was implemented in the mixing period of a STEAM sequence. The methine quartet of lactate at 4.09 is easily observed. The characteristics of the asymmetric adiabatic pulse used for the experiment were $B_{1(min)}$: 22 μT, pulse duration: 23 ms, freq. factor: 2, $|Freq_{invP}|$: 325 Hz. The experimental results verified the simulations and resulted in high quality phantom spectra.

Fig. S3. CRLB values for 18 metabolites from spectra acquired from eight volunteers (n = 8) with MC-semi-LASER and MC-STEAM. Red lines indicate median values (50% quartile) while the bottom and top box boundaries demonstrate 25% (Q1) and 75% (Q3) quartile respectively. A statistical comparison was performed using a two-tailed Wilcoxon signed rank test for equal and matched sample size. No statistically significant difference was observed after applying the Holm-Bonferroni method for multiple comparisons correction. Median, Q1 and Q3 values for CRLB values are reported in the Supporting Table S1.

Table S1. CRLB values [mM] for 18 metabolites from spectra acquired from eight volunteers (n = 8) with MC-semi-LASER and MC-STEAM. Results are reported in quartiles.

Table S2. Absolute concentrations [mM] for 18 metabolites from spectra acquired from eight volunteers (n = 8) with MC-semi-LASER and MC-STEAM. Results are reported in quartiles.

FULL PAPER

Magnetic Resonance in Medicine 00:00–00 (2018)

Characterization of Macromolecular Baseline of Human Brain Using Metabolite Cycled Semi-LASER at 9.4T

Ioannis-Angelos Giapitzakis,[1,2†]* Nikolai Avdievich,[1,3†] and Anke Henning[1,3]

Purpose: Macromolecular resonances (MM) arise mainly from cytosolic proteins and overlap with metabolites, influencing metabolite quantification. Macromolecules can serve as valuable biomarkers for diseases and pathologies. The objectives of this study were to characterize MM at 9.4T in the human brain (occipital and left parietal lobe) and to describe the RF coil setup used for MM acquisition in the two regions.

Methods: An adiabatic inversion pulse was optimised for metabolite nulling at 9.4T using double inversion recovery and was combined for the first time with metabolite cycled (MC) semi-LASER and appropriate coil configuration. MM spectra (seven volunteers) from two brain locations were averaged and smoothed creating MM templates, which were then parametrized using simulated Voigt-shaped lines within LCModel. Quantification was performed on individual data sets, including corrections for different tissue composition and the T_1 and T_2 relaxation of water.

Results: Our coil configuration method resulted in efficient B_1^+ ($>30\,T/\sqrt{kW}$) for both brain regions. The 15 MM components were detected and quantified in MM baselines of the two brain areas. No significant differences in concentration levels of MM between different regions were found. Two new MM peaks were reported (M7 & M8).

Conclusion: Double inversion, which was combined with MC semi-LASER, enabled the acquisition of high spectral resolution MM spectra for both brain regions at 9.4T. The 15 MM components were detected and quantified. Two new MM peaks were reported for the first time (M7 & M8) and preliminarily assigned to β-methylene protons of aspartyl-groups.

Magn Reson Med 000:000–000, 2018. © 2018 International Society for Magnetic Resonance in Medicine.

Key words: MC semi-LASER; macromolecular baseline; metabolite cycling; MR spectroscopy; ultra high field

INTRODUCTION

Macromolecular resonances (MM) arise mainly from cytosolic proteins and overlap with resonance lines of small metabolites in proton MR spectroscopy (^{1}H-MRS) (1–5). Consequently, MM can influence the precision and the accuracy of metabolite quantification due to baseline distortion. This effect becomes even more severe in the case of short echo times (TEs) due to the more pronounced presence of macromolecules (4,6).

Because of their short transverse relaxation time constant (T_2), MM appear on ^{1}H-MRS spectra as an underlying baseline consisting of several broad peaks. Initially, these broad resonances were attributed to lipids (7). However, later studies reported that polypeptides might contribute significantly to the observed ^{1}H-MRS baseline spectrum (3,8).

In 1993, Behar and Ogino showed that the nonmetabolite resonances observed in the ^{1}H-NMR spectrum of the rat brain tissue are the result of cytosolic proteins and assigned them to specific amino acids (e.g., alanine, valine, threonine) (1). One year later, they carried out a similar study on the human brain in which they used an inversion recovery (IR) experiment to null the metabolites' signal using the shorter longitudinal relaxation time (T_1) of MM in comparison with metabolites (4). Metabolite nulling using a single IR works efficiently under the assumption that metabolite resonances have similar T_1. However, in vivo, protons of methyl groups demonstrate longer T_1 than other protons (5). For this reason, Hofmann et al. proposed a metabolite nulling scheme based on a series of saturation recovery scans, which was less sensitive to the T_1 variations of different metabolites (9). A similar approach exploiting double IR had been previously implemented for the reduction of static tissue signal in angiograms (10).

In addition to their significance regarding the quantification of metabolite levels, macromolecules can potentially be valuable biomarkers for several diseases and pathologies (11–17). Several studies have investigated potential differences in MM between different age groups and brain regions. However, many of the reported results are contradictory to each other. Particularly, early studies at 3T demonstrated differences between various areas of the brain indicating that a region-specific MM baseline was required for quantification (9,18). Nevertheless, current studies using ultra high fields (UHF) scanners (≥ 7T) demonstrated that a general MM baseline might be adequate for the quantification of the neurochemical profile of different brain regions because no significant differences in MM components of the various regions were detected (6,19).

Moreover, the introduction of UHF enables the detection of up to 18 metabolites both in human and rodent brains (20–24) due to the increase in the signal-to-noise ratio (SNR) and higher frequency dispersion. This

[1]High-Field Magnetic Resonance, Max Planck Institute for Biological Cybernetics, Tübingen, Germany.

[2]IMPRS for Cognitive & Systems Neuroscience, Tübingen, Germany.

[3]Institute of Physics, University of Greifswald, Greifswald, Germany.

Grant sponsor: the European Social Fund and national funds; Grant number: NSRF 2007-2013; Grant sponsor: the Horizon 2020 CDS-QUAMRI grant; Grant number: 634541.

*Correspondence to: Ioannis-Angelos Giapitzakis M.Sc., High-Field Magnetic Resonance, Max Planck Institute for Biological Cybernetics, Tübingen, Germany. E-mail: ioannis.giapitzakis@tuebingen.mpg.de

†These authors contributed equally to this work.

Received 19 July 2017; revised 12 December 2017; accepted 12 December 2017

DOI 10.1002/mrm.27070

Published online 00 Month 2018 in Wiley Online Library (wileyonlinelibrary.com).

© 2018 International Society for Magnetic Resonance in Medicine

increased spectral resolution comes at the cost of more elaborate handling of the MM baseline for adequate quantification. More specifically, at low static magnetic fields, MM in ^{1}H-MRS spectra can be sufficiently handled by different fitting software (e.g., LCModel) (25) using polynomial functions (e.g., splines) or simulated macromolecule resonances (26,27). However, at higher fields, it has been shown that a measured MM baseline is required to be included in the fitting model due to the higher frequency resolution (5).

One technical challenge at UHF is the necessity of a high RF transmit (Tx) magnetic field, B_1^+. This requirement arises from the extensive usage of adiabatic full passage (AFP) pulses for the compensation of the increased B_1^+ inhomogeneity (28) and the need for high pulse bandwidths to counteract chemical shift displacement (CSD) artifacts, which are proportional to field strength, but inversely proportional to pulse bandwidth (29). Local transmit surface loops can be used for studies which deal with small regions of interest (ROIs) located peripherally (depth ~30–40 mm). This maximizes B_1^+ by focusing the entire RF power into a small volume. Alternatively, a multi-channel array circumscribing the entire head can be used (30). When the array is very well decoupled, it is possible to use only a few elements located closely to the ROI. This approach also allows the investigation of various ROIs located in different peripheral brain regions without the necessity of moving a subject out to switch the local transceiver array.

The purpose of this study was the quantitative characterization of the human brain macromolecular baseline of the occipital lobe (OccL) and the left parietal lobe (lPL) at 9.4T. For this purpose, a double IR scheme was combined, for the first time, with metabolite cycled semi-LASER (MC-semi-LASER) for metabolite nulling. A recent study demonstrated that MC-semi-LASER enables the improvement of SNR of the acquired spectra at 9.4T compared with MC STEAM, and 40% SNR improvement with frequency alignment versus no alignment (31). Additionally, a multi-channel array circumscribing the entire head (32–35) using appropriate phase arrangement and power distribution was used, enabling the production of high and efficient B_1^+ fields in both OccL and lPL. MM spectra were acquired from seven volunteers from these two brain regions, and volunteer's MM baselines were averaged and then smoothed using cubic splines creating a MM template which was parametrized using 15 simulated Voigt lineshapes within LCModel. Quantification was performed on individual data sets, including corrections for different tissue composition and the T_1 and T_2 relaxation of water.

METHODS

Technical Description and Subjects

All measurements were carried out on a Siemens 9.4T whole-body MRI scanner (Erlangen, Germany) equipped with a SC72 gradient system having a nominal maximal amplitude of 40 mT/m and a maximal slew rate of 200 T/m/s. A home-built proton coil circumscribing the head with eight transmit and sixteen receive channels was used (36). The coil was tuned and matched for each volunteer individually before the beginning of the experiment using a homebuilt tuning and matching box (37) and a portable probe tuning device (Morris Instruments Inc., Canada), ensuring minimal reflected power. Seven healthy volunteers (five males and two females, mean age: 28 ± 3 years) participated in this study. Written informed consent was given by all subjects before the examination, and the study was approved by the local ethics board.

Phased Array Design

The 16-element phased array consisted of 8 overlapped transceiver (TxRx) surface loops (10 cm in length) circumscribing a head, and 8 receive-only loops located at the center of each TxRx-loop perpendicularly to its surface, i.e., "vertical" loops (36). Decoupling of surface loops during both transmission and reception was provided entirely by geometrical overlapping of the loops. Vertical Rx-only loops were decoupled by preamplifier decoupling during reception and actively detuned during transmission (32). Excellent decoupling during transmission (-20 dB or better) was obtained for all surface loops (Supporting Fig. S1A, which is available online). Because all the elements were very well decoupled, any number of elements could be driven independently during transmission. More details on the array design are published elsewhere (36).

For the single voxel MRS experiments, only two to three coil elements adjacent to the ROI were used for transmission (Tx). For this purpose, we constructed two-way and unbalanced three-way Wilkinson splitters (Supporting Fig. S1C) enabling the driving of different coil elements. Specifically, for the excitation of an ROI in the OccL, a three-loop (loops 8, 1, and 2; Supporting Fig. S1B) mode was used (Fig. 1A), where 50% of the total power was delivered to the central coil (loop 1) and 25% to each of the other two (loops 2 and 8). Regarding the lPL region, a two-loop (loops 3 and 2) mode was used (Fig. 1B). For both 2-loop and 3-loop modes a 90° phase shift between the channels was used, which has been shown before to provide efficient local transmission (38). The Tx-efficiency and specific absorption rate (SAR) distributions for one-loop, two-loop, and three-loop modes, were also evaluated using electromagnetic (EM) simulations (Fig. 2). For comparison purposes, the circular polarized (CP) mode was also evaluated (Table 1). More details regarding the evaluation of Tx-efficiency and SAR of the coil are provided in the Supporting Information.

Development of the Double IR Technique for Metabolite Nulling at 9.4T

For the suppression of metabolite signals, a double IR technique was implemented and optimized because it is less susceptible to T_1 variations of metabolites (10). It was implemented in combination with a previously developed MC semi-LASER sequence (31). The inversion of the metabolites and MM was performed using an adiabatic HS1 pulse (39). More specifically, the amplitude modulation of the inversion pulse for metabolite nulling (InvP) with duration $T = 15$ ms, was constructed using a hyperbolic secant function $(sech(\beta \cdot (1 - 2t/T))$;

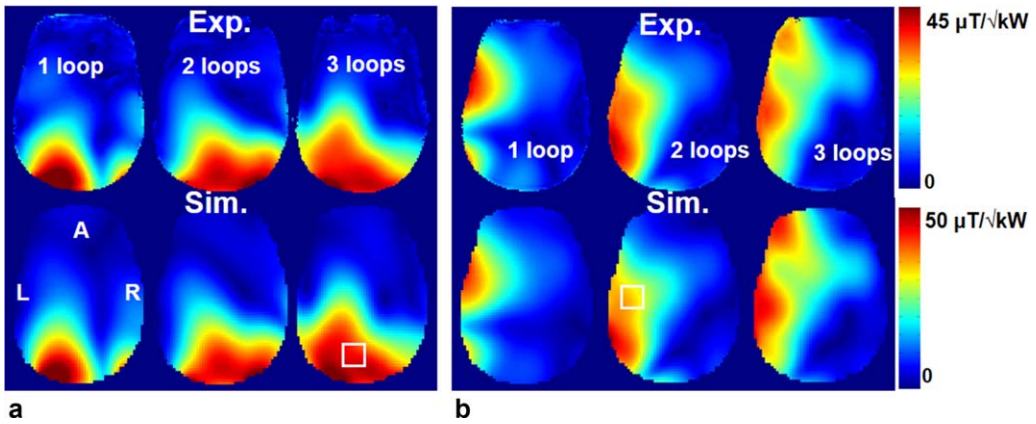

FIG. 1. **A,B**: Experimental (upper row) and EM simulated (bottom row) transversal B_1^+ maps (μT/√kW) obtained near the center of the array for the excitation of a voxel placed in occipital lobe and left parietal using the HS phantom and driving various number (1–3) of surface loops. For the occipital lobe **(A)**, in 1-loop, 2-loop, and 3-loop excitation modes the following loops were driven (for loop numbers, please refer to Supporting Fig. S1B): loop 1; loops 8 and 1; loops 8, 1, and 2, respectively. For left parietal lobe **(B)**, in 1-loop, 2-loop, and 3-loop excitation modes the following loops were driven (for loop numbers, please refer to Supporting Fig. S1B): loop 3; loops 2 and 3; loops 2, 3, and 4, respectively. In the 3-loop mode the RF power delivered to loop 1 (occipital lobe) or to loop 3 (left parietal lobe) was 2 times higher (output 1 in Supporting Fig. S1C) than the power delivered to the other two loops. White square boxes indicate in approximation the planned placement of the voxels (20 mm × 20 mm × 20 mm) for the acquisition of MM data from OccL and IPL. White letters L, R, and A stand for left, right, and anterior coordinates, respectively.

$\beta = 5.982$) and the frequency modulation using a hyperbolic tangent function $\left(\kappa \cdot tanh\left(\lambda \cdot (1 - 2t/T)\right); \kappa = 1017\ Hz,\ \lambda = 5.938\right)$ (Figs. 3A,B). The inversion bandwidth of the InvP, defined as the frequency region where the longitudinal magnetization of total magnetization (Mz/Mo) is equal to or less than -0.95, was approximately 1650 Hz and the minimum B_1^+ required for the adiabatic condition was 15 μT.

Bloch equation simulations were performed for the calculation of a set of IR times (TI_1 and TI_2) suitable for metabolite nulling. In particular, simulations were implemented assuming different T_1 for metabolites

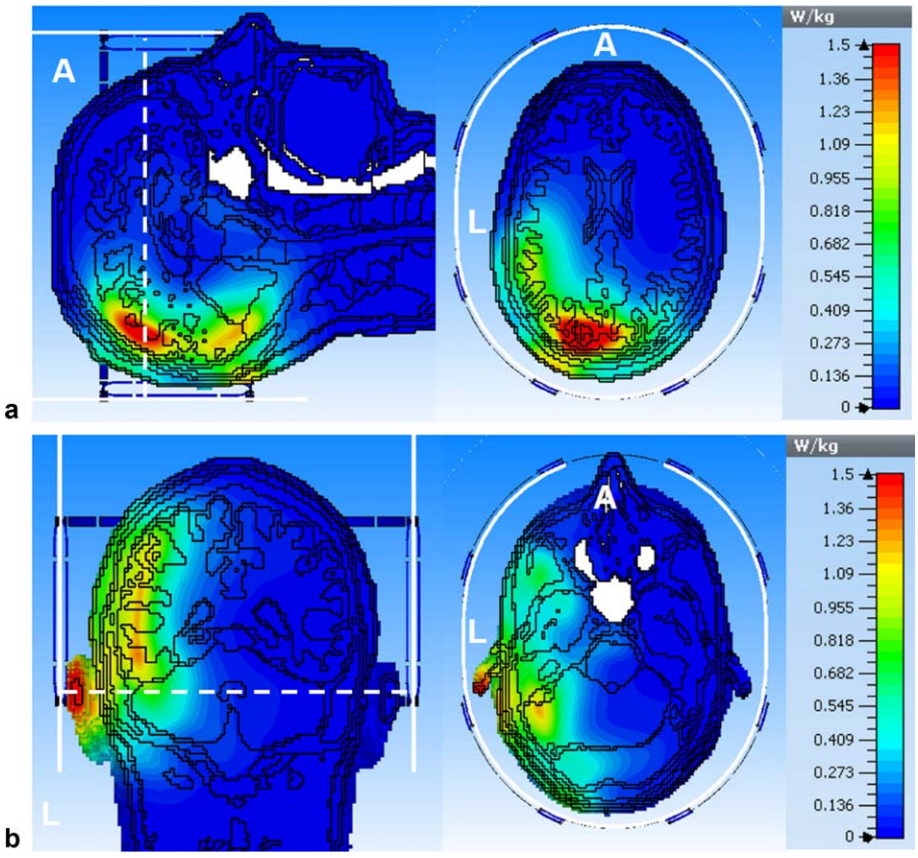

FIG. 2. Coronal, sagittal, and axial slices of the local SAR maps through the maximum obtained using EM simulations. **A**: SAR distribution for the three-loop mode used for the excitation of a voxel within occipital lobe. White letters L and A stand for left and anterior coordinates respectively. **B**: SAR distribution for the two-loop mode used for the excitation of a voxel within left parietal lobe. White dashed lines indicate the location of the presented axial images. White letters L and A stand for left and anterior coordinates, respectively.

Table 1
Simulated and Experimental Results for the 8Tx16Rx Array

Model	Mode (location)	$<B_1^+>/\sqrt{P}$[a], $\mu T/\sqrt{kW}$	$<B_1^+>$[a], $\mu T/V$	Ratio[b]	max SAR_{10G}[c], W/kG	$<B_1^+>/\sqrt{SAR_{10G}}$
HS	CP (OccL)	16.84	0.08	1	-	-
phantom	Ch1	33.36	0.15	1.98	-	-
(EM Sim.)	2 Chs.; 8,1	42.59	0.19	2.53	-	-
	3 Chs. 8,1,2	46.47	0.21	2.76	-	-
	CP (lPL)	8.96	0.04	1	-	-
	Ch3	17.59	0.08	1.96	-	-
	2 Chs.; 2,3	29.45	0.13	3.29	-	-
	3 Chs. 2,3,4	32.54	0.15	3.63	-	-
HS	CP (OccL)	13.77	0.06	1	-	-
phantom	Ch1	29.28	0.13	2.03		
(Exp.)	2 Chs.; 8,1	37.71	0.17	2.61		
	3 Chs. 8,1,2	36.79	0.16	2.55		
	CP (lPL)	14.45	0.06	1	-	-
	Ch3	16.76	0.07	1.22	-	-
	2 Chs.; 2,3	30.20	0.14	2.19	-	-
	3 Chs. 2,3,4	29.43	0.13	2.14	-	-
Duke	CP (OccL)	14.16	0.06	1	0.59	1
(EM Sim.)	Ch1	34.66	0.16	2.45	2.17	1.28
	2 Chs.; 8,1	41.11	0.18	2.90	1.92	1.61
	3 Chs. 8,1,2	45.04	0.20	3.18	2.05	1.71
	CP (lPL)	13.46	0.06	1	0.59	1
	Ch3	16.82	0.08	1.25	1.88	0.70
	2 Chs.; 2,3	30.68	0.14	2.28	1.58	1.39
	3 Chs. 2,3,4	33.54	0.15	2.49	1.28	1.69
Ella	CP (OccL)	17.04	0.08	1	0.63	1
(EM Sim.)	Ch1	36.86	0.16	2.16	2.01	1.21
	2 Chs.; 8,1	45.49	0.20	2.67	2.11	1.46
	3 Chs. 8,1,2	48.26	0.22	2.83	1.88	1.64
	CP (lPL)	9.37	0.04	1	0.63	1
	Ch3	18.7	0.08	2.00	1.35	1.36
	2 Chs.; 2,3	27.74	0.12	2.96	1.32	2.05
	3 Chs. 2,3,4	30.54	0.14	3.26	1.47	2.13

[a]Averaged over 20 mm x 20 mm x 20 mm white square box (see Fig. 1 A and B).
[b]Ratio to the $<B_1^+>$ measured for the corresponding location of the CP mode (see Supporting Information).
[c]Evaluated for the RF power of 1 W at the coil input.

(1000 ms to 2000 ms) and MM (400 ms) using reported values from studies at 7T and 9.4T (Fig. 4) (40,41). The InvP was incorporated into a double IR scheme preceding the localization scheme, in this case, MC semi-LASER (Fig. 4A) (31). The final selected inversion times were 2360 ms and 625 ms, respectively.

Macromolecular Data Acquisition

First, high-resolution images from 2D FLASH scans (in-plane resolution: $0.7 \times 0.7\,mm^2$, slice thickness: 3.5 mm, 25 slices) were acquired in three orientations (axial, sagittal and coronal) to facilitate the later placement of spectroscopic voxels. A 3D MPRAGE scan (42) was also acquired. Afterward, for each volunteer, spectroscopy voxels ($2 \times 2 \times 2\,cm^3$) were selected in a mixed gray matter (GM) and white matter (WM) area in the OccL, and the lPL (mainly WM) using the appropriate coil configuration as it is described in the Phased Array Design section. For both voxel placements, first- and second-order B_o shimming was performed using FAST(EST)MAP (43), and voxel-based power calibration was executed (44). Next, localized MM spectra using a double IR scheme along with MC semi-LASER (TE: 24 ms) (31) were acquired from each volunteer. The repetition time (TR) was set to 10000 ms to ensure complete T_1 recovery of macromolecular resonances. For each brain region, 64 MM averages were acquired with 4096 time-points and an 8 kHz receive-bandwidth. The transmit frequency of the IvP was shifted by -870 Hz compared with the water frequency to invert MM and metabolite resonances and affect the water peak partially. The voltage of the InvP was set every time to ensure that the resulting B_1^+ within the ROI was higher than the minimum required B_1^+ for the fulfillment of the adiabatic condition ($B_{1min}^+ = 15\,\mu T$).

Also, a phase cycling scheme of 16 steps was implemented (21). The transmit reference frequency for the localization pulses of MC semi-LASER was set at 2.3 ppm to reduce the misadjustment of the ROI based on the water MR image (measured with water on resonance at 4.7 ppm) and to minimize lipid excitation. In particular, the pulse excitation bandwidth was approximately 8 kHz resulting in a CSD of 5% per ppm for each voxel dimension. Neither water presaturation (WS) nor outer volume saturation were applied.

Finally, to avoid any influence of MC pulses on quantification based on water (assuming single proton resonances), water reference signals (NEX: 16) were

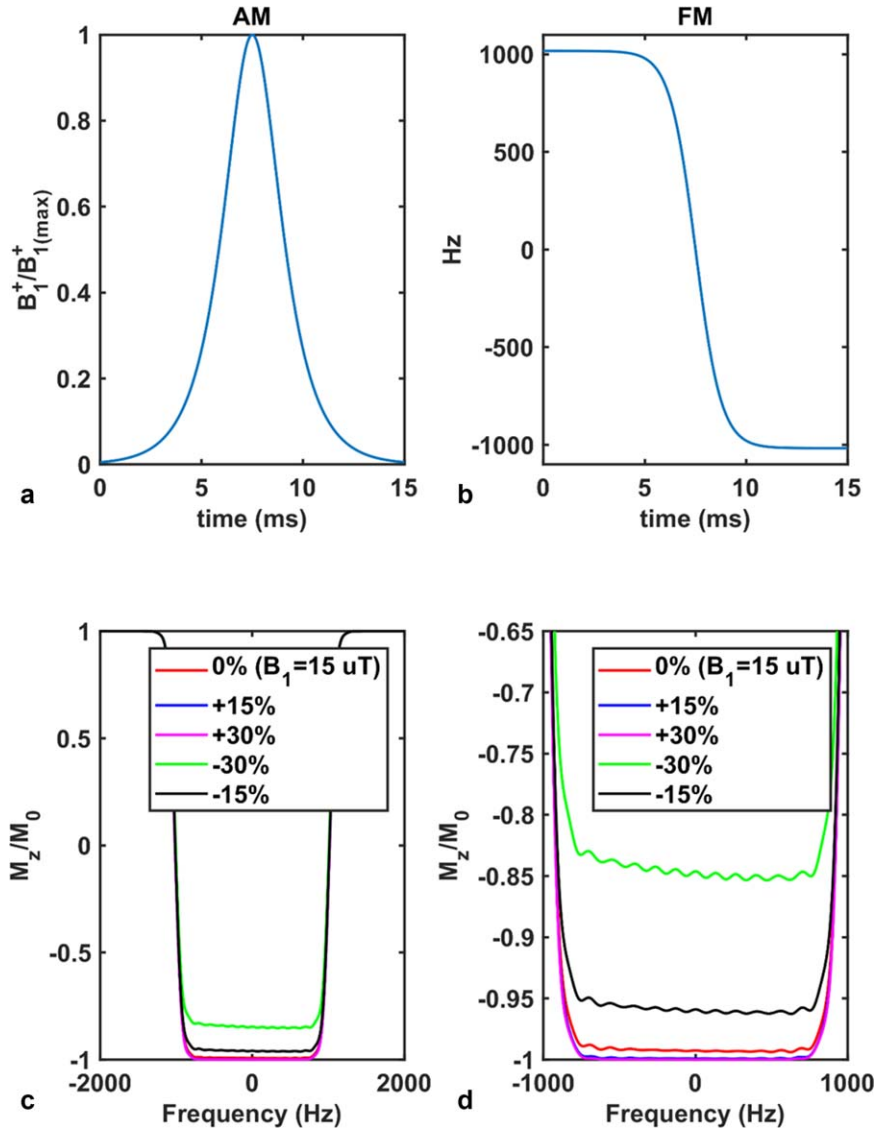

FIG. 3. Profile of the adiabatic inversion pulse (InvP) with duration T = 15 ms for metabolite nulling at 9.4T. **A**: Amplitude modulation (AM) (normalized) of InvP as a function of time (t). **B**: Frequency modulation (FM) function of InvP in Hz as a function of time (t). **C**: Inversion profile of InvP simulated using Bloch equation simulations for different B_1^+ levels assuming a pulse duration of 15 ms. The resulting inversion bandwidth is approximately 1650 Hz and the transition bandwidth roughly 500 Hz. **D**: Same as subplot C using a smaller frequency range for the illustration of inversion profile details.

measured with semi-LASER (TE: 24 ms) without MC or WS. In the case of OccL measurements, the TR was set to 6000 ms, while for lPL experiments, the TR used among different volunteers varied from 6000 ms to 7800 ms. The selection of TR enabled the minimization of the duration of the water reference scans while ensuring SAR levels remained within an acceptable range (31).

Macromolecular Data Postprocessing

The raw data were exported from the scanner, and all the analysis steps were performed in MATLAB (Version 2012b, The Mathworks, Natick, MA) with in-house processing routines. The data-processing procedure involved the following steps: (i) zero filling with a factor of two; (ii) frequency and phase alignment in the time domain based on the non-WS spectra (31,45); (iii) minimization of the residual water signal in the MC macromolecular spectrum: even numbered MC spectra were multiplied by a scaling factor between 0.90 to 0.97 before signal combination, as described in (46); (iv) water spectra were created by averaging odd and even numbered acquisitions, and macromolecular data were calculated by subtracting even numbered averages from odd numbered acquisitions; (v) truncation of MM signals at 150 ms; (vi) zero-order phase and eddy current correction using the phase information of the water signal (47); (vii) signals from all 16 receive channels were combined using a singular value decomposition method based on MC water data (48). No removal of any metabolite peak on MM spectra using postprocessing techniques was performed.

Macromolecular Baseline Model

For the creation of macromolecular template signals for OccL and lPL, all the subjects' macromolecular signals (Supporting Fig. S2) were first frequency aligned using the MC water peak (31) and then averaged. Finally, the averaged macromolecular spectrum was smoothed using cubic splines within MATLAB (smoothing parameter $p = 0.001$) for noise reduction without affecting the actual linewidth of MM peaks (Fig. 5). Then the averaged and smoothed MM baselines for both the OccL and the lPL were further analyzed for the extraction of the individual

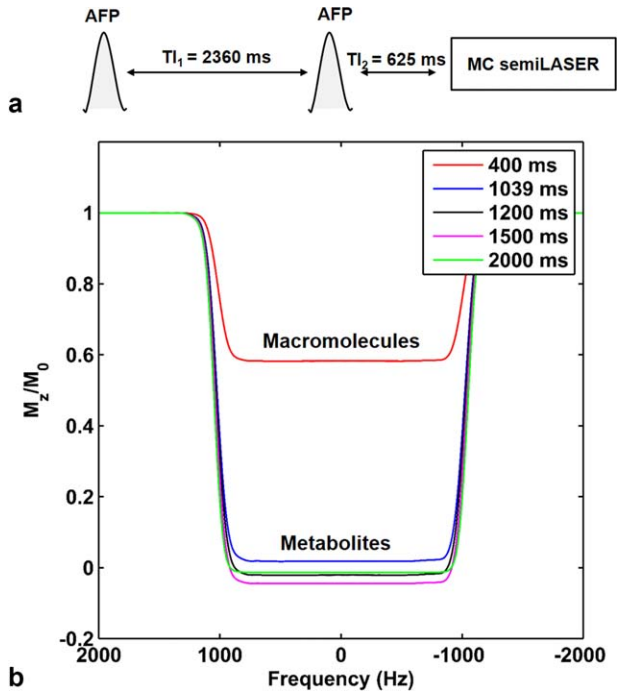

FIG. 4. Double inversion recovery scheme for metabolite nulling at 9.4T. **A**: Diagram of the sequence used for the acquisition of macromolecular spectra. Two adiabatic inversion pulses (AFP) preceded the actual localization scheme (MC semi-LASER) using optimized inversion times ($TI_1 = 2360$ ms and $TI_2 = 625$ ms). A schematic of the semi-LASER sequence used in this study can be found in Giapitzakiset al (31). **B**: Simulation of the effect of the double inversion recovery scheme in subplot A on the longitudinal magnetization for several T_1 recovery times. T_1 of macromolecules is assumed to be 400 ms and for other metabolites T_1 is higher (1000 ms to 2000 ms) using reported values from studies at 7T (40). The double inversion recovery scheme results in an efficient suppression of longer T_1 metabolites.

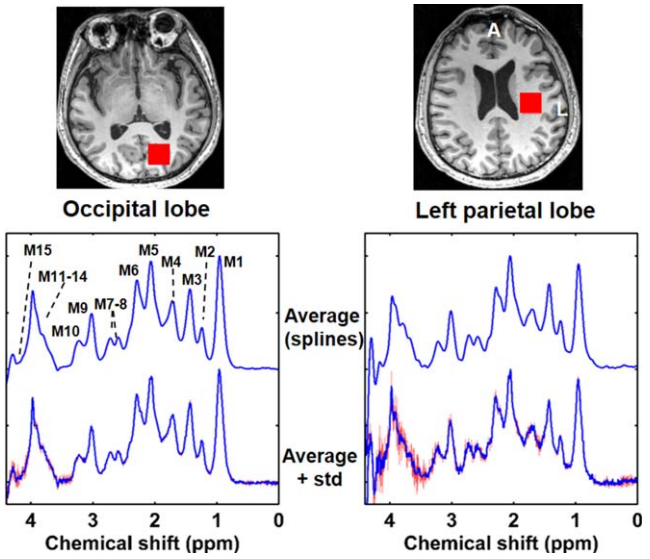

FIG. 5. Averaged MM spectra (bottom) the smoothed averaged MM spectra using cubic splines (top). Macromolecular spectra were acquired from 7 healthy within a voxel of $2 \times 2 \times 2\,cm^3$ (red square in anatomical images) placed in a mixed area of GM, WM, and CSF in the occipital lobe (left) and the left parietal lobe (right), respectively. The red area indicates the standard deviation (std), while the blue line the average of MM spectra among the seven volunteers (normalized to M1 peak). 15 MM peaks are observed by a visual inspection (M1-15). White letters L and A stand for left and anterior coordinates, respectively.

MM peaks. In particular, after visual inspection and using previously published results regarding the composition of MM baseline (1,9,23,49–51), 15 MM peaks were assumed to be present in the acquired MM baselines and the respective chemical shifts were extracted.

Using the simulated basis set option within LCModel (CHSIMU), which allows the simulation of Voigt peaks, the LCModel simulated Voigt lineshapes were fitted to the average-smoothed MM baselines (Fig. 6). The simulated basis set consisted of the following 15 MM components: M1 (0.94 ppm), M2 (1.22 ppm), M3 (1.43 ppm), M4 (1.69 ppm), M5 (2.04 ppm), M6 (2.27 ppm), M7 (2.57 ppm), M8 (2.74 ppm), M9 (3.01 ppm), M10 (3.21 ppm), M11 (3.71 ppm), M12 (3.79 ppm), M13 (3.85 ppm), M14 (3.87 ppm), M15 (4.20 ppm). The chemical shift tolerance of each simulated peak in LCModel was set to 0.04 ppm. Additionally, the selected values for the full width half maximum (FWHM) of the simulated peaks varied from 0.04 to 0.13 ppm with a tolerance of 0.005 ppm.

Quantification of Macromolecular Components

For the calculation of the macromolecular concentrations, the MM spectra of each volunteer for each brain location were analyzed individually using LCModel

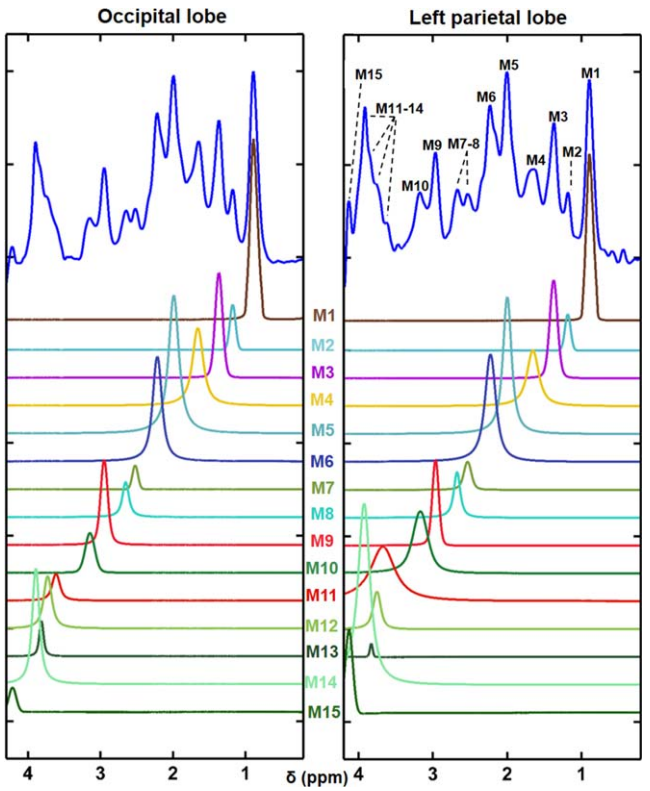

FIG. 6. Parametrization of smoothed and averaged MM baselines for two brain locations: (left) occipital lobe and (right) left parietal lobe. In total, 15 MM components are observed.

V6.3-1L (25). The basis consisted of the 15 simulated Voigt-shaped peaks exported during the establishment of the macromolecular baseline model (see above paragraph). During the LCModel fitting, the hidden parameter of LCModel DKNTMN was set to 0.4. This value controls the number of knots in the spline baseline and, hence, the rigidity of the spline function.

The macromolecular components concentrations in mmolal (μmol/g tissue water; $[MM]_{molal}$), corrected for T_1 and T_2 relaxation of different water compartments, were calculated using the LCModel signal intensity ratio between MM and water (S_{MM}/S_{H20}). These calculations assumed MM components with only one proton through the following equation (52):

$$[MM]_{mmolal} = \frac{S_{MM}}{S_{H20}} \times \frac{(f_{GM} \times R_{GM} + f_{WM} \times R_{WM} + f_{CSF} \times R_{CSF})}{1 - f_{CSF}} \times \frac{2}{1 + F_s} \times 55510\ mmolal$$

where 55510 mmolal is the molality of pure water at body temperature, f_{GM}, f_{WM}, and f_{CSF} are the water tissue fractions for GM, WM, and cerebrospinal fluid (CSF), respectively, as they are described in (52) using the relative densities of NMR-visible water ($a_{GM} = 0.78$, $a_{WM} = 0.65$, $a_{CSF} = 0.97$) (53), as well as, the GM, WM, and CSF volume fractions determined by the image segmentation procedure (see Supporting Information). R_{GM}, R_{WM}, R_{CSF} are correction factors for the different T_1 and T_2 relaxation of water ($R = e^{\frac{-TE}{T2}} \cdot \left(1 - e^{\frac{-TR}{T1}}\right)$) in GM, WM, and CSF, respectively. The T_1 values used for GM, WM, and CSF were 2000 ms, 1300 ms, and 4000 ms, respectively, and were calculated in approximation from (54), while the T_2 were 70 ms, 75 ms, and 143 ms, respectively, using published values at 7T (55). No correction was applied for T_2 and T_1 relaxation of macromolecules. The denominator $1 - f_{CSF}$ was implemented for partial-volume correction (25,53). The factor $\frac{2}{1+Fs}$ was introduced to correct for the multiplication of even numbered acquisitions with the scaling factor (F_s) (46). No exclusion criteria were used in the calculation of macromolecule concentration levels to avoid biased estimated mean concentrations (56).

SNR of M1 was measured as M1 amplitude (frequency domain) divided by the standard deviation of 1000 points from 14.7 ppm to 12.3 ppm. Statistical hypothesis testing was performed within MATLAB using a two-tailed nonparametric rank test (Wilcoxon signed rank test for equal and matched sample size) and the Holm-Bonferroni method for multiple comparisons correction.

RESULTS

Optimization of the Array

Simulated and experimentally measured B_1^+ maps, obtained from a transversal slice near the center of the array using the HS phantom for both locations (OccL and lPL), agreed well, with the simulated results being 10–20% higher (Fig. 1). This result was consistent with previously reported data for UHF head Tx-arrays (35,57). As seen from Table 1 and Figure 1, both, the 2-loop and 3-loop modes were substantially more Tx-efficient than the CP mode and 1-loop mode. Also, the 2-loop mode and 3-loop mode produced very similar B_1^+ (within 10% difference), but the 3-loop mode had higher maximum SAR for both locations (Table 1). The in vivo experiments demonstrated that the average maximum B_1^+ levels among all the volunteers for a voxel placed within the OccL and the lPL were 48 μT and 33 μT, respectively, with a maximum allowed voltage of 450 V.

Development of the Double Inversion Recovery Technique for Metabolite Nulling at 9.4T

Figure 3 illustrates the adiabatic behavior of the InvP. The resulting transition bandwidth ($|Mz/Mo| < 0.95$) of the InvP was approximately 500 Hz. Under the adiabatic regime, the inversion bandwidth exhibited a well-defined profile lacking intensive wiggles. Even for the case of a B_1^+ value 15% smaller ($B_1^+ = 12.75$ μT) than the minimum required B_1^+, the shape of the inversion bandwidth was only slightly distorted and preserved its characteristics such as the inversion profile. However, in conditions of lower B_1^+ levels than the minimum B_1^+ (-30%), the inversion profile was deformed.

Regarding the double IR, for inversion times TI_1 and TI_2, 2360 ms and 625 ms, respectively, the fast-T_1-recovered MM (~400 ms) resonances reached approximately 60% of their maximum magnetization, while the longitudinal magnetization of metabolites with longer T_1 relaxation (1000 to 2000 ms) was suppressed (Fig. 4).

Macromolecular Baseline Templates

Double IR in combination with the MC semi-LASER enabled the reliable acquisition of MM spectra with the absence of lipid contamination (Fig. 5 and Supporting Fig. S2). The pattern of MM baselines for the same brain region among different volunteers was consistent. However, potential differences in peak amplitudes between the various volunteers could be observed in the spectral area from 1 ppm to 2 ppm (M2 to M5) by visual inspection. Moreover, the average-smoothed MM baselines acquired from voxels within the OccL and the lPL did not manifest notable differences. Nevertheless, minor variations in peaks' amplitudes could be noticed in the frequency range from 3.8 ppm to 4 ppm (M12 to M15; Fig. 5). The average SNR of M1 peak (peak at 0.9 ppm; Fig. 5) in the occipital lobe and the left parietal lobe was 54 Hz and 24 Hz, respectively, exhibiting a statistical difference ($P < 0.05$). The FWHM of the M1 peak was 45 Hz and 41 Hz in both regions accordingly. The smoothing procedure using cubic splines did not affect the linewidth of MM peaks while improving the SNR of the MM baseline template.

Extraction of Macromolecular Peaks

Figure 6 demonstrates the results of the extraction of the MM peaks for the establishment of the MM model using the average and spline-smoothed MM. The final number of MM peaks included in the model were recognized visually, whilst also considering previously reported MM resonances (1,4–6,9,17,19,26,49,58). As a result, in this study 15 MM peaks were used to adequately model

Table 2
Concentration Levels in μmol/g (Assuming One Proton Resonances), Chemical Shift and Amino Acid Assignment of Macromolecules

	Occipital lobe			Left parietal lobe					
MM	Q1[a]	Median[a]	Q3[a]	Q1	Median	Q3	δ(ppm)[b]	Assignment	Ref.[c]
M1	7.99	8.31	8.60	6.44	7.05	7.34	0.94	Leucine, isoleucine valine	1,3
M2	1.50	1.82	2.43	1.65	2.63	4.29	1.22	Threonine alanine	1,3
M3	4.34	5.48	7.06	3.68	5.97	8.22	1.43	Threonine alanine	1,3
M4	5.33	8.63	11.19	3.60	5.34	8.87	1.69	Lysine arginine	1
M5	10.72	11.31	13.87	10.49	11.56	14.00	2.04	Glutamate glutamine	1
M6	8.23	9.54	10.34	8.64	9.42	10.62	2.27	Glutamate glutamine	1
M7	0.85	0.96	1.30	1.06	1.93	2.70	2.57	β-methylene protons of aspartyl groups	This study
M8	1.65	1.84	1.87	1.83	2.14	3.14	2.74	β-methylene protons of aspartyl groups	This study
M9	3.73	3.97	4.39	3.59	3.89	4.35	3.01	Lysine, arginine	1
M10	2.18	2.62	3.12	2.62	3.03	3.52	3.21	αCH protons[d]	1
M11	0.88	1.10	1.22	0.67	1.23	2.78	3.71	αCH protons[d]	1
M12	3.05	3.34	3.40	3.30	3.66	3.96	3.79	αCH protons[d]	1
M13	0.67	0.83	1.10	0.91	1.36	2.58	3.87	αCH protons[d]	1
M14	6.97	7.59	8.55	5.72	7.00	7.90	3.97	αCH protons[d]	1
M15	1.27	1.83	2.02	0.92	1.70	3.86	4.20	αCH protons[d]	1

[a]Q1: 25th percentile, Median: 50th percentile, Q3: 75th percentile.
[b]Chemical shifts (ppm) are in approximation.
[c]References in which the assignment of MM to specific amino acid is reported.
[d]αCH groups of the protein amino acids.

the cubic spline-smoothed average MM baseline templates. In particular, for both brain regions, the same number of simulated peaks was included in the LCModel. No noteworthy differences were observed in the resulting MM components after simple visual inspection. However, differences in the amplitudes of M10 to M15 were indicated (Fig. 6). The detailed description of the 15 MM peaks is reported in Table 2.

Quantification of Macromolecular Components

Segmentation of anatomical images resulted in 55% WM, 41% GM, and 4% CSF on average for the OccL and 80% WM, 18% GM, and 2% CSF for the lPL. LCModel fitting of individual MM spectra of each volunteer for both brain locations, using the 15 MM peaks extracted during the establishment of the MM model, resulted in well-fitted spectra with an almost flat baseline correction and without pronounced systematic residual peaks (Fig. 7 and Supporting Fig. S3).

Quantification results, corrected for different tissue types and T_1 relaxation times of various water compartments, did not show any statistically significant difference in MM concentration levels between the OccL and the lPL (Fig. 8). The only exception was the M1 peak, where there was a trend for potential difference ($P < 0.05$, not corrected for multiple comparisons). The interquartile range (defined as the difference between the

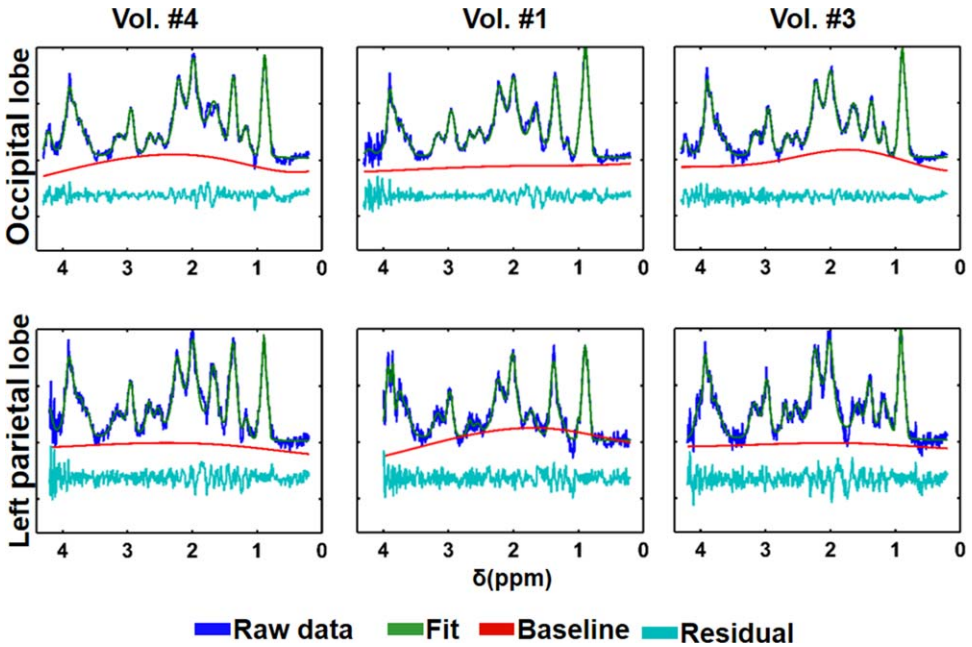

FIG. 7. LCModel fitting results of the individual MM spectra for three volunteers (Vol. #4, Vol. #1, and Vol. #3), for two different brain regions (top) occipital lobe and (bottom) left parietal lobe, using as a basis the 15 MM components created after the parametrization procedure (Fig. 5). The absence of pronounced residuals (light blue colored line) indicates that the basis set was adequate. The LCModel fitting results of the other four volunteers participated in this study (Vol. #7, Vol. #6, Vol. #5, and Vol. #2), are illustrated in Supporting Figure S3.

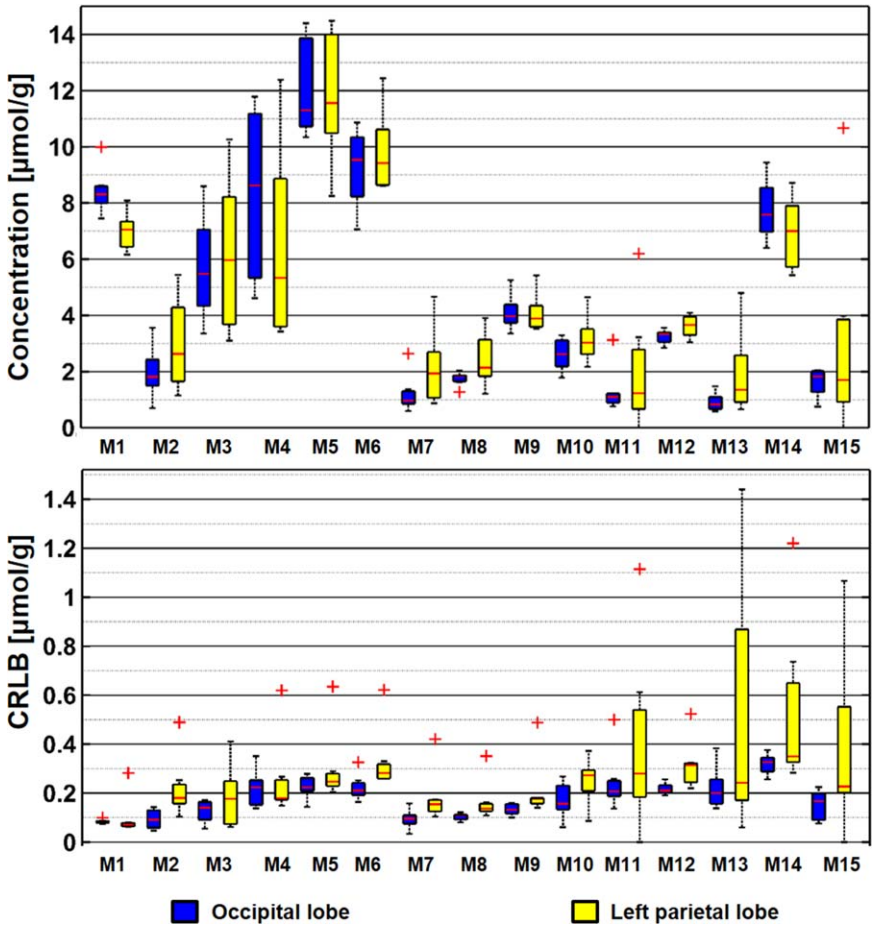

FIG. 8. Quantification results of 15 MM for two different brain areas, occipital lobe and left parietal lobe, from seven volunteers using LCModel. (Up) Concentrations levels in molal (assuming one proton per resonance), corrected for GM, WM, and CSF percentages and the different T_1 and T_2 relaxation of the water compartments. (Down) CRLB values in molal, calculated as: concentration level x CRLB (%). Data are presented in percentiles. In particular, box borders indicate the 25th (first quartile: Q1) and 75th (third quartile: Q3) percentiles while the horizontal red line the median value. Red crosses illustrate outliers. Black bars show the minimum and maximum values.

75th and 25th percentiles) of concentration levels for most MM resonances was smaller than 2, except for the MM region M3-5 (Table 2). Moreover, Cramer-Rao lower bound (CRLB) values for most MM peaks were at a similar level, except for the OccL macromolecules: M11, M13, M14, and M15, which were higher than 0.25 (μmol/g) (Fig. 8).

DISCUSSION

In this study, the approach to achieve B_1^+ can be viewed as a simplified version of RF shimming. Theoretically, it is also possible to focus the B_1^+ field locally within the brain when the array is driven using eight independent RF channels (pTx). This option is also available on many commercial UHF scanners. Unfortunately, this does not provide maximum power because each RF channel carries only up to 1 kW while half of it is lost in cables and interfaces on the way to the RF coil. Thus, for peripheral locations (depth: ~30–40 mm) where two to three channels contribute to the local B_1^+ field, only 1–1.5 kW (including losses) of maximum power can be used. Conversely, in our method, the entire power (8 kW; 4 kW after losses) of the power amplifiers was applied to the two- or three-way splitter. A minor inconvenience was produced from our technique due to the reconnecting of the splitter in the case that different locations needed to be measured within the same experiment. However, our method, which is mainly applicable for research studies and peripheral locations, provided a reasonable compromise between eight-channel RF shimming with high power capability without the necessity of using multiple local coils and moving the subject when various brain locations need to be studied. Additionally, the high B_1^+ efficiency provided by our RF coil configuration enabled the achievement of TE = 24 ms (31).

The InvP provided an efficient inversion bandwidth to cover the desired chemical shift range (0 ppm to 4.2 ppm) at 9.4T. The transition bandwidth of the InvP (~1 ppm) in combination with the frequency offset, led to a partial inversion of the water peak at 4.7 ppm. However, the residual water peak was sufficient for frequency and phase alignment of the different averages using the metabolite cycling technique. The selected parameters of the InvP (β, κ, λ) and duration of 15 ms resulted in a pulse with an efficient inversion bandwidth (1650 Hz) that worked under the adiabatic regime with a minimum B_1^+ of 15 μT (Fig. 3). Taking into consideration, the achieved B_1^+ of each coil configuration, the InvP could be applied in different brain regions. Additionally, the final pulse duration and the minimum required B_1^+ in combination with the TR =10000 ms, enabled the application of two InvP for double IR without SAR issues. As Figure 3 illustrates, the AFP profile demonstrated a B_1^+ sensitivity varying as a function of frequency offset, which increased for lower B_1^+ values. However, the

minimum B_1^+ achieved within the voxel was 20% to 40% higher than 15 μT (blue and pink colored lines in the Fig. 3). Thus, potential variations of the inversion profile of MM peaks with different frequency offsets were negligible.

The simulations of the double IR for the calculation of inversion times appropriate for metabolite nulling at 9.4T relied on reported T_1 values of metabolites measured in vivo at 7T and 9.4T (40,41). However, the quality and the characteristics of the resulting MM spectra (Fig. 5 and Supporting Fig. S2) were similar or better than other published MM baselines (1,4–6,9,17,19,26,49,58) verifying the efficient suppression of metabolites and especially of N-acetylaspartate (NAA; 2 ppm), total creatine (tCr), and total choline (tCh).

The averaged MM baselines for both brain locations did not demonstrate substantial differences upon visual inspection (Fig. 6). However, differences in the frequency range of 3.8 ppm to 4 ppm (MM11 to MM14) could be observed between the two brain locations due to B_0 inhomogeneity.

Some spectra contained what appear to be unspoiled coherences in the 3.5 to 4.2 ppm range (Fig. 5 and Supporting Fig. S3), which suggest incomplete spoiling in the sequence and possibility that stronger crusher gradients might be needed. Thus, this might lengthen the minimum achievable TE. These unwanted coherences were probably due to the high B_0 inhomogeneity outside the shim-voxel produced by the second-order shim terms (59). This issue was more pronounced in the lPL region, which translated into high variability in concentration and CRLB values for M11 to M15 (Fig. 8), because the voxel was closer to the ventricles.

MM spectra among different volunteers exhibited similar patterns except for macromolecules M2, M3, and M4, which was also confirmed from the variation of these MM in the quantification results (Fig. 8).The alteration of M2, M3, and M4 can be seen in another study (6). Moreover, data in Supporting Figure S2 suggested that there was lipid contamination, which could influence the appearance of those resonances. Thus, the deviations in those MM could indicate lipid contamination or physiological variations (e.g., motion of free proteins).

In this work, no postprocessing technique was applied for the removal of potential residuals of tCr, NAA, or tCh. Thus, for metabolites with T_1 close to 1039 ms such as tCr (41), a residual signal was expected (Fig. 4). In the MM data there was no obvious contamination. However, a potential contamination in MM9 and MM13–14 peaks could not be entirely excluded.

In this study, 15 MM components were used for the parametrization of macromolecular baselines as well as for the quantification of individual MM concentrations for each volunteer (Figs. 5 and 6). Figures 6 and 7 illustrate that this number of MM components was sufficient for the quantification of MM peaks because no significant residuals were observed after the fitting procedure. Most of the MM peaks have been previously reported from various studies (1,4–6,9,17,19,26,49,58) and assigned to specific amino acids (Table 2). However, in this work, more MM components were distinguished mainly due to the increased spectral resolution at UHF. A noteworthy finding is that two new MM peaks at 2.57 ppm (M7) and 2.74 ppm (M8) were easily resolved. These peaks appear in MM spectra of other studies in which more advanced MRS techniques are used (e.g., 2D COSY) (1,4,6). However, to the best of our knowledge, they have not been reported.

The direct assignment of M7 and M8 to specific amino acids was not possible in this work. Nonetheless, they can be indirectly ascribed to certain amino-acids using the study of Behar and Ogino (1). The M7 and M8 are most likely due to the beta-methylene protons of aspartyl groups within cellular proteins. In his paper, Figure 2b (2D COSY) shows these two peaks as corresponding to spin-coupled ^{1}H resonances, while Figure 3 (2D J-resolved spectrum) indicates that both peaks correspond to doublet-of-doublets in the 1D ^{1}H spectrum (with approximate J coupling constants of ~5 Hz, ~7 Hz, and ~19 Hz from the figure). In addition, the chemical shifts and coupling constants of the MM peaks correspond closely with aspartate (58).

Quantification results (Fig. 7 and Supporting Fig. S3) showed that between both brain regions there were no significant differences, except a small trend for M1. Single voxel spectroscopic studies performed at 7T also report small quantification differences between WM and GM regions in the brain (6,19).

However, the concentration levels have to be interpreted with caution. First, the T_1 times for the different water compartments used for relaxation correction were calculated in approximation, while the T_2 values were adapted from a study at 7T (55). Second, because no postprocessing method was implemented regarding the removal of potential contamination from metabolites such as tCr, NAA, and tCh, there is an additional uncertainty for the overlap of MM peaks with these metabolites (M5, M9, M10, M13, and M14). The great majority of the published papers regarding human brain macromolecules are dealing with the characterization of the human brain MM baseline and its influence on metabolite quantification rather than with the quantification of the individual MM components.

Consequently, a limited number of papers about the quantification of the human brain MM peaks exists in the literature (e.g., Hofmann et al and Snoussi et al) (9,19). Hence a direct comparison of the current MM quantification results with other published studies is not reliable. Moreover, relaxation correction is usually avoided in cases of short TE (<30 ms), and at UHF this assumption may introduce quantification errors due to the shorter T_2 of the MM peaks. Furthermore, in this study 15 Voigt-shaped peaks were used for quantification of the MM components due to the enhanced frequency resolution at UHF. However, in previous studies (9,19) fewer peaks were used.

Studies using MR spectroscopic imaging with high spatial resolution have shown potential differences in MM between WM and GM (51,60). However, in single voxel spectroscopy studies, like in this work, the voxel size is relatively large (in this case $2 \times 2 \times 2$ cm^3) and as a result, it is a mixture of different tissues. Consequently, differences in MM between GM and WM are difficult to detect.

CONCLUSIONS

In this study, we obtained macromolecular spectra acquired for the first time from two different regions of the human brain at 9.4T, in the occipital lobe and left parietal lobe, using a double inversion recovery technique in combination with MC semi-LASER. We demonstrated a coil setup enabling the achievement of efficient B_1^+ fields in different brain locations without the need for different coils. In addition, we demonstrated an optimized AFP appropriate for inversion of MM and metabolites at 9.4T. Double inversion, which was combined with MC semi-LASER, enabled the acquisition of high spectral resolution MM spectra. Particularly, 15 MM peaks were detected and quantified for both brain regions at 9.4T. MM baseline models for both locations were established, and mean concentration levels for each of the 15 MM components were calculated using water reference scans. Furthermore, two new MM peaks (M7 and M8) were reported and preliminarily assigned to β-methylene protons of aspartyl-groups.

ACKNOWLEDGMENTS

The authors of this study thank Mr. Liam Connah, Ms. Saipavitra Murali Manohar, Mr. Andrew Wright, and Dr. Nicole Fichtner for proofreading this manuscript as well as Prof. Dr. Kevin Behar for helpful suggestions and comments regarding the possible assignment of M6 and M7. This project was co-sponsored by the European Social Fund and national funds through the Greek State Scholarships Foundation (IKY; I-A.G.), as well as, by the Horizon 2020 CDS-QUAMRI grant (A.H.).

REFERENCES

1. Behar KL, Ogino T. Characterization of macromolecule resonances in the 1H NMR spectrum of rat brain. Magn Reson Med 1993;30:38–44.
2. Kauppinen RA, Niskanen T, Hakumäki J, Williams SR. Quantitative analysis of 1H NMR detected proteins in the rat cerebral cortex in vivo and in vitro. NMR Biomed 1993;6:242–247.
3. Kauppinen RA, Kokko H, Williams SR. Detection of mobile proteins by proton nuclear magnetic resonance spectroscopy in the guinea pig brain ex vivo and their partial purification. J Neurochem 1992;58: 967–974.
4. Behar KL, Rothman DL, Spencer DD, Petroff OA. Analysis of macromolecule resonances in 1H NMR spectra of human brain. Magn Reson Med 1994;32:294–302.
5. Cudalbu C, Mlynarik V, Gruetter R. Handling macromolecule signals in the quantification of the neurochemical profile. J Alzheimers Dis 2012;31(Suppl. 3):S101–S115.
6. Schaller B, Xin L, Gruetter R. Is the macromolecule signal tissue-specific in healthy human brain?. A 1H MRS study at 7 tesla in the occipital lobe. Magn Reson Med 2014;72:934–940.
7. Behar KL, den Hollander JA, Stromski ME, Ogino T, Shulman RG, Petroff OA, Prichard JW. High-resolution 1H nuclear magnetic resonance study of cerebral hypoxia in vivo. Proc Natl Acad Sci U S A 1983;80:4945–4948.
8. Arus C, Yen C, Barany M. Proton nuclear magnetic resonance spectra of excised rat brain. Assignment of resonances. Physiol Chem Phys Med NMR 1985;17:23–33.
9. Hofmann L, Slotboom J, Boesch C, Kreis R. Characterization of the macromolecule baseline in localized (1)H-MR spectra of human brain. Magn Reson Med 2001;46:855–863.
10. Dixon WT, Sardashti M, Castillo M, Stomp GP. Multiple inversion recovery reduces static tissue signal in angiograms. Magn Reson Med 1991;18:257–268.
11. Davie CA, Hawkins CP, Barker GJ, Brennan A, Tofts PS, Miller DH, McDonald WI. Detection of myelin breakdown products by proton magnetic resonance spectroscopy. Lancet 1993;341:630–631.
12. Opstad KS, Bell BA, Griffiths JR, Howe FA. Toward accurate quantification of metabolites, lipids, and macromolecules in HRMAS spectra of human brain tumor biopsies using LCModel. Magn Reson Med 2008;60:1237–1242.
13. Hwang JH, Graham GD, Behar KL, Alger JR, Prichard JW, Rothman DL. Short echo time proton magnetic resonance spectroscopic imaging of macromolecule and metabolite signal intensities in the human brain. Magn Reson Med 1996;35:633–639.
14. Graham GD, Hwang JH, Rothman DL, Prichard JW. Spectroscopic assessment of alterations in macromolecule and small-molecule metabolites in human brain after stroke. Stroke 2001;32:2797–2802.
15. Mader I, Seeger U, Karitzky J, Erb M, Schick F, Klose U. Proton magnetic resonance spectroscopy with metabolite nulling reveals regional differences of macromolecules in normal human brain. J Magn Reson Imaging 2002;16:538–546.
16. Saunders DE, Howe FA, van den Boogaart A, Griffiths JR, Brown MM. Discrimination of metabolite from lipid and macromolecule resonances in cerebral infarction in humans using short echo proton spectroscopy. J Magn Reson Imaging 1997;7:1116–1121.
17. Seeger U, Klose U, Mader I, Grodd W, Nagele T. Parameterized evaluation of macromolecules and lipids in proton MR spectroscopy of brain diseases. Magn Reson Med 2003;49:19–28.
18. Chong DG, Kreis R, Bolliger CS, Boesch C, Slotboom J. Two-dimensional linear-combination model fitting of magnetic resonance spectra to define the macromolecule baseline using FiTAID, a Fitting Tool for Arrays of Interrelated Datasets. MAGMA 2011;24:147–164.
19. Snoussi K, Gillen JS, Horska A, Puts NA, Pradhan S, Edden RA, Barker PB. Comparison of brain gray and white matter macromolecule resonances at 3 and 7 Tesla. Magn Reson Med 2015;74:607–613.
20. Hong ST, Balla DZ, Shajan G, Choi C, Ugurbil K, Pohmann R. Enhanced neurochemical profile of the rat brain using in vivo (1)H NMR spectroscopy at 16.4 T. Magn Reson Med 2011;65:28–34.
21. Boer VO, van Lier AL, Hoogduin JM, Wijnen JP, Luijten PR, Klomp DW. 7-T (1) H MRS with adiabatic refocusing at short TE using radiofrequency focusing with a dual-channel volume transmit coil. NMR Biomed 2011;24:1038–1046.
22. Mekle R, Mlynarik V, Gambarota G, Hergt M, Krueger G, Gruetter R. MR spectroscopy of the human brain with enhanced signal intensity at ultrashort echo times on a clinical platform at 3T and 7T. Magn Reson Med 2009;61:1279–1285.
23. Pfeuffer J, Tkac I, Provencher SW, Gruetter R. Toward an in vivo neurochemical profile: quantification of 18 metabolites in short-echo-time (1)H NMR spectra of the rat brain. J Magn Reson 1999;141:104–120.
24. Tkac I, Andersen P, Adriany G, Merkle H, Ugurbil K, Gruetter R. In vivo 1H NMR spectroscopy of the human brain at 7 T. Magn Reson Med 2001;46:451–456.
25. Provencher SW. Automatic quantitation of localized in vivo 1H spectra with LCModel. NMR Biomed 2001;14:260–264.
26. Fuchs A, Luttje M, Boesiger P, Henning A. SPECIAL semi-LASER with lipid artifact compensation for 1H MRS at 7 T. Magn Reson Med 2013;69:603–612.
27. Schaller B, Xin L, Cudalbu C, Gruetter R. Quantification of the neurochemical profile using simulated macromolecule resonances at 3 T. NMR Biomed 2013;26:593–599.
28. Vaughan JT, Garwood M, Collins CM, et al. 7T vs. 4T: RF power, homogeneity, and signal-to-noise comparison in head images. Magn Reson Med 2001;46:24–30.
29. Scheenen TW, Klomp DW, Wijnen JP, Heerschap A. Short echo time 1H-MRSI of the human brain at 3T with minimal chemical shift displacement errors using adiabatic refocusing pulses. Magn Reson Med 2008;59:1–6.
30. Avdievich NI, Giapitzakis I-A, Pfrommer A, Henning A. Decoupling of a tight-fit transceiver phased array for human brain imaging at 9.4T: loop overlapping rediscovered. Magn Reson Med 2017. doi: 10.1002/mrm.26754.
31. Giapitzakis I-A, Shao T, Avdievich N, Mekle R, Kreis R, Henning A. Metabolite-cycled STEAM and semi-LASER localization for MR spectroscopy of the human brain at 9.4T. Magn Reson Med 2017. doi: 10.1002/mrm.26873.
32. Avdievich NI. Transceiver-phased arrays for human brain studies at 7 T. Appl Magn Reson 2011;41:483–506.

33. Adriany G, Van de Moortele PF, Ritter J, Moeller S, Auerbach EJ, Akgun C, Snyder CJ, Vaughan T, Ugurbil K. A geometrically adjustable 16-channel transmit/receive transmission line array for improved RF efficiency and parallel imaging performance at 7 Tesla. Magn Reson Med 2008;59:590–597.
34. Gilbert KM, Belliveau JG, Curtis AT, Gati JS, Klassen LM, Menon RS. A conformal transceive array for 7 T neuroimaging. Magn Reson Med 2012;67:1487–1496.
35. Avdievich NI, Hoffmann J, Shajan G, Pfrommer A, Giapitzakis IA, Scheffler K, Henning A. Evaluation of transmit efficiency and SAR for a tight fit transceiver human head phased array at 9.4 T. NMR Biomed 2017;30:1–12.
36. Avdievich NI, Giapitzakis IA, Henning A. Optimization of the receive performance of a tight-fit transceiver phased array for human brain imaging at 9.4T. In Proceedings of the 25th Annual Meeting of ISMRM, Honolulu, USA, 2017. Abstract 4309.
37. Avdievich N, Walzog J, Steffen T, Henning A. Development of a low cost multi-channel tune and match device for transceiver arrays at high magnetic fields. In Proceedings of the 32nd Annual Scientific Meeting of the ESMRMB, Edinburgh, UK, 2015. Abstract S445.
38. Pfrommer A, Avdievich NI, Henning A. Four channel transceiver array for functional magnetic resonance spectroscopy in the human visual cortex at 9.4 T. In Proceedings of the 22nd Annual Meeting of ISMRM, Milan, Italy, 2014. Abstract 1305.
39. Tannús A, Garwood M. Improved performance of frequency-swept pulses using offset-independent adiabaticity. J Magn Reson A 1996; 120:133–137.
40. Xin L, Schaller B, Mlynarik V, Lu H, Gruetter R. Proton T1 relaxation times of metabolites in human occipital white and gray matter at 7 T. Magn Reson Med 2013;69:931–936.
41. Deelchand DK, Van de Moortele PF, Adriany G, Iltis I, Andersen P, Strupp JP, Vaughan JT, Ugurbil K, Henry PG. In vivo 1H NMR spectroscopy of the human brain at 9.4 T: initial results. J Magn Reson 2010;206:74–80.
42. Mugler JP III, Brookeman JR. Three-dimensional magnetization-prepared rapid gradient-echo imaging (3D MP RAGE). Magn Reson Med 1990;15:152–157.
43. Gruetter R, Tkac I. Field mapping without reference scan using asymmetric echo-planar techniques. Magn Reson Med 2000;43:319–323.
44. Versluis MJ, Kan HE, van Buchem MA, Webb AG. Improved signal to noise in proton spectroscopy of the human calf muscle at 7 T using localized B1 calibration. Magn Reson Med 2010;63:207–211.
45. Hock A, MacMillan EL, Fuchs A, Kreis R, Boesiger P, Kollias SS, Henning A. Non-water-suppressed proton MR spectroscopy improves spectral quality in the human spinal cord. Magn Reson Med 2013;69: 1253–1260.
46. Dreher W, Leibfritz D. New method for the simultaneous detection of metabolites and water in localized in vivo 1H nuclear magnetic resonance spectroscopy. Magn Reson Med 2005;54:190–195.
47. Klose U. In vivo proton spectroscopy in presence of eddy currents. Magn Reson Med 1990;14:26–30.
48. Bydder M, Hamilton G, Yokoo T, Sirlin CB. Optimal phased-array combination for spectroscopy. Magn Reson Imaging 2008;26:847–850.
49. Lopez-Kolkovsky AL, Meriaux S, Boumezbeur F. Metabolite and macromolecule T1 and T2 relaxation times in the rat brain in vivo at 17.2T. Magn Reson Med 2016;75:503–514.
50. de Graaf RA. In vivo NMR spectroscopy: principles and techniques: 2nd edition. Chichester, UK: John Wiley & Sons; 2007.
51. Považan M, Hangel G, Strasser B, Gruber S, Chmelik M, Trattnig S, Bogner W. Mapping of brain macromolecules and their use for spectral processing of 1H-MRSI data with an ultra-short acquisition delay at 7 T. NeuroImage 2015;121:126–135.
52. Gasparovic C, Song T, Devier D, Bockholt HJ, Caprihan A, Mullins PG, Posse S, Jung RE, Morrison LA. Use of tissue water as a concentration reference for proton spectroscopic imaging. Magn Reson Med 2006;55:1219–1226.
53. Ernst T, Kreis R, Ross BD. Absolute quantitation of water and metabolites in the human brain. I. Compartments and water. J Magn Reson B 1993;102:1–8.
54. Hagberg GE, Bause J, Ethofer T, et al. Whole brain MP2RAGE-based mapping of the longitudinal relaxation time at 9.4T. NeuroImage 2017;144:203–216.
55. Bartha R, Michaeli S, Merkle H, Adriany G, Andersen P, Chen W, Ugurbil K, Garwood M. In vivo 1H2O T2 + measurement in the human occipital lobe at 4T and 7T by Carr-Purcell MRI: detection of microscopic susceptibility contrast. Magn Reson Med 2002;47:742–750.
56. Kreis R. The trouble with quality filtering based on relative Cramér-Rao lower bounds. Magn Reson Med 2016;75:15–18.
57. Hoffmann J, Shajan G, Scheffler K, Pohmann R. Numerical and experimental evaluation of RF shimming in the human brain at 9.4 T using a dual-row transmit array. MAGMA 2014;27:373–386.
58. Behar KL, Ogino T. Assignment of resonance in the 1H spectrum of rat brain by two-dimensional shift correlated and J-resolved NMR spectroscopy. Magn Reson Med 1991;17:285–303.
59. Kreis R. Issues of spectral quality in clinical 1H-magnetic resonance spectroscopy and a gallery of artifacts. NMR Biomed 2004;17:361–381.
60. Nassirpour S, Chang P, Henning A. High resolution maps of individual macromolecule components in the human brain at 9.4T. In Proceedings of the 25th Ammual Meeting of ISMRM, Honolulu, 2017. Abstract 6826.

SUPPORTING INFORMATION

Additional Supporting Information may be found in the online version of this article.

FIG. S1. A: S_{12} matrix obtained using the HS phantom. **B**: Loop numbering in the 8Tx16Rx transceiver phased array. **C**: Block-diagram of the unbalanced 3-way splitter. The ratio of the output power measures 2:1:1 for ports 1, 2, and 3, respectively.
FIG. S2. Macromolecular spectra acquired from the 7 volunteers participated in this study (Vol. 1-7). Data were acquired from a voxel of $2 \times 2 \times 2\,cm^3$ placed in a mixed area of GM, WM, and CSF in the occipital lobe (left) and in the left parietal lobe (right), respectively.
FIG. S3. LCModel fitting results of the individual MM spectra for 4 volunteers (Vol. #7, Vol. #6, Vol. #5, and Vol. #2), for two different brain regions (right) occipital lobe and (left) left parietal lobe, using as a basis the 15 MM components created after the parametrization procedure (Fig. 5).

SPECTROSCOPIC METHODOLOGY – Full Papers

Magnetic Resonance in Medicine 79:2863–2873 (2018)

In Vivo Characterization of the Downfield Part of ^{1}H MR Spectra of Human Brain at 9.4 T: Magnetization Exchange With Water and Relation to Conventionally Determined Metabolite Content

Nicole D. Fichtner,[1,2,3,4†] Ioannis-Angelos Giapitzakis,[5,6†] Nikolai Avdievich,[5] Ralf Mekle,[7] Daniel Zaldivar,[5] Anke Henning,[5,8] and Roland Kreis [1,2]*

Purpose: To perform exchange-rate measurements on the in vivo human brain downfield spectrum (5–10 ppm) at 9.4 T and to compare the variation in concentrations of the downfield resonances and of known upfield metabolites to determine potential peak labels.

Methods: Non-water-suppressed metabolite cycling was used in combination with an inversion transfer technique in two brain locations in healthy volunteers to measure the exchange rates and T_1 values of exchanging peaks. Spectra were fitted with a heuristic model of a series of 13 or 14 Voigt lines, and a Bloch–McConnell model was used to fit the exchange rate curves. Concentrations from non-water-inverted spectra upfield and downfield were compared.

Results: Mean T_1 values ranged from 0.40 to 0.77 s, and exchange rates from 0.74 to 13.8 s^{-1}. There were no significant correlations between downfield and upfield concentrations, except for N-acetylaspartate, with a correlation coefficient of 0.63 and $P < 0.01$.

Conclusions: Using ultrahigh field allowed improved separation of peaks in the 8.2 to 8.5 ppm amide proton region, and the exchange rates of multiple downfield resonances including the 5.8-ppm peak, previously tentatively assigned to urea, were measured in vivo in human brain. Downfield peaks consisted of overlapping components, and largely missing correlations between upfield and downfield resonances—although not conclusive—indicate limited contributions from metabolites present upfield to the downfield spectrum. **Magn Reson Med 79:2863–2873, 2018. © 2017 International Society for Magnetic Resonance in Medicine.**

Key words: proton magnetic resonance spectroscopy; 9.4 T; human brain; metabolites; downfield; T_1 relaxation time; exchange rates

INTRODUCTION

Proton magnetic resonance spectroscopy is a noninvasive method that can detect metabolites and quantify their concentrations and other characteristics, as well as any pathological changes, in these parameters. Recent development and optimization of non-water-suppressed (nWS) spectroscopy for in vivo experiments (1,2) has expanded the range of measurable peak characteristics to include exchange rates. The use of water suppression causes exchanging peaks to be suppressed, complicating quantification. Using a nWS sequence allows not only for improved quantification, but also for exchange-rate measurements using methods such as inversion transfer. In particular, several peaks on the downfield side of water (typically between 5.0 and 10.0 ppm) have protons that exchange with water. In contrast, no peaks on the upfield (right) side of the water peak have direct chemical exchange with water, although there is some evidence of magnetization transfer effects (3). As yet, the downfield peaks remain mostly unlabeled, although previous studies on in vivo human downfield brain spectroscopy have investigated exchange rates or relaxation rates at a range of field strengths (2,4–6).

Exchange rates are of interest not only for optimization of spectroscopy experiments and sequence parameters, but also for pathology, where concentrations may vary with the degree of disease severity or metabolic activity, or where exchange rates may vary with changes in pH. Chemical exchange saturation transfer (CEST) experiments in particular take advantage of exchange to measure the enhanced signal from exchanging species (7), and have thus far been able to investigate tumor severity and treatment, such as using amide proton transfer and dynamic glucose-enhanced experiments (8,9). CEST can measure

[1]Department of Radiology, Neuroradiology, and Nuclear Medicine, University of Bern, Bern, Switzerland.

[2]Department for BioMedical Research, University of Bern, Bern, Switzerland.

[3]Graduate School for Cellular and Biomedical Sciences, University of Bern, Bern, Switzerland.

[4]Institute for Biomedical Engineering, UZH and ETH Zurich, Zurich, Switzerland.

[5]Max Planck Institute for Biological Cybernetics, Tübingen, Germany.

[6]Graduate School of Neural and Behavioural Sciences, Tübingen, Germany.

[7]Center for Stroke Research Berlin (CSB), Charité Universitätsmedizin Berlin, Berlin, Germany.

[8]Institute of Physics, Ernst-Moritz Arndt University Greifswald, Greifswald, Germany.

*Correspondence to: Roland Kreis, Ph.D., Department for BioMedical Research/AMSM, University of Bern, Erlachstrasse 9a, CH-3012 Bern, Switzerland. E-mail: roland.kreis@insel.ch

This work was supported by the Swiss National Science Foundation (No. 320030-156952). Part of the project (I.A.G.) was co-sponsored by the European Social Fund and national funds (NSRF 2007–2013) through the Greek State Scholarships Foundation (I.K.Y.).

†These authors contributed equally to this work.

Received 30 June 2017; revised 12 September 2017; accepted 22 September 2017

DOI 10.1002/mrm.26968

Published online 16 October 2017 in Wiley Online Library (wileyonlinelibrary.com).

© 2017 International Society for Magnetic Resonance in Medicine

exchange from a range of species with varying exchange rates, and mostly investigates species downfield of water; increased knowledge of the downfield resonances is therefore also of interest for the CEST community.

Although suggestions of labels for several downfield resonances have been made (4,10), most remain unlabeled. Additional characterization of downfield peaks and comparison to upfield concentrations in different brain locations may aid in determining peak labels. Furthermore, ultrahigh field strengths may aid due to the advantage of improved peak separation and increased signal-to-noise ratio, leading to acquisition of smaller, more homogeneous voxels within reasonable measurement times. However, as the field strength is increased, the shorter T_2 values of the peaks (11,12) require sequences with short echo time (TE), to minimize signal loss. In addition, at 9.4 T, even more so than at 7 T, B_1 radiofrequency (RF) field inhomogeneity and power drop-off within the brain may render it difficult to achieve sufficient transmit power in the areas of interest (13). Therefore, for these experiments performed at 9.4 T for improved peak separation, a home-built coil with appropriate power distribution and phase increment (14), and a short TE sequence (stimulated echo acquisition mode [STEAM] (15)) was used for enhanced acquisition. To perform exchange-rate measurements, the metabolite cycling (MC) (1) nWS sequence was used in combination with inversion transfer to investigate in vivo brain metabolites. Furthermore, both upfield and downfield data were acquired in two different brain locations to compare known metabolite concentrations to downfield peak concentrations.

METHODS

Subjects

Eleven healthy volunteers (mean age: 28 ± 3 years, 8 males, 3 females) were scanned for the occipital region study, and another 11 healthy volunteers (mean age: 27 ± 5 years, 7 males, 4 females) were scanned for the left parietal white matter (WM) study. Written informed consent was given by all subjects before the examination, and the study was approved by the local ethics board. Spectra from two volunteers from the WM group were not included in the analysis as a result of excessive motion artifacts in one or more of the data sets.

Hardware Setup and RF Coil

All measurements were carried out on a Siemens 9.4 T whole-body MRI scanner (Erlangen, Germany) equipped with a SC72 gradient system with a maximal nominal amplitude of 40 mT/m and a maximal slew rate of 200 T/m/s. A home-built proton coil with eight transmit and 16 receive channels was used (16). Available peak power from the amplifiers was 8 kW with 50% line loss. The coil was tuned and matched for each volunteer individually before the beginning of the experiment using a home-built tuning and matching box (17) and a portable probe tuning device (Morris Instruments, Ottawa, Canada), ensuring minimal reflected power.

For this work, we used a 16-channel phased array consisting of eight overlapped transceiver loops (10-cm square loops) placed on an elliptical holder (clearance 23 cm height $\times$ 20 cm width) parallel to its surface (i.e., "horizontal" loops), and eight receive-only loops each located at the center of the horizontal loops perpendicular to the surface of the holder (i.e., "vertical" loops) (16). To increase the amount of RF power delivered to the local surface coils, we used two-way and three-way splitters with 90° phase shift between the channels. More details on the array design are published elsewhere (16).

Data Acquisition

High-resolution images from 2-dimensional fast low-angle shot (FLASH) scans (in-plane resolution: $0.7 \times 0.7\,mm^2$; slice thickness: 3.5 mm; 25 slices) were acquired in axial, sagittal, and coronal orientations to facilitate the placement of spectroscopic voxels. For the study on a region of interest (ROI) in left parietal WM (subsequently referred to as the WM ROI), a $4.0 \times 2.0 \times 1.5\,cm^3$ voxel was placed in the left-cerebral WM (average composition (14): WM: 78.6%; gray matter (GM): 19.3%; cerebrospinal fluid (CSF): 2.0%). For the study on a slightly more GM-enriched area (subsequently referred to as the occipital ROI), a $2.0 \times 2.0 \times 3.0\,cm^3$ voxel was selected in a mixed GM and WM area in the occipital lobe (average composition (18): WM: 54.8%; GM: 41.5%; CSF: 3.6%). Both voxel positions are shown in Figure 1. In particular, for the voxel located in the occipital lobe, only the three bottom coil elements were used, whereas in the case of the left-cerebral WM, the two left-lateral coil elements were driven. For both voxel placements, first- and second-order B_0 shimming was performed using FASTESTMAP (19), and voxel-based power calibration was executed (20).

Localized single-voxel downfield (96 acquisitions) and upfield spectra (64 acquisitions) were acquired from each volunteer for both brain regions using MC STEAM (TE/mixing time/repetition time: 10/50/5000 ms). In particular, a STEAM sequence was incorporated with an asymmetric adiabatic inversion pulse (1) during the mixing time optimized for MC at 9.4 T (18). For the selection of the three orthogonal slices, a hamming-filtered 90° sinc pulse with a bandwidth of approximately 8 kHz was used. The asymmetric adiabatic inversion pulse had a duration T_p of 22.4 ms and was constructed from the first half of a sech pulse (hyperbolic secant $(HS)_{1/2}$, $R = 31.415$) for $0.9\,T_p$ and the second half of a tanh/tan pulse ($R = 100$) for $0.1\,T_p$. The detailed nomenclature and the pulse parameters are described in the study of Hwang et al (1). In this study, the asymmetric inversion pulse was applied with a minimum B_1^+ of 22 μT and transmit frequency of ± 350 Hz. Moreover, the frequency sweep range of the frequency modulation extended from −22.7 to 0.24 kHz (18).

For the measurement of magnetization transfer between water and protons from downfield resonances, the MC-STEAM localization scheme was preceded by a frequency-selective pulse of duration 40 ms for the inversion of the water resonance (Hamming-filtered sinc pulse, bandwidth: 100 Hz) with varying inversion delay times (41, 96, 171, 321, 671, 1321, and 3021 ms;

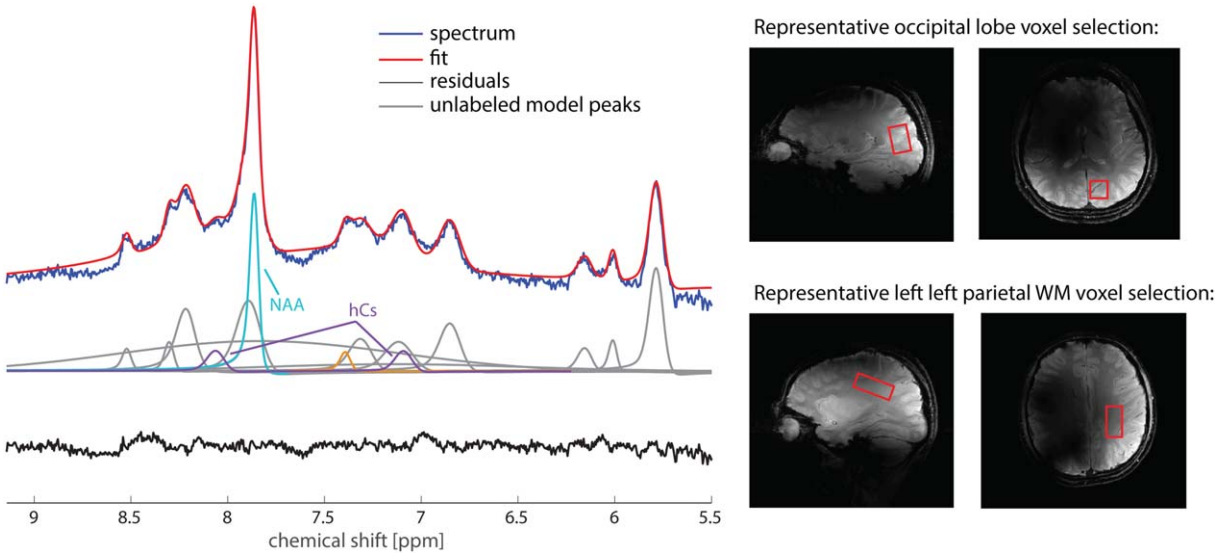

FIG. 1. Averaged downfield spectrum with no water pre-inversion for the occipital ROI series, overlaid with the fitted spectrum, the model peaks (gray for unlabeled, color for NAA and homocarnosine (hCs) with their respective labels), and with residuals shown below. Residuals indicate a decent fit for most peaks. No filtering was used. The WM ROI model is the same except for one removed peak, at 7.4 ppm, highlighted in orange. Also shown are representative locations of the voxels in the occipital lobe (above) and in the left-parietal WM region (below).

96 acquisitions). Data were acquired with 4096 time points and an 8-kHz spectral width. A phase cycling scheme of 16 steps was implemented. To center the voxel at the correct frequency, the transmit reference frequency for the localization pulses of MC STEAM was set at 7 ppm for the acquisition of downfield spectra and at 2.3 ppm for upfield data. Neither water presaturation nor outer volume suppression was applied. Finally, to avoid any influence of MC pulses on absolute quantification, water-reference signals (16 acquisitions) were measured without MC or water suppression. The total exam time for each subject was approximately 90 min.

Magnetic Resonance Spectroscopy Data Analysis

All data were saved in raw format and exported and reconstructed in MATLAB (MATLAB and Statistics Toolbox Release 2014b, The MathWorks Inc, Natick, MA). Data were processed using home-written software for frequency alignment in the time domain based on the nWS spectra (18,21), averaging, eddy current correction (22), and coil combination using singular-value decomposition based on the MC water data (23). Scaling of even- versus odd-numbered acquisitions with a scaling factor F_s was performed to account for the asymmetric effect of the metabolite cycling pulse applied alternately on either side of the water peak (1). Zeroth- and first-order phasing were performed manually on the individuals' spectra using jMRUI (24). The spectra from the different inversion times were aligned between volunteers, and the complete data sets from the best nine subjects from each of WM and GM were averaged to create the model spectra. nWS water data were processed using the same methods.

Both water and downfield metabolite spectra were fitted similarly to previous work (4) using the Fitting Tool for Arrays of Interrelated Datasets (FiTAID) (25) by developing a model using the averaged data sets. Prior knowledge was defined with 13 peaks for supraventricular and 14 peaks for occipital lobe in the region between 5.5 and 9 ppm (Fig. 1). The peak from N-acetylaspartate (NAA) at 7.82 ppm was defined as a binary pattern as modeled in VeSPA (26), while homocarnosine was defined at two locations, 7.05 and 8.02 ppm, as was previously found to be reasonable (4,27). Other lines used in the model were based on visual appearance of the peaks, and included several broad lines to account for the baseline of the spectrum, a line to fit the residual water, and numerical spectral patterns (25) as modeled in VeSPA to account for the upfield spectra and baseline. Fitting errors for the concentrations were determined as Cramer–Rao lower bounds (CRLB) (28). Peak concentrations from FiTAID were scaled by the appropriate average water-scaling factor: 75% (41,056 mM) for GM (18) and 69% (38,348 mM) for WM (14) based on previous work using the same voxel placement. To obtain these average water-scaling factors in the previous publication, average GM, WM, and CSF percentages for each examined voxel were calculated using a home-built MATLAB script that used segmentation algorithms within SPM8 (Institute of Neurology, University College London, United Kingdom) and 3-dimensional magnetization-prepared rapid gradient-echo (MPRAGE) images (voxel size: $1 \times 1 \times 1\,mm^3$) that had been acquired for each volunteer at 3 T. In particular, the 9.4T MPRAGE image from each volunteer was registered on the corresponding 3T image assuming a rigid body transformation, and the calculated transformation matrix was then used to transform the spectroscopy voxel to the 3T MPRAGE image. The specific values for the water scaling factor (W_{SF}) were calculated using the following equation:

$$W_{SF} = 55126\ \text{mM} \cdot \frac{(f_{GM} \cdot a_{GM} + f_{WM} \cdot a_{WM} + f_{CSF} \cdot a_{CSF})}{1 - f_{CSF}}$$

where 55,126 mM is the concentration of pure water at body temperature; f_{GM}, f_{WM}, and f_{CSF} correspond to the GM, WM, and CSF volume percentages, respectively; and the relative densities of NMR-visible water ($a_{GM} = 0.78$; $a_{WM} = 0.65$; $a_{CSF} = 0.97$) were taken from (29). Differences in downfield concentrations between occipital and WM ROIs were compared using the Wilcoxon rank-sum test.

Upfield spectra were fitted using LCModel (30), with methods similar to previously published work (18). In particular, a basis set consisting of 19 metabolites (alanine, aspartate, creatine, gamma-aminobutyric acid, glucose, glutathione, glutamate, glutamine, glycerophosphorylcholine, glycine, lactate, myo-inositol, NAA, N-acetylaspartylglutamic acid, phosphocholine, phosphocreatine, phosphorylethanolamine, scyllo-inositol, and taurine) was simulated with PyGAMMA (31) based on experimentally measured chemical shifts and J-coupling values (32–34). The MC-STEAM basis set was simulated using a STEAM sequence with ideal pulses. Measured macromolecular templates for both brain regions were included in the model (14). In addition, the hidden parameter of LCModel DKNTMN, which controls the baseline rigidity, was set to 0.6. A minor lipid contamination in a few subjects, caused by the absence of outer volume suppression, was handled by omitting a section of the spectrum from 1.1 to 1.8 ppm from the χ^2 fit range (using the PPMGAP parameter), to prevent a potential artifactual influence on the estimation of the macromolecular content. (It was made sure that the lipid artifact from the methylene protons was small enough, such that the rest of the lipid spectrum would be too small to substantially interfere outside the excluded fitting range.)

For the upfield spectrum, absolute metabolite concentrations in mM ($[\text{Met}]_{\text{mM}}$) without correction for relaxation were calculated using LCModel water normalized concentrations ($[\text{Met}]_{\text{Nwater}}$) through the following equation:

$$[\text{Met}]_{\text{mM}} = [\text{Met}]_{\text{Nwater}} \cdot W_{SF} \cdot \frac{2}{1 + F_s}$$

where W_{SF} is the mean water content as described previously, and the factor $2/(1 + F_s)$ was introduced to correct for the multiplication of even-numbered acquisitions with F_s (1). Because of likely effects of motion between the upfield scans (acquired first) and the non-MC, nWS water scans used for scaling (acquired last), the upfield GM concentrations showed large intersubject variations. To remove the effects of the variable water reference on the occipital ROI upfield data, the upfield occipital ROI metabolite concentrations were rescaled based on the total creatine peak. (More specifically, the cohort average of total creatine was conserved from the values obtained by water scaling, while all individual spectra were rescaled to yield identical total creatine content.)

For WM ROIs and for downfield occipital ROIs, the water variances were smaller; therefore, the concentrations were left relative to water. Spearman correlation coefficients and statistical significance were calculated between several downfield peak areas and upfield metabolite concentrations, and Spearman testing was used because of the small sample size ($N = 20$). The 6.8, 7.0, 7.3, 8.2, 8.3, and 8.5 ppm peaks were compared with glutathione, gamma-aminobutyric acid, glutamine, glutamate, or total glutamine/glutamate, which were several of the suggested assignments for those downfield peaks. Correlation coefficients were also calculated between the overall upfield macromolecule concentration and the 6.8, 7.0, and 7.3 ppm peaks downfield. For the WM ROI, in which concentrations were not rescaled relative to total creatine, comparisons were also made between the downfield peak at 6.8 ppm and total creatine from the upfield spectra.

Magnetization Exchange Model

Exchange between the longitudinal magnetization of inverted water and the downfield metabolites was modeled using the Bloch–McConnell equations for a two-pool system (35). The model started with an initial magnetization of zero for both pools, considered as saturation recovery after the STEAM localization sequence. The second step consisted of the subsequent inversion pulse and recovery, with the corresponding initial conditions after the saturation recovery phase, as in previous published downfield work (2). The third step included numerical simulations using the Bloch–McConnell equations, ideal pulses, and phase dispersion into four equal components to account for exchange and recovery during the STEAM sequence itself. The MC pulse was simplified as an ideal nonadiabatic RF pulse, with the assumption that only the metabolites were affected. The water T_1, equilibrium magnetization, and inversion pulse efficiency, which were used as constants in the fitting of the exchange curves of the metabolite peaks, were determined using an inversion recovery model in FiTAID (25), using three components for water: brain water, cerebrospinal fluid water, and myelin water, the latter two of which had upper limits of 10 and 5%, respectively, for GM, and 5 and 10%, respectively, for WM. The inversion pulse efficiency was found to be lower than expected (yielding an effective average flip angle of 117° for the WM ROI, and 126° for the occipital ROI), which made its inclusion in the model necessary to account for reduced inversion and therefore less exchange than expected for an ideal 180° pulse. Six peaks were modeled for exchange in WM: 5.8, 6.8, 8.2, 8.3, and 8.5 ppm, and a combined NAA and broader underlying component (taken separately, neither component yielded a reasonable exchange curve). An additional peak at 7.3 ppm was fitted for the occipital ROI. The exchange curves yielded T_1 and exchange rates for the various metabolite peaks fitted. For occipital lobe, the individual data sets for 7.3 ppm were not fitted because of larger errors in the individual points; for this case, only the average data set was fitted. Exchange rates and T_1 values were compared between occipital and WM ROIs using the Wilcoxon rank-sum test.

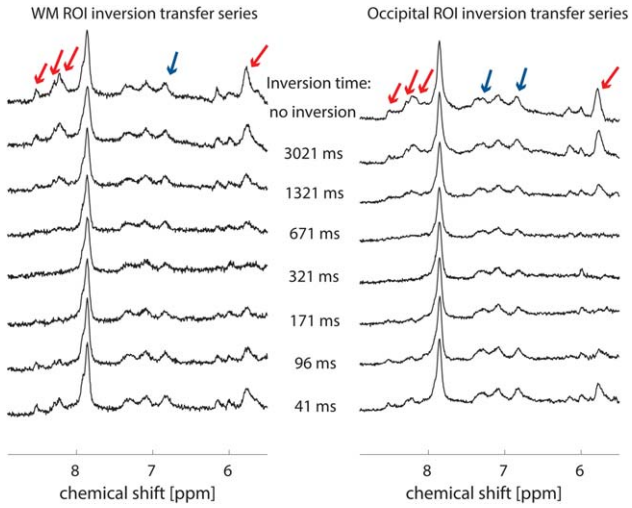

FIG. 2. Averaged inversion transfer series for WM and occipital ROIs. Peaks indicated by red arrows (at 5.8, 8.2, 8.3, and 8.5 ppm) show fast exchange, leading to almost complete disappearance of the respective signals for a water-inversion delay of approximately half a second. Peaks shown in blue also show exchange, but at a slower rate, perhaps because of the exchange being from underlying components or only part of the peak.

RESULTS

The averaged results for non–water inverted, nWS spectra for both WM and occipital ROIs are shown in Figure 2. Several peaks show exchange over the different inversion times, as they decrease in amplitude before recovering again, with the 5.8-ppm peak and the peaks in the region between 8.2 and 8.5 ppm in particular showing fast exchange, decreasing to close to 0 by 300 ms. Exchanging peaks fitted using the exchange model are highlighted by red arrows for fast exchange, and blue for apparent slower exchange, which was in some cases not quantifiable. An individual data set from one volunteer for the occipital ROI, including fit and residuals, is shown in Figure 3 as a sample of data quality (an individual data set from one volunteer for the WM ROI can be seen in Supporting Fig. S1). Appropriateness of the model can be determined from the residuals from both the model shown in Figure 1 and the individual data set. Upfield spectra from the same volunteers as in Figure 3 and Supporting Figure S1 are shown in Figure 4, along with the corresponding LCModel fits, baselines, and residuals.

Mean downfield concentrations found from the non-water-inverted spectra for the peaks of interest are provided in Table 1, with errors given as standard deviations over the cohort. Specifically, homocarnosine, the 6.0-ppm peak, the 7.3-ppm peak, the 8.3-ppm peak, and NAA show significant differences between WM and occipital lobe with $P < 0.05$. For comparisons between upfield and downfield peak areas, NAA was found to have a Spearman correlation coefficient of 0.63 and $P < 0.01$; the corresponding NAA scatter plot is shown in Figure 5. No other correlations with $P < 0.1$ were found for any of the combinations of the downfield peaks to upfield metabolite concentrations described in the methods; the corresponding scatter plots for these combinations are shown in Supporting Figure S2.

Box plots for T_1 values and exchange rates are shown in Figures 6 and 7, respectively. Table 2 lists the mean values for T_1 and exchange rates. Mean metabolite T_1 values ranged from 0.22 s for the 8.3-ppm peak in the occipital ROI up to 0.77 s for the 5.8-ppm peak in WM. Fitted exchange curves for the exchanging peaks are shown for the average WM and occipital ROI series in Figure 8. Exchange rates were within a range of 0.74 s^{-1} for the combined NAA peak in the occipital ROI to

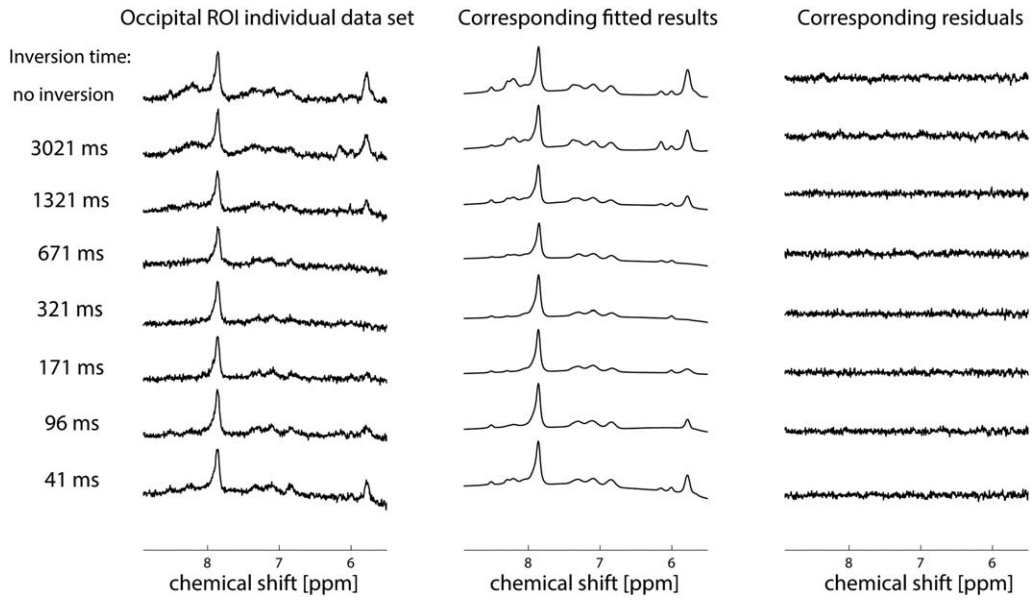

FIG. 3. Representative occipital ROI inversion transfer series from an individual volunteer, along with the corresponding fitted spectra and residuals, indicating the quality of the data and the suitability of the model. For a representative inversion transfer series for the WM ROI, see Supporting Figure S1.

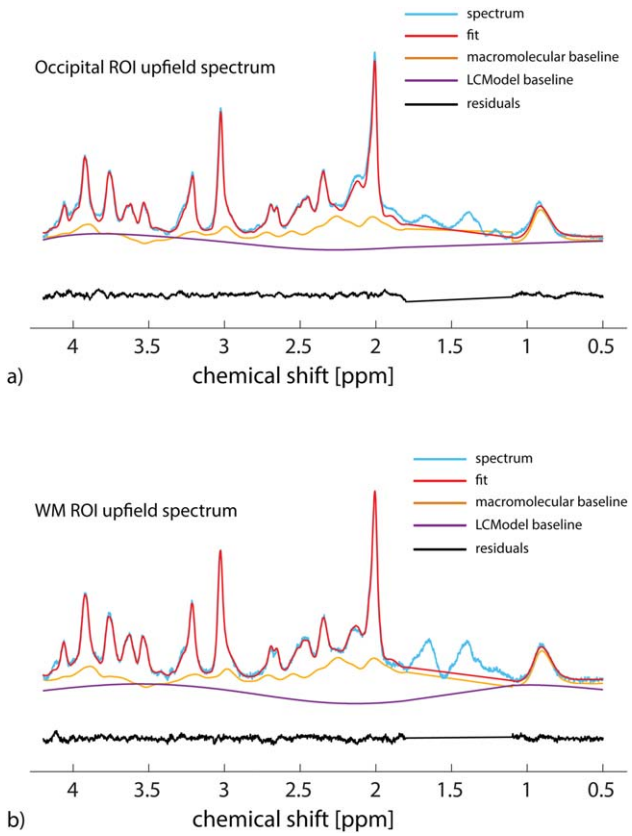

FIG. 4. Representative upfield spectra along with the LCModel fits, baselines, and residuals for the occipital ROI (**a**) and the WM ROI (**b**) from the same volunteers as in Figure 3 and Supporting Figure S1. The section between 1.1 and 1.8 ppm, which was not critical to the analysis, was removed from the LCModel χ^2 fit as a result of lipid artifacts, as described in the methods by the PPMGAP parameter.

13.8 s^{-1} for the 8.3-ppm peak in the occipital ROI. The 7.3-ppm peak for the average occipital ROI series yielded a T_1 of 0.42 s and an exchange rate of 1.9 s^{-1}. Between WM and occipital ROIs, the only significant differences found ($P < 0.05$) were for T_1 values for the 8.2- and 8.3-ppm peaks, as highlighted in Figure 6.

DISCUSSION

The nWS spectra acquired in this study provided improved spectral resolution and higher exchanging peak intensity compared with lower field strength (2) or experiments with water presaturation (4), yielding in particular further separable peaks in the region between 8.2 and 8.5 ppm as well as additional exchanging peaks closer to water. The inversion transfer experiments performed allowed the evaluation of 13 or 14 peaks for WM and occipital ROIs, respectively, for extraction of concentrations and, for several of the peaks, exchange rates and T_1 relaxation values. This study also included upfield data in both WM and occipital ROIs for additional peak concentration comparisons, to determine any correlations between known upfield metabolite concentrations and the unknown downfield resonances.

Concentrations

The concentrations of the downfield metabolites from the two ROIs were significantly ($P < 0.05$) different for a few peaks only: homocarnosine, the 6.0-, 7.3- and 8.3-ppm peaks, and NAA. They were not significantly different for the remainder. Standard deviations for most of the peaks were relatively small, indicating good agreement across subjects. The 5.8-ppm peak, being closer to water and therefore more prone to any artifacts related to imperfect water cancelation, was slightly more difficult to fit and hence has a somewhat larger standard deviation. The 7.3-ppm peak may be different as a result of the additional modeling of the 7.4 ppm for the occipital ROI. The concentration of the narrow NAA doublet in the occipital ROI was 10.5 ± 1.2 mM, and in the WM ROI it had a value of 8.4 ± 1.5 mM, which was found to be significantly different ($P < 0.05$). Both of these values are

Table 1
Mean Downfield Concentrations for Both WM and Occipital ROIs for the Peaks of Interest, Presented as Mean ± Standard Deviation Over the Cohort

	Occipital ROI		WM ROI	
	Mean concentration ± SD (mM)	Mean CRLB (mM)	Mean concentration ± SD (mM)	Mean CRLB (mM)
hCs[a]	1.02 ± 0.39	0.141	0.35 ± 0.21	0.147
5.8 ppm	4.58 ± 1.12	0.138	4.02 ± 1.89	0.357
6.0 ppm[a]	1.25 ± 0.73	0.117	0.62 ± 0.36	0.238
6.1 ppm	1.21 ± 0.74	0.124	0.81 ± 0.33	0.123
6.8 ppm	2.87 ± 0.68	0.183	2.96 ± 0.82	0.294
7.0 ppm	1.96 ± 1.14	0.290	2.96 ± 0.73	0.422
7.3 ppm[a]	1.94 ± 0.28	0.196	2.93 ± 0.84	0.351
7.4 ppm	0.56 ± 0.21	0.124	—	—
8.2 ppm	4.16 ± 0.45	0.219	3.93 ± 0.80	0.266
8.3 ppm[a]	0.92 ± 0.32	0.120	0.64 ± 0.12	0.114
8.5 ppm	0.89 ± 0.32	0.106	0.78 ± 0.21	0.118
NAA[a]	10.52 ± 1.16	0.404	8.43 ± 1.54	0.416
NAA shoulder	4.91 ± 0.79	0.293	5.07 ± 1.15	0.333

Note: Concentrations are obtained from the non-water-inverted spectra. Mean CRLB over the cohort are also included. The CRLB are only valid for a correct model, which is definitely not strictly the case in this setting, where we have composite peaks heuristically modeled as a single entity. SD, standard deviation; CRLB, Cramer–Rao lower bounds; hCs, homocarnosine.
[a]A significant difference was found between the occipital and the WM ROI concentrations with $P < 0.05$.

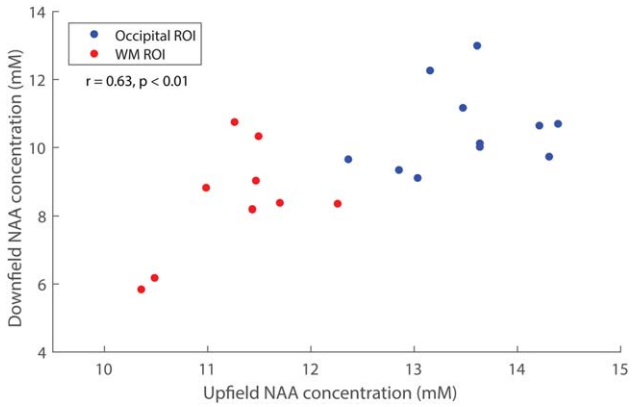

FIG. 5. Scatter plot of the downfield NAA peak concentrations versus the upfield NAA concentrations, plotted with separate colors to distinguish the WM ROI and occipital ROI concentrations. Scatter plots of the other correlations tested are shown in Supporting Figure S2.

in agreement with previously published work on NAA concentrations (36). Homocarnosine was found to be significantly higher in the occipital ROI at 1.02 ± 0.49 mM than in WM at 0.35 ± 0.21 mM. This difference may be the result of the fitting model and procedure, as the concentrations are low, but may also be caused by differences between voxel locations. However, previous literature is in disagreement about whether a difference is expected (37). If so, the WM ROI would be expected to have a higher concentration than occipital ROI, contrary to what was seen in the present study. Other resonances have concentrations that are lower than those found at 7 T (4), possibly related to the presence of broad underlying components that were additionally included in the fitting model at 9.4 T, such as in the range of 6.8 to 7.3 ppm, where the concentrations at 9.4 T are lower than at 7 T. Differences between the 9.4 T and 7 T experiments are also expected as a result of the use of water suppression at 7 T, where exchanging peaks would be reduced. Concentrations of the 6.0- and 6.1-ppm peaks are higher at 9.4 T than at 7 T, which is likely due to the presence of slow exchange. Similarly, concentrations of resonances in the 8.2- to 8.5-ppm region could not be compared as a result of fast exchange and the use of water suppression at 7 T.

Correlations between downfield peaks and upfield representations of metabolites were of particular interest for these experiments, to investigate potential labels for peaks as previously indicated in the literature (4,10). As expected, downfield NAA positively correlates with upfield NAA concentrations, with a Spearman correlation coefficient of $r = 0.63$ ($P < 0.01$). However, none of the other downfield peaks significantly correlates with upfield metabolite concentrations. Of course, significant correlations can only be expected if there is sufficient true variation in metabolite content within the cohort at a limited random variance level. For all of the tested candidate metabolites, the cohort variance in upfield concentration was larger than that for upfield NAA, and one could expect this variance to be reflected downfield, but no significant covariance was detected. Therefore, although these and other upfield metabolites may certainly still be present as small components of the different downfield peaks, they do not appear to dominate any of the downfield peaks.

Exchange Fitting

Although up to 14 peaks were fitted in the spectra, several did not evidence exchange in these experiments, or had such slow exchange that its quantification was not possible. Exchange rates and T_1 values were obtainable only through the Bloch–McConnell model used for fitting the exchanging peaks, and are therefore only presented for the exchange-modeled peaks. Many of the resonances downfield are quite broad, indicating a potential for several underlying components; even exchanging peaks may consist of more than one component, with potentially different exchange rates for different components. However, the required simplicity of the model led to fitting the visible resonances with single peaks, with the T_1 and exchange rates therefore corresponding to averages over the components. Moreover, the occipital ROI and WM ROI provide very similar exchange rates and T_1 times for the fitted peaks, as demonstrated in Figures 6 and 7, with only two significant

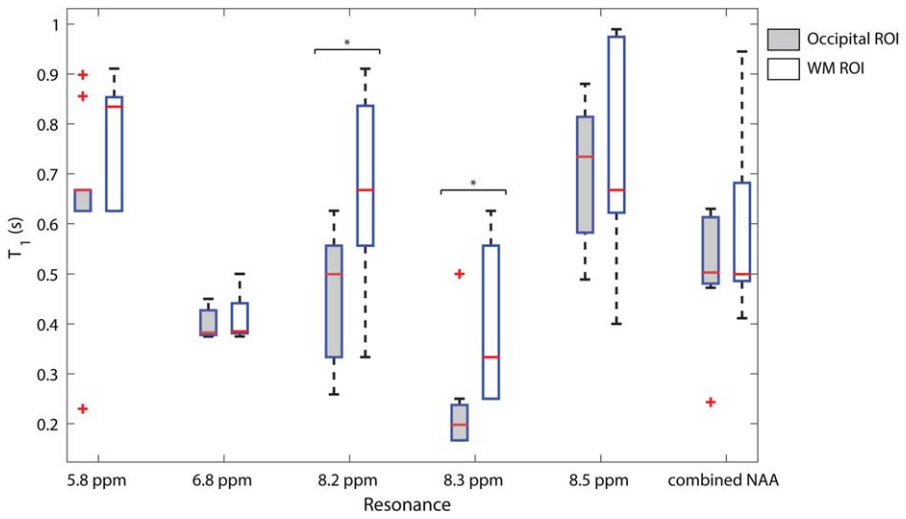

FIG. 6. Box plots indicating the range of T_1 values for the different resonances fitted with the Bloch–McConnell model. The edges of the box plots are at the 25th and 75th percentiles, while the red line in between indicates the median. Whiskers extend to the extremes of the data within 1.5 times the interquartile range (if no data are found within that range, they extend to the minimum or maximum). Outliers beyond the interquartile range are denoted by a cross. Significant differences ($P < 0.05$) between WM and occipital ROIs are denoted with asterisks.

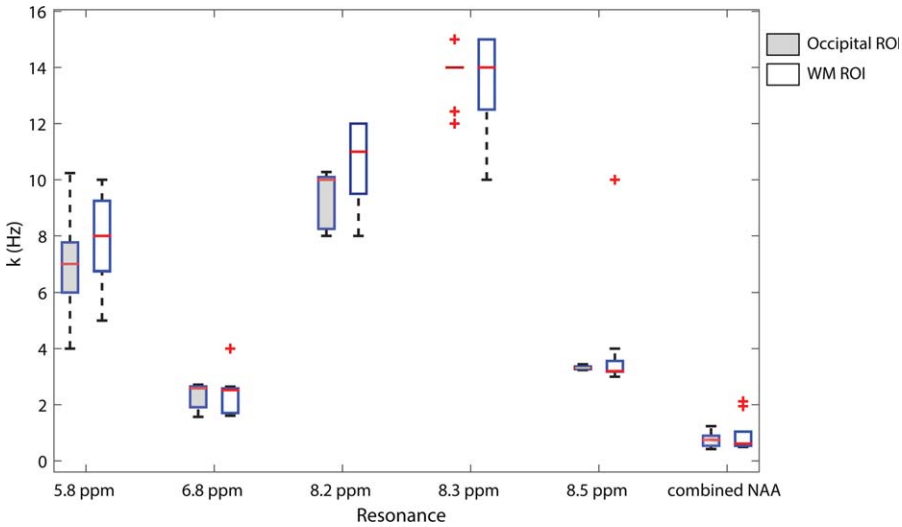

FIG. 7. Box plots indicating the range of exchange rates (*k*) for the different resonances fitted with the Bloch–McConnell model. The edges of the box plots are at the 25th and 75th percentiles, while the red line in between indicates the median. Whiskers extend to the extremes of the data within 1.5 times the interquartile range (if no data are found within that range, they extend to the minimum or maximum). Outliers beyond the interquartile range are denoted by a cross. No significant differences were found between the WM and GM exchange rates.

T_1 differences between the two voxels, for the 8.2- and 8.3-ppm peaks. Similar values are expected not only because of the fairly high percentage of WM in the occipital ROI, but also because of the equal proportions of metabolites and macromolecular baseline for WM and occipital ROIs upfield (38), therefore supporting the results found in this study.

Of particular interest are the peaks that were not fitted at 3 T (2), such as the 5.8-ppm peak, or the peaks that have improved separation, such as in the amide region from 8.2 to 8.5 ppm. The 5.8-ppm peak, which was previously suggested to originate from urea (4), has a mean exchange rate of 7.4 s^{-1} from the combined occipital ROI and WM ROI experiments. A low exchange rate on this order is expected, as this peak remains visible in experiments that use water suppression (4,39). The amide region has a range of exchange rates, from a mean of 3.7 s^{-1} for the 8.5-ppm peak, which is significantly slower than the 8.9 s^{-1} found at 3 T, to 9.9 and 13.6 s^{-1} for the 8.2- and 8.3-ppm peaks, respectively, which are higher rates than the 7.5 s^{-1} found for the broader 8.2-ppm peak fitted at 3 T (2). However, because of the differences of timing and localization between the current study and the 3T inversion transfer experiments (2), the limits of exchange that can be measured are also different. In this case, the measured amide peaks may consist of slightly different exchanging amides, and the model used for fitting may have also captured different peaks than before. Despite the minor differences between the 3T and 9.4T experiments, the exchange rates found in the current study are similarly in line with the lower end of what has been reported previously for the amide region using water exchange–filtered (WEX) experiments (40).

There is also limited exchange for the three peaks in the 6.8- to 7.3-ppm region, although at 3 T there appeared to be greater exchange visible. These differences may be explained by the addition of a broader peak in the 9.4T model, which would account for any subtler changes in the broader peaks that may be the result of macromolecular exchange, or other slow exchange from overlapping peaks. The combined NAA and its shoulder provided an average exchange rate of 0.8 s^{-1}, which is similar to what was found for the broader NAA peak that was modeled at 3 T; individually, neither the NAA doublet nor the broader shoulder provided meaningful exchange curves, and were therefore exchange-modeled together. It is possible that the fitting model had not been able to properly separate out the exchanging component.

Downfield T_1 relaxation values, varying from 0.22 to 0.77 s, are shorter than the previously published upfield values at 7 and 9.4 T (41,42), and are on the order of macromolecular T_1 values, which suggests that macromolecular components are contributing to the peaks. The downfield T_1 values are also higher than those found downfield at 3 T for similar experiments (2), a finding

Table 2
Mean Exchange Rates (*k*) and T_1 Values for Peaks Fitted Using the Bloch–McConnell Model for Occipital and WM ROIs, Presented as Mean ± Standard Deviation Over the Cohort

	Occipital ROI exchange rate Mean $k \pm$ SD (s^{-1})	WM ROI exchange rate Mean $k \pm$ SD (s^{-1})	Occipital ROI T_1 Mean $T_1 \pm$ SD (s)	WM ROI T_1 Mean $T_1 \pm$ SD (s)
5.8 ppm	6.76 ± 1.59	8.00 ± 1.63	0.65 ± 0.16	0.77 ± 0.11
6.8 ppm	2.34 ± 0.44	2.42 ± 0.69	0.40 ± 0.03	0.41 ± 0.04
8.2 ppm	9.32 ± 0.91	10.6 ± 1.50	0.46 ± 0.12	0.69 ± 0.18
8.3 ppm	13.8 ± 0.79	13.4 ± 1.77	0.22 ± 0.09[a]	0.41 ± 0.14[a]
8.5 ppm	3.31 ± 0.06	4.05 ± 2.12	0.71 ± 0.14[a]	0.76 ± 0.20[a]
Combined NAA	0.74 ± 0.23	0.92 ± 0.60	0.52 ± 0.11	0.58 ± 0.16

SD, standard deviation.
[a]A significant difference was found between the occipital and the WM ROI concentrations with $P < 0.05$.

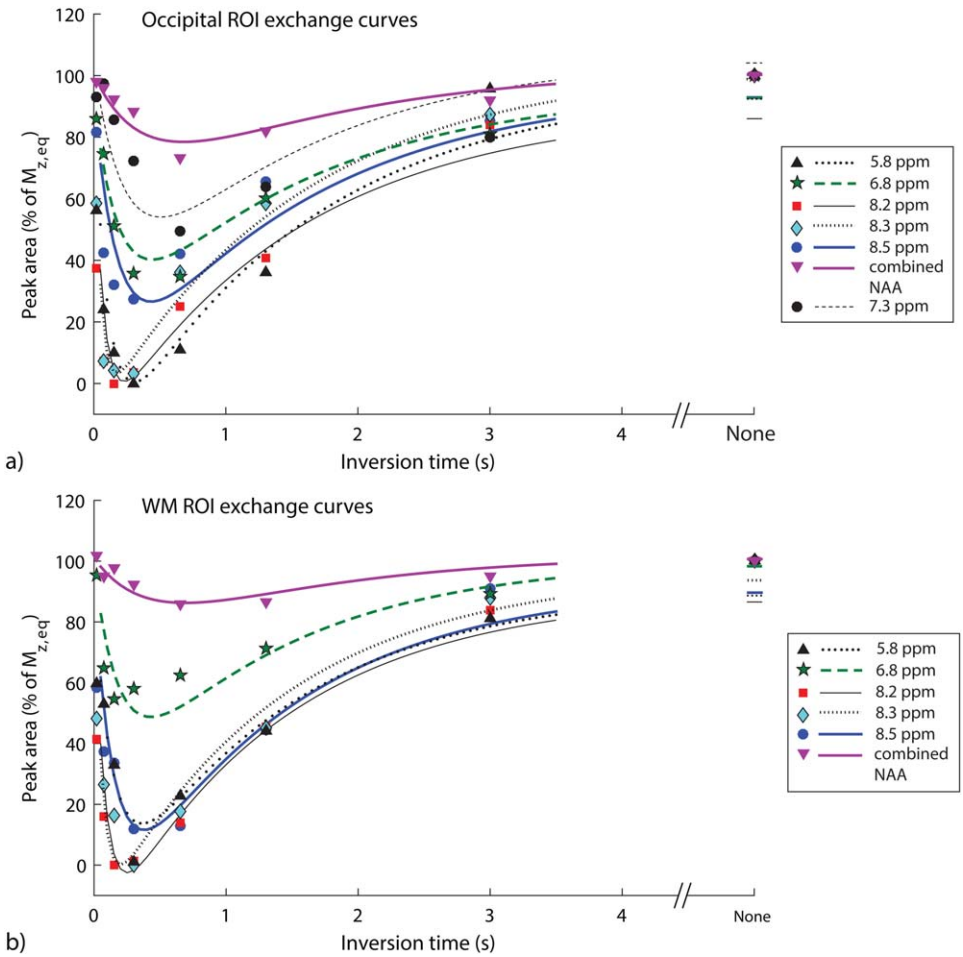

FIG. 8. Exchange curves showing the peak area as a percentage of the equilibrium magnetization for the occipital ROI metabolites (**a**) and the WM ROI metabolites (**b**) that were fitted for the average over all individuals.

that is expected, as proton T_1 relaxation times increase with field strength (12). Although the T_1 relaxation times are similar to those at 7 T, only the order of magnitude should be compared, as the current study extracted exchange-independent times, and a previous 7T study, which was a different experiment altogether, did not account for exchange effects (4). The 6.8-ppm peak has a mean T_1 of 0.41 s, which is similar to that found for the 6.8-ppm resonance at 7 T, and again on the order of the T_1s for macromolecules. The combined NAA peak here has a much lower T_1 than that found for NAA at 7 T; however, in this case the combined NAA peak cannot give us a meaningful estimate of T_1, and was of more interest for its exchange rate. At 3 T, this peak was modeled as one peak only, because of the broader peaks at lower field strengths. The T_1's for the faster exchanging peaks vary, although the low T_1 for the 8.3-ppm peak may have been partially compensated by the faster exchange rate.

Limitations

Exchange with inverted, as opposed to saturated, water magnetization has the potential to affect the metabolite peak sizes more strongly, such that for fast-exchanging species the peak may even be inverted. However, it was discovered upon fitting of the water inversion curves after all measurements had been completed that despite B_1 optimization, the effective flip angle for the water inversion pulse had not reached higher than 131°. Further investigation into the potential cause for the low inversion efficiency led to the suspicion that radiation damping (43) may have played a role in reducing the maximum signal achievable after applying the non-spatially selective inversion pulse. In addition, the long duration of the pulse (40 ms) may have allowed T_2 relaxation effects to reduce the signal during the RF pulse itself, as the pulse duration is on the order of brain-water T_2 at high fields (4,44). It is likely that with 100% efficiency and a shorter duration of the inversion pulse, the metabolite peaks would have evidenced exchange more strongly, improving the accuracy of exchange rate and T_1 calculations.

A further experimental issue found after completion of the study was that there was an unexpectedly large asymmetry for the water signal in up- versus downfield inverted spectra in MC. The size of the effect and the fact that downfield inverted scans showed larger water amplitude than upfield inverted acquisitions indicate that the asymmetry is not exchange-related, but more likely to be an effect of experimental asymmetry, including potential frequency drift after center-frequency adjustment.

The measurable exchange rates in this experiment are limited by several factors, including the TE and the

global water inversion pulse duration. The TE for these experiments was 10 ms, limiting our ability to measure exchange rates faster than 100 s^{-1} (corresponding to a lifetime of less than approximately 10 ms), as any spins exchanging too fast would no longer be properly refocused for measurement. Furthermore, the long inversion-pulse duration of 40 ms implied that any fast exchange of more than approximately 25 s^{-1} would be moderated even before the inversion-recovery period started, reducing the ability to properly quantify it. Although this pulse was optimized for a small bandwidth to reach close to water, it would be clearly more efficient to have a shorter inversion pulse for those resonances further away from water. Another limiting effect on measuring the exchange rates is evolution into out-of-phase signal as a result of exchange during the TM period, which was relatively long at 45 ms because of the MC pulse. This evolution into out-of-phase signal is caused by the differing effective chemical shifts in the half echo periods before and after TM (analogous to a single T_2 trace from a 2-dimensional exchange spectroscopy (45) experiment with an acquisition delay in T_2 equal to the T_1 dwell time (i.e., TE/2 in our case)). Based on simulations, there should be some measurable effect for faster-exchanging species. However, no such signal behavior was found in the data, leading to the conclusion that any fast-exchanging species that would lead to out-of-phase components were exchanging too fast to be measured by this experiment anyway.

For the fast-exchanging resonances, in particular at 8.2 and 8.3 ppm, the minimum of the exchange curve often occurred at the second inversion time, rendering accurate fitting of the exchange curve difficult due to the lack of points describing the initial decrease in the exchange curve. In those cases, the recovery component of the curve had more weighting, and the $M_{z,eq}$ could compensate for T_1 and k more than for the slower exchange curves. The 41-ms inversion time was already the minimum achievable on the system; however, additional points before 96 ms would have helped for the faster-exchanging resonances. Unfortunately, because of the restrictions on the duration of the experiment, further inversion times were not acquired.

Furthermore, with regard to the missing correlations leading to a labeling of downfield peaks, the fit model for the downfield spectrum is heuristic. The specific choice of components—although chosen as carefully as possible with Occam's razor in mind to represent the spectrum's main content—may hide some covariance with upfield metabolites, where again some of the variance will be spurious for the smaller spectral contributions.

CONCLUSIONS

This study presents the first in-depth investigation of downfield metabolites at 9.4 T, as well as first comparisons of downfield and upfield peak concentrations. Furthermore, exchange rates and T_1 values for at least 6 of the 12 measured resonances downfield were calculated. Increased peak separation of the 8.2- to 8.5-ppm region allowed for improved characterization of the amide region and corresponding exchange rates. Moreover, for the first time it was possible to quantify the exchange rate of the 5.8-ppm peak, tentatively assigned to urea (4,39), in vivo in human brain. Correlations between downfield peaks and known upfield metabolite concentrations were insignificant, except for NAA. This suggests that, although the compared metabolites might form components of these peaks, they probably do not make up a significant portion of them.

REFERENCES

1. Dreher W, Leibfritz D. New method for the simultaneous detection of metabolites and water in localized in vivo 1H nuclear magnetic resonance spectroscopy. Magn Reson Med 2005;54:190–195.
2. MacMillan EL, Chong DGQ, Dreher W, Henning A, Boesch C, Kreis R. Magnetization exchange with water and T1 relaxation of the downfield resonances in human brain spectra at 3.0 T. Magn Reson Med 2011;65:1239–1246.
3. McLean MA, Barker GJ. Concentrations and magnetization transfer ratios of metabolites in gray and white matter. Magn Reson Med 2006;56:1365-1370.
4. Fichtner ND, Henning A, Zoelch N, Boesch C, Kreis R. Elucidation of the downfield spectrum of human brain at 7T using multiple inversion recovery delays and echo times. Magn Reson Med 2017;78:11–19.
5. De Graaf RA, De Feyter HM, Brown PB, Nixon TW, Rothman DL, Behar KL. Detection of cerebral NAD+ in humans at 7T. Magn Reson Med 2017;78:828–835.
6. Vermathen P, Capizzano AA, Maudsley AA. Administration and (1)H MRS detection of histidine in human brain: application to in vivo pH measurement. Magn Reson Med 2000;43:665–675.
7. Ward KM, Aletras AH, Balaban RS. A new class of contrast agents for MRI based on proton chemical exchange dependent saturation transfer (CEST). J Magn Reson 2000;143:79–87.
8. Xu X, Yadav NN, Knutsson L, et al. Dynamic glucose-enhanced (DGE) MRI: translation to human scanning and first results in glioma patients. Tomography 2015;1:105–114.
9. Jones CK, Schlosser MJ, van Zijl PCM, Pomper MG, Golay X, Zhou J. Amide proton transfer imaging of human brain tumors at 3T. Magn Reson Med 2006;56:585–592.
10. Henning A, Fuchs A, Boesch C, Boesiger P, Kreis R. Downfield spectra at ultrahigh field. In Proceedings of the 16th Annual Meeting of ISMRM, Toronto, Canada, 2008. p. 777.
11. Crooks L, Arakawa M, Hoenninger J, McCarten B, Watts J, Kaufman L. Magnetic resonance imaging: effects of magnetic field strength. Radiology 1984;151:127–133.
12. De Graaf RA, Brown PB, McIntyre S, Nixon TW, Behar KL, Rothman DL. High magnetic field water and metabolite proton T1 and T2 relaxation in rat brain in vivo. Magn Reson Med 2006;56:386–394.
13. Vaughan JT, Garwood M, Collins CM, et al. 7T vs. 4T: RF power, homogeneity, and signal-to-noise comparison in head images. Magn Reson Med 2001;46:24–30.
14. Giapitzakis IA, Kreis R, Henning A. Characterization of the macromolecular baseline with a metabolite-cycled double-inversion recovery sequence in the human brain at 9.4T. In Proceedings of the 24th Annual Meeting of ISMRM, Singapore, 2016. p. 16.
15. Frahm J, Merboldt KD, Haenicke W. Localized proton spectroscopy using stimulated echoes. J Magn Reson 1987;72:502–508.
16. Avdievich N, Giapitzakis IA, Henning A. Optimization of the receive performance of a tight-fit transceiver phased array for human brain imaging at 9.4T. In Proceedings of the 25th Annual Meeting of ISMRM, Honolulu, Hawaii, USA, 2017. p. 4309.
17. Avdievich N, Walzog J, Steffen T, Henning A. Development of a low cost multi-channel tune and match device for transceiver arrays at high magnetic fields. In Proceedings of the 32nd Annual Scientific Meeting of ESMRMB, Edinburgh, United Kingdom, 2016. p. S445.
18. Giapitzakis IA, Shao T, Avdievich N, Mekle R, Kreis R, Henning A. Metabolite-cycled STEAM and semi-LASER localization for MR spectroscopy of the human brain at 9.4T. Magn Reson Med 2018;79:1841–1850.
19. Gruetter R, Tkac I. Field mapping without reference scan using asymmetric echo-planar techniques. Magn Reson Med 2000;43:319–323.

20. Versluis MJ, Kan HE, van Buchem MA, Webb AG. Improved signal to noise in proton spectroscopy of the human calf muscle at 7 T using localized B1 calibration. Magn Reson Med 2010;63:207–211.
21. Hock A, MacMillan EL, Fuchs A, Kreis R, Boesiger P, Kollias SS, Henning A. Non-water-suppressed proton MR spectroscopy improves spectral quality in the human spinal cord. Magn Reson Med 2013;69: 1253–1260.
22. Klose U. In vivo proton spectroscopy in presence of eddy currents. Magn Reson Med 1990;14:26–30.
23. Bydder M, Hamilton G, Yokoo T, Sirlin CB. Optimal phased array combination for spectroscopy. Magn Reson Imaging 2008;26:847–850.
24. Naressi A, Couturier C, Devos JM, Janssen M, Mangeat C, de Beer R, Graveron-Demilly D. Java-based graphical user interface for the MRUI quantitation package. Magn Reson Mater Phy 2001;12:141–152.
25. Chong DGQ, Kreis R, Bolliger C, Boesch C, Slotboom J. Two-dimensional linear-combination model fitting of magnetic resonance spectra to define the macromolecule baseline using FiTAID, a Fitting Tool for Arrays of Interrelated Datasets. Magn Reson Mater Phy 2011;24:147–164.
26. Soher B, Semanchuk P, Todd D, Steinberg J, Young K. VeSPA: integrated applications for RF pulse design, spectral simulation and MRS data analysis. In Proceedings of the 19th Annual Meeting of ISMRM, Montréal, Québec, Canada, 2011. p. 1410.
27. Rothman DL, Behar KL, Prichard JW, Petroff OA. Homocarnosine and the measurement of neuronal pH in patients with epilepsy. Magn Reson Med 1997;38:924–929.
28. Cavassila S, Deval S, Huegen C, van Ormondt D, Graveron-Demilly D. Cramer-Rao bounds: an evaluation tool for quantitation. NMR Biomed 2001;14:278–283.
29. Ernst T, Kreis R, Ross BD. Absolute quantitation of water and metabolites in the human brain. I. Compartments and water. J Magn Reson Series B 1993;102:1–8.
30. Provencher SW. Automatic quantitation of localized in vivo (1)H spectra with LCModel. NMR Biomed 2001;14:260–264.
31. Smith SA, Levante TO, Meier BH, Ernst RR. Computer simulations in magnetic resonance. An object-oriented programming approach. J Magn Reson Series A 1994;106:75–105.
32. Govind V, Young K, Maudsley AA. Corrigendum: proton NMR chemical shifts and coupling constants for brain metabolites. Govindaraju V, Young K, Maudsley AA, NMR Biomed. 2000; 13: 129–153. NMR Biomed 2015;28: 923–924.
33. Govindaraju V, Young K, Maudsley AA. Proton NMR chemical shifts and coupling constants for brain metabolites. NMR Biomed 2000;13: 129–153.
34. Kreis R, Bolliger CS. The need for updates of spin system parameters, illustrated for the case of gamma-aminobutyric acid. NMR Biomed 2012;25:1401–1403.
35. McConnell HM. Reaction rates by nuclear magnetic resonance. J Chem Phys 1958;28:430–431.
36. Pouwels PJW, Frahm J. Regional metabolite concentrations in human brain as determined by quantitative localized proton MRS. Magn Reson Med 1998;39:53–60.
37. Kanazawa A, Sano RM. A method of determination of homocarnosine and its distribution in mammalian tissues. J Neurochem 1967;14:211–214.
38. Snoussi K, Gillen JS, Horska A, Puts NAJ, Pradhan S, Edden RAE, Barker PB. Comparison of brain gray and white matter macromolecule resonances at 3 and 7 Tesla. Magn Reson Med 2015;74:607–613.
39. Watanabe T, Frahm J, Michaelis T. Amide proton signals as pH indicator for in vivo MRS and MRI of the brain—responses to hypercapnia and hypothermia. Neuroimage 2016;133:390–298.
40. van Zijl PC, Zhou J, Mori N, Payen JF, Wilson D, Mori S. Mechanism of magnetization transfer during on-resonance water saturation. A new approach to detect mobile proteins, peptides, and lipids. Magn Reson Med 2003;49:440–449.
41. Xin L, Schaller B, Mlynarik V, Lu H, Gruetter R. Proton T1 relaxation times of metabolites in human occipital white and gray matter at 7 T. Magn Reson Med 2013;69:931–936.
42. Deelchand DK, Van De Moortele PF, Adriany G, Iltis I, Andersen P, Strupp JP, Vaughan JT, Ugurbil K, Henry PG. In vivo 1H NMR spectroscopy of the human brain at 9.4 T: initial results. J Magn Reson 2010;206:74–80.
43. Krishnan VV, Murali N. Radiation damping in modern NMR experiments: progress and challenges. Prog Nucl Magn Reson Spectrosc 2013;68:41–57.
44. Marjanska M, Auerbach EJ, Valabrègue R, Van de Moortele P-F, Adriany G, Garwood M. Localized 1H NMR spectroscopy in different regions of human brain in vivo at 7 T: T2 relaxation times and concentrations of cerebral metabolites. NMR Biomed 2012;25:332–339.
45. Jeener J, Meier BH, Bachmann P, Ernst RR. Investigation of exchange processes by two-dimensional NMR spectroscopy. J Chem Phys 1979; 71:4546–4553.

SUPPORTING INFORMATION

Additional Supporting Information may be found in the online version of this article.

Fig. S1. Representative WM ROI inversion transfer series from an individual volunteer, along with the corresponding fitted spectra and residuals, indicating the quality of the data for the WM ROI and the suitability of the model.

Fig. S2. Scatter plots for the range of correlations tested between the upfield and downfield peak areas. Occipital ROI data points are shown in blue; WM ROI data points are shown in red. The downfield peaks are along the x-axes, and the upfield peaks along the y-axes, as labeled in the figure.